# Experimental characterization of turbulent superstructures in large aspect ratio Rayleigh-Bénard convection

## Dissertation

zur Erlangung des akademischen Grades

## Doktoringenieur
## (Dr.-Ing.)

vorgelegt der
Fakultät für Maschinenbau der
Technischen Universität Ilmenau

von Herrn

## M. Sc. Sebastian Moller

geboren am 16.05.1993 in Schweinfurt, Deutschland

1. Gutachter: Univ.-Prof. Dr.-Ing. Christian Cierpka
2. Gutachter: Univ.-Prof. Dr. rer. nat. habil. Christian J. Kähler
3. Gutachter: Univ.-Prof. Dr. rer. nat. Michael Wilczek

Tag der Einreichung: 06.07.2021
Tag der wissenschaftlichen Aussprache: 22.12.2021

# Abstract

Aiming at a better understanding of geophysical and astrophysical settings, the investigation of thermally driven fluid flows has attracted great attention in the last decades. In this context, the so-called Rayleigh-Bénard model has established as one of the most studied fluid-mechanical systems, since this reduces the hardly representable complexity of the natural environment with its enormous diversity to a fluid volume, which is uniformly heated from below and cooled from above. Despite this reduction of the complexity, this model is capable of representing the main characteristics of thermal convection. The flow in such a system, well-known as the Rayleigh-Bénard convection, exhibits flow structures on a large range of length scales. In this work, the so-called turbulent superstructures are studied. These horizontally stretched structures, which appear when the fluid layer has a much larger horizontal extent compared to the vertical distance between the hot and cold boundary, have mainly been investigated with numerical simulations so far. Therefore, the aim of the present work is to get a better impression of the turbulent superstructures from the experimental point of view for the first time. For the investigation of the superstructures a Rayleigh-Bénard cell with dimensions of $l \times w \times h = 700\,\mathrm{mm} \times 700\,\mathrm{mm} \times 28\,\mathrm{mm}$, thus having an aspect ratio of $\Gamma = l/h = 25$, is set up. Here, water is used as the working fluid in the cell for all the experiments. In order to analyze the Rayleigh-Bénard flow, thermochromic liquid crystals are applied as tracer particles in the flow, which allows to perform simultaneous measurements of the temperature and velocity field in horizontal planes of the cell. While the velocity field is measured via the temporal displacement of the thermochromic liquid crystals using the established Particle Image Velocimetry, the temperature field is determined by evaluating their color shade, which depends on the temperature upon illumination with white light. With regard to the accurate determination of the temperature, this measuring technique is extensively characterized and the main influencing factors on the measurement uncertainty are discussed. Since the investigation of the turbulent superstructures with this optical measuring technique requires optical access to the flat Rayleigh-Bénard cell, the setup is specially designed and allows to observe the flow through a transparent cooling plate. The design process from the engineering point of view is thoroughly explained. In the evaluation of the measurements the large-scale structures are uncovered in both the temperature and the velocity field. The size of the turbulent superstructures is investigated in dependency of the Rayleigh number Ra, which characterizes the thermal driving force of the flow and is here approximately varied in the range $2 \times 10^5 \leq \mathrm{Ra} \leq 2 \times 10^6$. On the basis of the measurements conducted over extended time intervals, the long-term behavior of the superstructures is analyzed, thereby demonstrating their gradual reorganization. Since the combined measurement of the temperature and of the velocity field in the horizontal planes enables to estimate the local heat flux, this possibility is presented as well. In order to assess the experimental results of this work, these are compared to the outcomes of numerical simulations.

# Kurzzusammenfassung

Die Untersuchung von thermisch induzierten Strömungen hat in den letzten Jahrzehnten eine enorme Aufmerksamkeit erfahren, um geophysikalische und astrophysikalische Systeme besser verstehen zu können. Hierfür hat sich das sogenannte Rayleigh-Bénard Modell als eines der meist untersuchten fluidmechanischen Systeme etabliert, da es die kaum abzubildende Komplexität von natürlichen Systemen in ihrer Mannigfaltigkeit auf ein Fluidvolumen reduziert, welches von unten isotherm erwärmt und von oben isotherm gekühlt wird. Trotz dieser Reduzierung an Komplexität können mit diesem Modell die wesentlichen Eigenschaften von thermischer Konvektion abgebildet werden. Die Strömung in einem solchen System, welche als Rayleigh-Bénard Konvektion bekannt ist, weist Strömungsstrukturen auf unterschiedlichsten Längenskalen auf. In der vorliegenden Arbeit werden die sogenannten Superstrukturen untersucht. Diese sich in horizontaler Richtung weit erstreckenden Strukturen treten in Erscheinung, wenn die horizontale Dimension der Fluidschicht wesentlich größer als der vertikale Abstand zwischen der erwärmten Unterseite und der gekühlten Oberseite ist. Da die Superstrukturen bisher im Wesentlichen anhand von numerischen Simulationen untersucht wurden, soll in dieser Arbeit erstmals vom experimentellen Standpunkt ein besserer Eindruck gewonnen werden. Zur Untersuchung der Superstrukturen wird eine Rayleigh-Bénard Zelle mit den Abmessungen $l \times w \times h = 700\,\mathrm{mm} \times 700\,\mathrm{mm} \times 28\,\mathrm{mm}$ und folglich mit einem Aspektverhältnis von $\Gamma = l/h = 25$ aufgebaut. Bei allen Experimenten wird diese Zelle mit Wasser als Arbeitsmedium befüllt. Um die Rayleigh-Bénard Strömung zu untersuchen, werden thermochrome Flüssigkristalle als Impfpartikel der Strömung beigefügt, sodass simultane Messungen des Temperatur- und Geschwindigkeitsfeldes in horizontalen Ebenen der Zelle vorgenommen werden können. Während das Geschwindigkeitsfeld mittels der Bewegung der thermochromen Flüssigkristalle im zeitlichen Verlauf anhand der etablierten Partikelbild-Geschwindigkeitsmessung (Particle Image Velocimetry) bestimmt wird, basiert die Messung des Temperaturfelds auf der farblichen Erscheinung der thermochromen Flüssigkristalle, welche unter der Beleuchtung von Weißlicht temperaturabhängig ist. Im Hinblick auf die genaue Bestimmung der Temperatur wird diese Messtechnik umfänglich charakterisiert, wobei die wesentlichen Einflussfaktoren auf die Messunsicherheit diskutiert werden. Da die Untersuchung der turbulenten Superstrukturen mittels dieser Messtechnik den optischen Zugang zur flachen Rayleigh-Bénard Zelle erfordert, ist der Aufbau speziell konstruiert und ermöglicht die Beobachtung der Strömung durch eine transparente Kühlplatte. Der Entwicklungsprozess wird in der Arbeit aus ingenieurstechnischer Sicht genauestens erklärt. Bei der Auswertung der Messungen kommen die großskaligen Strukturen sowohl im Temperaturfeld als auch im Geschwindigkeitsfeld zum Vorschein. Die Größe der Superstrukturen wird untersucht in Abhängigkeit der Rayleigh-Zahl Ra, welche den thermischen Antrieb der Strömung beschreibt und in der vorliegenden Arbeit etwa im Bereich $2 \times 10^5 \leq \mathrm{Ra} \leq 2 \times 10^6$ variiert wird. Auf der Basis dieser Messungen, welche

jeweils einen großen Zeitraum abdecken, wird das Langzeitverhalten der Superstrukturen analysiert, womit deren langsam voranschreitende Umstrukturierung gezeigt wird. Da die kombinierte Messung des Temperatur- und Geschwindigkeitsfeldes in den horizontalen Messebenen die Berechnung des lokalen Wärmestroms ermöglicht, wird diese Möglichkeit ebenfalls demonstriert. Um die experimentellen Ergebnisse dieser Arbeit bewerten zu können, werden jene mit den Resultaten aus numerischen Simulationen verglichen.

# Acknowledgments

and Dr. Rainer Hain from the *Universität der Bundeswehr München* for the lending of a scientific color camera, that has been applied for some measurements presented in this work.

As the experimental facility, which has been set up in the first two years of my time at the institute, consists of many components requiring a special manufacturing, some of those have been purchased from external companies. However, most of the components could be manufactured in the mechanical workshop of our university. The extensive labor of Jürgen Bretschneider and his team in the workshop is much appreciated. Moreover, I wish to thank Björn Herrnberger for his help concerning the buildup of glass components.

Even though the current work is based on experimental investigations, the results obtained from numerical simulations in our *Institute of Thermodynamics and Fluid Mechanics* have originally been the main motivation to build the experimental facility, such that the experimental and numerical findings can be compared. At this point I would like to thank Prof. Jörg Schumacher of the department for fluid mechanics and the former team-mate Dr. Ambrish Pandey for valuable discussions about the scientific problem. Furthermore, they provided some data of their numerical simulations, which was a great help to get deeper insights and is also acknowledged.

On the basis of the measurements performed in the scope of this thesis, several articles for conferences and peer-reviewed manuscripts have been published. In each case, this has been a lot of effort. I want to take this opportunity to thank once more Prof. Christian Cierpka, Dr. Christian Resagk and Dr. Jörg König, who have oftentimes been the co-authors and contributed many suggestions to improve the manuscripts.

The administrative support by our secretary Colette Wilhelm over the last years must not be forgotten, since it was really helpful, and I would like to thank her for that.

I also want to emphasize, that the years at the *Institute of Thermodynamics and Fluid Mechanics* were in general a great time, not only from the scientific point of view, but especially due to the working environment. It was a pleasure for me to work in this team together with all the nice colleagues.

Finally, I want to thank my family for the strong encouragement since the beginning of my studies. I cordially express many words of thanks to my parents, Waltraud and Robert, to my brother Christian and especially to my girlfriend Desirée. Their support in every respect has enabled all that and I cannot thank them enough.

# Contents

# Symbols and acronyms

Preliminary note: Many variables are used in different forms for the analysis in the scope of this work, meaning that these might for instance be non-dimensionalized or processed with filtering techniques, but such additional modifications are not included in the following list of the symbols used in this work. Furthermore, in order to keep the length of the list in limits, running indices and the symbols introduced for the description of the results in the appendix of the present work are not considered. However, each symbol is explained in the context of its use.

## Symbols - Roman characters

| Symbol | Description | Unit |
|---|---|---|
| $A$ | Horizontal cross-sectional area of the Rayleigh-Bénard cell | $\mathrm{m}^2$ |
| $B$ | Pixel intensity of the blue color channel | 1 |
| $\vec{B}$ | Magnetic flux density | T |
| $c_n$ | Coefficients for functional approximations | 1 |
| $c_{\mathrm{thres}}$ | Threshold for the characterization of the light sheet thickness | 1 |
| $c_{\mathrm{II}}$ | Sample Pearson's correlation coefficient | 1 |
| $d$ | Diameter of the cylindrical Rayleigh-Bénard cell | m |
| $e$ | Euler's number | 1 |
| $e_{\mathrm{r}}$ | Uncertainty ratio between the vertical and horizontal velocity components | 1 |
| $\vec{e}_z$ | Cartesian unit vector pointing against gravity | 1 |
| $E_k$ | Energy spectrum | $\mathrm{m}^3\,\mathrm{s}^{-2}$ |
| $f$ | Frequency | $\mathrm{s}^{-1}$ |
| $\vec{f}$ | Body force density | $\mathrm{m}\,\mathrm{s}^{-2}$ |
| $f_{\mathrm{foc}}$ | Focal length | m |
| $F, \hat{F}$ | Input and output of the Discrete/Fast Fourier Transform | nonspecific |
| $g$ | Magnitude of the gravitational acceleration | $\mathrm{m}\,\mathrm{s}^{-2}$ |
| $G$ | Pixel intensity of the green color channel | 1 |
| $h$ | Height of the Rayleigh-Bénard cell | m |
| $H$ | Hue extracted from an $RGB$-triplet | 1 |
| $i$ | Imaginary unit | 1 |
| $I, I'$ | Intensities of the pixels within the first and second image for the cross-correlation of PIV | 1 |

| Symbol | Description | Unit |
|---|---|---|
| $I_{\tilde{T},\mathrm{dir}}$, $I_{\tilde{u}_z,\mathrm{dir}}$ | Directional intensities of the power spectrum obtained from the non-dimensionalized field of the temperature and of the vertical velocity component | 1 |
| $I_{\tilde{T},\mathrm{wl}}$, $I_{\tilde{u}_z,\mathrm{wl}}$ | Wavelength intensities of the power spectrum obtained from the non-dimensionalized field of the temperature and of the vertical velocity component | 1 |
| $k$ | Wavenumber | $\mathrm{m}^{-1}$ |
| $l$ | Length of the cuboidal Rayleigh-Bénard cell | m |
| $l_{\mathrm{diff}}$ | Axial length of the diffusers in the cooling circuit | m |
| $L_{\mathrm{c}}$ | Characteristic length | m |
| $M_T, M_U$ | Number of pixels in each direction of the squared interrogation windows of the temperature and velocity field | 1 |
| $N_T, N_U$ | Number of interrogation windows for the investigation of the temperature and velocity field | 1 |
| Nu | Nusselt number | 1 |
| $\mathrm{Nu}_{\mathrm{loc}}$ | Local Nusselt number | 1 |
| $p$ | Pressure | $\mathrm{N\,m}^{-2}$ |
| $P_{\tilde{T}}, P_{\tilde{u}_z}$ | Power spectrum of the non-dimensionalized fields of the temperature and the vertical velocity component | 1 |
| Pr | Prandtl number | 1 |
| $\dot{Q}$ | Heat flux | W |
| $R$ | Pixel intensity of the red color channel | 1 |
| Ra | Rayleigh number | 1 |
| $\mathrm{Ra}_{\mathrm{c}}$ | Critical Rayleigh number | 1 |
| Re | Reynolds number | 1 |
| $s_T, s_U$ | Size of the squared interrogation windows of the temperature and velocity field | m |
| $S$ | Saturation extracted from an $RGB$-triplet | 1 |
| $t$ | Time | s |
| $t_{\mathrm{avg}}$ | Averaging time for the exposure of the turbulent superstructures | s |
| $t_{\mathrm{exp}}$ | Exposure time of the cameras | s |
| $t_{\mathrm{f}}$ | Free-fall time | s |
| $t_{\mathrm{rec}}$ | Recording time for the image series of the measurements | s |
| $t_{\mathrm{total}}$ | Total measuring time | s |
| $T$ | Temperature | K |
| $T_{\mathrm{cp}}, T_{\mathrm{hp}}$ | Temperature of the cooling and heating plate | K |
| $T_{\mathrm{cw}}, T_{\mathrm{hw}}$ | Temperature of the cooling and heating water | K |
| $T_{\mathrm{s}}$ | Set temperature during the calibration measurements | K |
| $u_{\mathrm{x}}, u_{\mathrm{y}}, u_{\mathrm{z}}$ | Velocity components in the Cartesian coordinate system yielding the velocity vector $\vec{u} = (u_{\mathrm{x}}, u_{\mathrm{y}}, u_{\mathrm{z}})$ | $\mathrm{m\,s}^{-1}$ |
| $U$ | Absolute value of the horizontal velocity | $\mathrm{m\,s}^{-1}$ |
| $U_{\mathrm{c}}$ | Characteristic velocity | $\mathrm{m\,s}^{-1}$ |
| $V$ | Value extracted from an $RGB$-triplet | 1 |

| Symbol | Description | Unit |
|---|---|---|
| $\dot{V}_\mathrm{cw}, \dot{V}_\mathrm{hw}$ | Flow rate of the cooling and heating water | $\mathrm{m^3\,s^{-1}}$ |
| $w$ | Width of the cuboidal Rayleigh-Bénard cell | m |
| $w_\mathrm{diff,in}$ | Inlet width of the diffusers in the cooling circuit | m |
| $x, y, z$ | Cartesian coordinates in the physical space yielding the position vector $\vec{x} = (x, y, z)$ | m |
| $x_\mathrm{fov}, y_\mathrm{fov}$ | Physical dimensions of the field of view of the cameras applied for the measurements | m |
| $X, Y$ | Cartesian coordinates within an image | pixel |
| $\vec{X}$ | Displacement vector of the PIV measurements | pixel |

# Symbols - Greek characters

| Symbol | Description | Unit |
|---|---|---|
| $\alpha$ | Volumetric thermal expansion coefficient | $\mathrm{K^{-1}}$ |
| $\beta_\mathrm{Nu}, \beta_\mathrm{Re}$ | Scaling exponents for Nu and Re | 1 |
| $\Gamma$ | Aspect ratio of the Rayleigh-Bénard cell | 1 |
| $\delta_\mathrm{ls}$ | Thickness of the white light sheet | m |
| $\delta_T, \delta_U$ | Thermal/viscous boundary layer thickness | m |
| $\Delta t_\mathrm{PIV}$ | Time delay between the images used for the cross-correlation of PIV measurements | s |
| $\Delta T$ | Temperature difference between the isothermal plates | K |
| $\Delta T_\mathrm{circuits}$ | Temperature difference between the heating and cooling water streaming through the isothermal plates | K |
| $\Theta_\mathrm{diff}$ | Opening angle of the diffusers in the cooling circuit | ° |
| $\Theta_\mathrm{lin}$ | Dimensionless temperature difference to the linear equilibrium profile | 1 |
| $\Theta_\mathrm{nozz}$ | Tapering angle of the nozzles in the cooling circuit | ° |
| $\Theta_\mathrm{obj}$ | Aperture angle of the objective lenses | ° |
| $\kappa$ | Thermal diffusivity | $\mathrm{m^2\,s^{-1}}$ |
| $\lambda$ | Wavelength | m |
| $\lambda_\mathrm{th}$ | Thermal conductivity | $\mathrm{W\,m^{-1}\,K^{-1}}$ |
| $\lambda_T$ | Wavelength corresponding to the turbulent superstructures in the temperature field | m |
| $\lambda_{u_z}$ | Wavelength corresponding to the turbulent superstructures in the field of the vertical velocity component | m |
| $\mu_I, \mu_{I'}$ | Average intensity of the pixels within the first and second image for the cross-correlation of PIV | 1 |
| $\nu$ | Kinematic viscosity | $\mathrm{m^2\,s^{-1}}$ |
| $\rho$ | Mass density | $\mathrm{kg\,m^{-3}}$ |
| $\sigma_H$ | Standard deviation of the hue | 1 |
| $\sigma_{\mathrm{Nu_{loc}}}$ | Standard deviation of the local Nusselt number | 1 |
| $\sigma_T$ | Standard deviation of the temperature | K |
| $\sigma_{u_\mathrm{i}}$ | Standard deviation of the velocity components $(u_\mathrm{x}, u_\mathrm{y}, u_\mathrm{z})$ | $\mathrm{m\,s^{-1}}$ |

| Symbol | Description | Unit |
|---|---|---|
| $\sigma_{|\vec{X}|}$ | Typical uncertainty for the determination of the displacement vector in PIV measurements | pixel |
| $\phi$ | Azimuthal angle in the power spectrum | rad |
| $\varphi_{\mathrm{cc}}$ | Observation angle adjusted at the color camera | ° |
| $\varphi_{\mathrm{mc}}$ | Observation angle adjusted at the monochrome cameras | ° |
| $\omega$ | Angular frequency for the functional approximation of hue | rad |

# Acronyms

| | |
|---|---|
| APTV | Astigmatism Particle Tracking Velocimetry |
| BR | Bayesian regularization |
| CSP | Cumulative spectral power |
| DFT | Discrete Fourier Transform |
| DNS | Direct numerical simulation |
| FFT | Fast Fourier Transform |
| *HSI* | hue-saturation-intensity |
| *HSV* | hue-saturation-value |
| LED | Light-emitting diode |
| LM | Levenberg-Marquardt |
| MAD | Mean absolute deviation |
| MSD | Mean signed deviation |
| PDF | Probability density function |
| PIV | Particle Image Velocimetry |
| PTU | Programmable timing unit |
| RBC | Rayleigh-Bénard convection |
| *RGB* | Red-Green-Blue |
| rms | root-mean-square |
| sCMOS | scientific complementary metal-oxide-semiconductor |
| SP | Spectral power |
| TLC | Thermochromic liquid crystal |

# Introduction

For many technical and natural systems the interaction of thermodynamics and fluid mechanics is of great importance. Especially, this interaction is often relevant for the investigation of heat transfer problems, which may be affected considerably by the motion of fluids. The possibility to strongly increase the heat transport at surfaces by a streaming fluid, also referred to as convective heat transfer, is frequently used for technical applications, such as for the effective cooling of electronic devices [1] and of the cooling water in power plants [2]. If the flow is actively driven by an external source like a fan or a pump, this type of fluid motion is called forced convection. However, convective heat transfer can also be induced by natural convection, meaning that the flow is generated due to the variation of the fluid's density within a gravitational field. The variation of the density can be caused by changes of the concentration of any solute in the corresponding solvent, as for example salt in seawater, or by temperature differences in a fluid volume. The focus of this theses will be on the latter, that is natural convection driven by temperature differences of a fluid. Here, the flow in a fluid volume, which is in the ideal case enclosed by adiabatic sidewalls and uniformly heated from below as well as cooled from above, is investigated. This type of flow is also known as the Rayleigh-Bénard convection (RBC), named after the French physicist Henri Bénard (1874 - 1933) and the British physicist Lord Rayleigh (1842 - 1919), and ranks among the most studied canonical flows in fluid mechanics for many years.

## 1.1 Motivation

Despite the simplicity of its boundary conditions the Rayleigh-Bénard model provides valuable insights into the complex mechanisms of thermally driven natural convection. Many laboratory experiments and numerical simulations have been performed in the last decades to study different characteristics of RBC, since this is relevant for a wide variety of problems. In particular, this type of convection is important for the fluid dynamics of the oceans [3] as well as of the earth's atmosphere [4] and mantle [5], which emphasizes its effect on the weather and the earth's climate. Hence, detailed investigations of RBC can, for example, help to gain deeper insights into the processes in the atmosphere, thereby improving the weather forecast. Furthermore, natural disasters, which are linked to events in the atmosphere or in the earth's mantle, e.g. thunderstorms, tornadoes, earthquakes and tsunamis, can be better understood. In addition, RBC is also of interest for other astrophysical systems such as the sun [6], that consists of different zones with one being the

convective zone, in which the energy is transported to the surface of the sun via thermally driven convection.

With regard to technical applications, RBC has particularly been studied in combination with forced convection, yielding important information for the design of ventilation systems in rooms and cabins, e.g. of an airplane or a train, so that the thermal comfort in passenger compartments can be optimized [7, 8]. Moreover, the solidification process of liquid metals is also affected by RBC and can be influenced by an additional magnetic field, which can for instance be used to improve the quality of steel castings [9]. Another technical application, that requires deeper insights into the mechanisms of thermal convection, is the crystal growth from the melt, since convective flow structures in the melt may cause inhomogeneities in the crystal's texture and thereby degrade its quality [10].

As a simple Rayleigh-Bénard model cannot represent the boundary conditions of complex technical systems as well as of geo- and astrophysical settings, such as mentioned above, it does not enable to analyze the evolving flows in their full complexity. However, this model allows to investigate general characteristics of convection driven by temperature differences, which are in many technical and natural systems one of the main flow driving forces. In order to better understand the mechanisms of thermal convection, it must be studied separately, which is why the Rayleigh-Bénard model is of fundamental relevance. Nevertheless, even though extensive research concerning RBC has already been carried out in the last decades, many questions remain still open. One important aspect, which is currently widely addressed and also in the focus of this work, is the investigation of so-called turbulent superstructures in RBC. These structures appear in Rayleigh-Bénard cells with large aspect ratios, i.e. in flat cells that are considerably more extended in the horizontal direction, and have a horizontal dimension larger than the cell's height [11]. The study of turbulent superstructures, which have the special characteristic to be clearly revealed after time-averaging of the velocity or temperature field, is of great importance, since they strongly affect the transport of heat and momentum in RBC. As it will be discussed in section 1.3.2, turbulent superstructures have mainly been investigated by numerical simulations so far, but experimental analysis are still rare. However, experimental investigations are on the one hand necessary to assess the numerical results and are on the other hand a good complement to numerical simulations, as experiments offer the possibility to analyze the flow over more extended time spans, while the numerical results are usually distinguished by a high spatial resolution. Therefore, this work especially aims to study turbulent superstructures from the experimental point of view.

## 1.2   Physical fundamentals

In the course of the studies about thermal convection by means of the Rayleigh-Bénard model, which have occupied scientists for several decades now, specific parameters of this model have been varied over a wide range. Hence, a great variety of results covering different flow regimes has been achieved based on the Rayleigh-Bénard model, which is explained in section 1.2.1. Furthermore, as turbulent superstructures in RBC are a central aspect of this work, an introduction about these structures is given in section 1.2.2.

### 1.2.1   The Rayleigh-Bénard model

The canonical Rayleigh-Bénard model consists of a fluid volume enclosed by a uniformly heated plate at the bottom with the temperature $T_\mathrm{h}$, a uniformly cooled plate at the top

with the temperature $T_c$ and adiabatic sidewalls, which impede the horizontal heat flux at the lateral boundary of the fluid volume. Resulting from the difference between the heating and cooling plate temperature $\Delta T = T_h - T_c$ the variation of the fluid's density may induce a flow termed as Rayleigh-Bénard convection, if the thermal driving force is strong enough [12]. A classical paradigm for the flow is illustrated in figure 1.1, showing a large circulating roll that nearly spans the whole cross-section of a cylindrical and of a cuboidal cell, which are the most commonly studied cell geometries in the fundamental research. As indicated in the figure, hot fluid with a lower density rises up from the bottom along the sidewall and cools down while streaming upward, yielding a higher density such that the fluid sinks down again on the opposite side and the circle gets closed. Even though this paradigm is often used to describe RBC, the characteristics of the flow may be considerably different and more complex, depending on the geometry of the cell, the temperature difference between the isothermal plates and the physical properties of the working fluid. Those factors of influence are usually specified by three dimensionless numbers, namely the aspect ratio $\Gamma$, the Rayleigh number Ra and the Prandtl number Pr, which are explained in the following.



(a) Cylindrical cell
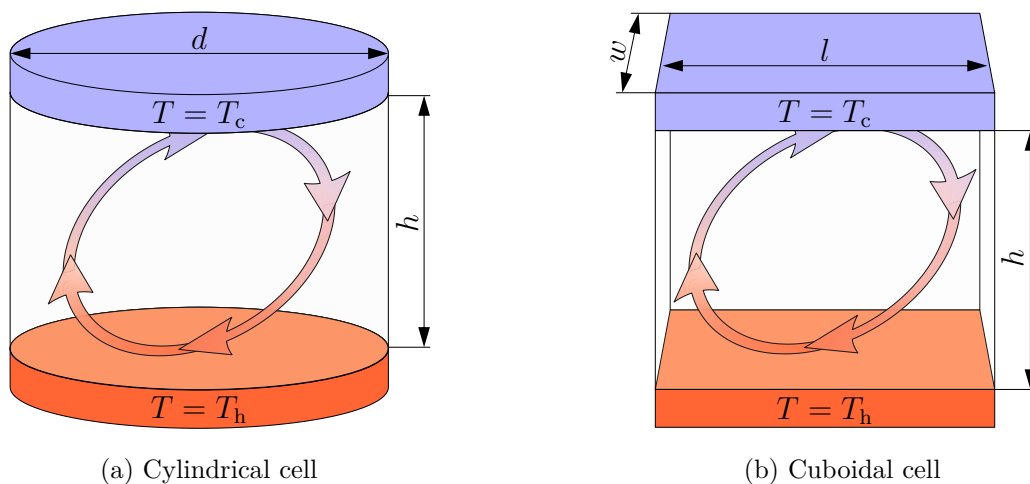
(b) Cuboidal cell

Figure 1.1: Typical paradigm for RBC with one large-scale circulation in a cylindrical (a) and cuboidal (b) cell.

The aspect ratio $\Gamma$ represents the geometry of a cylindrical or cuboidal cell by the ratio of its horizontal and vertical dimension according to the equation (1.1), with $d$ being the diameter of the cylindrical cell, $l$ and $w$ the horizontal edge lengths of the cuboidal cell and $h$ the cell's height, respectively. This dimensionless parameter fundamentally affects the arrangement of the flow structures and, therefore, the local heat transport in RBC. For example, one large-scale circulating roll as indicated in figure 1.1 can be observed in cells with similar vertical and horizontal dimensions, i.e. $\Gamma \approx 1$ [13, 14]. If either the horizontal or vertical dimension of the cell is increased, this one roll state becomes a multiple roll state of horizontally or vertically stacked counter-rotating rolls with the number of rolls depending on the aspect ratio [15, 16]. However, when investigating the flow in cells with a considerably larger horizontal than vertical dimension, those clearly separated rolls disappear and another kind of organization takes effect, which is related to the presence of the turbulent superstructures. Hence, for this study large aspect ratio cells are of interest.

$$\Gamma = \begin{cases} d/h & \text{for a cylindrical cell} \\ l/h & \text{for a cuboidal cell with } l = w \\ (\Gamma_l, \Gamma_w) = (l/h, w/h) & \text{for a cuboidal cell with } l \neq w \end{cases} \tag{1.1}$$

The Rayleigh number and the Prandtl number, which are the other two control parameters, can be derived from the Navier-Stokes-equations. For this, incompressibility of the working fluid may be assumed, since the typical velocities occurring in RBC are negligible in comparison to the speed of sound, resulting in the set of Navier-Stokes equations (1.2) - (1.4), that represent the conservation of mass, momentum and energy [17]. In those equations, the fields of velocity, temperature and pressure are denoted as $\vec{u}$, $T$ and $p$. The physical properties of the fluid are included by the kinematic viscosity $\nu$, the thermal diffusivity $\kappa$ and the mass density $\rho_0$ at a fixed reference temperature $T_0$, while the density of body forces is given by $\vec{f}$.

$$\text{mass conservation:} \quad \nabla \cdot \vec{u} = 0 \tag{1.2}$$

$$\text{momentum conservation:} \quad \frac{\partial \vec{u}}{\partial t} + (\vec{u} \cdot \nabla)\,\vec{u} = \frac{-\nabla p}{\rho_0} + \nu \nabla^2 \vec{u} + \vec{f} \tag{1.3}$$

$$\text{energy conservation:} \quad \frac{\partial T}{\partial t} + (\vec{u} \cdot \nabla)\,T = \kappa\,\nabla^2 T \tag{1.4}$$

In RBC the body force density is solely based on buoyancy and can be written as $\vec{f} = (\rho_0 - \rho)/\rho_0 \cdot g\,\vec{e}_z$, with $g$ being the value of the gravitational acceleration and $\vec{e}_z$ the unit vector pointing against gravity. The mass density $\rho$ in this term must be considered as temperature-dependent, since its fluctuations are caused by temperature differences and are the flow driving mechanism. However, applying the so-called Boussinesq approximation the mass density in the buoyancy term is in this case the only fluid property, which is included as a function of the temperature, while the mass density in the other terms as well as all the other fluid properties can be determined based on a reference temperature $T_0$ and are then assumed to be constant [18]. Even though the Navier Stokes equations are simplified with the Boussinesq approximation, this is a suitable approach commonly used for the numerical study of thermally driven flows, since the variation of the fluid properties within the temperature range of investigation can in many cases be neglected. In order to consider the temperature dependency of the mass density in the buoyancy term, it is linearly approximated with the thermal expansion coefficient $\alpha$ by the function (1.5).

$$\rho = \rho_0(1 - \alpha(T - T_0)) \tag{1.5}$$

Therefore, the last term of the equation for the momentum conservation (1.3) can also be expressed as $\vec{f} = \alpha\,(T - T_0)\,g\,\vec{e}_z$. Considering this, the Navier-Stokes equations (1.2) - (1.4) must now be non-dimensionalized, in order to derive the parameters, which control the Rayleigh-Bénard flow. For this, all the variables have to be scaled with characteristic reference values of the same physical unit. Hence, besides a characteristic length and temperature scale, given by the height $h$ of the Rayleigh-Bénard cell and the temperature difference between the isothermal plates $T_h - T_c$, a characteristic time scale is required to compose the units of all the occurring variables. As typical for systems that are dominated by effects of gravity, such as a Rayleigh-Bénard system, the so-called free-fall time

$$t_\mathrm{f} = \sqrt{h/(\alpha\,g\,\Delta T)} \tag{1.6}$$

is chosen as the time scale for the non-dimensionalization. Using those characteristic scales results in the dimensionless variables of the equations (1.7a) - (1.7e) for the spatial coordinates of a Cartesian coordinate system, the time, the velocity components, the pressure and the temperature, respectively. For the non-dimensionalization of the temperature according to equation (1.7e), either the temperature of the cooling plate $T_\mathrm{c}$ or the average temperature of the isothermal plates $(T_\mathrm{h} + T_\mathrm{c})/2$ is oftentimes chosen as the reference temperature $T_0$. Hence, since the temperatures occurring in RBC are distributed in the range $T \in [T_\mathrm{c}, T_\mathrm{h}]$, the resulting dimensionless temperatures range in between $0 \le \tilde{T} \le 1$ or $-1/2 \le \tilde{T} \le 1/2$, depending on the definition of the reference temperature.

$$\tilde{x} = \frac{x}{h}, \quad \tilde{y} = \frac{y}{h}, \quad \tilde{z} = \frac{z}{h} \tag{1.7a}$$

$$\tilde{t} = \frac{t}{t_\mathrm{f}} \tag{1.7b}$$

$$\tilde{u}_x = \frac{u_x}{h/t_\mathrm{f}}, \quad \tilde{u}_y = \frac{u_y}{h/t_\mathrm{f}}, \quad \tilde{u}_z = \frac{u_z}{h/t_\mathrm{f}} \tag{1.7c}$$

$$\tilde{p} = \frac{p}{\rho_0\,(h/t_\mathrm{f})^2} \tag{1.7d}$$

$$\tilde{T} = \frac{T - T_0}{T_\mathrm{h} - T_\mathrm{c}} \tag{1.7e}$$

Applying the non-dimensionalization to the Navier-Stokes equations yields the dimensionless notation in the equations (1.8) - (1.10), which reveals that the Rayleigh number Ra and Prandtl number Pr according to their definitions (1.11) - (1.12) are the controlling parameters. For the sake of clarity, it is noted that the tilde symbols indicating the dimensionless variables are omitted in the equations (1.8) - (1.10).

$$\text{mass conservation:} \quad \nabla \cdot \vec{u} = 0 \tag{1.8}$$

$$\text{momentum conservation:} \quad \frac{\partial \vec{u}}{\partial t} + (\vec{u} \cdot \nabla)\,\vec{u} = -\nabla p + \sqrt{\frac{\mathrm{Pr}}{\mathrm{Ra}}}\,\nabla^2 \vec{u} + T\,\vec{e}_z \tag{1.9}$$

$$\text{energy conservation:} \quad \frac{\partial T}{\partial t} + (\vec{u} \cdot \nabla)\,T = \frac{1}{\sqrt{\mathrm{Ra}\,\mathrm{Pr}}} \nabla^2 T \tag{1.10}$$

$$\mathrm{Ra} = \frac{\alpha\,g\,(T_\mathrm{h} - T_\mathrm{c})\,h^3}{\nu\,\kappa} = \frac{\alpha\,g\,\Delta T\,h^3}{\nu\,\kappa} \tag{1.11}$$

$$\mathrm{Pr} = \frac{\nu}{\kappa} \tag{1.12}$$

While RBC is induced by thermal buoyancy, it is dampened due to molecular friction and the equalization of temperature differences in a fluid, represented by the kinematic viscosity $\nu$ and thermal diffusivity $\kappa$ in the definition of the Rayleigh number Ra. Since the term $\alpha\,g\,\Delta T$ in the Rayleigh number quantifies the strength of the thermal buoyancy and, furthermore, a large characteristic length scale $h$ enables the fluid to freely move, the Rayleigh number can be considered as a ratio of the convection driving and hindering parameters. As the non-dimensionalization confirms, especially the vertical distance

between the isothermal plates, which is the characteristic length scale in this case, strongly influences the Rayleigh number with $Ra \sim h^3$. By stability analysis it can be shown that convective motion in a Rayleigh-Bénard cell first starts to occur when the Rayleigh number is larger than a critical Rayleigh number $Ra_c \approx 1708$, as in principle addressed in the studies [19, 20], and thus heat is only transported by conduction for $Ra < Ra_c$. In the case $Ra > Ra_c$ the Rayleigh number is in particular used for the classification of the flow into different regimes, ranging from laminar to fully developed turbulence with increasing Rayleigh number. However, fixed universal limits between the regimes do not exist, since the classification also depends on the Prandtl number of the working fluid as well as on the aspect ratio of the flow domain.

According to the equation (1.12), the Prandtl number is given by the ratio of the kinematic viscosity $\nu$ and the thermal diffusivity $\kappa$. Hence, for example highly thermally conductive liquid metals may have Prandtl numbers of $Pr < 10^{-2}$, while the Prandtl number of viscous media such as oils may amount to $Pr > 10^2$ depending on the temperature. Furthermore, the frequently for Rayleigh-Bénard experiments applied fluids water and air have a Prandtl number of $Pr_{water} \approx 7$ and $Pr_{air} \approx 0.7$ at an ambient temperature of $T = 20\,°C$. From the physical point of view this dimensionless number quantifies, if a fluid better transports heat or momentum, corresponding to $Pr < 1$ or $Pr > 1$, respectively. Therefore, the Prandtl number interconnects the temperature and velocity field of the flow, thereby also providing the information, whether the thermal boundary layer is thicker than the viscous boundary layer if $Pr < 1$ or vice versa if $Pr > 1$.

In addition to the three parameters $Ra$, $Pr$ and $\Gamma$, which determine the flow, the Reynolds number $Re$ and the Nusselt number $Nu$ are commonly used to characterize the resulting flow from the overall view with regard to the transport of momentum and heat. Hence, those two dimensionless numbers are very important for the analysis of RBC, giving rise to comprehensive studies of their scaling with the control parameters, i.e. $Re = f(Ra, Pr, \Gamma)$ and $Nu = f(Ra, Pr, \Gamma)$, as manifested in the well-known theory proposed by Grossmann and Lohse [21]. In general, the Reynolds number is defined to estimate, if the momentum in a flow is mainly transported by convection or diffusion. For this, in its definition the parameters representing inertial forces and viscous forces are set in relation according to equation (1.13), with $U_c$ and $L_c$ being the characteristic velocity and length scale of the flow, respectively. Therefore, since large velocities and characteristic length scales induce turbulence, which is weakened by the viscosity of the fluid, the Reynolds number is also considered as a quantity that indicates, whether a flow is laminar or turbulent. However, contrary to other applications such as a pipe flow or the flow over a flat plate with well-defined characteristic scales, several definitions of these scales are applied for the investigation of RBC. For the characteristic length scale commonly the height of the cell $h$ is used, but the velocity scale is determined on different ways depending on the special problem of interest [18], for example by taking a local magnitude of the velocity or the root-mean-square value of all velocity components in time and space.

$$Re = \frac{U_c L_c}{\nu} \qquad (1.13)$$

While the transport of momentum is characterized by the Reynolds number $Re$, the Nusselt number $Nu$ describes the transport of heat. As shown in equation (1.14), it compares the total amount of heat flux $\dot{Q}$ from the bottom to the top plate of the Rayleigh-Bénard cell with the conductive heat flux $\dot{Q}_{cond}$ between the plates for the case when

the fluid is at rest. In this context, the conductive heat flux is determined based on the horizontal cross-sectional area $A$ of the cell, the thermal conductivity $\lambda_{\text{th}}$ at the average temperature of the working fluid, the temperature difference $\Delta T$ between the isothermal plates as well as the vertical distance $h$ between them.

$$\text{Nu} = \frac{\dot{Q}}{\dot{Q}_{\text{cond}}} = \frac{\dot{Q}\,h}{\lambda_{\text{th}}\,A\,\Delta T} \tag{1.14}$$

Thus, if the thermal driving force is not strong enough to induce thermal convection when $\text{Ra} < \text{Ra}_{\text{c}}$ and heat is only transported by conduction, the Nusselt number is $\text{Nu} = 1$ and the temperature decreases linearly from $T_{\text{h}}$ at the bottom plate to $T_{\text{c}}$ at the top plate, illustrated in figure 1.2. However, if convection starts to occur for $\text{Ra} > \text{Ra}_{\text{c}}$, the heat flux $\dot{Q}$ always increases in comparison to the conductive heat flux $\dot{Q}_{\text{cond}}$, such that $\text{Nu} > 1$. It is well known, that in this case the fluid is thoroughly mixed due to convective motion in the main part of the cell, also referred to as the bulk region, which contains the whole fluid volume except for that in the regions very close to the isothermal plates. The vertical fluid motion is suppressed there by the plates and accordingly heat is only transported by conduction, yielding strong temperature gradients. For many theoretical analysis, variations of the temperature averaged over the horizontal cross-section in the $x$-$y$-plane $\langle T \rangle_{x,y}(z)$ are fully allocated to these small zones at the bottom and top plate, which represent the thermal boundary layers, while the temperature in the bulk region is taken as constant, illustrated in figure 1.2. Hence, within the thermal boundary layers the horizontally averaged temperature $\langle T \rangle_{x,y}(z)$ approaches the temperature of the bulk region $\langle T \rangle_{x,y}(z)|_{\text{bulk}} = (T_{\text{h}} + T_{\text{c}})/2$.
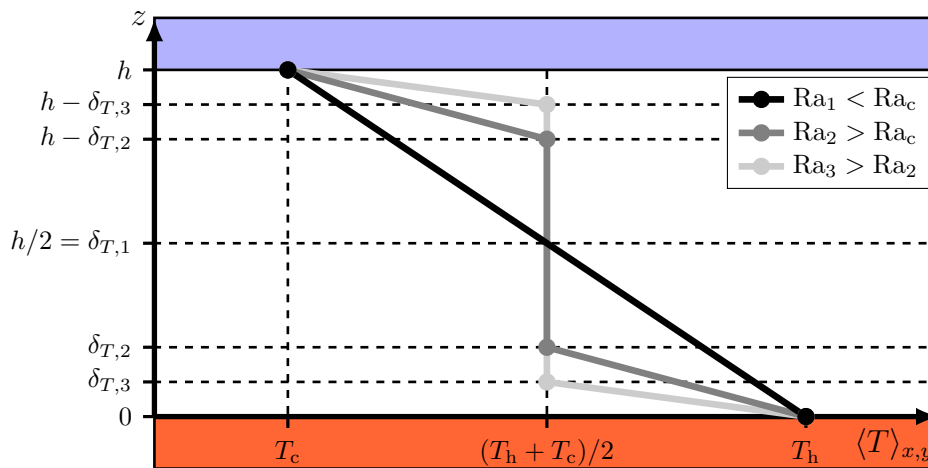


Figure 1.2: A sketch showing the variation of the thickness of the thermal boundary layer $\delta_T$ in dependency of the Rayleigh number Ra.

As indicated in figure 1.2, the temperature in the thermal boundary layer is assumed to be linearly dependent on the normal distance to the plates. Furthermore, it is also obvious from figure 1.2, that the thickness of the thermal boundary layer $\delta_T$ decreases with increasing Ra, meaning that for very high Rayleigh numbers the bulk region nearly covers the entire cell and heat is transported most efficiently due to convective mixing, thereby also increasing the Nusselt number Nu. Hence, as the length of the zones, in which heat is solely transported by conduction, determines the total amount of heat flux, the Nusselt

number can also be considered as the ratio of the cell's height to the length of the two thermal boundary layers according to equation (1.15) [22].

$$\text{Nu} = \frac{h}{2\,\delta_t} \tag{1.15}$$

## 1.2.2   Turbulent superstructures

As aforementioned, turbulent superstructures in RBC, which have a horizontal dimension larger than the cell's height, are clearly revealed after time-averaging of the temperature and velocity field, but the length of the averaging interval cannot be chosen arbitrarily. On the one hand, the averaging should cover a time span, that is large enough to eliminate the fast changing small-scale fluctuations from the fields. However, as the turbulent superstructures gradually relocate over time, this time span must also not be chosen too large, such that those structures are not smoothed out. Even though a strict rule concerning the averaging time $t_{\text{avg}}$ does not exist, an estimation is, for example, possible based on the method proposed in the study [11]. Following this method, the averaging time should fall into a certain range, in order to clearly uncover the turbulent superstructures. The lower limit of this range is given by the free-fall time according to equation (1.6). With regard to thermal convection, the free-fall time represents processes, that pass off on shorter time scales than the rearrangement of turbulent superstructures, e. g. the motion of thermal plumes and small-scale vortices. On the contrary, the upper limit of the range is given by the extended time scale of diffusive processes across the characteristic length scale of the system, which is the height $h$ of the Rayleigh-Bénard cell. Depending on the specific properties of the working fluid, either the diffusion of momentum by kinematic viscosity $\nu$ or the diffusion of temperature by thermal diffusivity $\kappa$ takes a longer time, resulting in the maximum time scale for diffusive processes $t_{\text{d}}$ according to equation (1.16).

$$t_{\text{d}} = \begin{cases} h^2/\nu & \text{if } \nu < \kappa \\ h^2/\kappa & \text{if } \nu > \kappa \end{cases} \tag{1.16}$$

Within such extended characteristic time scales of diffusive processes, turbulent superstructures may considerably rearrange, such that an averaging over the entire time span is not suited to capture these structures. Hence, it can be concluded, that the averaging time for the temperature and velocity field for the study of turbulent superstructures should fall into the range $t_{\text{f}} \ll t_{\text{avg}} \ll t_{\text{d}}$. However, this can only be considered as a rough estimation, since the free-fall time and the time scale for diffusive processes may differ by several orders of magnitude.

Without having introduced the experimental setup used for the investigations in this work, some illustrating results of an exemplary measurement are already depicted in figure 1.3, in order to get a better idea about turbulent superstructures at this point. Details about the experimental setup, the measuring technique and the settings during the experiments will be presented in the following sections. Yet, it should be noted that the results in figure 1.3 have been obtained from measurements in a horizontal plane of a Rayleigh-Bénard cell with a horizontal cross-sectional area of $l \times w = 700\,\text{mm} \times 700\,\text{mm}$ and a height of $h = 28\,\text{mm}$, thus having an aspect ratio of $\Gamma = l/h = 25$. The investigated section of the horizontal plane, which was located close to the cooling plate at $z = 24\,\text{mm}$ measured from the surface of the heating plate at $z = 0\,\text{mm}$, is indicated in figure 1.3. Furthermore, the cell was filled with deionized water, heated from below and cooled

from above with temperatures of the heating and cooling plate of $T_\mathrm{h} = 19.79\,^\circ\mathrm{C}$ and $T_\mathrm{c} = 19.09\,^\circ\mathrm{C}$, respectively, resulting in a Prandtl number of $\mathrm{Pr} \approx 7$ and a Rayleigh number of $\mathrm{Ra} \approx 2.1 \times 10^5$.
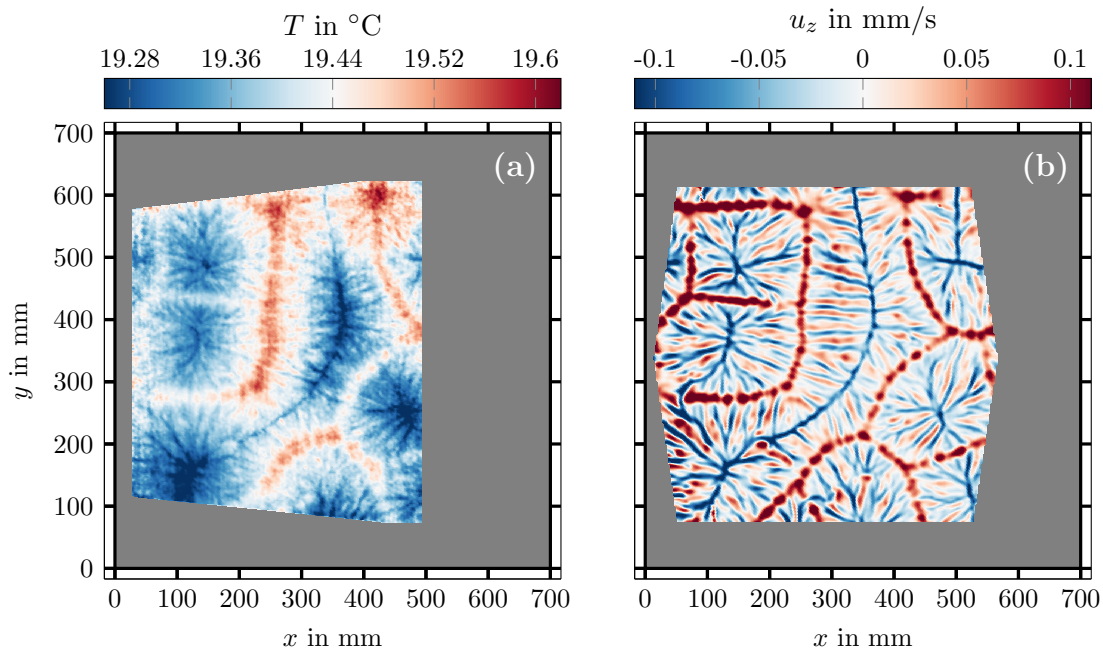


Figure 1.3: Exemplary time-averaged fields of the temperature (a) and of the corresponding vertical velocity component (b) obtained from a measurement in a horizontal plane close to the cooling plate of a Rayleigh-Bénard cell with an aspect ratio of $\Gamma = 25$ and temperatures of $T_\mathrm{h} = 19.79\,^\circ\mathrm{C}$ and $T_\mathrm{c} = 19.09\,^\circ\mathrm{C}$ at the heating and cooling plate. The time-averaging was performed over 299 instantaneous fields covering about 66 free-fall times.

The results show a time-averaged temperature field in figure 1.3a and the corresponding field of the vertical velocity component $u_z$ in figure 1.3b. In this case, the average was taken over a sequence of 299 instantaneous fields, recorded within a time span of 5 min, which corresponds to about 66 free-fall times. The turbulent superstructures are clearly uncovered in both the temperature and velocity field, respectively. Comparing the time-averaged fields an expectable correlation can be seen, as warm fluid forms the upstreaming parts of the turbulent superstructures, while cold fluid forms the downstreaming parts. Moreover, the results confirm that the horizontal dimensions of turbulent superstructures may cover a multiple of the cell's height $h$. Therefore, it also becomes obvious that these structures represent the global flow dynamics and are of great relevance for the transfer of heat and momentum. However, the size of the turbulent superstructures in this cell might also be smaller or even larger, depending on the temperature difference between the heating and cooling plate and the working fluid, i.e. their size varies with the Rayleigh number and Prandtl number. Furthermore, as mentioned above the turbulent superstructures rearrange on extended time scales. Thus, long-time investigations of the temperature and velocity fields are necessary, in order to study the reorganization in detail, which is addressed in this work.

# 1.3   State of research

Due to its relevance for many natural systems and technical applications, RBC has already been analyzed comprehensively [12, 18, 23]. Showing the great variety of the results in detail would go beyond the scope of this work, however, a brief overview about the main research topics and achievements is given in section 1.3.1. Moreover, with regard to the investigations about turbulent superstructures in RBC presented in this work, the previous studies about these structures are separately reviewed in section 1.3.2. It should further be noted at this point, that the introductive part of the section 1.3.2 has been taken from the author's study [24] with some minor adjustments.

## 1.3.1   Main research on Rayleigh-Bénard convection

Even though thermally driven convection had already been observed before, Henri Bénard was the first to investigate this systematically. In his experimental studies at the beginning of the twentieth century he especially focused on the organization of regular patterns of fluid motion in a thin layer of fluid, which is heated from below and has a free surface at the upper side. His scientific work and findings are for instance presented in the review [25]. An exemplary, very famous photograph of Bénard's experiments can be seen in figure 1.4, which shows a pattern of many adjacent hexagonal cells, also known as the Bénard cells, visualized within a thin fluid layer of spermaceti [26]. In the course of his extensive investigations, Henri Bénard determined the way the fluid is moving within those cells, namely ascending in the center of the hexagons, streaming sidewards at the free surface and downwards at the edges [25].
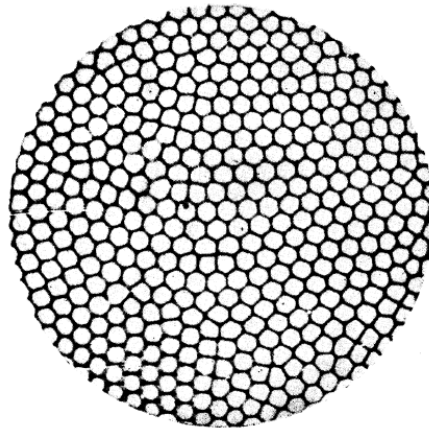


Figure 1.4: An exemplary photograph of Bénard's experiment, showing the typical hexagonal cells within in a fluid layer of spermaceti. This photograph can be found in the study [26] and is depicted here with permission from EDP Sciences.

However, it is important to note that the flow in such a fluid system with these boundary conditions is not only induced by thermal buoyancy, but also by the effects of surface tension at the upper side, with the latter predominating when the thickness of the fluid layer becomes very small [27]. Related to Bénard's experiment in thin fluid layers, the surface tension has first been clearly pointed out as the cause of fluid motion in the studies [28, 29]. This mechanism of fluid motion is also of great relevance and has further been studied in detail [30–32], but it must be strictly distinguished from the classical RBC with the rigid cooling plate at the top side as introduced in section 1.2.1.

In order to get a better understanding of thermally driven convection between two horizontal plates, with the lower one having a larger temperature, Lord Rayleigh conducted some theoretical analysis in the year 1916 [33]. One of the main results he obtained was that convective motion sets in at a critical temperature difference between the bottom and top. However, stress-free conditions were considered for the velocity at the rigid bottom and top boundary, thereby assuming that the vertical velocity vanishes, while the fluid may freely slip along the boundary in the horizontal direction, which is not realistic. Hence, the results of the analysis regarding the onset of convection in terms of the critical Rayleigh number $Ra_c$ considerably deviate from those presented in other studies [19, 20], where the more realistic no-slip velocity boundary condition has been applied, yielding the well-established value of $Ra_c = 1708$. Nevertheless, due the pioneering analysis by Lord Rayleigh, this threshold is known as the critical Rayleigh number.

Referring to Bénard's and Rayleigh's findings, several experimental investigations and further theoretical analysis have been performed in the mid of the twentieth century, to clarify which factors of influence determine the onset of thermally driven convection and the organization of the evolving flow structures. Since then the number of studies concerning RBC has grown substantially due to the rapid progress of engineering and computer science, allowing to set up extensive experiments with state-of-the-art measuring equipment and to run computationally expensive numerical simulations. Hence, the ongoing technical advance has opened up a wide field of possible research topics, including very specific ones that are not addressed here. However, some common research topics dealing with RBC are shortly described in the following. In addition, for each of these topics a small sketch is depicted in figure 1.5 for illustration.

**Characteristics of the flow structures**    With regard to RBC, the investigation of the evolving flow structures is a central task, since those determine the heat transport from the bottom to the top. Depending on the working fluid, on the physical dimensions of the cell and on the thermal driving force of the flow, the resulting flow structures may differ strongly with respect to their spatial arrangement and their temporal dynamics. As indicated in figure 1.5a, which is inspired by the investigations in the work [34], the flow structures may for example form concentric rings at the onset of convection, which are growing with increasing Rayleigh number Ra until the axisymmetry is broken up and cellular patterns start to emerge. In general, the flow structures in RBC range from large-scale motions such as the so-called global wind [15] to small-scale fluctuations [35], which especially occur in highly turbulent flows. Furthermore, the flow structures might either be stable and persist over extended time spans or oscillate [13] or even completely reorganize over time [24]. In many cases, the Rayleigh-Bénard flow features a combination of these characteristics and is therefore very complex. This demonstrates clearly the variety of the flow structures, which are comprehensively studied, in order to understand the interaction and their effect on the local as well as the global transport of heat and momentum.

**Scalar and vector fields**    For obtaining a first impression of a Rayleigh-Bénard flow to be investigated experimentally, it may be sufficient to apply simple methods, e.g. the seeding of the flow with small tracer particles, which are illuminated with intense light, enabling to observe the main flow structures visually. However, detailed analysis of the flow require quantitative studies of the scalar fields, for example of the temperature and pressure field, and of vector fields such as the velocity or vorticity field. Many efforts have been made to improve the measuring techniques and the numerical models for their determination, since these fields can in general be considered as a main basis for further

studies. For example, in this work the simultaneous measurements of temperature and velocity fields are used to reveal the turbulent superstructures in both fields as indicated in figure 1.5b, which shows an exemplary time-averaged temperature field in a qualitative manner with superimposed vectors that indicate the direction of the horizontal fluid motion. The temperature and velocity fields are in the following applied to analyze the characteristic wavelength of the turbulent superstructures and the associated local heat flux based on the coupling of the temperature and the vertical velocity component, which confirms their usefulness for further analysis.

**Boundary layers**     Another research topic of relevance, which is also based on the temperature and velocity field, is the investigation of the thermal and viscous boundary layer. As outlined in section 1.2.1 at the example of the thermal boundary layer, these represent small zones in close vicinity to the isothermal plates, in which the temperature and velocity feature strong gradients, respectively. The most common method to specify the thermal boundary layer thickness is to determine the tangent of the horizontally averaged temperature profile at the isothermal plate and to search for the point, where the tangent reaches the mean temperature $(T_\mathrm{h} + T_\mathrm{c})/2$. However, depending on the problem under investigation other definitions for the thermal boundary layer thickness have been applied as well [23]. Furthermore, for the viscous boundary layer thickness in the velocity field different definitions have been proposed, too. For example, one established method would be to take the vertical distance to the plate, at which the absolute value of the horizontal velocity $\langle U \rangle_{x,y}(z) = \langle (u_x^2 + u_y^2)^{1/2} \rangle_{x,y}$ reaches the local maximum [23] as illustrated in figure 1.5c. Especially for large Rayleigh numbers the thermal and viscous boundary layers become very small, making it very difficult to analyze those in experiments, but also in numerical simulations due to the rising computational effort for resolving the small length scales. However, since the boundary layers considerably affect the total amount of the transport of heat and momentum and their investigation is thus of vital importance, scientists have met this challenge by performing processing-intensive simulations with a high spatial resolution [36]. Furthermore, large-scale experimental setups such as the *Barrel of Ilmenau*, which is the largest Rayleigh-Bénard cell worldwide, have been built up, thereby providing the possibility to study the boundary layers in greater detail [37].

**Scaling of the dimensionless numbers**     As explained in the fundamentals in section 1.2.1, dimensionless numbers are the key quantities to describe a Rayleigh-Bénard flow from the overall view. In this context, the Nusselt number Nu and Reynolds number Re have established as the two most studied dimensionless numbers, depending on the input parameters of the Rayleigh number Ra, Prandtl number Pr and aspect ratio $\Gamma$. In particular, as illustrated in figure 1.5d, the scaling with the Rayleigh number has been analyzed, since this parameter can easily be varied in both the numerical simulation and the experiment. When reviewing the studies related to the scalings of $\mathrm{Nu} \sim \mathrm{Ra}^{\beta_\mathrm{Nu}}$ and $\mathrm{Re} \sim \mathrm{Ra}^{\beta_\mathrm{Re}}$, a strict consensus cannot be found, but estimations for the scaling in different regimes of the Rayleigh number are frequently given by the exponents in the range $1/4 \leq \beta_\mathrm{Nu} \leq 1/3$ for the Nusselt number and $2/5 \leq \beta_\mathrm{Re} \leq 2/3$ for the Reynolds number, as for instance shown in the study [23]. However, these ranges for the scaling exponents cannot be considered as universal, because the scaling of Nu and Re also depends on the properties of the working fluid represented by the Prandtl number Pr, resulting in different scaling laws manifested in the unifying theory by Grossmann and Lohse [21]. Moreover, towards very large Rayleigh numbers in the so-called ultimate regime the scaling exponent for the Nusselt number has been reported to asymptotically converge to $\beta_\mathrm{Nu} \approx 0.5$ [38, 39], due to the transition of the boundary layers to the turbulent state

and the associated increasing heat transport by turbulence. But this aspect is also very inconsistently discussed in the literature, as for example either strongly differing scaling exponents in the range $0.14 \leq \beta_{\mathrm{Nu}} \leq 0.42$ have been found in the ultimate regime [40] or the classical exponent $\beta_{\mathrm{Nu}} = 1/3$ is demonstrated to hold up to $\mathrm{Ra} = 10^{15}$ [22]. Despite the numerous studies about the scaling of the dimensionless numbers in the past, this topic is still investigated experimentally and numerically, aiming to get a better understanding for extended ranges of the controlling parameters Ra, Pr and $\Gamma$.

**Turbulence modeling** Since the turbulence in fluid mechanics has a large impact on many characteristics of the flow, e.g. on the associated heat transfer and the pressure loss, it needs to be well understood. Even though turbulence occurs in many systems with substantially varying boundary conditions, it features some typical, non system-specific properties. For example, according to the well-known concept proposed by Richardson [41] the energy in a turbulent system is produced on larger length scales and gradually transported towards smaller length scales until the energy is dissipated as heat, which is schematically depicted in figure 1.5e. As RBC may also be highly turbulent, depending on the thermal driving force of the flow, it serves as a classical paradigm for the investigation of turbulent thermal convection, which is a very important basis for the understanding of the flow in several natural systems such as the earth's atmosphere. However, the analysis of turbulent RBC are also useful for the study of other fluid mechanical systems, in which turbulence is present. Investigating turbulent RBC can, for instance, help to estimate the smallest time and length scales of turbulent flows in general, thereby enabling to choose a suitable spatial and temporal resolution for measurements as well as numerical simulations of flows exhibiting turbulent characteristics.

**Modifications of the boundary conditions** The standard Rayleigh-Bénard model is well suited to gain insights into the flow mechanisms of thermally driven convection. However, in order to cope with the variety of the boundary conditions of real natural systems, different modifications of the standard model are investigated, e.g. rotating Rayleigh-Bénard setups [42] and Rayleigh-Bénard setups with additional magnetic fields [43], spatially as well as temporally varying boundary conditions [44, 45] and surface roughness [46] as illustrated in figure 1.5f. In particular with respect to the conditions in the earth's atmosphere, moist RBC is studied comprehensively, too [47]. Furthermore, those modifications are also of interest for technical applications. For example, a magnetic field can be used to affect the fluid motion in thermally driven convection during the solidification process of liquid metals, thereby improving the quality of steel castings [9]. Moreover, adding distinctive surface roughness to a Rayleigh-Bénard model can be considered to study the heat transport on electronic devices aiming for a more effective cooling [48]. Hence, as modified Rayleigh-Bénard models allow to investigate many specific natural and technical systems in greater detail, those models are frequently applied.

## 1.3.2 Studies about turbulent superstructures

With respect to RBC, turbulent superstructures have mainly been investigated by means of numerical simulations so far. Even though those flow structures have not been termed like this in earlier studies, they have already been reported and discussed for different input parameters of the simulations, which determine the Rayleigh-Bénard flow. In this context, the geometry of the simulation domain, the properties of the fluid and the thermal driving force of the flow have been varied by applying different aspect ratios, Prandtl numbers and Rayleigh numbers, respectively. For example, the typical size of large-scale
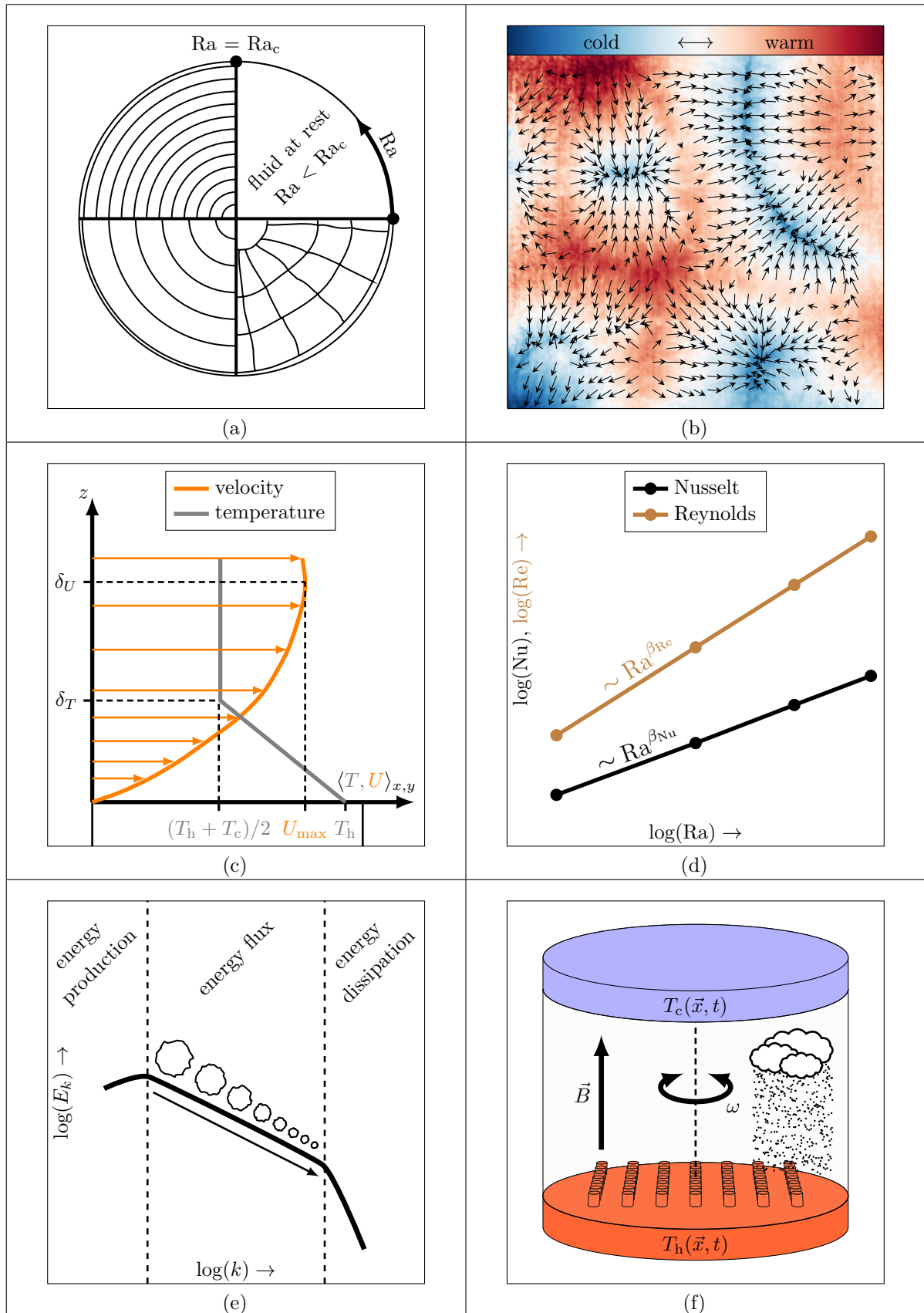
Figure 1.5: Common research topics on RBC: (a) Characteristics of the flow structures, (b) Scalar and vector fields, (c) Boundary layers, (d) Scaling of the dimensionless numbers, (e) Turbulence modeling, (f) Modifications of the boundary conditions.

structures in RBC has been investigated in the study [49] for Rayleigh numbers ranging from the onset of convection up to about Ra $\approx 10^7$ as well as for Prandtl numbers in the range approximately limited by Pr $\in [0.3, 100]$, using a simulation domain with an aspect ratio of $\Gamma = 10$ in most cases. An overview of the corresponding large-scale convection patterns and further results with regard to different types of mean flow components and the convective heat transport has been presented in the work [50]. In order to clarify also the effect of the aspect ratio of the simulation domain on the large-scale patterns, this parameter has been varied in later studies [51–53]. Furthermore, the drift of large-scale patterns in RBC and their robustness to side wall effects has been investigated as well [54]. By analyzing the time-averaged temperature fields of successive time intervals, the drift of large-scale patterns has been shown, too [55].

Later, in the study [11], in which the large scale-scale patterns have now been termed turbulent superstructures, those have been presented in dependency of the Rayleigh number and Prandtl number for aspect ratio $\Gamma = 25$. In comparison with the work [50], the Rayleigh number has also been varied up to Ra $= 10^7$, but the range of the Prandtl number has considerably been extended towards lower values of Pr $\ll 0.1$, which requires massively parallel supercomputing. Furthermore, characteristic time and length scales that separate fast turbulent fluctuations on small scales from the slowly evolving turbulent superstructures on larger scales have been identified [11]. Moreover, alternative novel approaches for the investigation of turbulent superstructures are discussed in further studies, such as using Lagrangian trajectory clusters [56] and deep-learning algorithms [57]. Most recently, turbulent superstructures have been analyzed based on the fluctuation fields of the temperature and the vertical velocity for $10^5 \leq$ Ra $\leq 10^9$ at fixed Pr $= 1$ and $\Gamma = 32$ [58], thereby explicitly pointing out, that superstructures of the same size exist in both fields, contrary to the findings of prior studies. Finally, the interplay between small-scale fluctuations and turbulent superstructures by means of resolved energy budgets for $10^4 \leq$ Ra $\leq 10^8$ has been studied, also applying a fixed Pr $= 1$ and $\Gamma = 24$ [59].

As the main results of the present work are obtained from measurements in a Rayleigh-Bénard cell with aspect ratio $\Gamma = 25$, the studies [11] and [57], which are both based on numerical simulations for the same aspect ratio, are of central interest to assess the results. Since water is used as the working fluid in the Rayleigh-Bénard cell for this experimental study, especially the investigations of the turbulent superstructures for the corresponding Prandtl number Pr $= 7$ and varying Rayleigh number in reference [57] are well suited for a comparison, because the three Rayleigh numbers Ra$_1 = 10^5$, Ra$_2 = 10^6$ and Ra$_3 = 10^7$ applied in this numerical study also cover the experiments' range of the Rayleigh number. In order to get an impression of the numerical results, the time-averaged fields of the temperature and the vertical velocity component in the horizontal mid plane of the Rayleigh-Bénard cell for these Rayleigh numbers are depicted in figure 1.6. Due to the fact that the non-dimensionalized set of the Navier-Stokes equations (1.8) - (1.10) has been considered for the simulations, the spatial coordinates as well as the resulting temperature and velocity fields are dimensionless, i.e. $\tilde{x} = x/h$, $\tilde{y} = y/h$, $\tilde{T} = (T - T_{\mathrm{c}})/(T_{\mathrm{h}} - T_{\mathrm{c}})$ and $\tilde{u}_z = u_z/u_{\mathrm{f}}$, as introduced in section 1.2.1.

In the time-averaged fields in figure 1.6 the turbulent superstructures can be seen clearly for the three different Rayleigh numbers. Especially, the structures become obvious from the temperature fields in the top row, as the temperature is advected within the investigated planes by the horizontal velocity components, yielding the distinctive patterns that represent the turbulent superstructures. Furthermore, as it can be expected the range of the occurring dimensionless temperatures after time-averaging considerably decreases
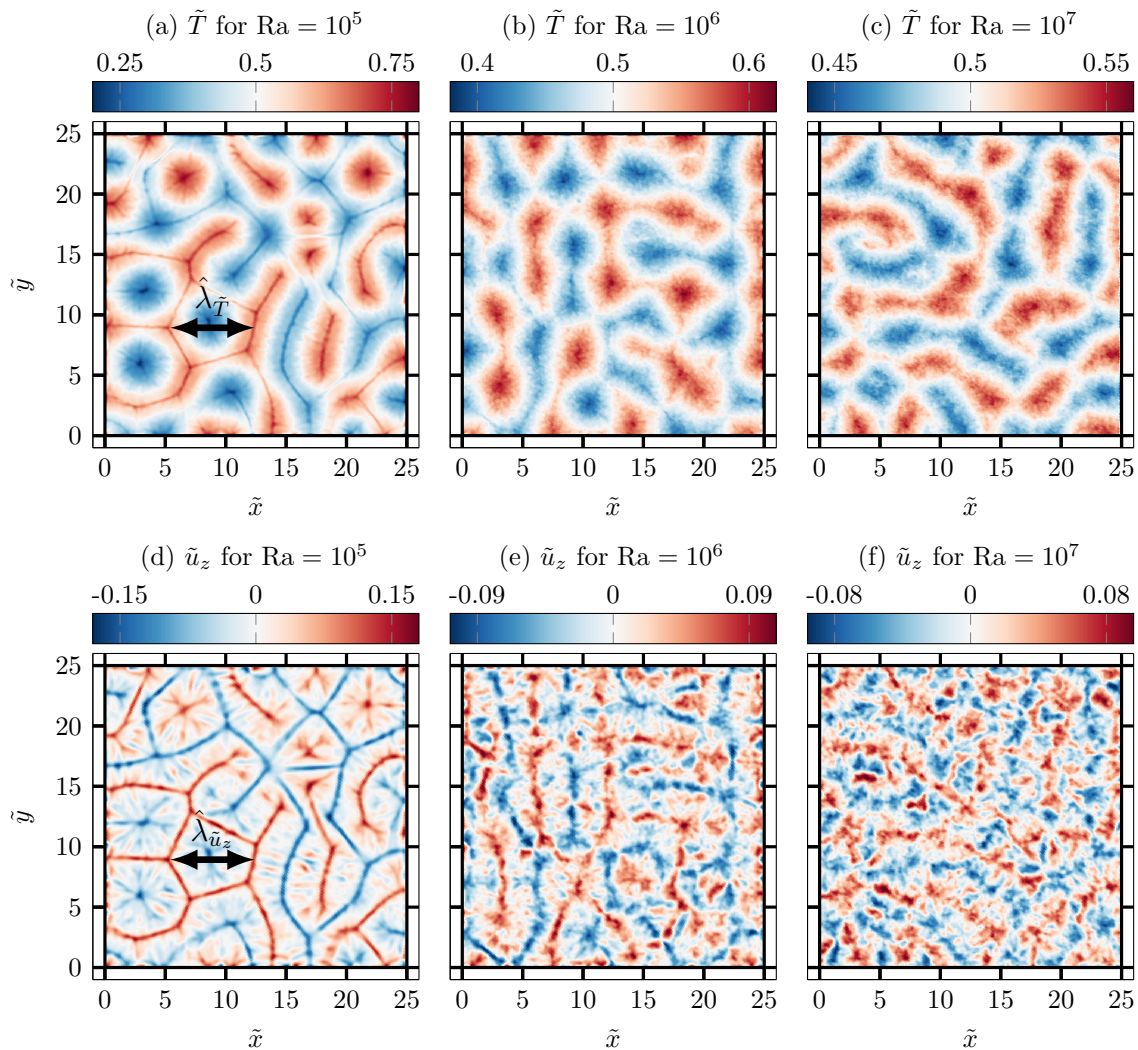
Figure 1.6: Time-averaged fields of the temperature (a-c) and of the vertical velocity component (d-f) for the Prandtl number $Pr = 7$ and the three Rayleigh numbers $Ra = 10^5$ (a,d), $Ra = 10^6$ (b,e) as well as $Ra = 10^7$ (c,f) in the mid plane of a Rayleigh-Bénard cell with aspect ratio $\Gamma = 25$ obtained from numerical simulations. These results have been published in the work [57] and the numerical data have been provided by the authors for the inclusion in this work. It should be noted that only the style of the representation has been changed for this figure.

with increasing Rayleigh number, indicated by the colorbars on the top of the temperature fields, since the turbulent fluctuations grow stronger, which results in an enhanced mixing of the fluid. Regarding the time-averaged fields of the vertical velocity component it can be stated that the dominant structures coincide well with those of the corresponding temperature field for the lowest Rayleigh number $Ra = 10^5$. This mainly applies also to the higher Rayleigh numbers, but due to the stronger horizontal advection of the temperature the patterns in the velocity field appear smaller [11] and incorporate some local variations that cannot be found from the temperature field. Moreover, comparing the velocity fields it can be seen that the maximum magnitude of the velocity in the vertical direction decreases for the higher Rayleigh numbers. However, for the sake of completeness it should be emphasized that the decreasing range for both the temperature and the velocity fields is a result of the non-dimensionalization. Tracing back the fields to physical dimensions reveals that the temperatures and vertical velocity components vary within a larger range when the Rayleigh number is increased.

Another important aspect to be pointed out is the size of the turbulent superstructures. As indicated in figure 1.6a and 1.6d, within the scope of the present work the size is quantified by means of their wavelength, i.e. the distance between the patterns with similar temperature or vertical velocity. However, since the patterns are not uniformly arranged, special methods have to be applied to determine the most characteristic wavelength from the time-averaged temperature and velocity fields. For example, on the basis of a two-dimensional Fast Fourier Transform (FFT) of these fields the wavelength corresponding to the peak of the wavelength spectra has been related to the size of the turbulent superstructures [11], thereby showing that the characteristic wavelength of the superstructures by trend increases with the Rayleigh number for $Pr = 0.7$. Looking at the results in figure 1.6 for $Pr = 7$, a significant trend of a growing wavelength cannot be seen. This is also confirmed by the wavelengths given in the study [57], which were obtained using the same method and for the Rayleigh numbers of $Ra = 10^5$, $Ra = 10^6$ and $Ra = 10^7$ amount to $\hat{\lambda}_{\tilde{T}} = \{6.3, 6.3, 6.2\}$ in the temperature field and $\hat{\lambda}_{\tilde{u}_z} = \{5.4, 5.7, 4.3\}$ in the velocity field. Hence, the wavelength deserves closer attention from the experimental point of view to improve the reliability of the analysis by comparing the data.

All the studies regarding turbulent superstructures outlined above are based on numerical simulations. In contrast, results obtained from experimental investigations have rarely been published so far. However, especially experiments offer the possibility to capture the slowly evolving reorganization of turbulent superstructures over several hours and are therefore complementary to spatially highly resolved numerical data, which are usually not available for such extended time periods. Some exemplary results, which show the existence of turbulent superstructures in RBC, have been shown in the study [60] by means of velocity measurements via Particle Image Velocimetry [61] in the so-called SCALEX facility [62]. For these measurements pressurized air as well as sulfur hexafluoride ($SF_6$) were used as the working fluid in a Rayleigh-Bénard cell with $\Gamma = 10$, thereby achieving a Rayleigh number of $Ra = 5 \times 10^5$, but the investigations were not primarily focused on turbulent superstructures. The first experimental results with the focus on the turbulent superstructures in RBC were presented in the study [24], in which the reorganization of turbulent superstructures in water and the enhancement of the local heat flux by those structures was shown. To the best of the author's knowledge other experimental analysis are not available yet, so that the current work is in general intended to investigate turbulent superstructures experimentally more in detail.

## 1.4 Objectives of the work

For the study of the turbulent superstructures in RBC, a new experimental setup has to be built up. The superstructures are investigated in horizontal planes of the Rayleigh-Bénard cell by means of simultaneous temperature and velocity fields, which are determined with optical measurement techniques. While the temperature measurements are performed via the color signal of so-called thermochromic liquid crystals (TLCs), that are dispersed in the working fluid inside the Rayleigh-Bénard cell, the temporal displacement of the TLCs is used to compute the velocity fields according to the established Particle Image Velocimetry (PIV). Hence, for the velocity field measurements a commercial solution is applied, but the temperature measurement technique has to be set up and comprehensively characterized in preparation of the measurements in RBC. Based on the measurement data of the temperature and velocity fields, the Rayleigh-Bénard flow has to be analyzed,

in particular with regard to the turbulent superstructures. Thus, the whole work can be divided in four work packages, which are briefly outlined in the following aiming for a better overview.

**Development of the experimental setup**    In order to investigate the turbulent superstructures experimentally, a suitable experimental setup has to be developed. In the design of the setup special emphasis has to be given to the dimensions of the Rayleigh-Bénard cell, which requires to consider different aspects. In this context, a compromise must be found, such that turbulent superstructures can be investigated in a large section of the cell with an appropriate spatial resolution, the achievable range regarding the Rayleigh number is comparable to that of numerical simulations and the experimental setup can be handled under common laboratory conditions. However, the most important aspect is that turbulent superstructures clearly occur in the flow, which is the case when the cell has a large aspect ratio. Since the temperature and velocity fields are measured with an optical measurement technique, the cell must be optically accessible, but at the same time the ideal boundary conditions of the Rayleigh-Bénard experiment have to be considered, i. e. the homogeneous temperature distribution at the isothermal plates and the suppression of the heat flux across the side walls of the cell. Furthermore, the setup should also offer the possibility to place cells with a different height between the heating and cooling plate, thereby enabling to vary the Rayleigh number over a larger range.

**Setup and characterization of the temperature measurement technique**    As aforementioned, TLCs are used to simultaneously measure the temperature and velocity fields. For the measurements, the TLCs must be illuminated with white light to show different colors in dependency of the temperature. However, since the turbulent super-structures will be investigated in horizontal planes of the Rayleigh-Bénard cell, which spans a considerably wider area compared to the vertical planes due to the large aspect ratio, a special light source must be designed. This light source must enable to shape a white light sheet with almost constant thickness over the whole horizontal cross-sectional area of the cell. The vertical position of the light source should also be adjustable, in order to investigate the flow at different heights. Moreover, a suitable calibration technique for the temperature measurements based on the color signal of the TLCs must be developed, which has to be characterized in detail with regard to the measurement uncertainty and the measurable temperature range.

**Measurements in Rayleigh-Bénard convection**    The simultaneous measurements of the temperature and velocity fields have to be performed in different horizontal planes of the Rayleigh-Bénard cell for varying temperature differences between the heating and cooling plate, yielding different Rayleigh numbers. The range of the Rayleigh numbers should be adapted in a way that the characteristics of the flow can be compared to those obtained from numerical simulations. Furthermore, the velocity measurements should not only provide the information of the horizontal velocity components, but also of the vertical velocity component, as the latter is especially important for the estimation of the local heat flux in RBC. Since the focus of this work is on the investigation of the turbulent superstructures, the measurements should cover time spans that are large enough to observe the reorganization of the structures over extended time spans of several hours.

**Analysis of the measurement data**    In the evaluation of the measurement data different aspects have to be considered. Especially, the characteristic wavelength of the turbulent superstructures must be investigated in dependency of the Rayleigh number. In this context, the method for the determination of the wavelength should be discussed in

detail, as different methods have been suggested in previous studies. Furthermore, the simultaneous temperature and velocity fields must be utilized to determine the local heat flux, thereby demonstrating that the turbulent superstructures strongly enhance the heat transfer in RBC. Moreover, the long-term reorganization of the superstructures has to be analyzed, which is one of the main advantages of these experimental studies compared to numerical simulations, since those do usually not cover such extended time spans up to date. In order to assess the applicability of both, the experimental method presented in this work and numerical methods, the results of the measurements have to be compared with the outcomes of numerical studies in the field of turbulent superstructures in RBC.

# Liquid crystal thermography

Even though the main concept of the experimental facility could be developed at the beginning, it was not possible to specify each detail without a deeper investigation of the measuring technique. For example, in order to reliably determine the temperature fields via the color signal of TLCs, the camera required for the optical temperature measurement needs to be arranged according to specific features of the measuring technique, however, those features must be figured out at first. Hence, after a brief overview of the temperature measuring technique based on the color of TLCs in section 2.1, a detailed characterization of the main influencing factors on the measuring technique is given in section 2.2, while further factors having a minor influence in the present case are shortly outlined in section 2.3. Furthermore, three different calibration techniques for the temperature measurements using TLCs are presented in section 2.4, including the comparison of the techniques with regard to the measurement uncertainty. Finally, an exemplary application of TLCs for temperature field measurements is demonstrated in section 2.5.

## 2.1   Brief overview of the measuring technique

In order to understand the basic principle of the liquid crystal thermography from the physical point of view, their molecular structure must be considered. In general, liquid crystals are also called mesophase materials, since their properties are determined by the transition between the crystalline solid and isotropic liquid phase [63,64]. Hence, liquid crystals do neither completely behave like a solid nor like a liquid. On the one hand the molecules of liquid crystals may be highly ordered as typical for solids, but on the other hand their arrangement also enables the shifting of the molecules, which is characteristic for liquids in terms of fluidity [65]. However, the liquid crystallinity cannot only be considered as a combination of the individual characteristics of both solids and fluids, because the mesophase state shows very specific properties. In the context of liquid crystal thermography, especially the unique optical properties of the so-called thermotropic liquid crystals are of interest [66]. Those have the characteristic to show the liquid crystallinity due to the action of heat, meaning that the mesophase is either achieved upon heating of the crystalline solid or upon cooling of the isotropic liquid [67]. According to the system proposed in the work [68], thermotropic liquid crystals appear in three different forms regarding their molecular organization, depending on the chemical compound and on the temperature [69]. It should be noted at this point that several specific modifications of the three phases outlined in the following exist [70], but in order to keep the focus, only the standard molecular arrangement for each of the phases is addressed here.

In the case that a crystalline solid is heated and a certain temperature is exceeded, the molecules of the emerging liquid crystal are usually uniaxially ordered and additionally arranged in layers, known as the smectic phase, which is depicted in figure 2.1a. As characteristic for the liquid crystallinity, the material behaves partly like a fluid and like a solid in the smectic phase, since the single layers can freely slide over one another, but cannot interpenetrate in the perpendicular direction [71]. When the temperature of the liquid crystals is increased, the arrangement of the molecules becomes less ordered and either the so-called nematic phase or cholesteric phase, which is also referred to as the chiral nematic phase, starts to occur. This depends on the chemical compound of the liquid crystal, because for the formation of the cholesteric phase a non symmetric structure of the molecules is necessary, i.e. it requires chirality [72]. In the nematic phase the molecules are uniaxially aligned, which is the only kind of order in this phase as shown in figure 2.1b. A uniaxial arrangement of the molecules is also characteristic for the cholesteric phase, which is why cholesteric liquid crystals are considered as a particular type of nematic liquid crystals [70]. However, compared to the randomly distributed molecules in the common nematic phase according to figure 2.1b, the molecules in the cholesteric phase are uniaxially arranged in parallel layers as illustrated in figure 2.1c. Furthermore, the cholesteric phase has the special feature, that the orientation of the uniaxially aligned molecules varies along the different layers in a helical manner, yielding useful optical properties [71]. This feature of the cholesteric phase is of great interest for liquid crystal thermography.

When illuminated with white light, the cholesteric liquid crystal selectively reflects a small wavelength range of the illumination spectrum depending on the angular change of the molecules between two adjacent layers, while the other wavelengths are mainly transmitted. In order to relate the angle of twist to the reflected wavelength range, most commonly the so-called pitch length indicated in figure 2.1c is used as a representative length scale for the distance between two layers with the same molecular arrangement [73]. Since the twist of the molecules between the adjacent layers continuously increases with temperature, meaning that the pitch length decreases, the reflected wavelength range and consequently the color appearance of the cholesteric liquid crystals illuminated with white light changes as a function of the temperature. Considering that a decreasing pitch length results in a smaller central wavelength of the reflected wavelength range according to Bragg's law [73], it can therefore be concluded, that the color appearance of cholesteric liquid crystals continuously varies along the visible wavelength spectrum from red at lower temperatures to blue at larger temperatures [74]. Furthermore, the temperature range of the cholesteric phase can be adjusted on the basis of the chemical compound [75], however, it is limited, such that the special optical behavior ceases to exist, when exceeding the temperature beyond the upper limit of the range with optical activity of the liquid crystal. In this case, the material is not anymore in the mesophase state, but has become an isotropic liquid with disordered molecules.

Due to the fact, that thermotropic liquid crystals may in general occur in the described three phases, but only the special features of the cholesteric phase are utilized for liquid crystal thermography, temperature-sensitive cholesteric liquid crystals are termed thermochromic liquid crystals (TLCs) for a better distinguishability. Since the temperature, at which the TLCs start to get red, as well as their optically active temperature range between the red and blue color appearance can be adjusted in the manufacturing, their specifications can be adapted to different applications. While for standard TLC mixtures the temperature corresponding to the so-called red start can be varied from about $-30\,°C$ to $120\,°C$, the temperature range between the red start and blue start can usually be

(a) The smectic phase

(b) The nematic phase



(c) The cholesteric phase
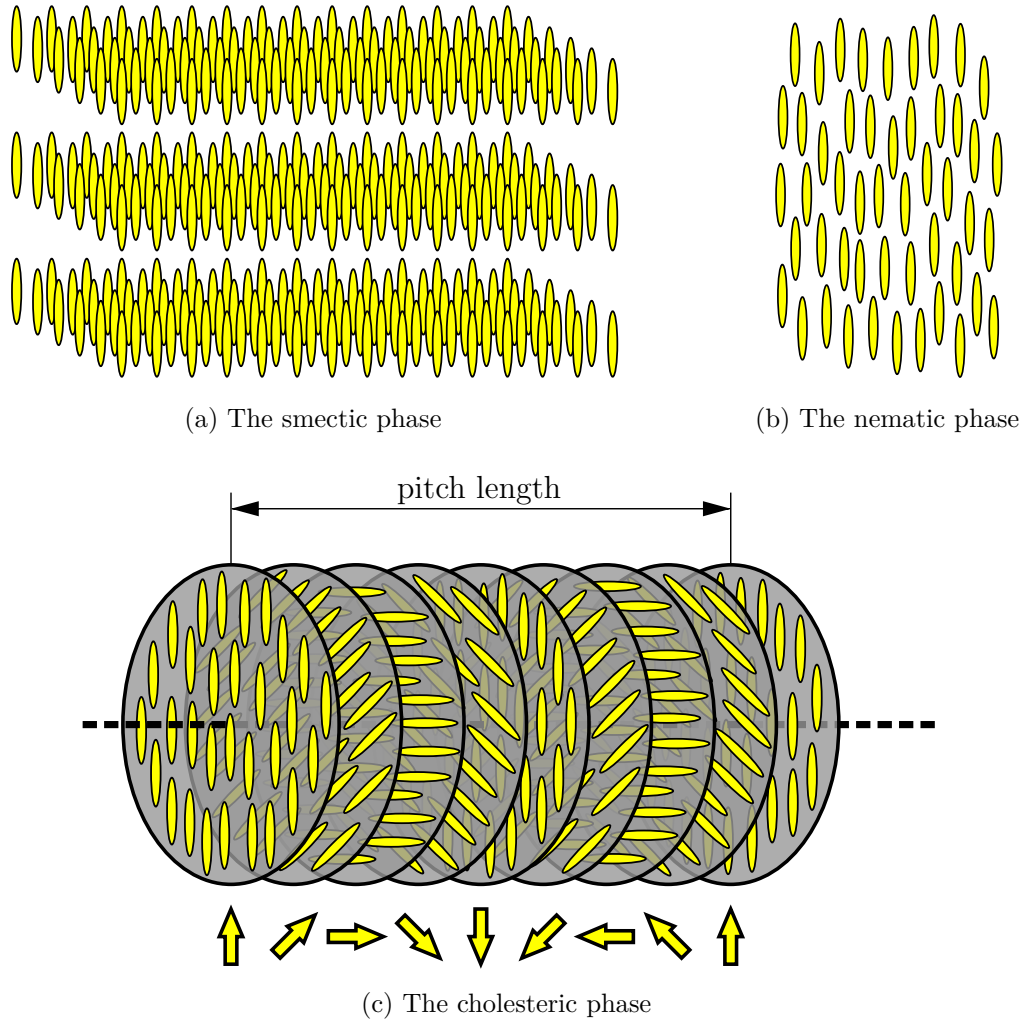
Figure 2.1: Illustration of the molecular alignment in liquid crystals with three different types of organization, adapted from the references [63] and [73]. The arrows at the bottom side of the figure 2.1c indicate the orientation of the molecules within the single layers, which varies helically along the center axis.

adjusted in between $0.5\,\mathrm{K}$ and $20\,\mathrm{K}$ [76], respectively. However, by modifications of their chemical composition, TLCs can also be custom-made to cover larger temperature ranges such as for the present work, in which besides TLCs with a temperature range of $20\,\mathrm{K}$ another type with a range of $50\,\mathrm{K}$ is used. Even though this allows for flexibility in the use of TLCs, it must be mentioned that the typical specifications of TLCs given by the manufacturers can only be considered as nominal values. Based on those, the temperature range corresponding to the color change can be roughly estimated, but the TLCs may have significantly differing specifications in the application, as their color appearance strongly depends on the angle between illumination and observation [77, 78]. In comparison to the nominal specifications, which are valid for the case that the TLCs are illuminated and observed from the same direction, particularly the optically active temperature range might substantially differ and be much smaller for specific applications, which oftentimes require an oblique or perpendicular arrangement of the illumination source and the device used for the observation of the TLCs. Because of the strong influence of the angle between illumination and observation, which is investigated in the following section 2.2, usually

calibration measurements must be performed for the determination of temperature fields based on the color appearance of TLCs, as will be explained in detail in section 2.4.
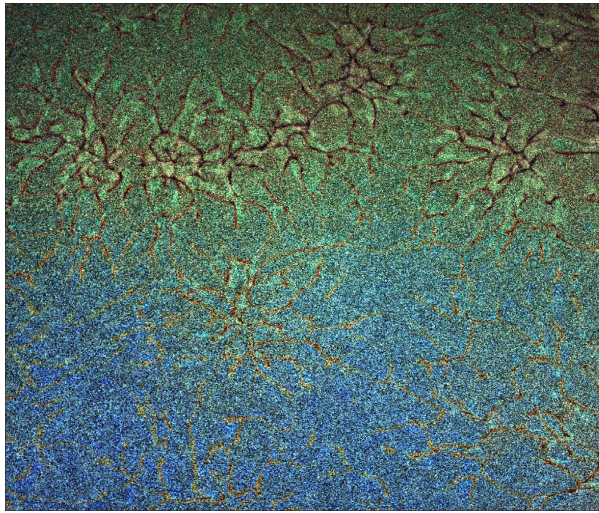


(a) Visualization of the temperature field in a horizontal plane in the Rayleigh-Bénard cell used in this work by means of the color appearance of TLCs. The color trend from the bottom to the top side arises from the angular dependency of the color appearance of thermochromic liquid crystals, which must be taken into account for the temperature measurements.
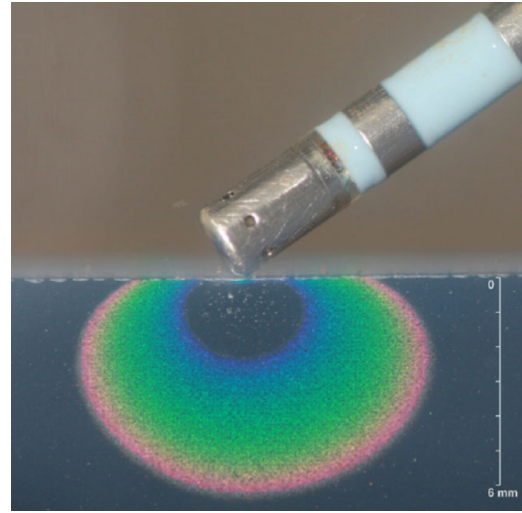
(b) Using a thermochromic film for the thermal mapping of radiofrequency catheter ablation applied to a myocardial phantom. With permission from *John Wiley & Sons, Inc.* this image has been taken from reference [79], in which the details can be found.
©2013 Wiley Periodicals, Inc.

Figure 2.2: An exemplary image of thermochromic liquid crystals as tracer particles in a flow (a) and of a thermochromic film (b).

In order to give a better impression of the measuring technique at this point, two exemplary applications of TLCs are shown in figure 2.2, which represents the two main different forms of TLCs. As it can be seen in figure 2.2a, TLCs can be used for the visualization of the temperature field in flows via their color appearance, which can also be evaluated for quantitative investigations [71]. For this type of application, TLCs are dispersed in the flow as very small particles with a diameter of a few microns to indicate the local temperatures. In many cases, TLCs embedded in microcapsules with a diameter of a few microns are inserted into the flow for protection [73], as the temperature sensitive material is very susceptible to damages, which might for example be caused by impurities in the flow. As the figure 2.2a confirms at the example of a horizontal measurement plane in the Rayleigh-Bénard cell presented in chapter 3, TLCs can clearly indicate the temperature differences occurring in a flow. Due to the fact, that the temperatures can be measured noninvasively based on their color and the TLCs can also serve as tracer particles for the determination of the velocity field by means of the established PIV technique, the use of TLCs is highly attractive for detailed flow analysis. Hence, in the last decades TLCs were frequently applied for studies in different fields of fluid mechanics, especially for the investigation of flows, in which convective heat transfer determined by the relation of the temperature and velocity field is of great interest. Thus, for example many experimental studies using TLCs have been performed with regard to natural convection [80–82], mixed convection [83, 84] and the heat transfer at bodies inserted into a flow [85, 86]. Besides the application for those macroscopic analysis, the temperature measuring technique based on the color of TLCs has also been investigated with a view to microfluidic applications [87],

also in combination with velocity tracking techniques for simultaneous three-dimensional measurements temperature and velocity fields [88].

As exemplarily demonstrated in figure 2.2b, which shows the color play of a thermochromic film on a myocardial phantom for the examination of the thermal impact of radiofrequency catheter ablation [79], TLCs can also be utilized for determining temperature distributions on surfaces. The thermal mapping of surfaces covered with a thermochromic film has proven to be beneficial, because this technique allows to easily detect thermal inhomogeneities, which is of interest for several investigations, such as in further medical applications [76], in the design of electronic devices [89] and in studies related to the heat transfer on surfaces [90, 91]. Hence, either dispersed in a flow or in form of a thermochromic film for surface temperature measurements, TLCs are used for a great variety of studies, which are not addressed in further detail in the scope of this work. However, for deeper insights into different applications of TLCs, the interested reader is referred to the references [71] and [76]. Finally, it should also be noted, that the measuring technique itself and the approaches for the determination of the temperature by means of the color of TLCs have also been studied comprehensively, as will be discussed in the following sections.

## 2.2 Influence of the illumination spectrum and observation angle

Even though the measuring technique based on the color appearance of TLCs seems promising, in particular because their specifications can be suitably chosen with respect to the present application, some aspects must be considered when TLCs are used. Especially important is in this context, that materials with a cholesteric structure, such as TLCs in the temperature range of color play, change their reflectivity for different wavelengths with a varying angle between illumination and observation, as shown in the studies [92, 93]. Hence, their color appearance depends not only on the temperature, but also on that angle. This effect has already been analyzed in several studies, in which temperature measurements by means of a TLC film have been characterized with regard to measuring the temperature distribution on surfaces [94–97] or the convective heat transfer at the surfaces [98, 99]. However, as the application of a TLC film strongly differs from that of dispersed TLCs for temperature measurements in a flow, especially concerning the range of the applied angles between illumination and observation, the measuring technique for the current study should not be characterized based on the previous findings obtained from experiments with a TLC film.

Related to temperature measurements in fluid flows, the angular dependency of the color appearance of dispersed TLCs has frequently been reported [100–105], but to the author's knowledge the influence of applying specific angles between illumination and observation on the correlation between the color and temperature has only been addressed in the works [77] and [80]. Even though those studies already provide important insights as further discussed below, the measuring technique must be investigated in greater detail with respect to its general applicability and the design of the experimental facility. Therefore, an additional smaller experiment has been set up, which is sketched on the left side of figure 2.3.

The central part of this experiment is a cylindrical cell made of glass, which has an inner diameter of 110 mm and an outer diameter of 120 mm. As it can be seen on the right
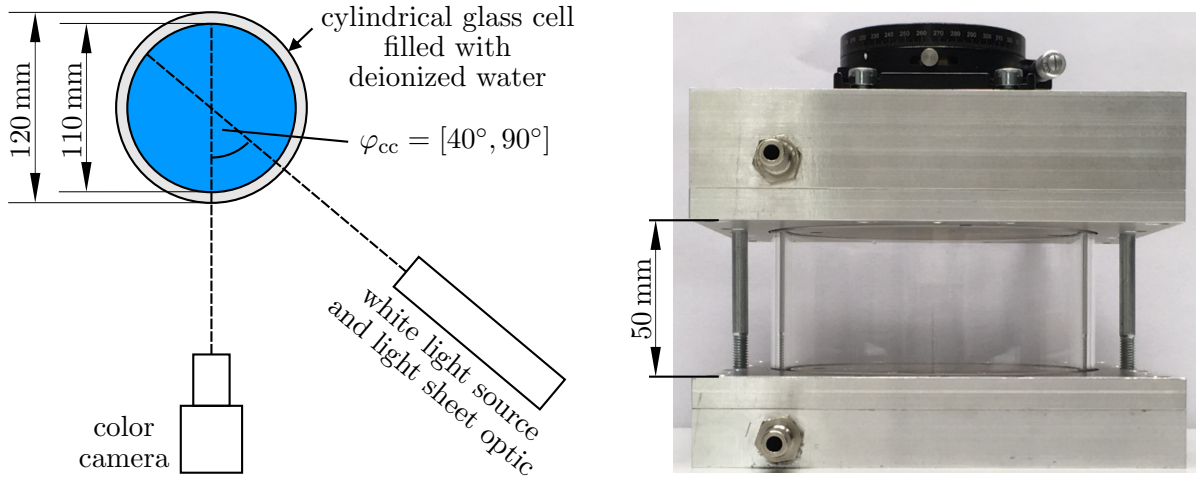
Figure 2.3: Sketch of the experiment for the characterization of the temperature measuring technique from the top view (left) and a photograph of the experiment's central unit, consisting of a cylindrical glass cell mounted in between two aluminum plates with adjustable temperature (right). The rotation stage on the top aluminum plate allows to easily vary the angle between the white light sheet and the axis of the color camera.

side of figure 2.3, the glass cell with its height of 50 mm is placed in between two plates. For the experimental investigations the cell is filled with deionized water and a small additive of TLCs of the type R20C20W (LCR Hallcrest Ltd). This specification indicates, that the TLCs nominally start to appear red at $T = 20\,°C$ and continuously change their color appearance over a temperature range of 20 °C across the visible wavelength spectrum until they are blue colored at $T = 40\,°C$, when illuminated with white light and observed from the same direction. Deionized water is the working fluid in this case, since this will also be used for the measurements in the larger Rayleigh-Bénard facility. Hence, based on the results of the experiments in the smaller cell, the temperature measuring technique can directly be characterized without any considerations about the influence of the working fluid.

In order to study the measuring technique in detail, the experimental setup according to the sketch on the left side of figure 2.3 allows to vary different parameters. First of all, the temperature of the working fluid in the cell can be adjusted by the temperature of the enclosing plates. For this, both plates have a meander channel in the interior, which is flown through by water within an external circuit, driven by the same thermostatic bath. The temperature of each plate is measured with a PT100 element, which is located in the central area of the plate, in close vicinity to the surface inside the cell. Furthermore, the plates are made of aluminum to impede considerable temperature inhomogeneities on their surface. However, as the adjustment of the temperature inside the cell by the diffusion from the upper and lower boundary into the bulk area would take a long time, this process can be strongly accelerated in the experiments by a small magnetic stirrer placed in the border area of cell.

As illustrated in figure 2.3, besides the temperature also the angle between illumination and observation can be changed to investigate the effect on the color of the TLCs. In this case, the color appearance is recorded with a color camera (sCMOS pco edge 5.5 color, PCO AG), which is equipped with a Bayer filter for color detection and will be applied for all the temperature measurements in this study. While the camera is mounted on an

optical rail and not moved during the experiments, an optical fiber connected to the white light source (Spectra X Light Engine, Lumencor Inc.) is attached to a flat bar, which is fixed at a manual rotation stage in the center of the top aluminum plate. Moreover, a light sheet optic is mounted in front of the optical fiber on the flat bar, in order to shape a white light sheet for the illumination of the TLCs in a vertical cross section through the center of the cell. The rotation stage on the top of the setup, which can be seen in the photograph in figure 2.3, enables to vary the angle between the vertical white light sheet and the optical axis of the camera. Since the measurements with this setup do not require a high spatial resolution in the direction of the light sheet's thickness, the light sheet optic was adapted to obtain a thickness of about 4 mm inside the cell, thereby illuminating a sufficiently large number of particles for a reliable evaluation. In addition, the applied white light source also provides the possibility to vary the illumination spectrum. Due to the fact, that the light source incorporates six solid-state light-emitting diodes (LEDs) covering different color bands across the visible spectrum (violet, blue, cyan, green, red and near-infrared) with independently tunable intensity, the spectral output can be significantly changed. Hence, in the following the influence of the angle between illumination and observation, which is from here on also denoted as the observation angle $\varphi_{cc}$, as well as of the illumination spectrum on the correlation between the color appearance and the temperature of TLCs is investigated.

Based on measurements with glycerol for $\varphi_{cc} = 50°$, $\varphi_{cc} = 70°$ and $\varphi_{cc} = 90°$ it has been shown in the work [77] that the temperature range, in which the color of dispersed TLCs (R35C20W) changes from red to blue, considerably decreases with increasing observation angle. While this change of color covers a temperature range of more than 10 K for $\varphi_{cc} = 50°$, the transition approximately passes over 5 K and 2 K for $\varphi_{cc} = 70°$ and $\varphi_{cc} = 90°$, respectively. In the study [77], besides glycerol also deionized water has been used as the working fluid, however, only for an observation angle of $\varphi_{cc} = 90°$. By the comparison of the measurements with glycerol and water for $\varphi_{cc} = 90°$ it has been demonstrated, that the refractive index of the fluid has an influence on the correlation between the temperature and the color. The color of the TLCs in water does not only change on a different way from red to blue, but the temperature corresponding to the red start also decreases by about 1 K according the results obtained in the reference [77]. Furthermore, also the temperature range between the red start and blue start tends to shrink when using water as the working fluid.

In order to better understand, how the temperature dependency of the color of the TLCs in water is affected by the observation angle, the angle between the fixed axis of the color camera and the white light sheet has been varied from $\varphi_{cc} = 40°$ up to $\varphi_{cc} = 90°$ in steps of 10° in the scope of this work. While smaller angles have not been adjusted due to their impracticality for measurements with a light sheet, larger angles have not been applied, since the TLCs show their useful color play in the direction of backward scattering, but mainly the reflection of white light can be observed in the direction of forward scattering, which is almost useless for temperature measurements. This is also affirmed by the results in the study [80], in which the angular dependency of TLCs dispersed in water for $\varphi_{cc} = 60°$, $\varphi_{cc} = 90°$ and $\varphi_{cc} = 120°$ has been investigated with respect to simultaneous measurements of temperature and velocity fields in RBC using two color cameras in a stereoscopic arrangement. Moreover, it should also be mentioned, that TLCs exhibit a symmetrical scattering behavior with respect to the axis of illumination. Referring to the sketch in figure 2.3 this means, that it does not make a difference, whether the light source is arranged on the left or right side from the color camera.

For analyzing the influence of the illumination spectrum, two different settings have been adjusted at the light source, yielding the distributions of the spectral power depicted in figure 2.4. Those two distributions are from here on denoted as the first spectrum and second spectrum, respectively. In the case of the first spectrum, each of the six LEDs was operated at the maximum intensity, except for the green LED with a central wavelength of $\lambda = 550\,\mathrm{nm}$. Due to its high power in comparison to the other LEDs, the intensity of the green LED was set to 50%. However, as shown in the following, the first spectrum is not appropriate to achieve a distinctive color play of the TLCs with temperature, as the integral intensities in the lower and central part of the wavelength spectrum are dominant. Hence, even though for smaller temperatures larger wavelengths are stronger reflected by the TLCs, the resulting color appearance mainly varies between green and blue. Based on this finding, the spectral intensities in the blue and green wavelength range have been decreased for the second spectrum. Furthermore, the violet and the near-infrared LED have been switched off, since the color camera with the Bayer filter is mainly sensitive in the wavelength range from $\lambda = 400\,\mathrm{nm}$ to $\lambda = 700\,\mathrm{nm}$. Therefore, only the blue, cyan, green and red LEDs were applied, with the intensities adjusted to 40%, 30%, 40% and 100%, respectively. Using this setting, the results could be considerably improved, as will be discussed in this section.
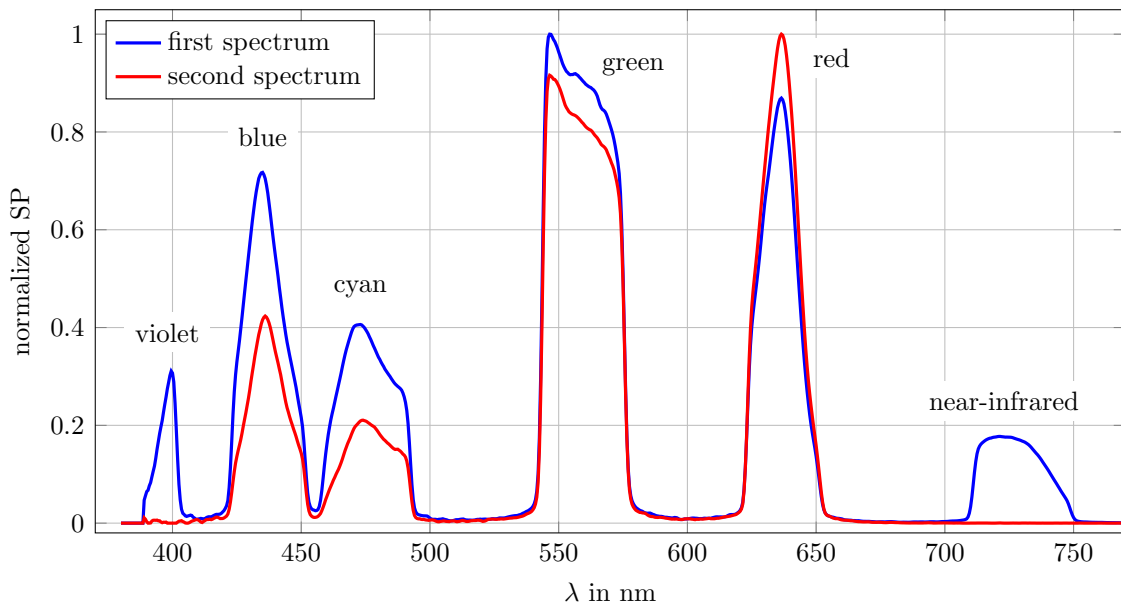


Figure 2.4: Distributions of the normalized spectral power (SP) for the illumination of the TLCs.

In order to study the correlation between the color and the temperature of the TLCs for the different observation angles and illumination spectra, calibration measurements were performed. At the beginning of those measurements, the temperature of the deionized water with the dispersed TLCs was set to $T_\mathrm{s} = 17\,^\circ\mathrm{C}$. Therefore, the initial temperature is smaller than the lower end of the temperature range corresponding to the color play of the here applied TLCs R20C20W, which are expected to show their red start at around $T_\mathrm{s} = 20\,^\circ\mathrm{C}$. Nevertheless, starting at $T_\mathrm{s} = 17\,^\circ\mathrm{C}$, fifty images of the TLCs were recorded with the color camera and a frequency of $f = 5\,\mathrm{Hz}$ for all the observation angles between $\varphi_\mathrm{cc} = 40^\circ$ and $\varphi_\mathrm{cc} = 90^\circ$. Subsequently, 32 different temperature levels up to $T_\mathrm{s} = 40\,^\circ\mathrm{C}$ were adjusted and the images for the different observation angles were recorded with the mentioned frequency, respectively. Aiming for the isothermal state in the cell for each of

the recordings, about 20 minutes has been waited after adjusting a new temperature level at the thermostatic bath. During this period of time, the magnetic stirrer in the cell was frequently rotating to suppress any temperature inhomogeneities. The whole procedure has been performed twice, i.e. once for each illumination spectrum, thereby impeding numerous readjustments at the light source.

Prior to explaining the evaluation, four exemplary images of the TLCs are depicted in figure 2.5 to give a better impression. These image shows the TLCs R20C20W over nearly the whole illuminated cross section of the cell at temperature levels of $T_\mathrm{s} = 19\,°\mathrm{C}$ and $T_\mathrm{s} = 21\,°\mathrm{C}$ for the observation angles $\varphi_\mathrm{cc} = 60°$ and $\varphi_\mathrm{cc} = 70°$ in the center of the field of view, using the second spectrum for illumination. Only a very small strip of the cell's entire cross section with its dimensions of $110\,\mathrm{mm} \times 50\,\mathrm{mm}$ has been clipped at each lateral boundary, where the TLCs are covered by screws. At the first glance it can be seen that the color of the TLCs changes with the temperature and with the angle between illumination and observation. However, since the observation angle is not only changed when turning the white light sheet around the axis of the color camera, but also varies in the camera's field of view, a distinctive color trend becomes apparent in each of the images despite the isothermal state in the cell. However, the color trend can only be observed from the left to the right side in each case, while the color does not change along the vertical axis. Hence, a considerable color play due to a varying observation angle only occurs in the direction of the incidence of light. Furthermore, towards the lateral boundaries the observation angle is also strongly affected by the refraction of the light at the cylindrical wall, yielding a significant variation of the angle compared to the central area and thus a conspicuous color change in close vicinity to the sidewall. Therefore, in order to study the effect of the angle between illumination and observation on the color appearance of the TLCs, it is advantageous to restrict the evaluation on a small region in the center of the cell, in which the effect of refraction is negligible and the color can be considered as uniform. Accordingly, the region must have a small horizontal size, but can be larger in the vertical direction. On this way, it is also possible to easily determine the observation angle by means of a scale on the rotation stage on the upper aluminum plate, without taking into account the refraction at the cell's sidewall.

The central region, which has been chosen for the following investigations is indicated by the yellow frames in figure 2.5 and consists of $96 \times 656$ pixel, roughly corresponding to $5\,\mathrm{mm} \times 33\,\mathrm{mm}$ for $\varphi_\mathrm{cc} = 90°$. With decreasing angle the physical dimensions of this section change and especially the horizontal dimension becomes larger. For the observation angle of $\varphi_\mathrm{cc} = 40°$ the horizontal dimension can be estimated to about $8\,\mathrm{mm}$. However, for the investigation of the color signal it is not necessary to strictly keep the physical dimensions constant for all the different observation angles. Hence, a camera calibration has not been performed in this case and the same part of the image with the size of $96 \times 656$ pixel is used in each case. In this region of interest the color of the TLCs has been analyzed for all of the adjusted temperature levels and observation angles separately. For this, the red, green and blue intensities, which are given by an internal algorithm of the camera for each pixel, are taken into account. Aiming for a reliable characterization of the color, the minimum intensity of each pixel over the 50 image recordings is subtracted, respectively, to improve the contrast of the TLCs against the background. For the sake of clearness it should be noted, that the subtraction of the minimum intensity has already been applied to the images of the TLCs in figure 2.5. Furthermore, thresholds are used to exclude dark pixels resulting from the background as well as very bright pixels, which might locally appear due to the agglomeration of some TLC particles. The intensities of the three
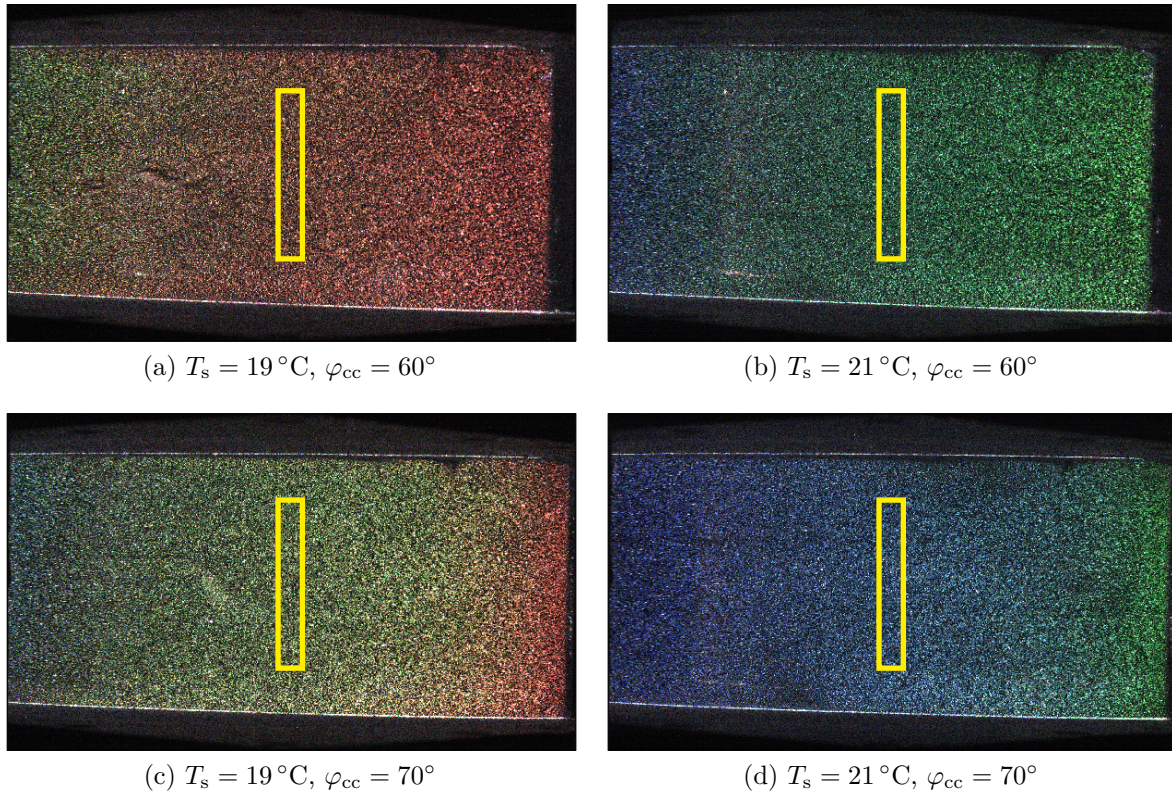
(a) $T_\mathrm{s} = 19\,°\mathrm{C}$, $\varphi_\mathrm{cc} = 60°$



(b) $T_\mathrm{s} = 21\,°\mathrm{C}$, $\varphi_\mathrm{cc} = 60°$



(c) $T_\mathrm{s} = 19\,°\mathrm{C}$, $\varphi_\mathrm{cc} = 70°$



(d) $T_\mathrm{s} = 21\,°\mathrm{C}$, $\varphi_\mathrm{cc} = 70°$

Figure 2.5: Image of the TLCs R20C20W at the temperature levels $T_\mathrm{s} = 19\,°\mathrm{C}$ (a,c) and $T_\mathrm{s} = 21\,°\mathrm{C}$ (b,d) for the observation angles $\varphi_\mathrm{cc} = 60°$ (a,b) and $\varphi_\mathrm{cc} = 70°$ (c,d) after subtracting the minimum intensity of each pixel over time. In this case, the second spectrum according to figure 2.4 was used for illumination.

primary colors of the remaining pixels are then separately averaged over the central region of interest. Hence, for every combination of the temperature level and observation angle the color of the TLCs is in the end represented by three values, namely the averaged red, green and blue intensities of the pixels.

However, with a view to the temperature measurements, the color appearance of the TLCs should not be characterized based on the absolute intensities, as those also depend on the power of the light source and the seeding concentration of the TLCs. While the former can here be considered as almost constant, this does not apply to the latter, since the seeding concentration varies in the experiments due the sedimentation of the TLC particles. Even though the mass density of TLCs, which is roughly in between $1.00\,\mathrm{g/cm^3} \le \rho_\mathrm{TLC} \le 1.02\,\mathrm{g/cm^3}$ according to the manufacturer's data, nearly matches that of water for common temperature ranges, the seeding concentration may considerably decrease during long-time measurements and can also not be exactly reproduced in independent measurements. In order to overcome this issue and thereby quantitatively describe the color of TLCs without being affected by inconsistencies of the absolute intensities, typically either normalized intensities are used [106] or a transformation from the $RGB$-colorspace to the $HSI$-colorspace ($H$ - hue, $S$ - saturation, $I$ - intensity) or similar colorspaces is performed, as for example shown in reference [71].

In this work, the intensities are transformed to the $HSV$-colorspace, in which $H$, $S$ and $V$ denote the so-called hue, saturation and value. For the transformation the averaged $RGB$-triplets obtained from the region of interest are normalized by the maximum occurring intensity over the whole set of the different measurement series, such that

all the normalized intensities are comparable and range in $R_n, G_n, B_n \in [0,1]$. With this normalization the hue, saturation and value are defined according to the equations (2.1a), (2.1b) and (2.1c) [107]. The maximum intensity $\max(R_n, G_n, B_n)$ and minimum intensity $\min(R_n, G_n, B_n)$ of each triplet is denoted by MAX and MIN in those equations, respectively.

$$H = \begin{cases} 0° & \text{if } R_n = G_n = B_n \\ 60° \cdot \frac{G_n - B_n}{\text{MAX} - \text{MIN}} & \text{if } \text{MAX} = R_n \\ 60° \cdot \left(2 + \frac{B_n - R_n}{\text{MAX} - \text{MIN}}\right) & \text{if } \text{MAX} = G_n \\ 60° \cdot \left(4 + \frac{R_n - G_n}{\text{MAX} - \text{MIN}}\right) & \text{if } \text{MAX} = B_n \end{cases} \tag{2.1a}$$

$$S = \begin{cases} 0 & \text{if } R_n = G_n = B_n \\ \frac{\text{MAX} - \text{MIN}}{\text{MAX}} & \text{else} \end{cases} \tag{2.1b}$$

$$V = \text{MAX} \tag{2.1c}$$

This definition of color better conforms to the visual perception of human beings, as the chromatic information ($H$, $S$) of an image is separated from its intensity information ($V$) [108]. While the hue $H$ assigns a specific pure color shade to an object, the saturation $S$ represents the dilution of the pure color shade by white light and the value $V$ specifies the brightness. In many cases, hue is quantified by an angle ranging between $H \in [0°, 360°]$, which is normalized in the scope of this work, yielding $H \in [0,1]$. Based on this normalization, the color shade varies continuously along the visible wavelength spectrum from red at $H = 0$ over green at $H = 1/3$ and blue at $H = 2/3$ to violet at $H = 3/4$. For the representation of color shades on the so-called purple line in the chromaticity diagram [109], which cannot be related to a single wavelength, but result from mixtures of light in the red and violet wavelength range, the normalized hue is defined up to $H = 1$, which stands again for the same red color shade as $H = 0$. Hence, the hue is cyclically defined, for instance illustrated in the work [110]. Furthermore, the saturation ranges in $S \in [0,1]$, with an increasing magnitude indicating more pure color shades, which are less diluted by white light. The value is also in between $V \in [0,1]$ and enables to distinguish darker parts of an image with smaller values from brighter parts with larger values. However, with regard to the temperature measurements, the hue has turned out as the most important quantity in this work, since the color shade of the TLCs exhibits a clear and robust dependency on the temperature. Therefore, at first the determination of the hue is considered in the following.

Based on the averaged red, green and blue intensities from the central region of interest, one value of the hue is calculated according to equation (2.1a) for each of the fifty images recorded per temperature level and observation angle. For characterizing the color shade of the TLCs, the hue is then temporally averaged over the fifty images, denoted by $\langle H \rangle_t$, yielding the results for the correlation between the hue and temperature for the two different illumination spectra in figure 2.6a and 2.6b. It is emphasized, that the value of the hue must be unambiguously correlated to the temperature for reliable temperature measurements. Accordingly, the following investigations refer to the temperature range from the minimum of each curve, which is marked with a red circle, towards higher temperatures. Comparing the figures 2.6a and 2.6b, one aspect becomes directly apparent. When considering the total of the six different observation angles, the hue roughly varies in between $0.45 \leq \langle H \rangle_t \leq 0.65$ when the TLCs are illuminated with the first spectrum
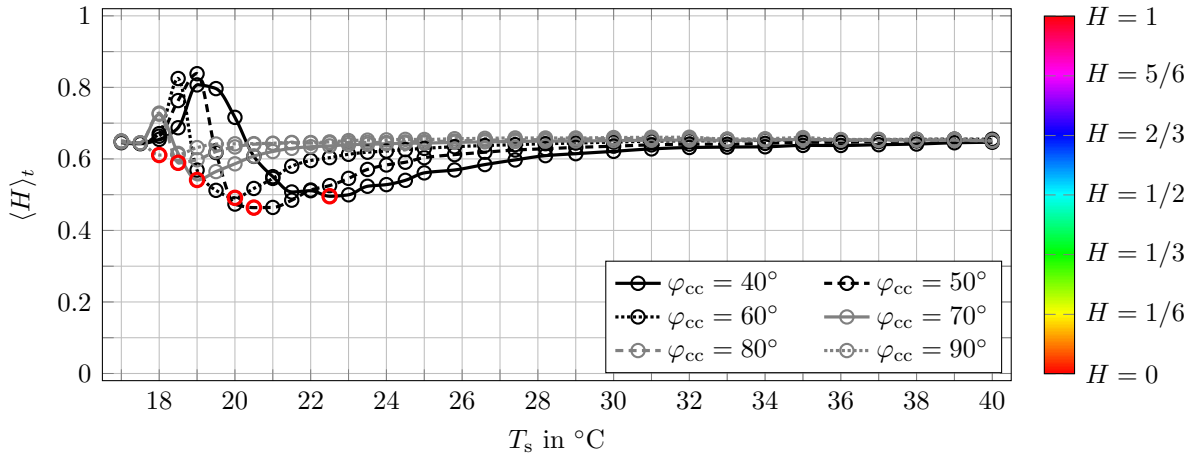
(a) Illuminated by the first spectrum.
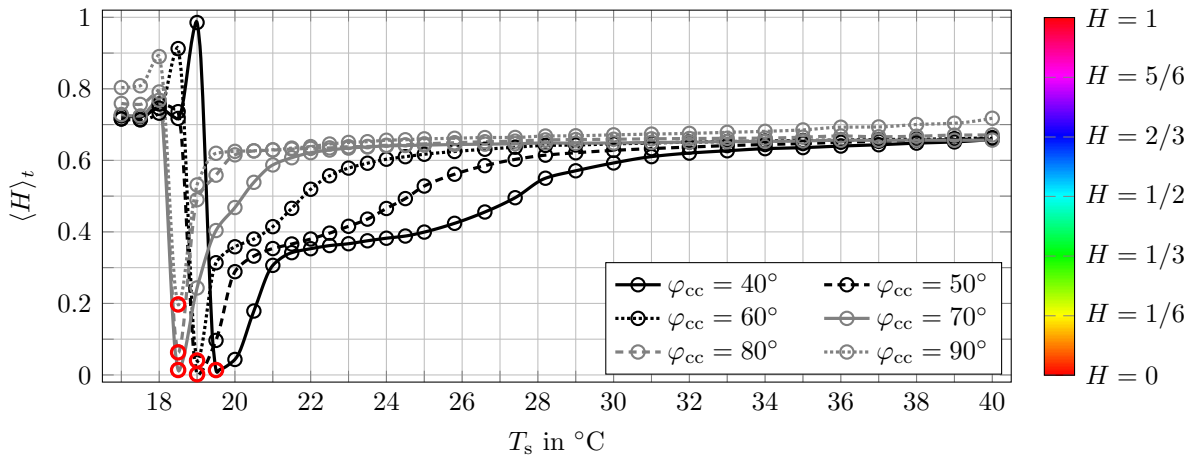


(b) Illuminated by the second spectrum.

Figure 2.6: Color appearance of the TLCs R20C20W in terms of the hue $\langle H \rangle_t$ in dependency of the set temperature $T_s$ for a varying observation angle $\varphi_{cc}$ and both spectra of illumination. For a better illustration, the colorbar on the right side shows the change of the color appearance with hue. The red markers at the minimum of each curve indicate the onset of the investigated temperature range with unambiguous correlation to the color appearance of the TLCs, respectively. The results are obtained from the region of interest indicated in figure 2.5.

from figure 2.4, while the dynamic range is much larger for the illumination with the second spectrum, since the hue overall ranges from about $\langle H \rangle_t = 0$ up to $\langle H \rangle_t = 0.7$ in this case. This indicates that the color of the TLCs varies from red to blue with increasing temperature when illuminated with the second spectrum, but only varies in between cyan and blue when the first spectrum is applied, due to the dominance of the integral intensities in the blue and green wavelength range. Since slight changes of the hue with temperature are disadvantageous to precisely determine the temperature, which can be expected and has also been demonstrated in the study [78], the second spectrum is better suited for the temperature measurements with TLCs. The importance of the illumination spectrum is thus confirmed, however, as the application of another type of camera for the observation of the TLCs may yield different results, very specific recommendations for the illumination spectrum cannot be given. Nevertheless, it can be stated that the integral intensities of

the illumination spectrum in the range of red, green and blue light must be well-adjusted to prevent a preferential color in the image of the TLCs.

The curves in figure 2.6 also show that the observation angle has a significant influence on the color of the TLCs. It can be seen, that the minimum indicated with the red circle is mostly shifted to the left side with increasing observation angle, meaning that the range with an unambiguous correlation between the hue and temperature already starts at lower temperatures. In most cases the minimum is in the range $18\,°C < T_s < 20\,°C$ and, therefore, below the nominal red start of the TLCs. Furthermore, with regard to the influence of the observation angle it is very important to consider the slope of the curves. Because of the steeper increasing hue at the minimum of the curves, the temperature range with the main color change becomes smaller for larger observation angles, which is in particular obvious from the results obtained with the second illumination spectrum in figure 2.6b. Thus, the width of the temperature range between the nominal red start and blue start, which is $20\,K$ for $\varphi_{cc} = 0°$, is drastically decreased. After the steep increase for low temperatures, the hue only slightly changes towards higher temperatures over an extended range when large observation angles are used, resulting in a larger measurement uncertainty in this temperature range [78]. Based on this finding it can be concluded, that the standard setup for the recording of tracer particles in a flow with one camera, which is perpendicularly arranged to the direction of the light sheet, is in many cases not suited when temperature fields are measured via the color of TLCs, since the measuring range with a low measurement uncertainty is strongly limited. On the contrary, in general flat observation angles such as $\varphi_{cc} = 40°$ may be problematic concerning the uniform imaging of the measurement plane, as large differences of the magnification can appear in the camera's image. Taking this into account, observation angles in between $50° \leq \varphi_{cc} \leq 80°$ can be considered as a suitable tradeoff.

Finally, the results for the other two quantities of the $HSV$-colorspace, namely the saturation $S$ and the value $V$ of the images of the TLCs, is shortly discussed. Those quantities are depicted in figure 2.7, but only the results for the better suited illumination spectrum, i.e. the second spectrum, and for the observation angles between $\varphi_{cc} = 50°$ and $\varphi_{cc} = 80°$ are plotted, because those angles have turned out as the most promising based on the previous findings. For each of the angles, the saturation $\langle S \rangle_t$ and the value $\langle V \rangle_t$, which are also time-averaged over the fifty images recorded in every single measurement, a steep increase can be seen at about $T_s = 18\,°C$. This is in line with the results for the hue, as the red color shade of the TLCs starts to appear around this temperature. However, after the steep increase several local maxima and minima of the saturation and value can be found. Especially, the inordinate behavior of the value can probably be traced back to the experimental conditions to some extent, since the TLCs were stirred in between the measurements to ensure the isothermal conditions, thereby affecting the distribution of the seeding in the cell and accordingly also the local intensity of the light reflected by the TLCs. All in all, the saturation and the value do not show such a clear dependency on the temperature, contrary to the hue value. Therefore, it is confirmed that the hue is the most important and robust quantity in the $HSV$-colorspace for the determination of the temperature of TLCs, due to the unambiguous correlation starting from the minimum hue towards larger temperatures, as discussed by means of figure 2.6. Aiming for reliable temperature measurements, which are not highly susceptible to slight changes of the experimental conditions, such as of the seeding concentration of the TLCs, the saturation and the value are not considered in the scope of this work.
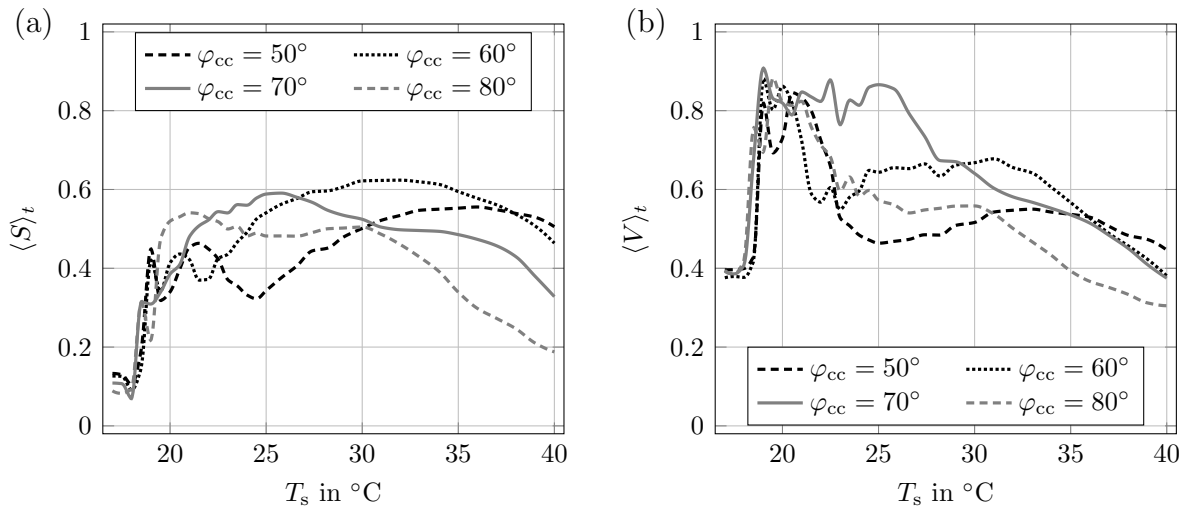
(a)



(b)



Figure 2.7: Time-averaged saturation $\langle S \rangle_t$ (a) and value $\langle V \rangle_t$ (b) of the TLCs R20C20W in dependency of the set temperature $T_s$ for different observation angles applying the second spectrum of illumination according to figure 2.4. The results are obtained from the region of interest indicated in figure 2.5.

## 2.3   Discussion of further influencing factors

The factors with the most relevant influence on the temperature measurements using TLCs have been discussed in section 2.2. Nevertheless, besides the influence of the illumination spectrum and observation angle there are further characteristics of this measuring technique, which may downgrade the results in particular cases. Some of these characteristics regarding the temperature measurements with TLCs should be addressed with a view to the measurements in the current work and are briefly outlined in the following.

**Effect of hysteresis** In the studies [111, 112] it has been reported in detail, that the color appearance of TLCs may show a hysteresis behavior, meaning that it differs for the same temperature, depending on the fact, whether this temperature is achieved upon heating or cooling of the TLCs. Of course, this characteristic would strongly disturb the temperature measurements in the present application, as the Rayleigh-Bénard flow is distinguished by fluctuations. However, it has been demonstrated, that this effect is of minor influence, when the TLCs are not excessively heated or cooled to temperatures, which are significantly outside their nominal temperature range for usage [111–113]. Since the TLCs are moderately cooled and heated in this case, mainly in between the temperature range of color play, the texture of the temperature sensitive material is not altered and the effects of hysteresis are negligible.

**Effect of background light** When performing temperature measurements with TLCs, the lighting conditions in the lab environment must be taken into account. In this regard, different conditions have been tested in the work [94], thereby showing that the correlation between the hue and temperature is affected. An approach for the correction of varying lighting conditions has been presented and successfully used in the study [94]. For the experimental investigations in this work, daylight is blocked out from the lab, the room lighting in the lab is always switched off and small displays as well as control lamps at electronic devices are covered, such that the TLCs in the Rayleigh-Béard cell are only

illuminated by the white light source. Hence, the effects of the ambient light are suppressed, such that any corrections in this respect are not necessary.

**Effect of TLC aging** The pure TLC material is susceptible to damages by ultraviolet light and contaminations in the working fluid, making it unusable after some hours without protection [114]. In order to prevent a fast aging process, in many cases TLCs are isolated from the surrounding fluid with a microencapsulation made of a thin continuous polymer coating. Microencapsulated TLCs are also used in this work, however, it must be noted that their durability is limited as well. With regard to the application of microencapsulated TLCs in the form of a very thin TLC film for surface temperature measurements, it has for example been shown in the study [115], that the correlation between the hue and temperature is slightly shifted over several hours of operation. On the contrary, calibration curves for a film of microencapsulated TLCs have repeatedly been measured in the work [116] and it has been demonstrated, that nearly the same correlation between the hue and temperature can be obtained after three weeks of aging on the test surface. This indicates, that the reproducibility of calibration measurements strongly depends on the specific experimental conditions, such as the intensity and the spectral distribution of the illumination, the duration of the illumination, the contact of the TLC material to any contaminations and the degree of ultraviolet radiation. Even though the application of a TLC film for surface temperature measurements cannot be compared with TLCs dispersed in a fluid one-to-one, because the aging process is also affected by the thickness of the film [115], those findings suggest that special care must be taken for the set of different long-time measurements with the TLCs in this work. Hence, prior to each long-time measurement in the larger Rayleigh-Bénard facility presented in section 3, the working fluid is completely replaced and fresh TLC material is inserted into the cell just before the start of the measurement. In addition, particular attention is paid to the constancy of the color play of the TLCs over the whole period of the different measurements, to ensure that the specifications of the TLCs have not altered during their storage, which would result in a systematic error in the temperature measurements.

**Effect of response time** Another effect to be considered is the response time of the TLCs to temperature variations. While the pure TLC material responds to temperature changes after a few milliseconds [117], such that the color indicates the local temperature almost without any time delay, the microencapsulation of TLCs results in a slightly larger response time. For the investigation of the local temperatures in a flow with very high velocities this might be a crucial drawback, especially when the correlation between the temperature and velocity is required for some analysis. However, as shown in the review [71], it has been estimated in several studies that the response time of microencapsulated TLCs to temperature changes is still in the order of several milliseconds. Therefore, this factor can here be neglected, since the maximum velocities in the slowly evolving Rayleigh-Bénard flow are in the order of 1 mm/s in the measurements conducted for the present work, which allows to determine the corresponding local temperatures and velocities.

## 2.4   Calibration techniques

Due to the dependency of the color appearance of TLCs on the illumination spectrum and the observation angle, it is in most cases not possible to consider the nominal specifications of the TLCs for accurate temperature measurements. Hence, usually calibration measurements for a specific experimental setup are inevitable. Furthermore, especially

when a region of interest with a large range of observation angles has to be investigated, it is of great importance to use a local calibration approach. Using such an approach, the images of the TLCs for different temperature levels are split into several subregions and the correlation between the color and temperature is extracted locally to account for the effect of the observation angle [71]. Compared to a global calibration approach with only one correlation between the color and temperature for the entire region of interest, the measurement uncertainty is considerably lowered [78, 100, 113, 118, 119]. Therefore, only local calibration approaches are taken into account for the determination of the temperature fields in this study.

Various calibration approaches have been presented with regard to liquid crystal thermography. Many of those are solely based on the dependency of the hue on the temperature, while others make also use of the saturation and value of the $HSV$- colorspace or are derived in the $RGB$- colorspace. Moreover, a local calibration approach using the temperature dependency of the reflectance of TLCs in a narrow wavelength band has been demonstrated in the study [120], where the possibility for a significant extension of the temperature measuring range by means of this technique has been reported. However, since the reflectance of the TLCs may strongly decrease over time, considering only a narrow wavelength band for the determination of the temperature fields is expected to yield errors in long-time measurements. The same problem arises, when the absolute red, green and blue intensities of the $RGB$- colorspace or the value $V$ of the $HSV$- colorspace are applied for the calibration, as those are directly affected by a varying brightness of the light reflected by the TLCs, for example caused by sedimentation. Hence, mostly ratios of the red, green and blue intensities or the color shade of the TLCs in terms of the hue are used, thereby making the evaluation less susceptible to changes of the brightness. In addition to the hue $H$, in some studies also the saturation $S$ has been used for the calibration [103], however, as shown at the end of section 2.2, the saturation cannot always be considered as a trustworthy indicator for the temperature. Calibration techniques incorporating multiple variables are frequently utilized, as they are capable of extending the temperature measuring range [106, 121] and reducing the measurement uncertainty compared to single variable approaches [103, 122]. Nevertheless, they rely on the fact that all the input variables of the calibration show almost the same dependency on the temperature in the application and the calibration measurements, which is very difficult to control in practice. Special techniques can be applied to reduce the errors resulting from this issue [121], but cannot fully compensate it. Throughout the whole study, the hue has proven to be the most useful and robust quantity with respect to its temperature dependency. Thus, having in mind that the temperature measuring range can also be adapted by applying different types of TLCs, as shown in the appendix E, it is one of the main goals of the current work to establish a reliable calibration exclusively based on the hue.

The measurement data obtained from the experiment with the TLCs R20C20W are now used to study different local calibration approaches on the basis of the hue with regard to the uncertainty of the temperature measurements. Since the first results have already indicated that the second illumination spectrum according to figure 2.4 is better suited for the illumination due to the stronger color play of the TLCs with temperature, only the data resulting from the application of the second spectrum are considered. For the local calibration approach the whole field of view of the color camera is in this case split into interrogation windows with a size of $32 \times 32$ pixel with an overlap of $50\,\%$ in each direction. This is an appropriate size for the current investigations, as the number of TLC

particles in each interrogation window is sufficiently large for a reliable evaluation, while it also yields an adequate spatial resolution for the temperature measurements in a flow induced in the measurement cell, as will be shown in section 2.5. However, for estimating the influence of the observation angle on the uncertainty of the temperature measurement, the field of view is at first again restricted to the central region of interest indicated in figure 2.5, since the variation of the observation angle in this region is negligible. Hence, when the central region with its size of $96 \times 656$ pixel is divided into small interrogation windows with a size of $32 \times 32$ pixel and an overlap of $50\,\%$, $5 \times 40$ data points of the hue are provided per image. Using the spatially resolved and temporally averaged data of the hue in this region of interest, where the temporal average is taken over the total of fifty images recorded per temperature level, the local calibration is performed for each of the most suitable observation angles $50° \leq \varphi_{cc} = 80°$ separately. Based on the previous finding that the color of the TLCs does not significantly change anymore when approaching the upper end of the temperature range of color play, only the temperature levels $T_s \leq 24\,°\mathrm{C}$ are taken into account for the calibration.

For the local calibration three different approaches are demonstrated in the sections 2.4.1 - 2.4.3. Before explaining these approaches, it shall also be mentioned, that the data of the hue are processed to improve the results, which is demonstrated in figure 2.8 by means of an exemplary local calibration curve obtained from a single interrogation window in the center of the region of interest for an observation angle of $\varphi_{cc} = 70°$. Besides the original calibration points and the different steps of the processing at the bottom part of the figure 2.8, the temporal standard deviation of the local hue is depicted at its top, which must be considered for understanding the first step of the processing of the hue. It can be seen that the standard deviations are the largest at the lower end of the temperature range. Since the higher standard deviations for $17\,°\mathrm{C} \leq T_s \leq 18\,°\mathrm{C}$ are caused by the fact, that the intensity of the light reflected by the TLCs is still very small in this temperature range for $\varphi_{cc} = 70°$, these temperatures should not be taken into account for measurements with this observation angle. As demonstrated in figure 2.7b, the intensity considerably increases at $T_s = 18.5\,°\mathrm{C}$, such that the temporal standard deviation of the measured hue can be expected to decrease. However, at this temperature level the standard deviation reaches its maximum. This issue arises from the aforementioned cyclic definition of the hue, meaning that $H = 0$ and $H = 1$ represent the same red color shade. Hence, even though the TLCs have a distinctive red color at $T_s = 18.5\,°\mathrm{C}$, i.e. the red intensities measured with the color camera are much larger than the green and blue intensities, the hue may strongly vary. Either the hue is around $H = 0$, when the green intensity is slightly larger than the blue intensity, or the hue is close to $H = 1$ in the opposite case. In this particular example, the local hue of the investigated interrogation window is for only two of the fifty calibration images at $T_s = 18.5\,°\mathrm{C}$ close to the upper end of the hue range, however, due to the large difference those two data points yield the clearly noticeable peak of the standard deviation. In order to account for this in the measurements, all the temporally resolved values of the hue with $H > 0.8$ are reduced by one, resulting in negative values, but keeping the color shade due to the cyclic definition of the hue, which is referred to as a conditional offset in figure 2.8. A similar technique has been used in the study [123] for better distinguishing the red color shade of TLCs. As the hue for larger temperatures only varies up to about $H = 2/3$ in average and just slightly fluctuates in most cases, the determination of larger temperatures is not in conflict with this step.

After time-averaging the temporally resolved values of the hue, a sliding median filter is applied. This filter incorporates the hue of the two adjacent interrogation windows

in column-wise direction of the image, thereby not smoothing out the color trend of the TLCs in the horizontal direction, which is clearly obvious from figure 2.5. In this case, the median filter does not show a significant effect and has therefore been combined with the previous step for a better illustration in figure 2.8. Nevertheless, using such a sliding median filter along the direction with almost uniform color is recommended for the evaluation of the calibration images, as this filter allows to eliminate outliers, that might for example be caused by the lack of TLCs at a small spot in the image or by imperfections in the background [122]. In the next step, the calibration points are corrected with respect to an unambiguous correlation between the color and temperature of the TLCs. Therefore, the points at the lower end of the temperature range are excluded. The minimum related to the red start of the TLCs, which may either have a positive or negative hue, is searched for with a refined algorithm, to prevent the detection of an outlier as the minimum for the calibration curve. Furthermore, the correction of ambiguity includes that infrequently appearing local minima towards larger temperatures are deleted and replaced by linear interpolation of the neighboring points. In the last step, a piecewise cubic interpolation is applied to specify the correlation between the hue and temperature with enhanced resolution. Even though most of the measured hue values should in general fall into the range $0 \leq H \leq 2/3$, corresponding to the typical color change from red to blue, the hue might vary in between $-0.2 \leq H \leq 0.8$, when considering the described conditional offset. Hence, aiming for the determination of the temperature from each of the possible hue values in the application, the calibration curve is linearly extrapolated towards the lower and upper end of the range. Since the interpolated points over the whole curve are computed with a resolution of the hue of $\Delta H = 0.001$, each curve consists of 1001 points in the end, such that the transition of the gradient can almost be considered as continuous.



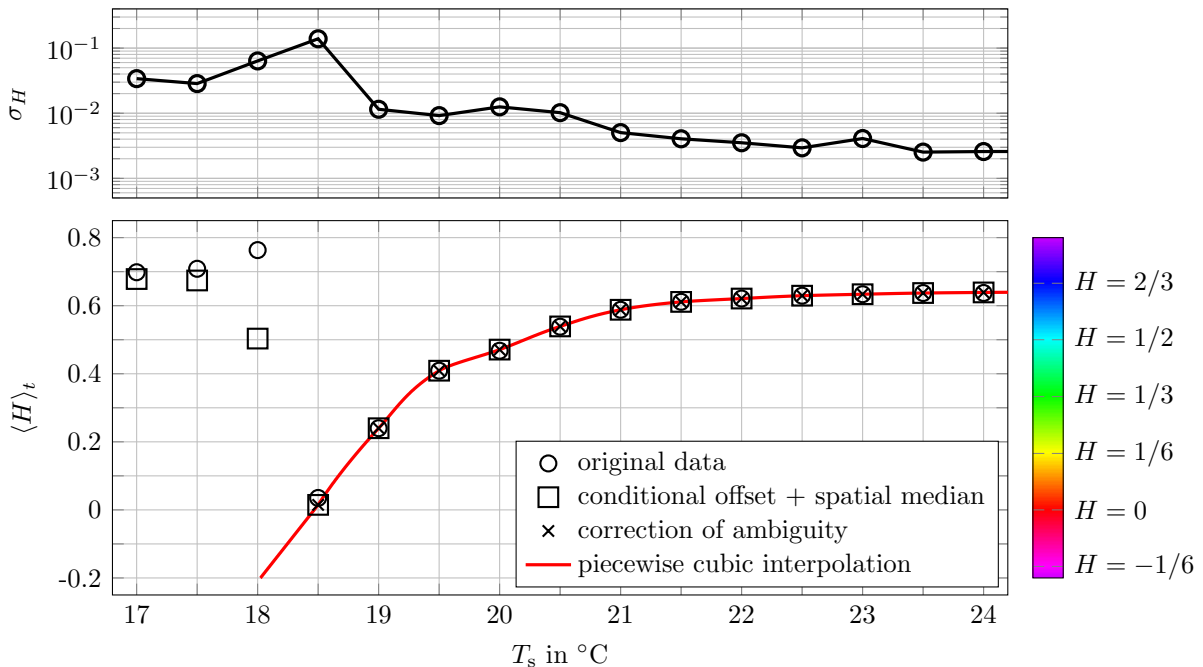Figure 2.8: Processing steps applied to the local calibration curves demonstrated at an exemplary curve for the observation angle of $\varphi_{cc} = 70°$. The calibration data are obtained from an interrogation window in the center of the region of interest indicated in figure 2.5. In addition, the temporal standard deviation of the local hue in the original data is shown at the top part of the figure.

## 2.4.1 Linear interpolation in local calibration curves

The first calibration approach directly utilizes the smooth local calibration curves for the determination of the temperature via linear interpolation of the hue between the two neighboring points within the curves. The main advantage of this approach is that measurement errors due to deviations resulting from functional approximations or from an inaccurate modeling of the correlation between the hue and temperature are completely eliminated. Due to its transparency, this approach is also best suited to characterize the measuring technique and to assess its limits. Here, the accuracy of this approach is estimated by its capability to reproduce the known isothermal temperature distributions of the calibration measurements. Thus, for this estimation the local hue values obtained from the measurements with the color camera for the different temperature levels are used to calculate the local temperatures, which are then compared with the target values, given by the temperatures adjusted at the thermostatic bath, respectively. These set temperatures almost coincide with the temperatures measured with the PT100 sensors during the recording of the calibration images. However, since the single calibration curves represent the temporally averaged hue values at the different temperature levels, the local temperatures must not be determined on the basis of those average values, as this would automatically yield the desired target values, if the local hue value is not shifted by the median filtering or the correction of ambiguity in the processing of the data according to figure 2.8. Instead, the temperature distributions must be calculated based on the hue values of the temporally resolved calibration images, in order to take into account that the local hue measured in the calibration slightly varies around the temporal mean, yielding fluctuations of the calculated temperatures around the target value. For a better imagination, the principle of the calculation is sketched in figure 2.9 by means of a local calibration curve taken from the center of the mentioned region of interest. Furthermore, an inset can be seen in this figure, showing the temperatures calculated in the corresponding interrogation window at the example of the set temperature $T_\mathrm{s} = 19\,^\circ\mathrm{C}$. In this case, all the temperatures vary within a very narrow range around the target value, but rarely outliers may also occur, for example due to the lack of TLCs within a small spot at a certain instant of time. In order to account for this, the temperatures which do not comply with the condition

$$\mathrm{med}(T|_{T_{\mathrm{s}},n}) - 2 \cdot \sigma_{T|_{T_{\mathrm{s}},n}} < T|_{T_{\mathrm{s}},n}(X,Y,t) < \mathrm{med}(T|_{T_{\mathrm{s}},n}) + 2 \cdot \sigma_{T|_{T_{\mathrm{s}},n}} \qquad (2.2)$$

are removed. In this condition, $\mathrm{med}(T|_{T_{\mathrm{s}},n})$ and $\sigma_{T|_{T_{\mathrm{s}},n}}$ denote the median value and the standard deviation of the whole calculated temperatures for a given temperature level of the calibration.

The deviation of the calculated temperatures has been studied for each temperature level in the range $18.5\,^\circ\mathrm{C} \leq T_\mathrm{s} \leq 24\,^\circ\mathrm{C}$ and the observation angles between $50^\circ \leq \varphi_\mathrm{cc} = 80^\circ$. In this regard, the mean signed deviation (MSD), which is $\mathrm{MSD} = \langle T|_{T_{\mathrm{s}},n} - T_{\mathrm{s},n} \rangle$, and the standard deviation of the calculated temperatures $\sigma_T|_{T_{\mathrm{s}},n}$ have been investigated. This combination allows to evaluate the calibration approach with respect to systematic errors and the variation of the calculated temperatures around the average. The results for the mean signed deviation and the standard deviation are depicted in the figures 2.10a and 2.10b. It becomes obvious that distinct systematic errors are not present for the angles $50^\circ \leq \varphi_\mathrm{cc} = 70^\circ$, since the absolute value of the MSD does not exceed $|\mathrm{MSD}| = 0.1\,\mathrm{K}$ in the investigated temperature range and mostly even varies in between $-0.01\,\mathrm{K} \leq |\mathrm{MSD}| \leq 0.01\,\mathrm{K}$. The results for $\varphi_\mathrm{cc} = 80^\circ$ clearly demonstrate that the temperature range with small measurement errors decreases with increasing observation
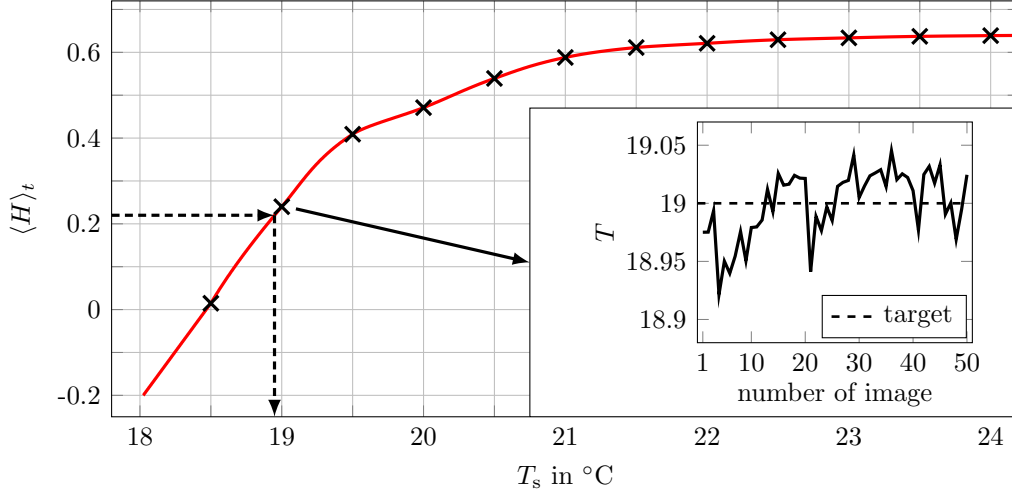
Figure 2.9: Principle of the temperature determination based on linear interpolation of the hue demonstrated at a local calibration curve obtained from an interrogation window in the center of the region of interest. For this interrogation window the inset shows the variation of the calculated temperatures around the exemplary target value $T_{\mathrm{s}} = 19\,^{\circ}\mathrm{C}$.

angle. Due to the flatness of the local calibration curves for $\varphi_{\mathrm{cc}} = 80°$ at larger temperatures, in particular the standard deviation becomes very high and reaches up to $\sigma_{T_{\mathrm{calc}}} \approx 1\,\mathrm{K}$ for $T = 24\,^{\circ}\mathrm{C}$, which is also the case for $\varphi_{\mathrm{cc}} = 70°$. However, while the angle $\varphi_{\mathrm{cc}} = 80°$ should not be considered for measuring temperatures larger than $T = 21\,^{\circ}\mathrm{C}$, the angle $\varphi_{\mathrm{cc}} = 70°$ is suited to determine temperatures in the range $18.5\,^{\circ}\mathrm{C} \leq T \leq 22\,^{\circ}\mathrm{C}$, in which the mean signed deviation is kept within $-0.01\,\mathrm{K} < \mathrm{MSD} < 0.01\,\mathrm{K}$ and the standard deviation does not exceed $\sigma_T = 0.2\,\mathrm{K}$. Because of the more gradual color change of the TLCs with temperature for the angles $\varphi_{\mathrm{cc}} = 50°$ and $\varphi_{\mathrm{cc}} = 60°$, those could be applied to reduce the measurement errors for the highest temperature levels, but smaller observation angles are disadvantageous for the uniform imaging of the measurement plane. Considering this, observation angles in the range $60° \leq \varphi_{\mathrm{cc}} \leq 70°$ are most appropriate.

## 2.4.2   Functional approximation of local calibration curves

The second calibration approach is based on functional approximation of the local calibration curves, with the time averaged hue $\langle H \rangle_t$ as the argument of the function and the temperature being the calculated function variable. As shown in the study [78], for example the use of polynomial functions performs considerably worse compared to the linear interpolation approach, when the fitting is only applied to the measured calibration points. However, if the entire cubic interpolated points are also incorporated into the functional approximation, the derived fitting function better follows the calibration points. Here, polynomial fits of the 6th and 8th degree, i.e. $T = \sum_{n=0}^{6} c_n \langle H \rangle_t^n$ and $T = \sum_{n=0}^{8} c_n \langle H \rangle_t^n$ have exemplarily been used for the investigation of the resulting measurement error. Furthermore, an exponential fit $T = c_1 e^{c_2 \langle H \rangle_t} + c_3 e^{c_4 \langle H \rangle_t}$ and a Fourier fit of the form $T = c_0 + \sum_{n=1}^{8} c_{\mathrm{sin},n} \sin(n\,\omega\,\langle H \rangle_t) + c_{\mathrm{cos},n} \cos(n\,\omega\,\langle H \rangle_t)$ have been tested. The coefficients $c_n$ of the polynomial fits and of the exponential fit as well as the offset $c_0$, the coefficients $c_{\mathrm{sin},n}$, $c_{\mathrm{cos},n}$ and the angular frequency $\omega$ of the Fourier fit have been determined using algorithms of *Matlab R2020b*.

For comparing the different functional approximations, those have been applied to reproduce the local temperatures in the central region of interest of the temporally resolved
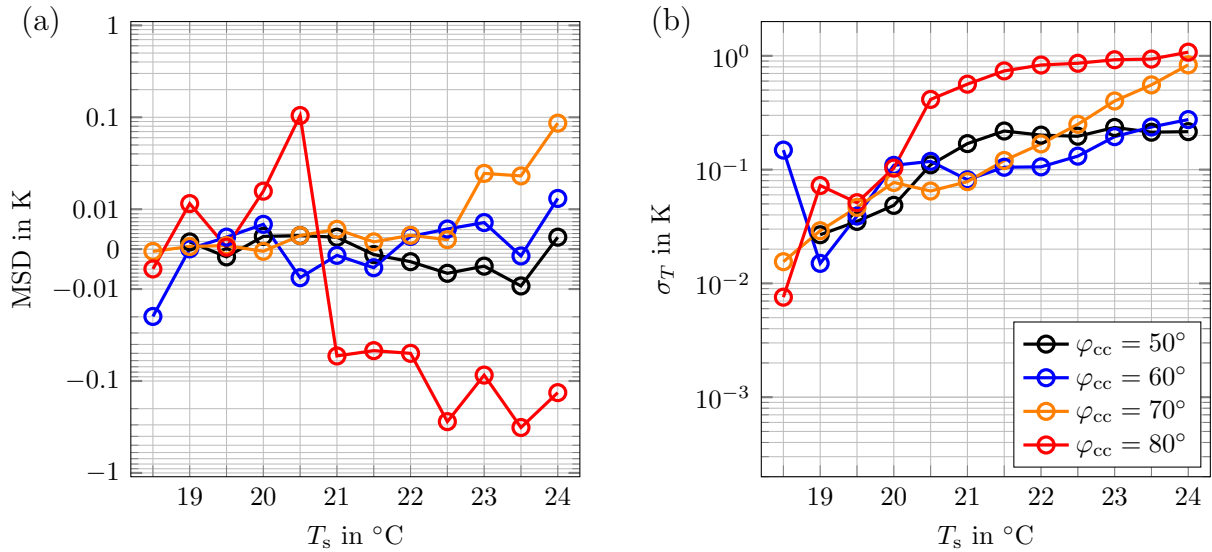
Figure 2.10: The mean signed deviation MSD (a) and the standard deviation $\sigma_T$ (b) of the temperature measurement for different observation angles, resulting from the calibration approach based on linear interpolation of the hue in local calibration curves.

calibration images for $\varphi_{\mathrm{cc}} = 70°$, since this angle has in the last section turned out to be suitable for temperature measurements. The results for the mean signed deviation and standard deviation with the outlier removal according to condition (2.2), shown in the figures 2.11a and 2.11b, feature similar characteristics in each case. While the former varies between positive and negative values, indicating that the functional fits yield in average either an overestimation or an underestimation at certain temperature levels, the latter mainly increases with temperature. For most of the temperature levels the smallest MSD is achieved with the 8th degree polynomial fit or the Fourier fit, however, especially in the temperature range $22\,°\mathrm{C} \leq T \leq 24\,°\mathrm{C}$ these functional approaches result in higher standard deviations. This can be traced back to the fact, that the functions are more susceptible to variations of the local hue around the temporal mean for larger temperatures. Nevertheless, all the approximations could be used for temperature measurements from $18.5\,°\mathrm{C}$ up to at least $22\,°\mathrm{C}$, as the absolute value of the mean signed deviation does not exceed $|\mathrm{MSD}| = 0.2\,\mathrm{K}$ and also the standard deviation is kept below $\sigma_T = 0.2\,\mathrm{K}$.

## 2.4.3 Neural network training with the local calibration data

While the two approaches for the determination of the temperature shown in the previous sections are directly related to the local calibration curves, the third calibration approach makes use of neural networks, which are capable of learning the relations of a system in analogy to the human brain by means of a set of training data [124]. Due to this feature neural networks are very powerful and are applied to a great variety of different problems, such as pattern classification, clustering, functional approximation, forecasting, optimization and control engineering [125]. In order to improve the performance of neural networks, a large amount of training data is used in many cases, which is accompanied by the demand for extensive computing resources. However, since the computing power is continuously upgraded, the use of neural networks becomes more and more popular.

With regard to liquid crystal thermography, neural networks have been applied in several works [106, 122, 126–128]. These studies are not reviewed individually at this point,
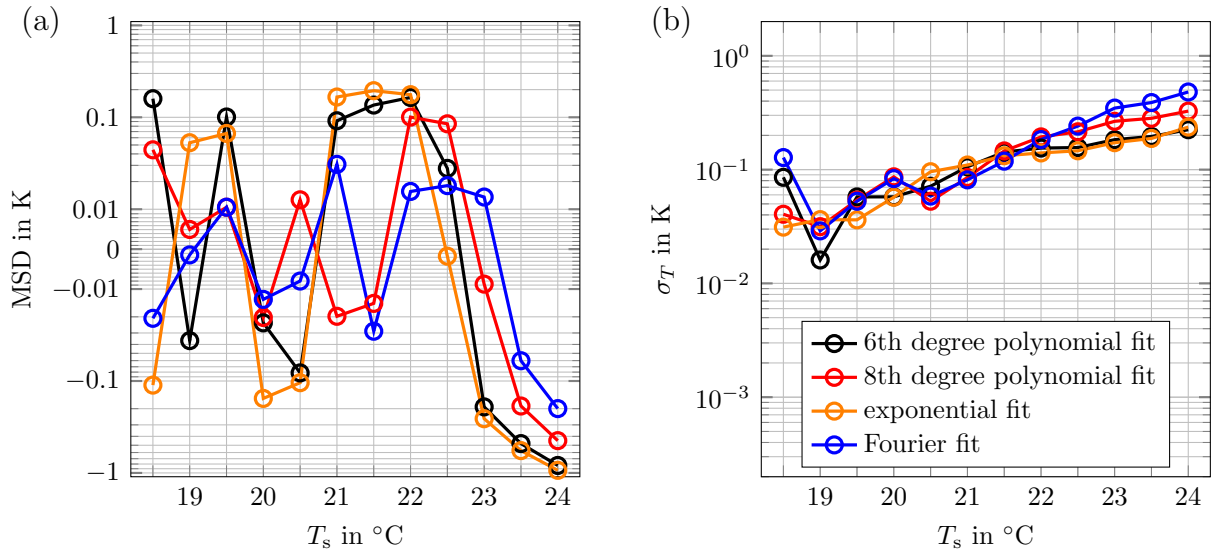
Figure 2.11: The mean signed deviation MSD (a) and the standard deviation $\sigma_T$ (b) of the temperature measurement for the observation angle $\varphi_{\mathrm{cc}} = 70°$, resulting from the calibration approach based on curve fitting techniques.

but it should be mentioned that neural networks have partly been utilized because of their ability to be trained with several variables at the same time. This is undoubtedly a beneficial attribute, but in any case care must be taken, as the training data might also incorporate information, that cannot be transferred to the application of the neural network. In order to prevent the effect of inappropriate training data, the hue is the only temperature dependent variable used as an input for the neural network, as this variable has proven to be the most stable one. However, despite the exclusion of less stable temperature dependent variables, such as the saturation $S$ or the value $V$, the capabilities of neural networks are used in this case. Compared to the approach based on functional approximation discussed in section 2.4.2, there is no need to define a specific type of function, which should almost strictly represent the relation between the hue and temperature, as the network attempts to internally figure out this relation. This is in particular of advantage, when functional approximations fail to represent the desired relation. Furthermore, besides the hue also the coordinates of the corresponding interrogation window are used as an input for the neural network, such that the output value of the temperature is determined based on three input parameters, namely the local hue value $H$ as well as the position of the interrogation windows in the horizontal and vertical direction, given as $X$ and $Y$ in pixels.

The way of determining the temperature from the input parameters is optimized during the training process of the neural network, which is performed with the *Deep Learning Toolbox* of *Matlab R2020b* in this case. As schematically illustrated in figure 2.12, the input parameters in the input layer are transformed to the temperature in the output layer via the so-called hidden layers, which incorporate the basic functional units in form of the neurons. Those operate on their input on the basis of an activation function in combination with a weight, which is iteratively adapted in the training. In this case, the activation function of the neurons within the hidden layers is the *Hyperbolic tangent sigmoid transfer function*, which allows the neural network to learn nonlinear relationships between the input and output of each neuron, while the last transformation for the output layer is a pure linear one, as commonly for function approximations [129]. The illustration shows a

neural network with three hidden layers consisting of 30, 20 and 10 neurons, respectively. In general, the number of hidden layers and neurons per layer can be freely chosen, however, as this considerably affects the training time, the benefit of a highly branched structure of the network should be estimated a priori. In addition to the variation of the structure of the neural network, its training algorithm and the way of interaction between the neurons can be adapted to the specific problem. For example, the data may not only be transferred in forward direction through the network, but can also be propagated backward, which is the case in the so-called recurrent neural networks [130]. Numerous types of neural networks have been developed in recent years to cope with the great variety of applications, but in order to keep the focus, the standard feedforward neural network [124] has been used in this work.
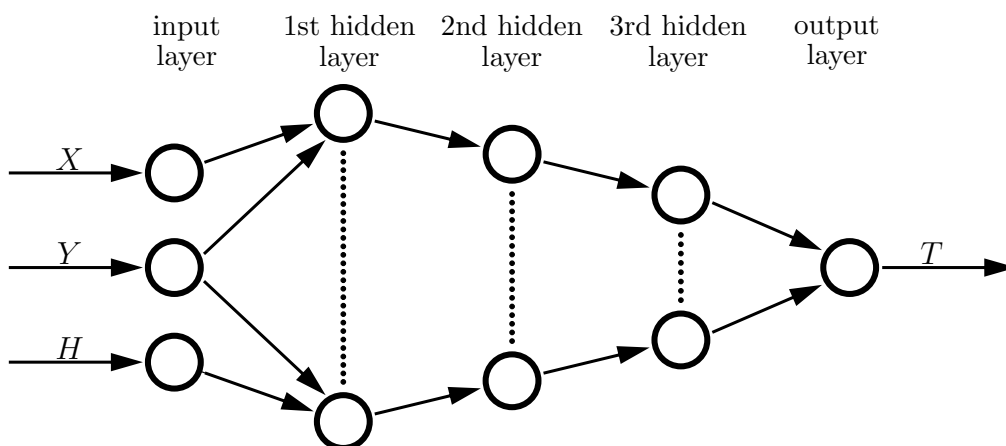


Figure 2.12: A schematic illustration of an exemplary feedforward neural network with the input and output parameters in the corresponding layer. Here, the configuration for the determination of the unknown temperature $T$ is shown. On the contrary, during the training process the temperature is known, as it is given by the different levels of the set temperature $T_\mathrm{s}$ of the calibration measurements and then connected to the input parameters $X$, $Y$ and $\langle H \rangle_t$.

Several structures of the neural network have been investigated, starting with only a few neurons in a single hidden layer. The number of neurons and hidden layers has successively been increased to study the improvement. In the first instance, the networks were trained with the Levenberg-Marquardt algorithm [131, 132], which is one of the most frequently used algorithms for numerical optimizations and holds a lot of promise to provide good results due to its stable divergence [133]. For each structure of the network, five training runs have been performed, yielding very similar results, however, the training run with the smallest mean signed deviation in the reproduction of the calibration temperatures is considered for the comparison. Moreover, besides the Levenberg-Marquardt algorithm also the Bayesian regularization [134] has exemplarily been tested as the training algorithm. In each case the whole set of the input triplets consisting of $\langle H \rangle_t$, $X$ and $Y$ as well as the corresponding target value of the temperature $T_\mathrm{s}$ was randomly divided into three parts, whereof 70% were used for the training itself, while 15% were reserved for the internal validation during the training and first testing purposes, respectively. The results for the mean signed deviation and standard deviation obtained with selected structures of the neural networks applied to the temporally resolved data of the hue values for the observation angle $\varphi_\mathrm{cc} = 70°$ are depicted in the figures 2.13a and 2.13b. For ensuring the comparability with the other two calibration approaches, the calculated temperatures were also filtered according to the condition (2.2). The legend in figure 2.13b denotes the

algorithm of the training and the structure of the neural network, e.g. LM 2 represents the network, which has been trained with the Levenberg-Marquardt algorithm and incorporates two neurons in a single hidden layer, while the use of the Bayesian regularization for the training of a network with 30, 20 and 10 neurons in the first, second and third hidden layer is abbreviated with BR 30-20-10. This notation is consistently used in the following.
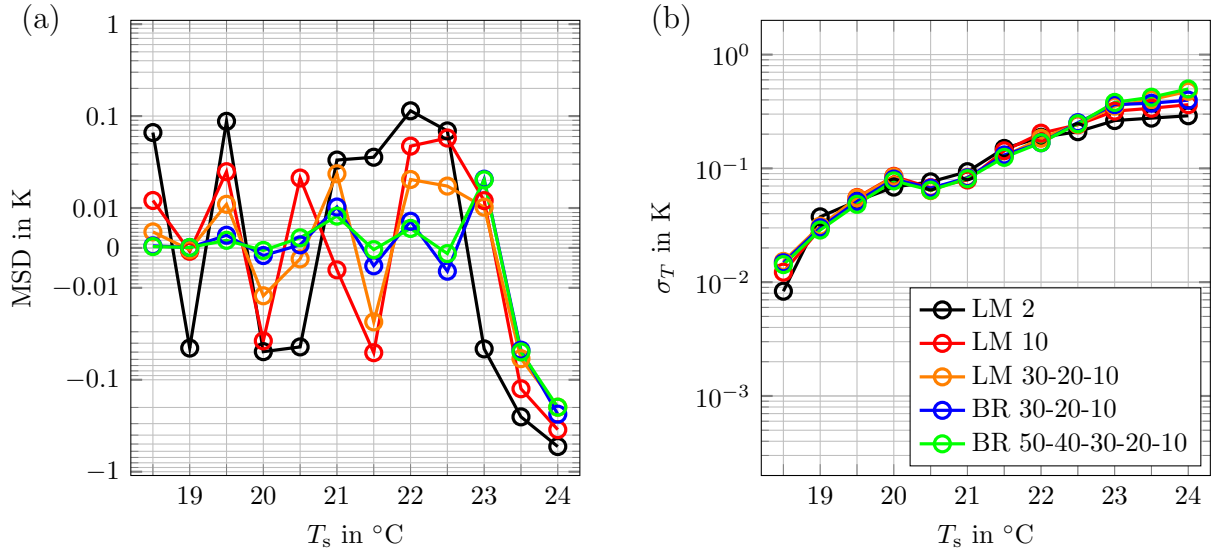


Figure 2.13: The mean signed deviation MSD (a) and the standard deviation $\sigma_T$ (b) of the temperature measurement for the observation angle $\varphi_{cc} = 70°$, resulting from the calibration approach based on neural networks.

In figure 2.13 it can be seen that the network LM 2 can already be used to roughly reproduce the isothermal temperature distribution in the region of interest of the calibration images. At the example of the results for the network LM 10 it becomes obvious, that with increasing number of neurons in the single hidden layer the absolute value of the mean signed deviation is mostly decreased, while the standard deviation is nearly the same. Nevertheless, the mean signed deviation of the temperature measurement can be further reduced when using a larger number of neurons in multiple hidden layers, as demonstrated by the results for LM 30-20-10 and BR 30-20-10. The standard deviation is hardly affected with except for the highest temperature levels, at which the networks LM2 and LM 10 perform slightly better. The time required for one training run of those types of the neural networks took either only a few seconds for LM 2 and LM 10 or some minutes for LM 30-20-10 and BR 30-20-10, which confirms the efficient learning process of neural networks. It should be noted, that also larger neural networks with more extended structures, such as LM 50-40-30-20-10 and BR 50-40-30-20-10 have been tested, however, apart from the drastic increase in the training time, no significant changes can be reported. This is demonstrated in figure 2.13 at the example of the network BR 50-40-30-20-10, for which only one training run covering a time span of approximately six hours has been performed. Comparing the results for LM 30-20-10 and BR 30-20-10 it can be stated, that better results are achieved with the latter one. Accordingly, the network BR 30-20-10 can be considered as suitable, because it provides good results regarding the error of the temperature measurements, while its training required only a small period of time. In the temperature range $18.5\,°C \le T \le 22\,°C$, which has also been addressed in the discussion of the other two calibration approaches in the previous sections, the absolute value of

the mean signed deviation amounts to a maximum of about $|\text{MSD}| = 0.01\,\text{K}$ and the standard deviation is always smaller than $\sigma_T = 0.2\,\text{K}$, when using the network BR 30-20-10. Therefore, the applicability of neural networks for temperature measurements via the color of TLCs is promising.

### 2.4.4 Comparison of the calibration techniques

In the sections 2.4.1 - 2.4.3 it has been shown that the presented local calibration approaches are suited to reproduce the isothermal temperature distribution of the calibration measurements. Only the central region of interest delineated in the figure 2.5 has been considered to study the effect of the different adjustments of the observation angle on the measurement uncertainty. Therefore, even a single correlation between the hue and the temperature of the TLCs could have been used to approximately reproduce the temperature of the calibration measurements, due to the negligible change of the observation angle within the small region of interest itself. However, in practice local calibration approaches must usually be applied, since the observation angle considerably varies within the field of view in many cases and thereby affects the correlation between the hue and the temperature. The necessity of local calibration approaches becomes obvious from figure 2.14, where an image of the TLCs at $T_{\text{s}} = 19\,^{\circ}\text{C}$ with the nominal observation angle $\varphi_{\text{cc}} = 70°$ in the center is opposed to the corresponding field of the hue. It can be seen, that the hue considerably differs from $H \approx 0$ on the right side to $H \approx 0.5$ on the left side, representing the color change from red towards blue.
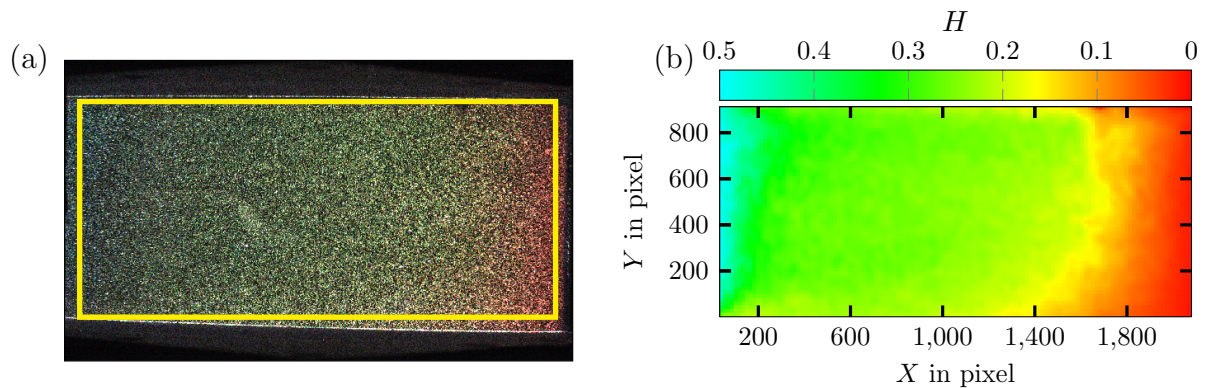


Figure 2.14: (a) An exemplary image of the TLCs R20C20W at the temperature level $T_{\text{s}} = 19\,^{\circ}\text{C}$, applying an observation angle of $\varphi_{\text{cc}} = 70°$. The yellow rectangle indicates the larger investigated section of the field of view. (b) The corresponding hue field.

At the example of the nominal observation angle $\varphi_{\text{cc}} = 70°$, the measurement technique has also been applied to a large section of the field of view, which is indicated in figure 2.14a. The error of the temperature measurement has also been analyzed based on the deviations resulting from the reproduction of the isothermal temperature distribution of the calibration. For a compact characterization of the deviations, the mean absolute deviation $\text{MAD} = \left\langle \left| (T|_{T_{\text{s},i}} - T_{\text{s},i}) \right| \right\rangle$ is considered instead of the mean signed deviation and the standard deviation at this point. However, in order to highlight the effect of the distinctive color change in the horizontal direction on the absolute deviation of the temperature measurement, the average is only taken along the vertical axis of the field of view at first. Hence, the local mean absolute deviation can be analyzed in dependency

of the horizontal position, denoted as $\mathrm{MAD}_X$ in the following. The results of the local mean absolute deviation for the three different local calibration approaches can directly be compared in figure 2.15. For the results obtained with the functional approximation and with the neural network, depicted in figure 2.15b and 2.15c, the 8th degree polynomial fit and the neural network BR 30-20-10 outlined in the previous sections have been considered.



(a) Linear interpolation            (b) Functional approximation            (c) Neural network

Figure 2.15: The local mean absolute deviation $\mathrm{MAD}_X$ of the temperature measurements in dependency of the $x$-coordinate and the set temperature level $T_\mathrm{s}$ for the different local calibration approaches applied to the whole section indicated in figure 2.14a.

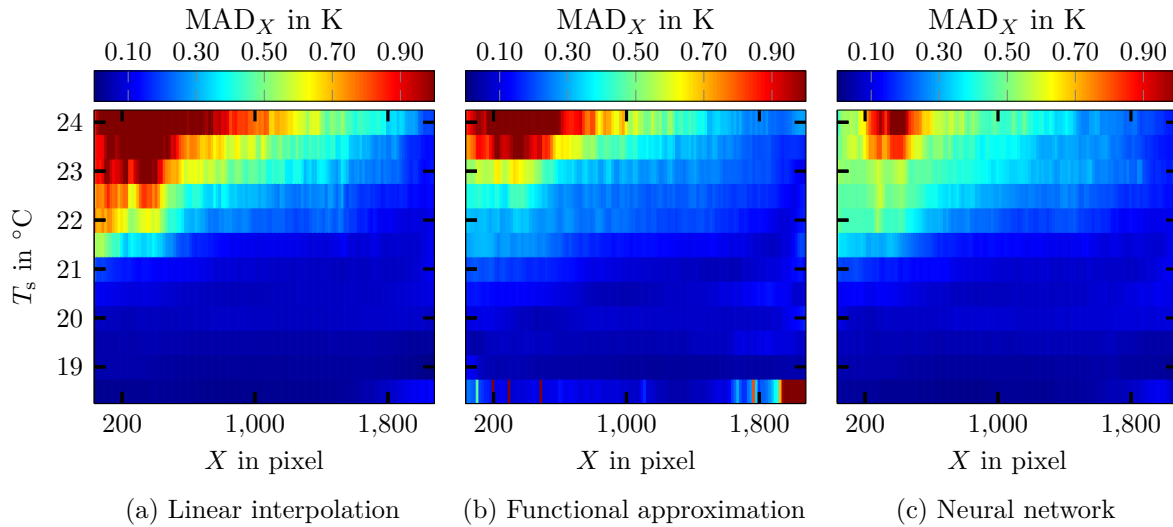The figures 2.15a - 2.15c clearly demonstrate that lower temperatures are determined more correctly over the entire field of view. The only exception occurs in the case of using the functional approximation, which partly fails to reproduce the lowest temperature level of $T_\mathrm{s} = 18.8\,^\circ\mathrm{C}$, particularly at the right side of the investigated section. It is very conspicuous, that the three different local calibration approaches show the largest deviations for the highest temperature levels towards the left side, caused by the fact that at the left side of the section the TLCs appear bluish already for lower temperatures, as it can be seen in figure 2.14. As the blue color shade of the TLCs hardly varies anymore upon temperature changes, measurement errors are more likely to occur. This issue especially affects the determination of the temperature via linear interpolation and the polynomial fit, while the neural network seems to better level this out. However, for $T_\mathrm{s} > 22\,^\circ\mathrm{C}$ even the neural network yields deviations of $\mathrm{MAD}_X \geq 0.5\,\mathrm{K}$ towards the left side of the field of view. From this it can be concluded, that a suitable temperature range for measurements with TLCs must not be figured in a narrow test section, but considering the whole field of view of the actual measurements with the same arrangement of the experimental components.

The results for the mean absolute deviation MAD over the whole section, which is indicated in figure 2.14a, can be seen in figure 2.16. Besides the outlier of the functional approximation with the 8th degree polynomial fit at $T_\mathrm{s} = 18.5\,^\circ\mathrm{C}$, the results show the same trend of the increase of the MAD with temperature for all local calibration approaches. Furthermore, it is confirmed again that the neural network yields the smallest MAD for the highest temperature levels, in particular compared to the approach based on linear interpolation of the hue. However, in general the deviations are too large for $T_\mathrm{s} > 22\,^\circ\mathrm{C}$, having in mind that this technique shall later be applied to precisely measure temperature fields in RBC. Looking at the results for $T_\mathrm{s} \leq 22\,^\circ\mathrm{C}$ it becomes obvious, that the smallest

MAD is in most cases obtained with the linear interpolation approach. This is the result of the fact, that this method strictly uses the measured calibration points, which are partly just slightly corrected according to the procedure illustrated in figure 2.8. In addition, with a view to the later application this method does not carry any risks, which are difficult to estimate a priori, such as systematic measurement errors due to the deviation of the functional approximation from the calibration curve or due to typical issues related to neural networks, like for example the problem of overfitting [135, 136]. Hence, the linear interpolation of the hue in the local calibration curves is used in the scope of this work to perform temperature measurements by means of the color of TLCs.
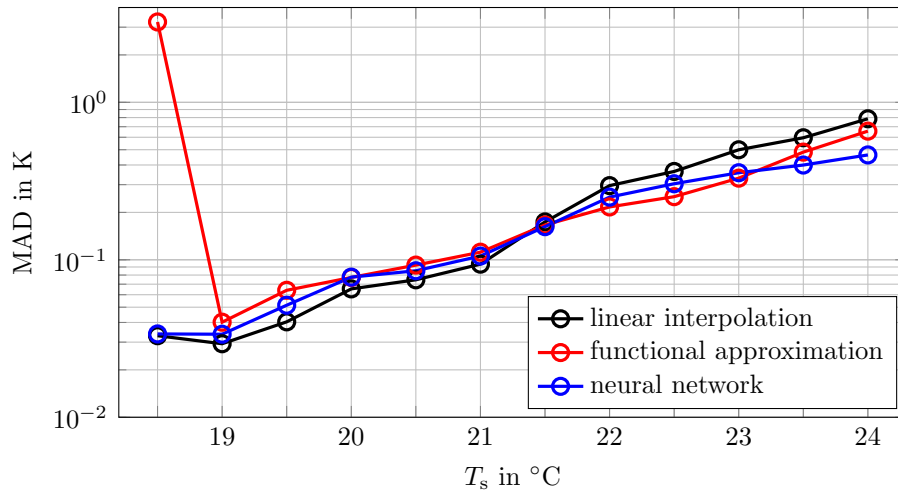


Figure 2.16: The mean absolute deviation MAD of the temperature measurements for the different local calibration approaches applied to the whole section indicated in figure 2.14a.

## 2.5 Exemplary application of the measuring technique

In order to demonstrate the applicability of this measuring technique for temperature field measurements in a flow, the experimental setup depicted in figure 2.3 is slightly modified. Instead of using only one thermostatic bath to drive the flow of the water through the aluminum plates enclosing the cylindrical cell, both the bottom and top plate are connected to a separate thermostatic bath. This enables to adjust a larger temperature at the bottom side, thereby inducing RBC inside the cell, which is again filled with deionized water. Exemplary images of the TLCs R20C20W dispersed in the flow can be seen in the figures 2.17a and 2.17c for different instants of time. While the first image shows the TLCs for an observation angle of $\varphi_{cc} = 70°$, the observation angle in the second image is $\varphi_{cc} = 80°$. The temperature of the heating plate at the bottom $T_h$ and of the cooling plate at the top $T_c$ have been adjusted to $T_h = 21\,°C$ and $T_c = 17.8\,°C$, yielding an average temperature of $(T_h + T_c)/2 = 19.4\,°C$ in the bulk area. Around this average temperature, the color play of the TLCs can be observed for both observation angles. However, the so-called thermal plumes, which either arise from the bottom plate or fall down from the top plate resulting from the change of the fluid's density, can be better distinguished for $\varphi_{cc} = 70°$. Due to distinctive color contrast, especially the downwelling TLCs with the red color shade are very conspicuous.

Since the arrangement of the color camera and the white light source has not been changed in comparison to the previous calibration measurements, those can now be used to

(a)

(b)

$T$ in °C

(c)

(d)

$T$ in °C
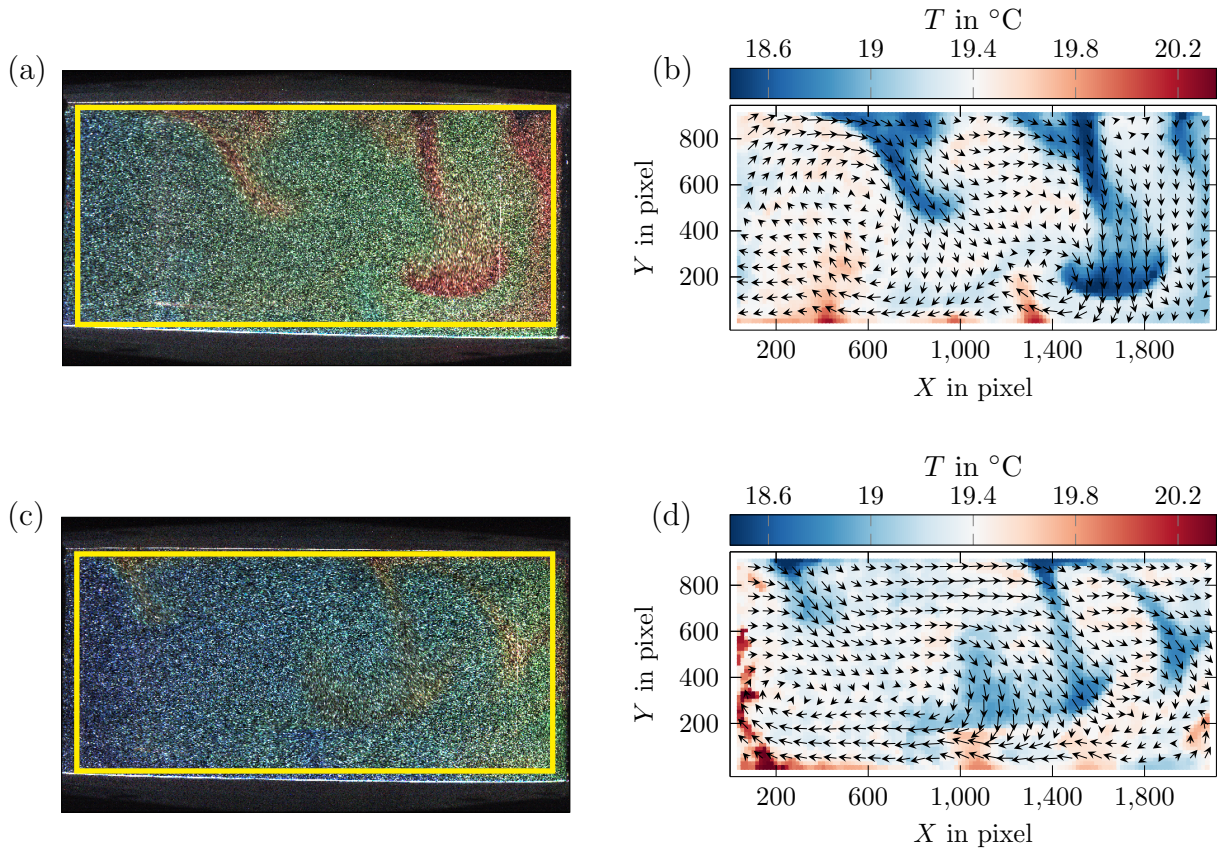
Figure 2.17: Images of the TLCs R20C20W (a,c) in RBC with a heating and cooling plate temperature of $T_h = 21\,°C$ and $T_c = 17.8\,°C$ as well as the corresponding temperature fields (b,d) with superimposed vectors, which indicate the direction of the fluid motion. The results in the upper row have been obtained with the observation angle $\varphi_{cc} = 70°$, while the lower row shows the results for the observation angle $\varphi_{cc} = 80°$.

calculate the corresponding temperature fields, which are depicted in the figures 2.17b and 2.17d. In coincidence with the color of the TLCs, the thermal plumes are clearly visible in the temperature fields. Furthermore, the velocity components along the measurement plane have been determined based on the temporal displacement of the TLCs via Particle Image Velocimetry, which is explained in section 4.3. For the velocity field larger interrogation windows with a size of $64 \times 64$ pixel and an overlap of $50\%$ have been used. The velocity vectors are superimposed in the figures 2.17b and 2.17d, but only every second vector is shown in each direction for a better illustration. However, it must be noted that the vectors can only be considered as an estimation regarding the direction of the fluid motion. The magnitude of the velocity, which is here not of further interest, cannot be specified, because a camera calibration has not been performed in this case. Nevertheless, in particular from the thermal plumes it becomes obvious that the direction of the fluid flow matches the temperature fields, since warm fluid induces an upward motion, while cold fluid causes a downward motion. As expected, most of the temperatures in the bulk area are close to the mean of the heating and cooling plate temperature and only the thermal plumes yield extreme values.

It can therefore be concluded, that the chosen local calibration approach is suited

to measure the temperature fields in a flow. In general, observation angles in the range $60° \leq \varphi_{cc} \leq 70°$ seem to be most appropriate for accurate temperature measurements, as discussed in the previous sections. Smaller angles may yield nonuniformities in the imaging of the measurement plane, while only a narrow temperature range with a low uncertainty of measurement remains when larger angles close to $\varphi_{cc} = 90°$ are applied due to the rapid transition from the red towards the blue color shade of the TLCs. However, depending on the range of the temperatures occurring in the specific application, also observation angles $\varphi_{cc} > 70°$ can be taken into account, as demonstrated by the results in figure 2.17d. In any case, the observation angle should be adapted to obtain a strong color play of the TLCs in the required temperature range, given that TLCs with suitable specifications are used for the measurements.

# Design of the experimental facility

For the investigation of large aspect ratio Rayleigh-Bénard convection a new experimental facility has been built up. At the beginning of this chapter, the main components of the facility are shown and the essential requirements as well as challenges of the development process are discussed in section 3.1. The white light source, which is a basic component of the temperature measurement technique applied in this work, is separately presented in section 3.2. Furthermore, the cameras and the equipment used for the simultaneous measurements of the temperature and velocity fields in horizontal planes of large aspect ratio Rayleigh-Bénard convection are shown in section 3.3.

## 3.1 The Rayleigh-Bénard setup

Designing the experimental facility was a very extensive process, as different requirements had to be fulfilled. For the implementation of the main parts of the experimental facility, i.e. the heating and cooling plate as well as the Rayleigh-Bénard cell itself, different concepts have been developed and compared. The constructional details are not addressed in this work, however, since great importance was attached to an accurate development of the experimental setup, which is necessary for performing reliable measurements, the most relevant aspects are outlined.

   One of the key decisions for the design of the experimental setup was the choice of the working fluid for the Rayleigh-Bénard cell. Frequently, either air or water are used, since these fluids are very easy to access and do not require special precautions. Moreover, their transparency allows the application of established optical measurement techniques, which is of vital importance for the measurements in the scope of this work. Here, water is used as the working fluid for all the measurements, as this is much better suited for the experimental investigation of the flow using the measurement technique explained in chapter 4. Furthermore, with regard to the comparison of the experimental results to the outcomes of numerical simulations, choosing water as the working fluid is of advantage for the achievable range of the Rayleigh number, as will be shown in this chapter.

   Another question, that had to be considered in the earliest stage of the design, concerns the geometry of the Rayleigh-Bénard cell and the measurement area to be studied within the cell, in particular with regard to the turbulent superstructures. As already depicted in section 1.3.2, the arrangement of turbulent superstructures can most clearly be observed in horizontal planes of the Rayleigh-Bénard cell. Therefore, all the measurements are performed in horizontal cross-sectional areas of the cell. Furthermore, because turbulent

superstructures span horizontal dimensions of a multiple of the cell's height $h$, its horizontal dimension $l$ must be considerably larger, such that the typical patterns can be obtained from the temperature and velocity fields. Due to the large dimensions of the cell required in the horizontal direction, the bottom area of the cell is chosen to be squared, since both common geometries, i.e. cells with a cylindrical or squared bottom area, allow for a comparison of experimental and numerical results, but building up a squared cell with those dimensions is advantageous from the practical point of view.

In addition, either the entire horizontal planes or at least a large section must be investigated to study the patterns of the turbulent superstructures reliably. However, this is especially challenging for cells with a large aspect ratio $\Gamma = l/h$, if optical measurement techniques are applied like in the present case, because the horizontal planes are optically difficult to access. This problem has been discussed in the work [62], where also possibilities are illustrated to gain optical access to the horizontal planes for the investigation of the flow using a camera. On the one hand, only a small section of the horizontal planes in cells with large aspect ratios can be captured by the camera, when the flow is observed through a small window inserted in one of the isothermal plates, that are usually not transparent. On the other hand, the camera could also be arranged in a way, such that the flow in the horizontal planes could be analyzed through a transparent sidewall, but this approach is not suited due to the flat observation angles, which do not allow for accurate flow measurements. For a better imagination, those two methods are depicted in figure 3.1.



<center>(a)                                                                         (b)</center>
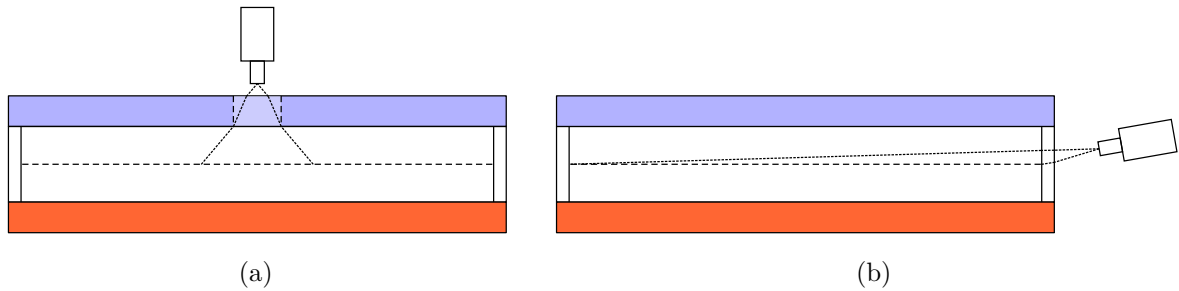
Figure 3.1: Limited optical access to the horizontal planes in a Rayleigh-Bénard cell with a large aspect ratio through a transparent window in one of the isothermal plates (a) and a transparent sidewall (b).

The study of the turbulent superstructures over a large section of the horizontal planes could, for example, be enabled by increasing the size of the window in one of the isothermal plates according to figure 3.1a. However, this method is not recommended, since a large window with material properties differing from the other part of the isothermal plate is expected to considerably disturb the homogeneous temperature distribution on the plate. Hence, the only remaining possibility is to apply a heating or cooling plate made of a transparent material. Considering this as a fixed requirement from here on, the dimensions of the Rayleigh-Bénard cell must be determined in the next step, as this is of importance for the options in the design of the transparent isothermal plate, e.g. with respect to the material selection and to the question, how the temperature on its surface can be adjusted.

Aiming for the comparability of the results, which will be obtained from this experiment, with numerical results up to date, the cell's dimensions are designed by taking into account two dimensionless controlling parameters of the flow introduced in section 1.2.1, namely the Rayleigh number Ra and the aspect ratio $\Gamma$. As mentioned above, for the study of turbulent superstructures the Rayleigh-Bénard cell must have considerably larger horizontal

than vertical dimensions, such that a distinctive pattern of the superstructures can be observed. According to the results of numerical simulations shown in figure 1.6, the turbulent superstructures for a Prandtl number $Pr = 7$, corresponding to that of water with a temperature around $T = 20\,°C$, can clearly be studied in a cell with an aspect ratio $\Gamma = 25$. From the study [53] for $Pr = 1$ it can be found that this aspect ratio might be too small, if large Rayleigh numbers around $Ra = 10^8$ are applied, as the horizontal extent of the superstructures then still depends on the aspect ratio itself. It is reported that for such high Rayleigh numbers the aspect ratio should be at least $\Gamma = 64$ to achieve convergence, meaning that the size of the superstructures does not vary with the aspect ratio anymore. However, in the present study the Rayleigh numbers will be in the order to $Ra = 10^5$ and $Ra = 10^6$, as it will be shown in the following. Having a look at the results in the study [53] it can be estimated that for this range of the Rayleigh number the aspect ratio $\Gamma = 25$ is sufficiently large. Hence, for the experimental investigations presented in this study a cell with this aspect ratio is used, since this can still be considered suitable from the practical point of view, whereas an aspect ratio of $\Gamma = 64$ is expected to yield more difficulties.

On the basis of the aspect ratio an appropriate height of the cell must be determined, considering the corresponding horizontal dimension with regard to the practical suitability of the setup, but also taking into account that the achievable Rayleigh numbers enable the comparison of the experimental results to those of numerical simulations. In this respect, also the total heat flux from the bottom to the top plate of the cell, which depends on its horizontal and vertical dimensions, must be roughly estimated in advance, thereby ensuring that the power demand of the facility is kept within reasonable limits for common temperature differences between the isothermal plates. Considering all these aspects, a height of $h = 28\,mm$ has proven to be suitable, resulting in the horizontal dimensions of $l \times w = 700\,mm \times 700\,mm$ for the squared bottom area of the cell. The Rayleigh numbers, which can theoretically be achieved with this cell for moderate temperature differences between the heating and cooling plate up to $\Delta T = 10\,K$, can be seen in figure 3.2a. The physical properties of water for calculating the Rayleigh number were determined on the basis of the average temperature in the cell $\langle T \rangle = T_c + \Delta T/2$, assuming different temperatures of the cooling plate from $T_c = 10\,°C$ up to $T_c = 40\,°C$ in this case.
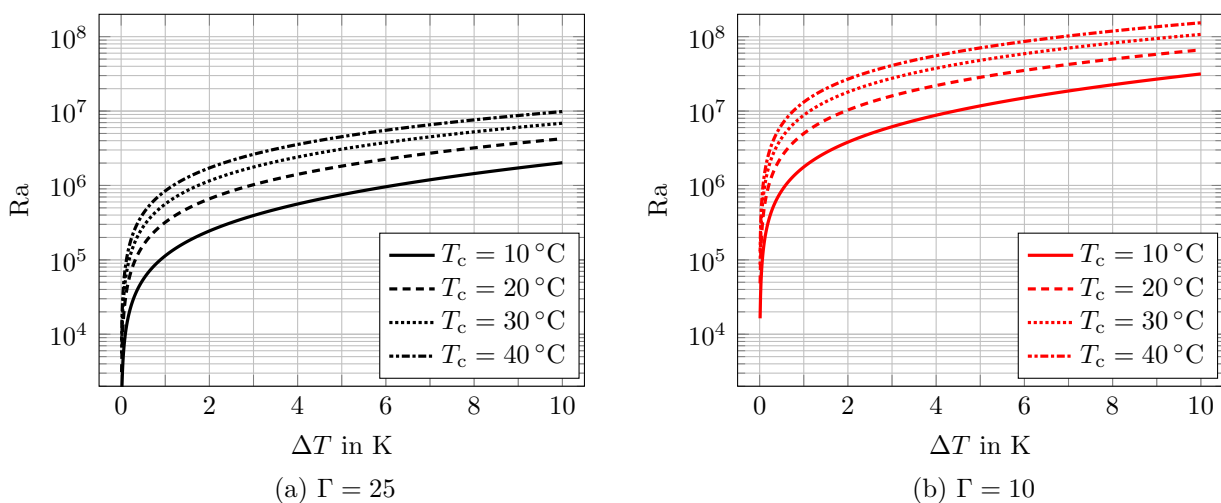


(a) $\Gamma = 25$        (b) $\Gamma = 10$

Figure 3.2: The Rayleigh number in dependency of the temperature difference between the heating and cooling plate $\Delta T = T_h - T_c$ for the aspect ratios $\Gamma = 25$ and $\Gamma = 10$.

It becomes obvious from figure 3.2a, that the Rayleigh number cannot only be enhanced by increasing the temperature difference, but also considerably by shifting the temperature interval towards higher values. However, in the scope of this study the temperature of the cooling plate always falls into the range $T_c \in [15\,°\mathrm{C}, 25\,°\mathrm{C}]$, such that the average temperature in the cell does not strongly differ from a common ambient temperature in the lab of about $T_{amb} \approx 20\,°\mathrm{C}$ and, therefore, the temperature difference $(T_h + T_c)/2 - T_{amb}$ driving the heat flux across the sidewalls is small. Thus, on the basis of figure 3.2a the Rayleigh numbers for $\Gamma = 25$ can be estimated to range in between $\mathrm{Ra} \in [10^5, 5 \times 10^6]$, which allows for a comparison of the experimental results with those of numerical simulations.

With a view to other studies with this experimental facility, which must not necessarily be related to turbulent superstructures, the possible investigations should not be restricted by the fact that only the aspect ratio $\Gamma = 25$ can be applied. Hence, the distance between the heating and cooling plate is made adjustable, such that Rayleigh-Bénard cells with the same horizontal dimensions, but different heights can be placed in between. Besides the cell with aspect ratio $\Gamma = 25$, two other cells with the aspect ratios $\Gamma = 10$ and $\Gamma = 20$ have already been built up. Due to their larger heights, those allow to study RBC at larger Rayleigh numbers. As it can be seen in figure 3.2b, especially the cell with $\Gamma = 10$ having dimensions of $l \times w \times h = 700\,\mathrm{mm} \times 700\,\mathrm{mm} \times 70\,\mathrm{mm}$ provides the possibility to achieve Rayleigh numbers, which are approximately one order of magnitude larger compared to that for $\Gamma = 25$ at the same temperature differences, yielding $\mathrm{Ra} \in [10^6, 5 \times 10^7]$ as a rough estimation for cooling plate temperatures $T_c \in [15\,°\mathrm{C}, 25\,°\mathrm{C}]$. Even though the results of the flow measurements, which will be presented in this work, are all obtained with aspect ratio $\Gamma = 25$, some aspects regarding the experimental parameters are also addressed for $\Gamma = 10$ in this section. However, in order to keep the focus, the cell with $\Gamma = 20$ is not addressed anymore, since all the parameters can be estimated based on that for $\Gamma = 25$ and $\Gamma = 10$.

As aforementioned, the total heat flux from the bottom to the top plate of the Rayleigh-Bénard cell must also be considered for the design of its dimensions. In this context, thermal radiation is not taken into account, since its contribution is very small in the temperature ranges of this work. The total heat flux is therefore determined based on the conductive heat flux $\dot{Q}_{cond} = \lambda_{th}\, A\, \Delta T / h$ and the Nusselt number $\mathrm{Nu}$ defined in equation (1.14), however, the relation for the Nusselt number $\mathrm{Nu} = \alpha_{\mathrm{Nu}}\,\mathrm{Ra}^{\beta_{\mathrm{Nu}}}$ must be known from previous experiments or numerical simulations with similar boundary conditions. For the Prandtl number $\mathrm{Pr} = 7$ and the aspect ratio $\Gamma = 25$, the three Nusselt numbers $\mathrm{Nu}_1 = 4.1$, $\mathrm{Nu}_2 = 8.3$ and $\mathrm{Nu}_3 = 16.2$ are given in the study [57] on the basis of numerical simulations for the Rayleigh numbers $\mathrm{Ra}_1 = 10^5$, $\mathrm{Ra}_2 = 10^6$ and $\mathrm{Ra}_3 = 10^7$, respectively. Applying an exponential fit to these three points yields $\mathrm{Nu} = 0.133\,\mathrm{Ra}^{0.298}$, which is used for the estimation of the Nusselt number and the total heat flux for the cell with the aspect ratio $\Gamma = 25$. Furthermore, in order to estimate the total heat flux for the cell with the aspect ratio $\Gamma = 10$, the relation $\mathrm{Nu} = 0.152\,\mathrm{Ra}^{0.290}$ obtained from numerical simulations for this aspect ratio and $\mathrm{Pr} = 7$ [137] is applied. The results for the conductive heat flux $\dot{Q}_{cond}$ and the total heat flux $\dot{Q} = \mathrm{Nu}\,\dot{Q}_{cond}$ in dependency of the temperature difference between the isothermal plates $\Delta T$ are depicted in figure 3.3 for the case $T_c = 20\,°\mathrm{C}$. As it can be expected the amount of the conductive heat flux is larger for the cell with aspect ratio $\Gamma = 25$, since the distance between the heating and cooling plate is smaller, but due to the larger Rayleigh numbers and Nusselt numbers for the cell with $\Gamma = 10$ the total heat flux is similar. In both cases, the total heat flux $\dot{Q}$ is kept in the range $0\,\mathrm{W} < \dot{Q} < 2000\,\mathrm{W}$ and can thus, for instance, be provided by a common thermostatic bath.
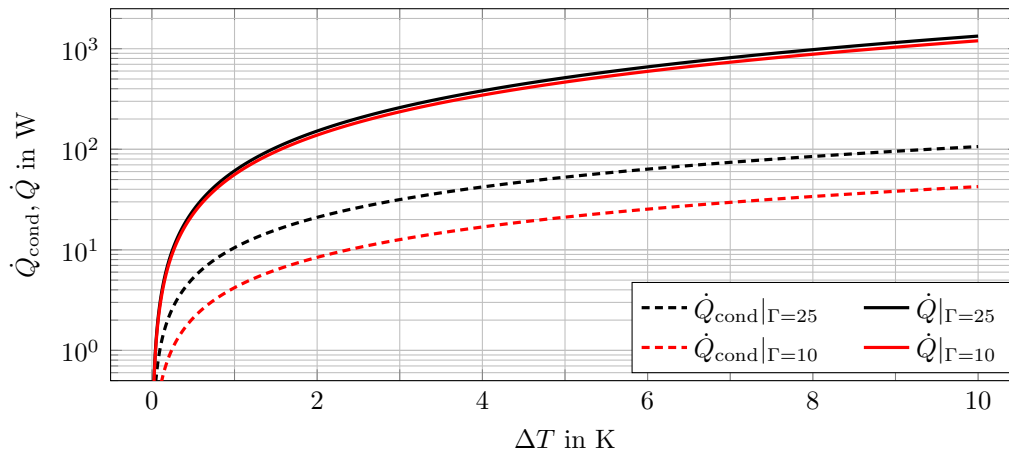
Figure 3.3: The conductive heat flux $\dot{Q}_{\mathrm{cond}}$ and the total heat flux $\dot{Q}$ for the Rayleigh-Bénard cells with the aspect ratio $\Gamma = 25$ and $\Gamma = 10$. The temperature of the cooling plate was set to $T_{\mathrm{c}} = 20\,^{\circ}\mathrm{C}$ for this estimation.

With the given dimensions of the Rayleigh-Bénard cells an appropriate method for providing the optical access to the cells must be figured out in the next step. As outlined at the beginning of this section, the observation of a wide horizontal cross-sectional area of a Rayleigh-Bénard cell with a large aspect ratio is only possible through a transparent heating or cooling plate. A special method for a transparent heating plate of a cell with a large aspect ratio of $\Gamma = 10$ has already been presented in the work [62], in which a glass plate coated with a thin sheet of transparent and electrically conducting indium-tin-oxide (ITO) has been used. On this way, a varying electric current can be supplied to this sheet to control the temperature at the surface of the heating plate. As this plate in the study [62] has been used for a Rayleigh-Bénard cell with horizontal dimensions of $300\,\mathrm{mm} \times 300\,\mathrm{mm}$, its entire area is $500\,\mathrm{mm} \times 500\,\mathrm{mm}$, in order to impede strong temperature inhomogeneities at the lateral boundaries of the cell. Analogously, using this technique in the present case would require a coated plate with dimensions of about $1\,\mathrm{m} \times 1\,\mathrm{m}$ for the cell's horizontal dimensions of $700\,\mathrm{mm} \times 700\,\mathrm{mm}$. This has turned out to be problematic, since the special coating of such a large plate is very challenging and local discrepancies of the coating's thickness may occur. The influence of the latter on the homogeneity of the temperature distribution is difficult to estimate a priori, such that this technique is not applied here.

Furthermore, in the present case not the heating plate at the bottom, but the cooling plate at the top of the cell was chosen for providing the optical access, since the working fluid inside the cell can then easily be observed from the top, either by the experimentalist during the preparation of the measurements or by the cameras of an optical measurement system. As indicated in the sketch of the experimental facility in figure 3.4, the cameras can thus be mounted above the Rayleigh-Bénard cell at a suitable distance, thereby allowing to optically investigate the area of interest. The reason for using the different types of cameras shown in the sketch and their arrangement will be further explained in section 3.3. In order to enable the observation of the flow through the cooling plate, it is made of glass and its temperature is controlled by water flowing above it in an external cooling water circuit, which is covered by a second glas plate at the top as indicated in figure 3.4, such that the optical access is not impeded. The heating plate at the bottom of the cell is made of aluminum and also flown through by water in a second external circuit for adjusting the temperature on its surface. Moreover, the sidewalls of the cells are made of glass, which is necessary for the measurement technique applied in this study, as tracer

particles dispersed in the working fluid have to be illuminated with a white light sheet through one of the sidewalls for the simultaneous measurements of the temperature and velocity fields in horizontal planes. As it can be seen in figure 3.4, the vertical position of the white light source can be adapted in this case, thereby offering the possibility to study the flow in the cell at different heights.

For a better imagination of the experimental facility, a photograph is depicted in figure 3.5. In addition, other views of the facility can be found in the appendix A. It can be seen in figure 3.5 that both the heating and the cooling plate are covered with thick insulating material to minimize the heat loss to the surroundings or the heat absorption from the surroundings. When performing the experiments, the sidewalls of the cell are also covered by a thick insulating foam, which is just removed at the sidewall where the light sheet enters the cell for the duration of the illumination and the recording of the images with the cameras. Thus, the adiabatic boundary condition of the Rayleigh-Bénard experiment can be considered as fulfilled in a good approximation, since the heat flux across the sidewalls is minimal, taking into account that the ambient temperature in the lab is also adapted to the mean temperature in the cell and the sidewalls are made of glass with 8 mm in thickness, which is a strong resistance to the heat flux. Even though the main components of the experimental facility are shown in figure 3.4 and 3.5, the sketch and the photograph only serve as a rough overview, but do not provide further important insights. Therefore, the three central elements of the experimental setup, i.e. the Rayleigh-Bénard cell itself, the heating circuit and the cooling circuit, are described in the following sections 3.1.1 - 3.1.3.
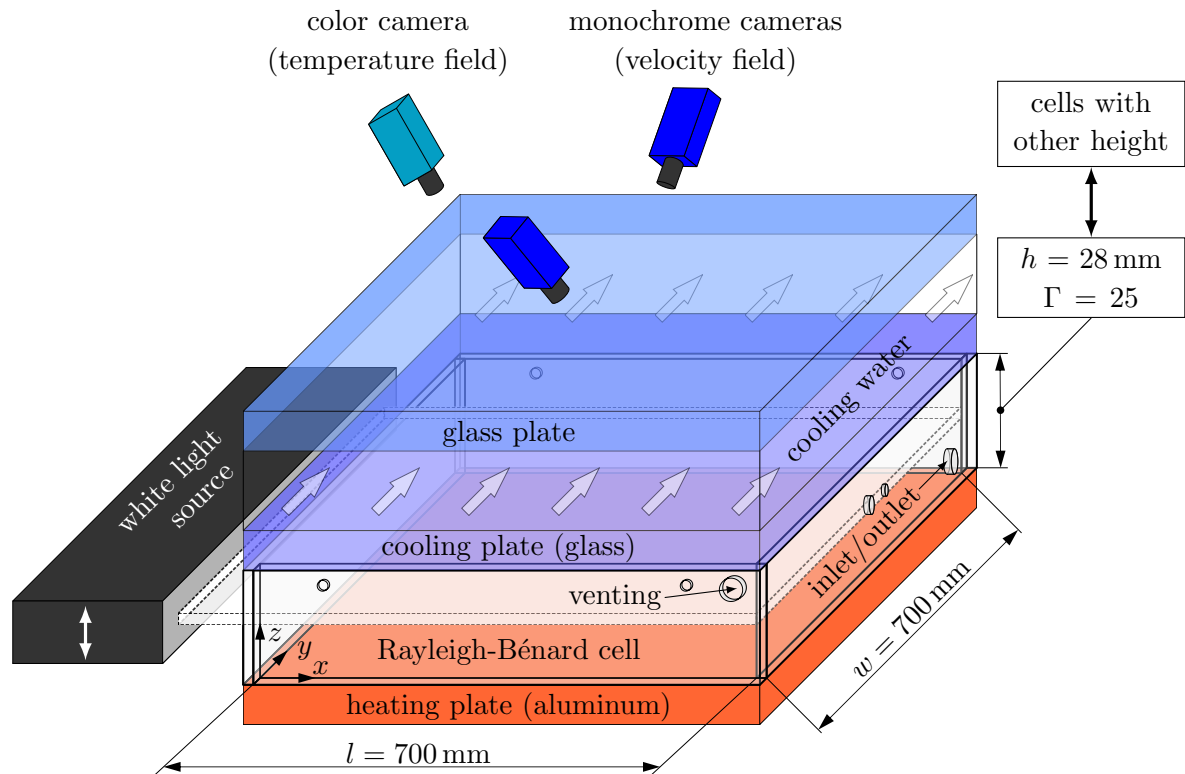


Figure 3.4: Sketch of the experimental setup for simultaneous velocity and temperature field measurements in horizontal planes of the Rayleigh-Bénard cell. The coordinate system in the left corner of the sketch is valid for all of the following investigations.
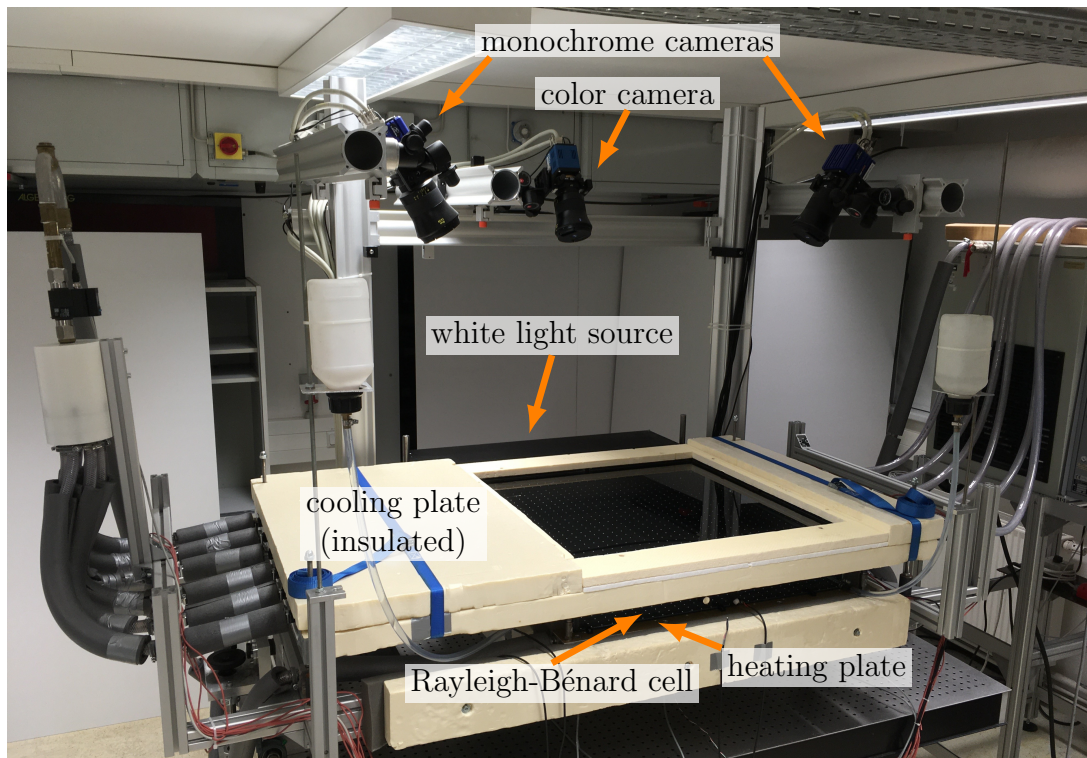
Figure 3.5: A photograph of the experimental facility. For a better illustration, the Rayleigh-Bénard cell with aspect ratio $\Gamma = 10$ is shown due to its larger height.

## 3.1.1 The Rayleigh-Bénard cell

Due to the large horizontal dimensions of the Rayleigh-Bénard cell applied for the measurements in this study, it is important to consider that the experimental setup can still be handled comfortably. Especially, mounting and demounting the cell between the heating and cooling circuit must be possible with reasonable effort, since this will frequently be necessary to thoroughly remove the impurities at the isothermal plates caused by the seeding particles for the temperature and velocity measurements. For this reason, all the transparent components, i.e. the sidewalls and the top plate, are bonded together with a water-resistant adhesive, which is cured with ultraviolet light. Thus, the cell can easily be removed and again built in between the heating and cooling circuit. An image of the demounted glass cell with the aspect ratio $\Gamma = 25$ can be seen in figure A.8 in the appendix A.

For the characterization of the flow in the Rayleigh-Bénard cell the thermal driving force must be known, which requires to measure the temperatures at the isothermal plates. In order to determine the temperatures reliably, those are measured at different positions as shown in figure 3.6, using PT100 elements in each case. The temperature at the heating plate is measured in its center and in the vicinity of each corner with temperature probes, that are screwed in from the bottom side with the sensor element nearly reaching the top surface of the plate. Since the temperature sensors cannot be fixed like this at the cooling plate made of glass, small PT100 elements with very thin wires are directly bonded onto the lower surface of the cooling plate. However, with regard to the optical access to the Rayleigh-Bénard flow through the transparent plate, no sensor element is placed in the central region. Furthermore, a sensor element located on central height at one

of the sidewalls is used to check the temperatures measured at the heating and cooling plate, considering that their mean value should fluctuate around the temperature on central height of the cell. In addition, the temperature inside the Rayleigh-Bénard cell can optionally be measured with a temperature lance inserted through the sidewall as depicted in figure 3.6.

In the illustration of the Rayleigh-Bénard cell it can also be seen, that the cell can be filled with the working fluid through a small hole at the lower rim of the sidewall, that is used as inlet and outlet for the fluid, too. Moreover, another small hole at the upper rim of the sidewall allows to get the air out of the cell during the filling process, which is very important, since air bubbles in the cell would strongly affect the measurements. Hence, as shown in figure A.6 in the appendix A, the mounting frame of the cell can be inclined around two axis, such that the hole is the top point of the cell and the air can be fully removed. Furthermore, in order to compensate for the volume change of the water in the cell resulting from temperature variations, a reservoir is connected to each of the holes via a hose, which can be seen in the photograph of the facility in figure 3.5.
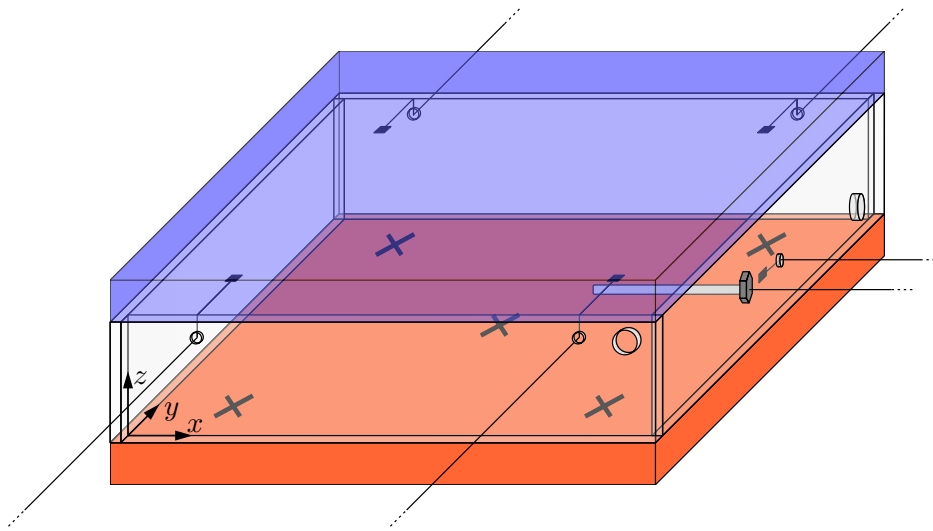


Figure 3.6: Illustration of the Rayleigh-Bénard cell equipped with temperature sensors. The cross symbols at the bottom plate indicate the position of small sensor elements directly underneath the surface.

## 3.1.2   The heating circuit

In order to heat up the surface of the heating plate at the bottom of the cell, two commonly applied techniques have been considered. On the one hand, using an electric heating plate with an internal current flow for controlling the temperature and, on the other hand, transferring the heat from a warm fluid streaming underneath the surface has been taken into account. In this case, the latter technique is used, since on an electric heating plate a considerable temperature drop from the center to the edges may occur, if the current is not very specially controlled. On the contrary, the adjustment of the temperature with a fluid streaming below the surface of the plate usually results in a better homogeneity of the temperature distribution, when the flow circuit is appropriately designed. Therefore, several aspects were considered to optimize the homogeneous temperature distribution aiming for the isothermal boundary conditions of the Rayleigh-Bénard experiment. As

illustrated in figure 3.7, the water is streaming through two meander channels inside the heating plate. In comparison to the configuration with only one meander circuit across the whole plate, a smaller flow resistance and accordingly a higher total flow rate can be obtained, thereby reducing the temperature drop of the heating water from the inlet to the outlet of the plate. Since the flow resistance in the remaining part of the circuit is kept small by using tubes with a large diameter and a length as small as possible in consideration of suitable curvatures, a flow rate of the heating water of about $\dot{V}_{\mathrm{hw}} = 30\,\mathrm{l/min}$ can be achieved, yielding only small temperature differences between the inlet and outlet. As indicated in figure 3.7, the flow is driven by a thermostatic bath (TT‑157 E, Tool‑Temp Ltd), which contains an internal heating unit and is connected to an external cooling aggregate for controlling the temperature. The flow rate is measured at the outlet of the thermostatic bath, while the temperature of the water is measured in each of the two inlets as well as outlets at the plate with immersible PT100 temperature probes. The mean temperature drop of the heating water from the inlet to the outlet $\Delta T_{\mathrm{hw,in}\to\mathrm{out}} = \langle T_{\mathrm{hw},n}\rangle_{n=(3,4)} - \langle T_{\mathrm{hw},n}\rangle_{n=(1,2)}$ amounts to a few hundredth Kelvin in most cases. Even for the experiments with the largest heat transfer from the bottom to the top of the cell, the temperature drop is smaller than $|\Delta T_{\mathrm{hw,in}\to\mathrm{out}}| = 0.2\,\mathrm{K}$ as a result of the high flow rate and the large heat capacity of water. Furthermore, as the meander system within the heating plate is covered at the top with an aluminum plate with a thickness of 6 mm, the temperature differences on its upper surface are further minimized by heat conduction due to the high thermal conductivity of aluminum. Thus, the temperature distribution on the heating plate is expected to comply with the isothermal boundary condition in a good approximation.
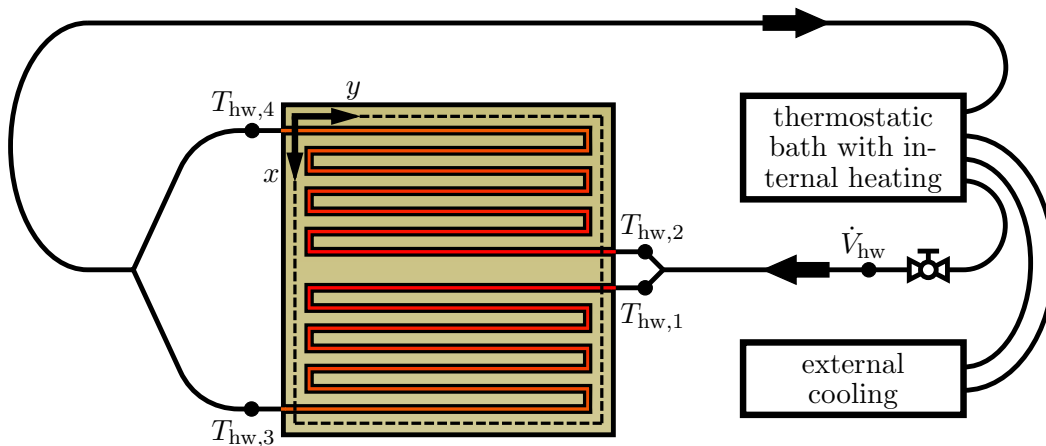


Figure 3.7: Schematic of the heating circuit with a view of the meander system inside the heating plate. The dashed rectangle indicates the position of the Rayleigh-Bénard cell.

### 3.1.3   The cooling circuit

Since the flow in the Rayleigh-Bénard cell is observed through the transparent top plate in this case, an extensive design of the cooling circuit was necessary. In this respect, especially the temperature homogeneity of the transparent cooling plate and its mechanical stability had to be considered. As aforementioned, the temperature of the plate is controlled by cooling water flowing above it in an external circuit, which is schematically illustrated in

figure 3.8. The flow driven by a thermostatic bath (UKS 3000 H, LAUDA - Brinkmann LP) with an internal heating and cooling unit is passing through a frame made of aluminum, consisting of a base with specifically designed cavities to guide the flow and a flat covering element. Both the base and the covering element have a large cutout positioned right above the Rayleigh-Bénard cell, in order to provide the optical access to the whole cell through the cooling water and another glass plate at the top side of the frame as a covering of the cooling circuit. At this point it should be noted, that the observation of the flow through the cooling water requires to completely remove the air trapped in the circuit. For this, the whole facility is inclined several times in varying directions during the filling process via the tiltable mounting frame, such that the cooling circuit can be vented at the upper glass plate as shown in figure A.7 in the appendix A.

The frame on top of the cooling plate is sketched in figure 3.8 without the covering element to show the geometry of the base. As shown in the figure, the total flow rate is split before entering the frame, such that the flow is streaming uniformly over the transparent cooling plate, yielding an improved homogeneity of its temperature distribution. The flow distributor designed to equally split the total flow rate can be seen at the left side of figure 3.5, however, for a better view of the distributor and the inlet area of the water into the frame above the Rayleigh-Bénard cell the reader is referred to the figures A.5, A.6 and A.10 in the appendix A.
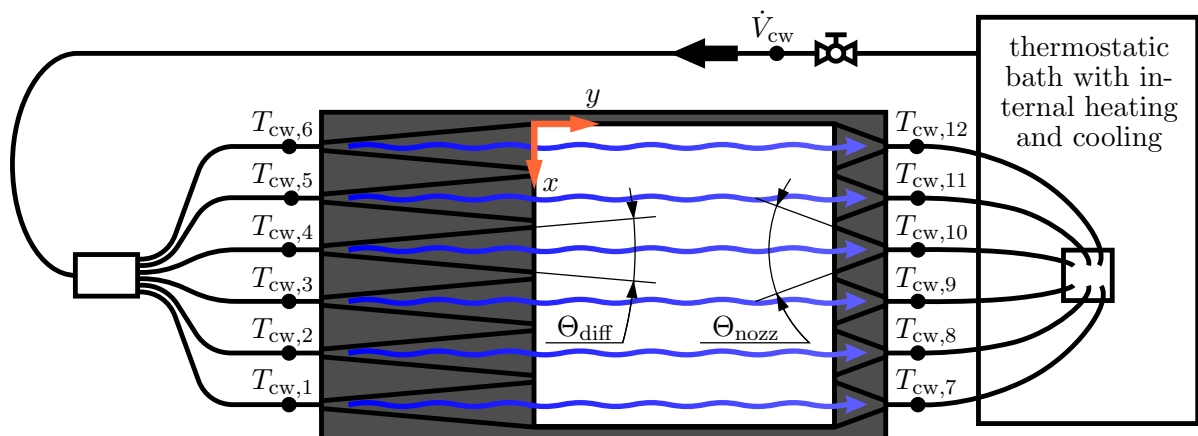


Figure 3.8: Schematic of the cooling circuit showing the flow above the transparent top plate of the Rayleigh-Bénard cell.

Aiming for the uniform flow above the cell, the flow entering the frame via hoses is expanded slowly by diffusers, in order to obtain a directed flow over the whole cross section without any stagnation or flow reversal. Therefore, an accurate design of the diffusers was necessary, as the flow downstream of a diffuser is in general highly sensitive to changes of its geometry. For a better understanding regarding the design, the comprehensive studies about diffusers [138, 139] have been considered in this case. Contrary to many other studies, which only address the influence of the diffuser angle $\Theta_{\text{diff}}$ indicated in figure 3.8, in those two studies the effect of the length of diffusers $l_{\text{diff}}$ on the flow field is impressively demonstrated, too. In this context it is shown, that there is not any universal limit for the diffuser angle to impede stall, i.e. the separation of the flow from the contour of the diffuser resulting in small eddies or even large recirculation zones, but the critical angle for the occurrence of stall significantly depends on the ratio between the diffuser's length

in flow direction $l_{\mathrm{diff}}$ and the inlet width $w_{\mathrm{diff,in}}$.

Considering the resulting entire dimensions of the experimental facility it could be estimated on the basis of those two studies, that the use of six diffusers with $\Theta_{\mathrm{diff}} = 10°$ and $l_{\mathrm{diff}}/w_{\mathrm{diff,in}} \approx 30$ might be suited to widen up the flow area from the hoses at the inlet to the entire area of the transparent cooling plate. In order to confirm this, two-dimensional numerical simulations of the cooling water flow have been performed, thereby reassuring the suitability of the design, since the flow does not separate from the contour of the surrounding frame. The flow field for this design and further outcomes of the numerical simulations for varying diffuser angles of $10° < \Theta_{\mathrm{diff}} < 20°$ are depicted in the appendix B.1 for comparison. Regarding the angle of the nozzles at the outlet the simulations have shown that this angle can be steeper without affecting the flow considerably, which is advantageous to keep the length of the frame in limits. However, reducing the flow area abruptly is of course not possible, since it would cause a drastic increasing of the flow resistance at the outlet and accordingly a much higher pressure inside the frame. For reasons of safety, this must prevented in any case, as the cooling plate made of glass might burst. Therefore, the nozzles taper the flow with an angle of $\Theta_{\mathrm{nozz}} = 40°$ and, in order to further limit the pressure, the cooling water streaming out of the frame is directly led back into the tank of the thermostatic bath through six hoses as depicted in figure 3.8. For a better illustration, the base of the frame can be seen in figure 3.9 from the top view, which also shows the heating plate within the large cutout of the frame. The pattern of white dots on a black adhesive foil fixed on the heating plate in the background is used for the calibration of the physical dimensions, as will be explained in section 4.1.
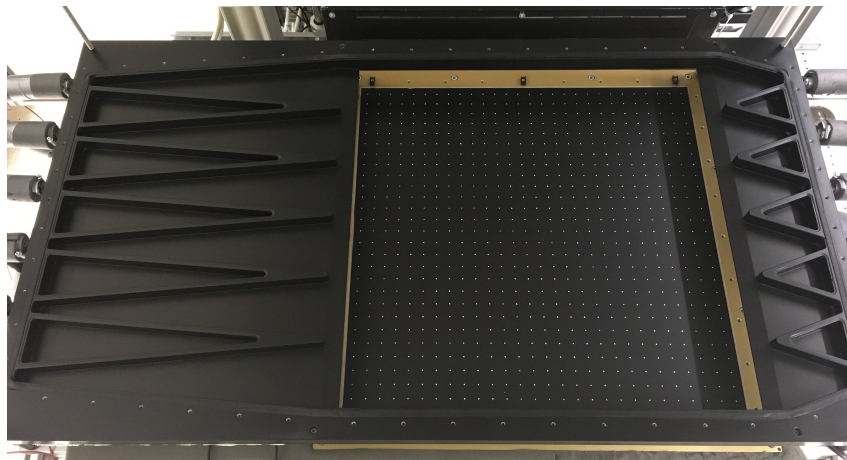


Figure 3.9: A view of the frame for the cooling water flow without the covering plate. For the measurements the Rayleigh-Bénard cell with its transparent top plate is placed in between the heating plate and the frame, such that the flow can be observed through the large cutout.

Despite the measures taken for the reduction of the pressure in the cooling circuit, the two transparent plates enclosing the flow must have a certain thickness due to the material properties of glass and the large area subject to pressure, such that a safe operation mode of the cooling plate is guaranteed. Taking this into account is especially important with regard to a high flow rate in the cooling circuit, which is necessary to impede considerable temperature inhomogeneities on the cooling plate resulting from the temperature increase of the cooling water in flow direction. However, the thickness of the plates must not be arbitrarily overdimensioned, as the achievable temperature differences in the Rayleigh-Bénard cell are strongly limited by a thick glass plate because of its

low thermal conductivity. Hence, the thickness has been carefully designed by means of mechanical simulations, enabling to estimate the mechanical stress of the transparent plates, as shown in the appendix B.2. On the basis of those simulations, a thickness of 8mm has been chosen for both plates, i.e. for the cooling plate of the Rayleigh-Bénard cell and the covering plate on top of the frame above the cooling plate. On the one hand, this thickness allows for a high flow rate of the cooling water of $\dot{V}_{cw} = 30\,l/min$, which was adjusted for all the experiments with a ball valve and measured with a flow rate sensor at the outlet of the thermostatic bath. However, on the other hand this design of the cooling plate also enables to achieve certain temperature differences in the Rayleigh-Bénard cell, yielding suitable Rayleigh numbers for the comparison of the experimental results with those of numerical simulations.

The range of possible temperature differences $\Delta T = T_h - T_c$ has been estimated analytically for the aspect ratios $\Gamma = 25$ and $\Gamma = 10$ during the design of the experimental setup, as outlined in the appendix C. In addition, the temperature difference $\Delta T$ has been analyzed at the real experimental setup for those two aspect ratios in dependency of the temperature difference between the heating and cooling water $\Delta T_{circuits} = T_{hw} - T_{cw}$. As illustrated in figure 3.8, the temperature of the cooling water is measured in each of the inlets as well as outlets with immersible PT100 temperature probes and, since the temperature is slightly changing in flow direction, the mean value is taken to specify the temperature of the cooling water $T_{cw} = \langle T_{cw,n} \rangle_{n=(1,...,12)}$. Analogously, the mean temperature of the heating water is given by $T_{hw} = \langle T_{hw,n} \rangle_{n=(1,...,4)}$. In order to determine the temperature of the heating and cooling plate, the temperatures measured with the sensors at the plates indicated in figure 3.6 are averaged, respectively, i.e. $T_h = \langle T_{h,n} \rangle_{n=(1,...,5)}$ and $T_c = \langle T_{c,n} \rangle_{n=(1,...,4)}$. For the estimation of the possible temperature differences between the heating and cooling plate of the Rayleigh-Bénard cell, the temperature of the cooling water was kept fixed at $T_{cw} \approx 14\,°C$, while the temperature of the heating water was increased stepwise in the range of about $15\,°C \leq T_{hw} \leq 44\,°C$, yielding the results depicted in figure 3.10. Furthermore, the temperature differences between the cooling plate and the cooling water are also shown, indicating the large temperature drop across the glass plate. From this it can be concluded that the temperature drop across the heating plate made of aluminum is very small, since the sum of the two temperature differences $(T_h - T_c) + (T_c - T_{cw}) = (T_h - T_{cw})$ is close to the whole temperature difference $\Delta T_{circuits}$. Even though the transparent cooling plate strongly limits the temperature difference in the cell, the results demonstrate that moderate temperature differences up to $\Delta T_{max} \approx 8\,K$ can be achieved for $\Delta T_{circuits} < 30\,°C$. Assuming a minimal temperature difference of $\Delta T_{min} \approx 0.5\,K$ with respect to the controlling of the boundary conditions by the thermostatic baths, the achievable ranges of the Rayleigh number $Ra \in [10^5, 5 \times 10^6]$ for $\Gamma = 25$ and $Ra \in [10^6, 5 \times 10^7]$ for $\Gamma = 10$, as estimated above by means of figure 3.2, can be considered valid. It should be noted, that the results regarding the possible temperature differences and Rayleigh numbers obtained with the analytical model in the appendix C are also in good agreement with the experimental results.

Due to the large heat capacity and the high flow rate of the cooling water, its temperature only slightly increases along the cooling plate. The temperature increase is checked with the temperature probes in the inlet and outlet, yielding a mean difference $\Delta T_{cw,in \to out} = \langle T_{cw,n} \rangle_{n=(7,...,12)} - \langle T_{cw,n} \rangle_{n=(1,...,6)}$, which is similar to the temperature decrease in the heating water circuit, i.e. even for the experiments with the maximum heat transfer the temperature increase is smaller than $\Delta T_{cw,in \to out} = 0.2\,K$. However, while the heating plate made of aluminum further lowers the temperature differences of the heating
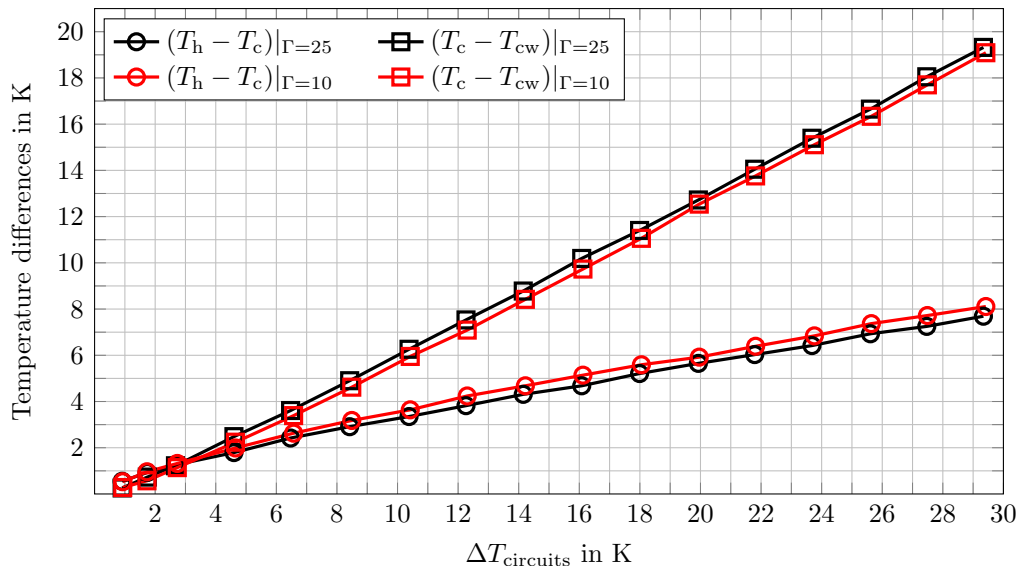
Figure 3.10: Measured temperature difference between the heating and cooling plate of the two Rayleigh-Bénard cells with the aspect ratio $\Gamma = 25$ and $\Gamma = 10$ in dependency of the temperature difference between the heating and cooling water $\Delta T_{\text{circuits}} = T_{\text{hw}} - T_{\text{cw}}$. For comparison, the temperature drop across the cooling plate $T_{\text{c}} - T_{\text{cw}}$ is plotted, too.

water because of its high thermal conductivity, the cooling plate made of glass does not considerably compensate for the temperature differences of the cooling water. Hence, even though those temperature differences measured with the temperature probes are small and consequently an almost homogeneous temperature distribution in the cooling water flow can be expected, the effect of the latter on the temperature homogeneity of the cooling plate needs to be further analyzed. For this, an infrared camera (VarioCAM hr head, InfraTec GmbH) has been applied to study the temperature distribution on the upper surface of the top glass plate. This allows to estimate the temperature variations on the lower side of the cooling plate resulting from the cooling water flow, since the plates have the same thickness and symmetrically enclose the flow.

As shown in the appendix D, the infrared measurements have been performed for different flow rates of the cooling water and also for varying temperature differences between the heating and cooling plate $\Delta T$. For the flow rate of $\dot{V}_{\text{cw}} = 30 \, \text{l/min}$, which is used for all the Rayleigh-Bénard experiments in this work, a maximum temperature difference of $\Delta T = 4.8 \, \text{K}$ has been adjusted, since this roughly matches the largest temperature difference imposed for those experiments. In this case, the maximum temperature increase on the surface of the upper glass plate in flow direction of the cooling water amounts to $\langle \Delta T_{\text{gp,top}} \rangle_x^* \approx 0.19 \, \text{K}$ as explained in the appendix D. In comparison, for the same measurement the sensors in the inlets and outlets for the cooling water yield a temperature increase of $\Delta T_{\text{cw,in} \rightarrow \text{out}} = 0.16 \, \text{K}$ on average, which is consistent when considering the measurement uncertainties. For further details of the infrared measurements, such as the smaller temperature variations transverse to the flow direction of the cooling water for $\dot{V}_{\text{cw}} = 30 \, \text{l/min}$, the reader is referred to the appendix D. Hence, the results obtained from the temperature measurements in the inlets and outlets of both the heating and the cooling plate as wells as the infrared measurements on the surface of the upper glass plate of the cooling circuit by means of the infrared camera indicate, that only small temperature inhomogeneities are supposed to occur on the plates.

However, so far it has not been considered that the Rayleigh-Bénard flow in the cell

affects the temperature homogeneity on the plates. In the present case this is also intuitively understandable, especially when thinking of the turbulent superstructures impinging on the plates. It is a natural consequence that the temperature distribution on the plates in the cell cannot not remain unaffected by that. This is exemplarily demonstrated in figure 3.11a, where the black curve shows the temperatures measured every 10 s with one of the four sensors at the cooling plate during a Rayleigh-Bénard experiment. From this curve fast fluctuations become apparent, but these do not indicate strong variations of the temperature at the cooling plate. The fast fluctuations can be traced back to the fact that the sensor element is at some time instants affected by the small-scale thermal plumes occurring in RBC. Even though the temperature sensor is directly adhered to the cooling plate with a thermal glue and is very flat, the effect cannot be fully suppressed. While the fast fluctuations in the black curve do not indicate a fast variation of the cooling plate temperature, the overlaid red curve with removed fast fluctuations is interpreted as an indication of a varying temperature of the cooling plate. This is not the result of the temporally changing temperature in the cooling water flow, which varies in a range of about $\pm 0.05$ K around the mean in another manner, as determined from the sensors in the inlet of the cooling plate. Hence, this must be related to the occurrence of the turbulent superstructures in the flow, which gradually rearrange over time and locally affect the temperature of the plate. Even though this is of course not desirable, it cannot be impeded, as the thermal diffusivity of any material is limited in practice. In particular glass and plastics, as for instance polycarbonate, which have come into question as the material for the cooling plate, have a low thermal diffusivity and are thus usually not well suited as the bottom or top plate of a Rayleigh-Bénard cell. However, here the optical access must be provided, such that this has to be accepted. From the results in figure 3.11b, which show the temperature measured with the sensor in the center of the heating plate in the same experiment, it is seen that the variation over large time intervals is almost negligible because of the much higher thermal conductivity of aluminum. It should be noted again, that the sensors at the heating plate are not adhered to the upper side of the surface, but are screwed in from the bottom side and do not fully reach the surface. However, the sensors are very close to the surface, so that slowly evolving variations of the temperature to the extent of those at the cooling plate could be detected. On the contrary, the very fast and strongly pronounced fluctuations arising from thermal plumes are not apparent from the temperature measured at the heating plate, as the sensors are not directly exposed to the flow. The black curve in figure 3.11b only shows the slight change of the temperature caused by the regulation of the heating water temperature.

Due to the fluctuations of the measured temperatures, in general only the values with a maximum deviation of two times the standard deviation from the median are taken into account to determine the average temperature for each sensor separately, thereby excluding the extreme values. All the temporally averaged temperatures of the different sensors are then incorporated to determine the spatial average at each plate, resulting in the heating and cooling plate temperatures specified in the present work. The temporal averages obtained with the four sensors at the lower side of the cooling plate from the entire duration of the experiment typically vary in a range of about 0.1 K. The average temperatures measured with the two sensors towards the outlet of the cooling water flow are mostly larger due to the increasing temperature of the cooling water in flow direction, which is agreement with the previous results. It should also be noted, that the deviations of the temperatures measured directly underneath the surface of the heating plate are even smaller due to the large thermal conductivity of the covering aluminum plate. At the

example of the experiment, which has been considered for the results shown in figure 3.11, the temporally and spatially averaging yields $T_{\mathrm{h}} = 20.22\,^{\circ}\mathrm{C}$ and $T_{\mathrm{c}} = 18.76\,^{\circ}\mathrm{C}$. Hence, the temperature difference between the plates is in this case $\Delta T = 1.46\,\mathrm{K}$, which is still much larger than the locally occurring temperature variations on large time intervals, represented by the red curves in figure 3.11.

At the end of the section 3.1 it can be concluded, that some deviations from the homogeneous temperature distribution appear on both the heating and cooling plate because of the influence of the Rayleigh-Bénard flow in the cell. Despite the great efforts made in the design of the heating and cooling water circuit this issue cannot be circumvented due to the limitation of the thermal diffusivity, which is especially noticeable at the cooling plate made of glass. However, at the example of the results discussed by means of figure 3.11 it can be seen that the temperature difference between the plates is much larger. This is the case in each of the experiments performed for the present work. Therefore, the Rayleigh-Bénard flow is not strictly predetermined by any inhomogeneities. Otherwise the change of the temperature on large time scales, which is not primarily caused by variations of the heating and cooling water temperature, could not have been seen in figure 3.11. Thus, the rearrangement of the turbulent superstructures can at this point already be expected and will be demonstrated in section 5.2.6.
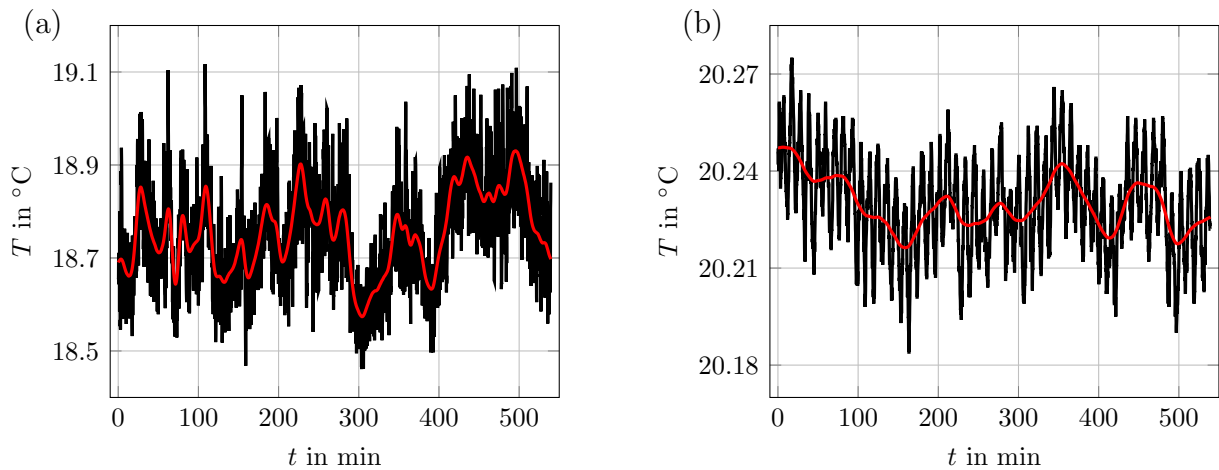


Figure 3.11: The variation of the temperature at the cooling plate (a) and at the heating plate (b) measured with local temperature sensors in a Rayleigh-Bénard experiment.

## 3.2 The illumination source

The temperature measuring technique based on the color signal of TLCs, which is explained and thoroughly characterized in chapter 2, requires to use a white light source for the temperature measurements of the flow in the Rayleigh-Bénard cell. Since the measurements are performed in the large horizontal cross-sections of the Rayleigh-Bénard cell, a special light source has to be designed for providing a white light sheet with a thickness that allows to measure the temperature fields with a suitable spatial resolution in direction of the light sheet's thickness. In this respect, especially the uniformity of the thickness is very challenging, due to the divergence of the light emitted by conventional white light sources, which is significantly larger compared to that of laser light as commonly applied for the generation of a light sheet for flow studies. At this point it should be

mentioned, that using a so-called supercontinuum laser enables to generate a light sheet with a wide range of wavelengths, since the emission spectrum of those lasers typically covers $400\,\text{nm} \leq \lambda \leq 2400\,\text{nm}$ [140], which can be adjusted to the specific application. As a proof of concept, such a laser has already been used for temperature measurements via evaluating the color signal of TLCs [141]. Due to the possibility to shape a thin light sheet with almost uniform thickness, this laser allows for measurements with a high spatial resolution, however, because the light emitted through a fiber has to be expanded to a light sheet, chromatic aberrations may yield considerable inhomogeneities regarding the intensities of the wavelengths across the light sheet. In particular, when large areas must be illuminated, such as the horizontal cross-section of the Rayleigh-Bénard cell in the present experimental setup, this effect is difficult to correct. As it has been addressed in the study [141], those local differences of the wavelength distribution across the light sheet affect the temperature measurements with TLCs. Thus, in order to overcome this issue, a light source with a single fiber is not used in this case. Instead of that the light sheet is generated with 90 white LEDs (Platinum Dragon, Osram GmbH), which are horizontally aligned along the whole length of one of the cell's sidewalls. According to the principle shown in reference [142], small lenses are directly clipped onto the LEDs to reduce the divergence of the emitted light, which is then passing through a slit aperture with adjustable width and Fresnel lenses to shape the light sheet as sketched in figure 3.12. Two adhesive foil stripes are attached to the outer side of the Fresnel lenses to further block scattered light from the interior of the light source, which can be seen in the photograph on the right side of figure 3.12.
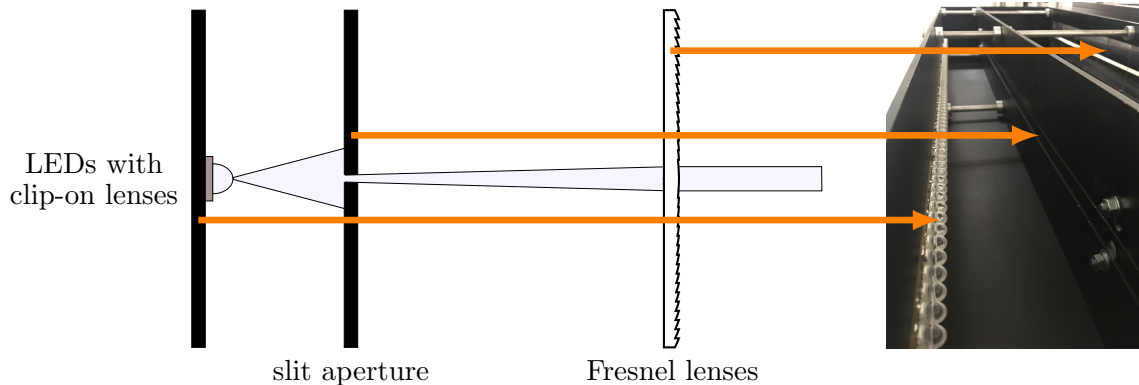


Figure 3.12: Sketch of the light sheet optics (left) and a photograph showing the interior of the light source for the generation of a white light sheet (right).

As the flat Rayleigh-Bénard cell with the aspect ratio $\Gamma = 25$ has a height of only $h = 28\,\text{mm}$, the thickness of the white light sheet should be kept as small as possible to limit the spatial averaging across the measurement plane. However, because the TLCs are also used for the velocity measurements with PIV as explained in section 4.3, the light sheet must have a certain thickness to reliably measure all the velocity components of the three-dimensional Rayleigh-Bénard flow, demonstrated in the study [60]. Considering this, a light sheet thickness of about $\delta_{\text{ls}} = 3\,\text{mm}$ turns out to be appropriate in this case. Hence, the distance between the components along the optical path of the light sheet optic and the width of the slit aperture have been adapted iteratively, aiming for a white light sheet with a nearly constant thickness of about $\delta_{\text{ls}} = 3\,\text{mm}$ over the whole horizontal cross-sectional area of the Rayleigh-Bénard cell. Furthermore, Fresnel lenses with a shorter focal length of $f_{\text{foc}} = 2\,\text{in}$ and a larger focal length of $f_{\text{foc}} = 6\,\text{in}$ have been inserted in the

light sheet optic for investigating the effect of the lenses. Based on this it has been found, that the focal length $f_{\text{foc}} = 6$ in is much better suited with respect to the uniformity of the light sheet thickness, such that the Fresnel lenses with this focal length are applied.

Having figured out suitable settings for the light sheet optic, the thickness of the light sheet has been measured. However, not the large light source as depicted on the right side of figure 3.12 has been used for this, but a smaller light source, which has been built for the studies with the small cylindrical Rayleigh-Bénard cell in the appendix E. This light source is designed equally except for the width and, therefore, only 15 white LEDs of the same type are arranged along a line, such that the emitted light sheet covers a width of about 150 mm directly at the Fresnel lenses. In comparison, the light sheet emitted by the large light source has a width of around 800 mm directly at the Fresnel lenses, which is necessary to illuminate the whole horizontal cross-section of the cell. Since the width of the light source does not considerably affect the thickness of the light sheet, it is reasonable to measure the thickness with the smaller light source due to its easy handling. Thus, the arrangement of the optical components and the width of the slit aperture were accurately adapted according to the settings of the large light source.
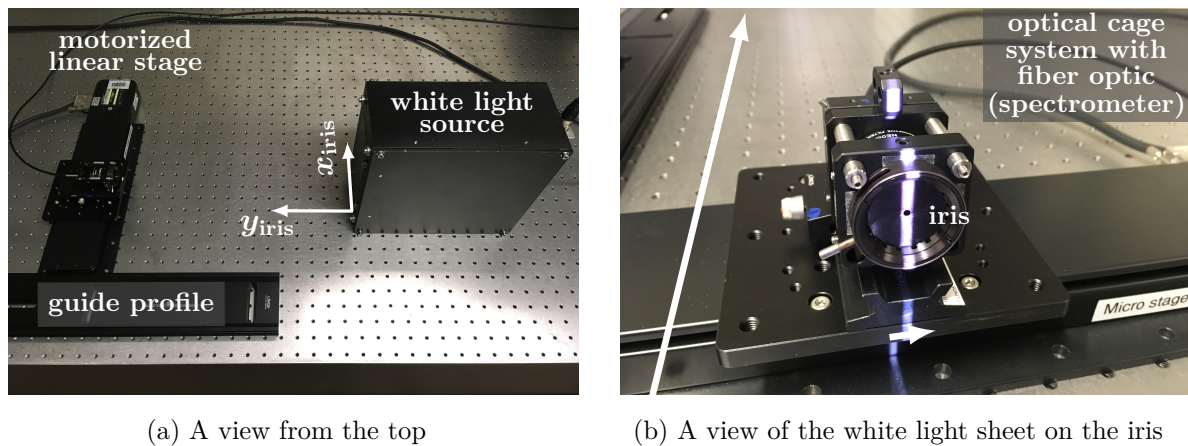


(a) A view from the top  (b) A view of the white light sheet on the iris

Figure 3.13: The experimental setup for measuring the thickness of the white light sheet. In order to visualize the variation of the measuring positions in direction of the emission of the light sheet and in transversal direction, white arrows are sketched in the right figure.

For the measurements of the thickness the small light source was put upright, such that the LEDs and accordingly also the light sheet are vertically aligned. As indicated in figure 3.13, a motorized linear stage was used to traverse the fiber of a spectrometer across the thickness of the light sheet for different distances between the fiber and the light source. The fiber was screwed into an optical cage system mounted on the stage with an iris at the front side, which can be seen in figure 3.13b, such that only a narrow part of the light sheet illuminates the fiber. Hence, the comparison of the spectral intensities at the different positions allows to determine the thickness of the light sheet on the one hand, but on the other hand also enables to assess, if chromatic aberration affects the wavelength distribution across the light sheet thickness. It should also be mentioned, that neutral density filters were inserted behind the iris to prevent the fiber from any damage caused by a too high spectral power. Since the transmittance of the filters for different wavelengths is not absolutely uniform, this was taken into account by correcting the intensities measured with the spectrometer according to the transmission data given by the manufacturer (Thorlabs, Inc.). The optical cage with the fiber behind the iris was traversed through the light sheet over a distance of $\Delta x_{\text{iris}} = 12$ mm in steps of $0.5$ mm for

19 different distances between the iris and the Fresnel lenses, ranging from $y_{\text{iris}} = 0.1\,\text{m}$ to $y_{\text{iris}} = 1\,\text{m}$ in steps of $0.05\,\text{m}$. For a better imagination, the spectral power distributions for different positions across the light sheet and a distance of $y_{\text{iris}} = 0.4\,\text{m}$ between the iris and the Fresnel lenses are depicted in figure 3.14.
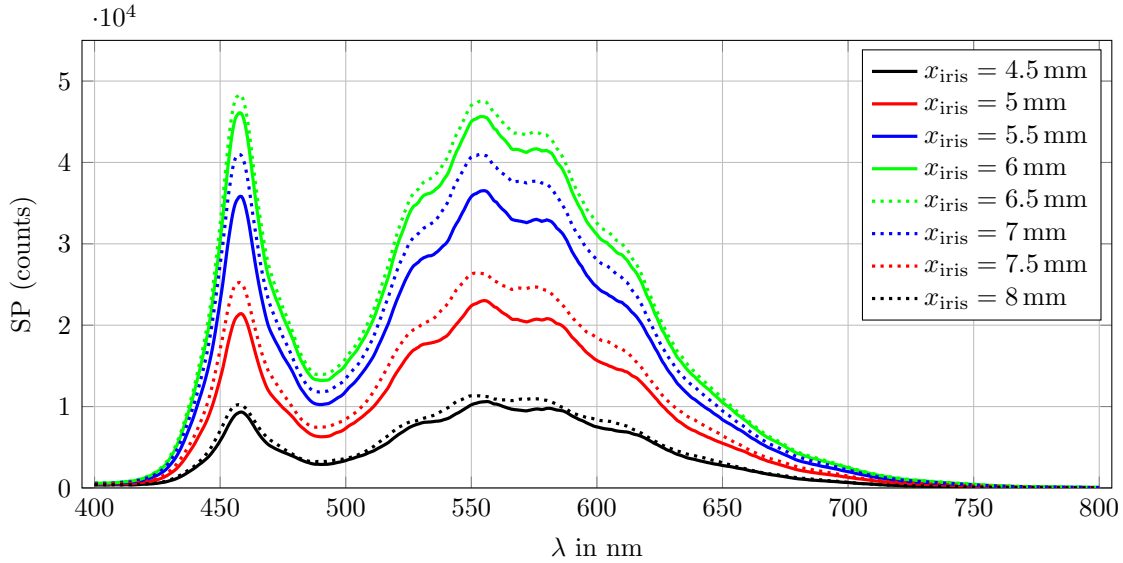


Figure 3.14: Distribution of the spectral power (SP) at different transversal positions in the white light sheet for an exemplary distance of $y_{\text{iris}} = 0.4\,\text{m}$ between the iris and the Fresnel lenses.

As expected, the spectral power distributions clearly show that the maximum intensities are in this case obtained for $x_{\text{iris}} = 6.5\,\text{mm}$, which is close to the center of the traversed range $\Delta x_{\text{iris}} = 12\,\text{mm}$, while the intensities significantly decrease approaching the margins. However, qualitatively the spectral power distributions look very similar in each case. In this regard, especially the two maxima located at $\lambda \approx 460\,\text{nm}$ and $\lambda \approx 550\,\text{nm}$ are very conspicuous. Having a closer look to figure 3.14, it becomes obvious that the ratio of the spectral power corresponding to the two maxima does not considerably change. This qualitative similarity could also be obtained for all the other distances between the iris and the Fresnel lenses, confirming that chromatic aberration is here of minor importance.

In order to estimate the light sheet thickness, the values of the spectral power of each curve were first summed up, respectively, yielding a cumulative spectral power CSP for every position of the iris. The cumulative spectral power is depicted in figure 3.15 for different distances between the iris and the Fresnel lenses, normalized with the corresponding maximum value in each case. Even though the maximum was always obtained for similar transversal positions of the iris in close vicinity to the center of the traversed range, the curves of the cumulative spectral power were shifted along the abscissa, such that the maxima are exactly at the same position. The results in figure 3.15 are only plotted up to a distance of $5\,\text{mm}$ from the center of the traversed range, since the cumulative spectral power close to the margin is very low and thus irrelevant. Furthermore, it should be noted that a piecewise cubic interpolation was applied to smooth each of the curves, however, the original data points are not affected by that.

For the estimation of the light sheet thickness based on the normalized cumulative spectral power, a threshold $c_{\text{thres}}$ must be defined as the lower limit, in order to determine the thickness according to the condition $\text{CSP}/\max\left(\text{CSP}\right) \geq c_{\text{thres}}$. For this, the values $c_{\text{thres}} = 0.5$, $c_{\text{thres}} = 1/\text{e}$ and $c_{\text{thres}} = 1/\text{e}^2$, which may be considered for specifying the diameter of a beam [143], are used, yielding the results in figure 3.16. It can be seen that
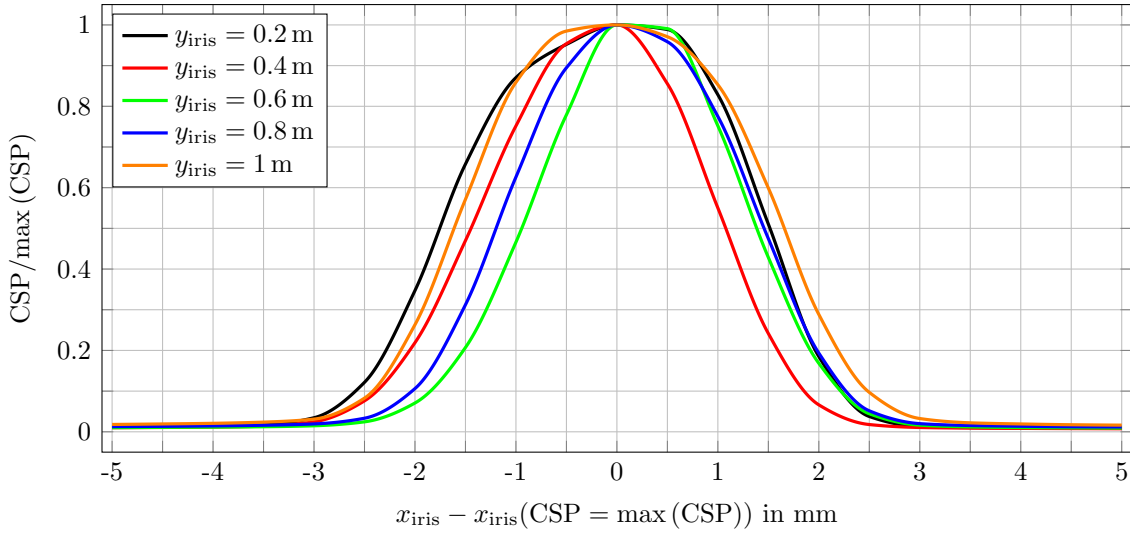
Figure 3.15: Normalized cumulative spectral power (CSP) in dependency of the transversal position within the white light sheet for some exemplary distances between the iris and the Fresnel lenses.

the light sheet thickness is the smallest for $0.5\,\mathrm{m} \leq y_{\mathrm{iris}} \leq 0.6\,\mathrm{m}$ and almost symmetrically increases for lower and larger distances from the light source. Hence, in order to achieve a small variation of the light sheet thickness across the Rayleigh-Bénard cell, the light source should be mounted in a way, such that the distance between the Fresnel lenses and the cell's sidewall is roughly in between $20\,\mathrm{cm}$ and $25\,\mathrm{cm}$. Considering this, the thickness of the light sheet in the Rayleigh-Bénard cell can be estimated to $3\,\mathrm{mm} \leq \delta_{\mathrm{ls}} \leq 4\,\mathrm{mm}$, when all the different definitions of the threshold $c_{\mathrm{thres}}$ are taken into account for averaging.
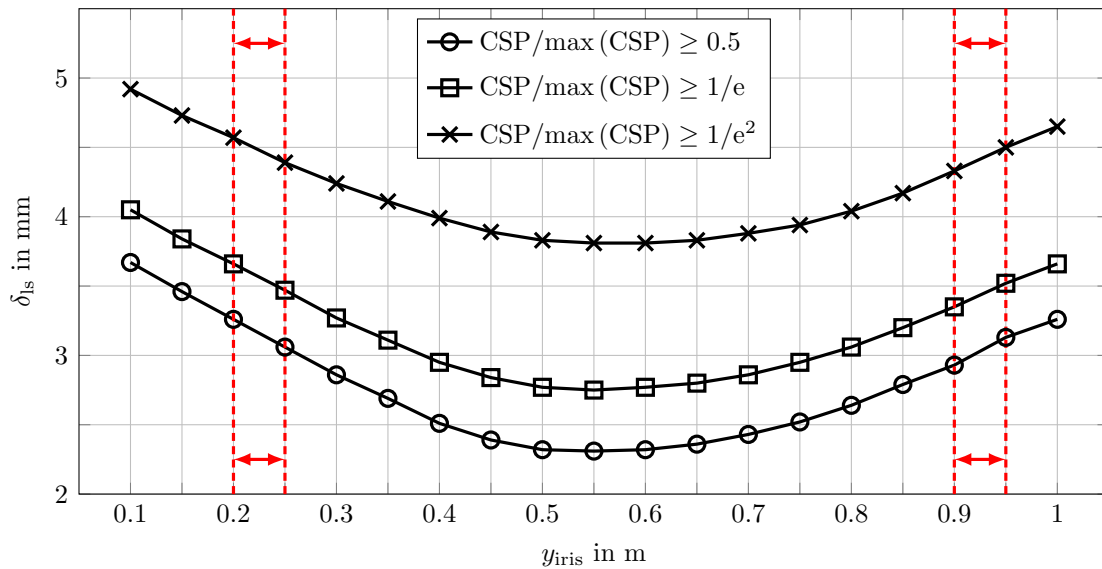


Figure 3.16: The thickness of the white light sheet in dependency of the distance between the iris and the Fresnel lenses using different thresholds for the minimum normalized cumulative spectral power in figure 3.15. The dashed red lines indicate, which distance the Fresnel lenses of the white light source should have to the front and back sidewall of the Rayleigh-Bénard cell to minimize the variation of the light sheet thickness in the cell with its dimensions of $l \times b = 700\,\mathrm{mm} \times 700\,\mathrm{mm}$.

# 3.3   Camera arrangement and equipment

As mentioned in the previous sections, optical measuring techniques are applied in this work to simultaneously measure the temperature and velocity field in horizontal planes of the Rayleigh-Bénard cell. Both of the fields are measured in the illuminated horizontal plane by means of the TLCs dispersed in the flow. While their color is recorded with a color camera (sCMOS pco edge 5.5 color, PCO AG) for the determination of the temperature field, the velocity field is computed based on the motion of the TLCs recorded with two additional monochrome cameras (sCMOS pco edge 5.5, PCO AG). Therefore, the cameras can be arranged independently to optimize the results for both fields. Here, two monochrome cameras are applied, since this is necessary to determine not only the horizontal components of the velocity parallel to the illuminated plane, but also the velocity component in the vertical direction, which is of great interest for the investigation of the heat flux in RBC. The measuring technique for the velocity field, well-known as the Stereoscopic Particle Image Velocimetry, is further described in section 4.3. All the three cameras are equipped with high quality objective lenses (Zeiss Otus 1.4/28, Carl Zeiss AG), which allow to observe a large field of view due to their focal length of $f_{\mathrm{foc}} = 28\,\mathrm{mm}$. In combination with the applied cameras, this focal length results in an aperture angle of about $\Theta_{\mathrm{obj,min}} = 28°$ and $\Theta_{\mathrm{obj,max}} = 33°$ for the smaller and larger side of the cameras' sensor, respectively. Furthermore, tilt adapters are used as the connection between the cameras and the objective lenses to comply with the so-called Scheimpflug condition [144], so that the whole measurement plane is projected as sharply as possible onto the cameras' sensors.

In order to perform reliable measurements of the temperature and velocity field over a large field of view, the cameras are arranged properly. Especially, the arrangement of the color camera requires special attention, as the temperature range with a low measurement uncertainty depends on the angle between the light sheet and the optical axis of the color camera. According to the results in section 2.2, a standard perpendicular orientation of the camera to the measurement plane is not appropriate for most applications, because the color of the TLCs changes from red to blue within a very small temperature range, such that the measuring range is strongly limited. It has been shown in section 2.4, that observation angles of $50° \leq \varphi_{\mathrm{cc}} \leq 70°$ are best suited to reliably measure temperatures covering moderate ranges up to about $3\,\mathrm{K}$, when the TLCs R20C20W are used. For performing temperature measurements over larger ranges with those observation angles, the TLCs R25C50W can be applied, as described in the appendix E. Considering their specifications it can be estimated, that the useful temperature measuring range of the TLCs R25C50W should approximately be twice as high. More detailed analysis of the measurement uncertainty for these types of TLCs can be found in the section 4.2.

When decreasing the observation angle of the color camera $\varphi_{\mathrm{cc}}$, which is indicated in figure 3.17a, it must be taken into account that larger nonuniformities in the camera's image are caused by a varying magnification. In particular, when the observation angle $\varphi_{\mathrm{cc}}$ is reduced to still observe a large field of view for small distances between the color camera and the measurement plane, the discrepancies regarding the magnification become undesirably stronger, which can be concluded from the analysis in the study [145]. Considering all the effects of the observation angle $\varphi_{\mathrm{cc}}$ on the temperature measurements and on the uniformity of the imaging, the angle was adjusted to $\varphi_{\mathrm{cc}} = 65°$ in this case. It is also obvious from figure 3.17a, that this angle adjusted at the camera is only a nominal value, as the observation angle varies in the camera's field of view and is affected by refraction of

the light, which passes several interfaces of water, glass and air between the measurement plane and the camera. With the smaller aperture angle of $\Theta_{\mathrm{obj,min}} = 28°$ in the $x$-$z$-plane according to figure 3.17a, it can be estimated based on Snell's law [146] that the observation angle in the field of view of the color camera approximately varies in between 60° and 80°. This arrangement of the color camera is a tradeoff, which allows for an accurate determination of the temperature fields in RBC with temperature differences between the heating and cooling plate up to about $\Delta T = 5\,\mathrm{K}$ as it will be shown in section 4.2, while the variation of the magnification across the field of view is kept in reasonable limits, especially due to the large distance between the measurement plane and the image plane of around $1\,\mathrm{m}$.



(a) Arrangement in the $x$-$z$-plane

(b) Arrangement in the $y$-$z$-plane
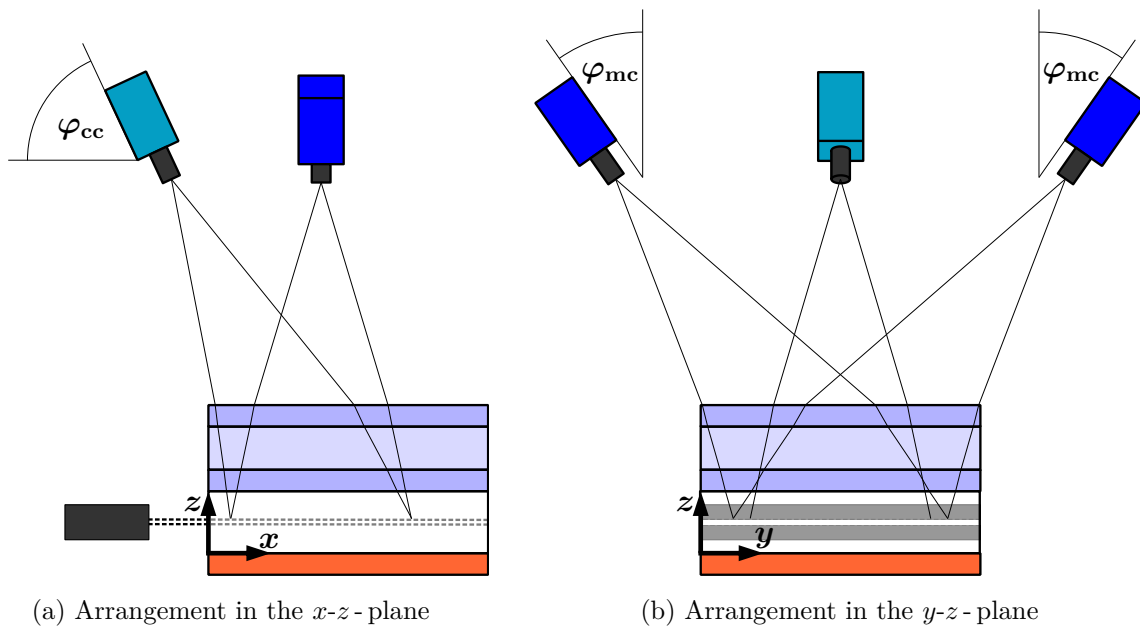
Figure 3.17: The arrangement of the color camera (light blue) for the temperature measurements and of the two monochrome cameras (dark blue) for the velocity measurements via Stereoscopic Particle Image Velocimetry.

Just as the arrangement of the color camera must be thoroughly planned with regard to the temperature measurements, the arrangement of the monochrome cameras is very important for the velocity measurements. In this respect, choosing a suitable observation angle is essential again to precisely measure both the horizontal and the vertical velocity components. As sketched in figure 3.17b, the two monochrome cameras are symmetrically arranged in the $y$-$z$-plane. Aiming for a similar measurement uncertainty for the horizontal and vertical velocity components, an angle of $\varphi_{\mathrm{mc}} = 45°$ should be adjusted, but of course the issues concerning the uniform imaging of the measurement plane arising from the angular observation apply to the monochrome cameras as well. Therefore, the angle between the optical axis of the cameras and the vertical axis $\varphi_{\mathrm{mc}}$ was in this case decreased to $\varphi_{\mathrm{mc}} = 35°$, yielding a slightly larger uncertainty for the determination of the vertical velocity components compared to horizontal velocity components. However, based on the findings in the work [147] it can be estimated, that the ratio of the uncertainties of the vertical and horizontal velocity components $e_{\mathrm{r}}$ is basically $e_{\mathrm{r}} \leq 1.5$ for $\varphi_{\mathrm{mc}} = 35°$. Thus, this angle is suited for measuring all the velocity components. Moreover, as obvious from figure 3.17a, the monochrome cameras are not inclined in the $x$-$z$-plane, yielding an

angle of 90° between the incident white light sheet and the optical axis of the cameras in this plane. Hence, since the temperature range of the Rayleigh-Bénard flow in the cell is adapted with respect to a strong color variation in the field of view of the color camera, the TLCs mainly appear bluish in the field of view of the monochrome cameras, resulting from the color characteristics of the TLCs presented in section 2.2. Accordingly, the grayscale images of the monochrome cameras are not affected by a considerably varying local color appearance of the TLCs, which might have an influence on the determination of the velocity fields.

In the figure 3.17 it can also be seen that the cameras are arranged in the way, that the center of their field of view coincides with the center of the Rayleigh-Bénard cell in $y$-direction, while the field of view is not centered in $x$-direction. In this direction it is shifted towards the white light source, as the experiments have shown that the measurements can be performed more reliably in this part of the cell. The reason for this mainly lies in the fact that the TLCs scatter much of the incident white light into forward direction at flat angles, resulting in a stronger diffusive reflection of the scattered light on the surface of the heating plate on the opposite side of the light source. Even though the surface of the heating plate has been covered with a matt black adhesive foil, such that the TLCs can be better observed from the top side against a dark background, the strong diffusive reflection on the heating plate towards the sidewall on the opposite side of the light source disturbs the measurements. Hence, not the whole horizontal cross-section of the cell is observed with the cameras, but the measurement is restricted to an area closer to the light source as indicated in figure 3.17a. It should be mentioned, that the effect of the light reflected from the heating plate could be reduced by filtering the incident light and the light reflected by the TLCs with circular polarizers in front of the light source and the cameras' lenses as well [88]. However, since the transmittance of the polarizers is limited, the intensity of the light received from the camera sensors would be significantly decreased, which is why this technique is not applied here. Although studying the whole horizontal cross-sectional area of the Rayleigh-Bénard cell would be advantageous to analyze the pattern of the turbulent superstructures, the measurement area has been decreased due to this issue, so that the temperature and velocity fields can be determined more reliably and, in addition, with a higher spatial resolution. Nevertheless, the field of view is still large enough to observe and investigate the turbulent superstructures.

# The measuring techniques

Thermochromic liquid crystals are applied in this study to simultaneously measure temperature and velocity fields in RBC based on digital images recorded with cameras. For the quantitative investigation of the flow, a dimensional calibration of the cameras' images must be performed, as outlined in section 4.1. The temperature measuring technique using the color appearance of the TLCs has already been explained in section 2 in detail, however, basically general characteristics of this method and possible calibration techniques have been discussed. Therefore, its applicability for temperature measurements in the large Rayleigh-Bénard facility is shown in section 4.2. Moreover, the fundamentals of the velocity measuring technique Particle Image Velocimetry are presented in section 4.3.

## 4.1 Dimensional calibration of the measurements

Since this work does not only aim for visualizing the flow in horizontal planes of the Rayleigh-Bénard cell with aspect ratio $\Gamma = 25$, but in particular for the quantitative investigation by means of temperature and velocity field measurements, it is necessary to determine the physical dimensions from the images recorded with the cameras in the arrangement according to figure 3.17. For quantitative flow measurements with cameras, the physical dimensions are frequently derived using a calibration target with a pattern of markers, that are equidistantly arranged and have a known distance to each other. Commonly, the dimensional calibration is performed separately from the actual measurements, meaning that the calibration target is placed with the pattern along the measurement plane, images of the pattern are recorded with all the cameras and subsequently the calibration target is removed again, such that it does not affect the flow in the actual measurements. Based on the images of the pattern, which might be strongly distorted depending on the observation angle and the media between the cameras and the calibration target, the physical dimensions of the measurement plane can be calculated. For this purpose typically pinhole camera models [148], either with a direct linear transformation [149] or advanced corrections to account for distortions [150], and polynomial fits as proposed in the work [151] are used.

In principal, the described procedure is applied for the dimensional calibration in the present case. However, in order to precisely determine all the velocity components of the flow via the Stereoscopic Particle Image Velocimetry explained in section 4.3, it is in general recommended to record images of a pattern of markers with known distances in at least two different planes. Here, this recommendation is obeyed to conduct accurate

velocity measurements. One of the planes is the surface of the heating plate with the pattern of dots printed on the black adhesive foil, which is permanently attached and obvious from figure 3.9, while the images in the second horizontal plane are obtained from an additional flat calibration target, which can be seen in the figure A.9 of the appendix A. This has the same pattern of the equidistant dots with the diameter of about 2 mm and the distance of 25 mm printed on its surface and is temporarily placed on the heating plate within the cell for the purpose of the calibration. Images are separately taken of the pattern on the heating plate and on the calibration target with the color camera and the two monochrome cameras. In order to perform an accurate calibration, the images are recorded in the same experimental configuration as in the flow measurements to ensure identical conditions with regard to the optical imaging. This implies for example, that the Rayleigh-Bénard cell and the cooling circuit on top are filled with water, the cooling water is covered with the glass plate and driven by the thermostatic bath with the same flow rate as in the flow measurements. Therefore, the minimal deformation of the glass plates due to the pressure in the cooling circuit is taken into account in the calibration, too. Furthermore, special emphasis is given that any works on the setup between the calibration and the flow measurements are reduced to a minimum, thereby preventing that the cameras might be shifted inadvertently due to strong vibrations or mechanical contact.

However, the measurements in RBC have not been performed in close vicinity to the heating plate, where the calibration target is placed, but in the horizontal mid plane and in another horizontal plane close to the top of the Rayleigh-Bénard cell. Measured from the surface of the heating plate, the measurement planes in the cell with the aspect ratio $\Gamma = 25$ and the height of $h = 28$ mm are located at $z = 14$ mm and $z = 24$ mm. As illustrated in figure 4.1, the shift of the measurement plane from the calibration plane yields the mapping of one point in space to disparate positions in the calibration plane, if the point is observed from different directions. With regard to the present work this would result in the problem, that one and the same TLC particle in the measurement plane would be allocated to different points in space for each of the three cameras. Hence, the standard calibration technique, which requires images of a pattern of markers in the measurement plane itself, cannot be applied here. For this, it would have been necessary to accurately adjust the position of the calibration target in accordance with the measurement plane, respectively.

In order to circumvent the measures for ensuring that the pattern is well aligned with the measurement plane in each case, the established stereoscopic self-calibration [152], which is a common tool used to correct the displacement between the measurement and calibration plane, is applied. This technique is implemented in DaVis 8.4 (LaVision GmbH), which is the software solution used for the imaging and several postprocessing steps of the images throughout the whole work. In the first step of the stereoscopic self-calibration the shift of the particles, mapped from the measurement plane to the calibration plane, is determined via cross-correlation for different interrogation windows in the field of view of two cameras. The combination of all the local shifts, represented by vectors in the so-called disparity map, is then utilized to correct the mapping functions of the two cameras in the way, that the shift of the particles in the dewarped cameras' images is minimized. For details about the procedure of the correction and the capabilities of this calibration technique the interested reader is referred to the work [152].

Aiming for the same position of the TLC particles in the dewarped images of the three cameras, the stereoscopic self-calibration is applied twice for each measurement plane, once for the two monochrome cameras and once for the color camera with one of
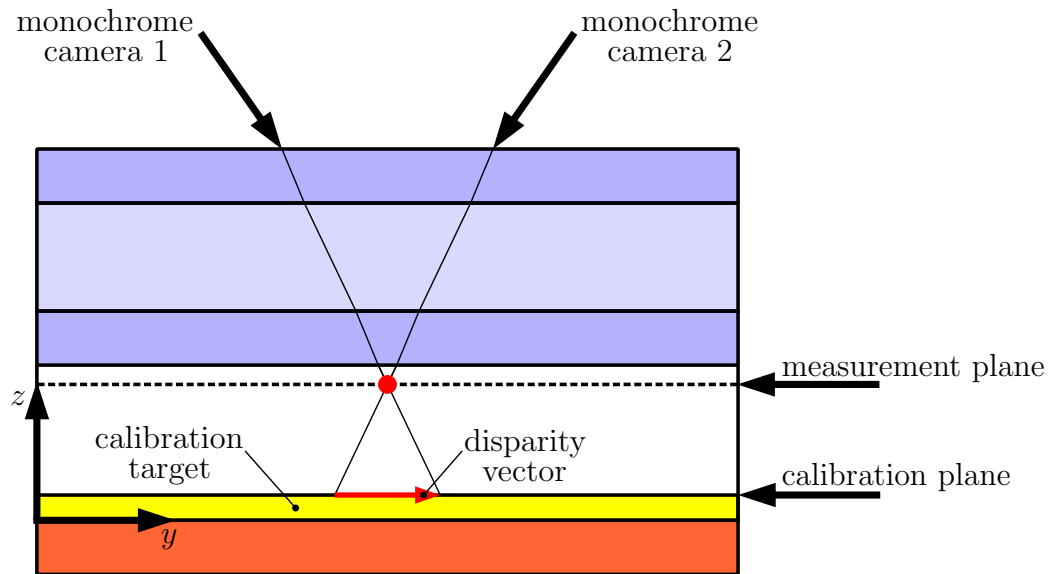
Figure 4.1: Illustration of the disparity when mapping a point in the measurement plane to physical dimensions based on a calibration in another plane. The sketch exemplifies the disparity in the image of the two monochrome cameras according to the arrangement in figure 3.17b for the measurements in the horizontal plane in close vicinity to the cooling plate of the Rayleigh-Bénard cell.

the monochrome cameras. The disparity map is computed on the basis of 100 images taken from an exemplary measurement set of each measurement plane, as using only one image of the particles in the measurement plane of each camera is in most cases not sufficient to accurately determine the disparity vectors [152]. Those are calculated locally in interrogation windows with a size of $256 \times 256$ pixel, yielding $26 \times 23$ vectors for the correction of the initial calibration for the two measurement planes. The remaining disparity is approximately $0.3\,\mathrm{mm}$ in average, considering the two pairwise combinations of the three cameras for the correction of the calibration in both measurement planes, and is therefore significantly decreased compared to the original disparities. These range in between a few millimeters up to about $2\,\mathrm{cm}$, such that the necessity of the correction is emphasized.

It should also be noted, that a customized two-level calibration target could have been used instead of the flat calibration target and the pattern of dots on the heating plate, which may be considered as disturbing in the background of the cameras' images during the flow measurements. However, as the dots are very small, they do not strongly affect the optical imaging of the seeding particles in the flow measurements. Nevertheless, as it will be addressed in the sections 4.2 and 4.3, for each of the cameras a filter is applied in the postprocessing to account for any interferences resulting from the background of the images. For the determination of the temperature field based on the images of the color camera, the pattern of dots in the background is even completely masked out. On this way, the pattern in the cameras' images can anytime be utilized to indicate, if the setup is in the right position for the flow measurements and the arrangement of the cameras has not slightly changed over time, which has proven to be very valuable in the course of the work and justifies minor disadvantages in the evaluation.

## 4.2    Temperature measuring technique

The temperature measuring technique using the color appearance of TLCs has been characterized in greater detail in section 2. It has been mentioned at the end of section 2.4.4, that the calibration technique based on linear interpolation of the color shade in terms of the hue is utilized to determine the temperature fields in this work due to its reliability. In the appendix E it is also shown that the temperature measuring range can easily be varied by applying TLCs with different specifications. However, all those investigations have been performed with the smaller cylindrical Rayleigh-Bénard cell presented in section 2.2. Even though the conclusions regarding the influence of the illumination spectrum and observation angle have been considered to design the larger experimental facility and the associated white light source, the findings cannot be transferred one-to-one, as every setup has its own characteristics. In particular, providing sufficient lighting of the TLCs is much easier in the small cell, as the illumination area covers only a small fraction compared to that of the larger cell. Therefore, in this section the temperature-dependent color change of the applied TLCs R20C20W and R25C50W is demonstrated with regard to the temperature measurements in the larger experimental facility.

In principal, the relationship between the color and temperature of the TLCs is obtained with the same procedure of the calibration measurements as described in section 2.2 for the small experimental setup. Thus, after inserting the TLCs into the water in the Rayleigh-Bénard cell, several isothermal states are adjusted by matching the temperature of the heating and cooling plate, respectively. For each temperature level, 100 images of the TLCs are recorded with the color camera at a frequency of $f = 5\,\mathrm{Hz}$ and an exposure time of $t_{\mathrm{exp}} = 100\,\mathrm{ms}$. Around thirty minutes is waited between changing the temperature at the thermostatic baths and the recording of the images. Contrary to the calibration measurements in the small cell, using a magnetic stirrer to accelerate achieving the stationary state of the temperature is not applicable in this case. Thus, through one of the two hoses, which are connected to the sidewall of the cell and are also used for the filling as well as the emptying of the cell, the working fluid is frequently stirred during the adjustment of the different temperature levels via slight pressure impulses to ensure that the temperature distribution is almost uniform. In order to relate the color of the TLCs to the temperature, the latter is measured with a PT100 temperature probe, that is inserted through one of the sidewalls as it can be seen in figure A.8. In addition, the temperature is determined with the sensors on the heating and cooling plate as well as on the inside of cell's sidewall for comparison. In each case the measured values are distributed in a narrow range of about $0.1\,\mathrm{K}$, confirming the temperature uniformity of the water inside the Rayleigh-Bénard cell during the calibration measurements.

Besides some calibration measurements for test purposes, which have been performed to figure out the temperature range of color play and suitable temperature levels for each of the TLCs, one accurate calibration run has been conducted for the temperature measurements in RBC with the TLCs R20C20W and R25C50W, respectively. As aforementioned, the measurements in RBC are performed in two different horizontal planes of the cell, with one being at mid-height and another in close vicinity to the cooling plate. However, as the measurement planes are very close to each other in the flat cell in relation to the distance of the camera from the measurement planes, which is roughly $1\,\mathrm{m}$, any effects on the color appearance of the TLCs can hardly be seen in the camera's image when switching between the measurement planes. Therefore, the calibration measurements have only been performed in the top measurement plane and the dimensional calibration has

been corrected with the stereoscopic self-calibration explained in the previous section 4.1.

It is emphasized that figuring out suitable experimental conditions for the temperature measurements was a very elaborate work. Especially, the arrangement of the color camera had to be adapted, such that the turbulent superstructures can be investigated over a large section of the field of view and the occurring temperatures can be measured accurately with an appropriate spatial resolution applying a suitable observation angle $\varphi_{cc}$, which is indicated in figure 3.17a. Upon completion of the experimental facility, many measurements have been performed with the observation angle of $\varphi_{cc} = 70°$ to assess the measuring technique and to get an impression of the Rayleigh-Bénard flow in the cell. Some exemplary results of the measurements are presented in the study [78] with the focus on different calibration techniques. However, for the present work the field of view has been enlarged by adapting the distance between the color camera and the measurement plane, so that the organization of the turbulent superstructures can be studied more deeply. Furthermore, as outlined in section 3.3, the observation angle has been adjusted to $\varphi_{cc} = 65°$, thereby slightly extending the temperature range, in which precise temperature measurements are possible, but keeping the nonuniformities of the imaging still in reasonable limits.

For ensuring the suitability of the image recordings of the TLCs preliminary improvements were necessary, so that reliable temperature measurements are possible at all. In this regard, the heating plate in the background of the TLCs has turned as an important factor. The initial test runs have shown that the TLCs are difficult to distinguish from the surface of the heating plate made of aluminum, which is anodized to be persistent. In the postprocessing of the images, satisfying results could not be achieved, such that the heating plate has afterwards been covered with a thin matt black adhesive foil to enhance the contrast of the color of the TLCs, yielding a significant improvement. However, as the heating plate is close the measurement planes in the flat Rayleigh-Bénard cell and is also illuminated by the light scattered from the TLCs, the background is still not as dark as desired. For example, some larger agglomerated TLC particles, which may quickly settle down on the heating plate, and the pattern of dots printed on its surface for the dimensional calibration can clearly be seen in the raw images of the color camera, shown in figure 4.2a for the exemplary set temperature level $T_s = 19.7\,°C$ of the calibration measurement with the TLCs R20C20W. Thus, the raw images of the TLCs are further processed with regard to the determination of the temperature fields. In the following, the procedure of the postprocessing is explained at the example of the instantaneous image of the calibration measurements depicted in figure 4.2a, in which the TLCs are illuminated from the left side.

As already addressed in section 2.2, two different filters are applied to account for both very bright and dark pixels in the background of the TLCs. At first the minimum intensity of each pixel over the 100 images per temperature level is subtracted for each instant of time. This requires that the TLCs relocate over time, which is the case for the measurements in RBC, but during the calibration measurements with isothermal conditions in the cell no fluid motion is present a priori. Therefore, just before each recording of the TLCs at a certain temperature level of the calibration measurements, a slow fluid motion is induced by slight external pressure impulses through one of the two hoses connected to the cell. Due to the subtraction of the minimum of each pixel, the intensity of the less bright pixels in the background is further reduced to a very low level, such that the TLCs can be observed more clearly, which is obvious from figure 4.2b. The second filter simply uses a lower and an upper threshold to fully exclude very dark and

(a) TLCs at $T_\mathrm{s} = 19.7\,^\circ$C

(b) Subtracting the minimum over time for each pixel

(c) Using intensity thresholds and masking the dot pattern

(d) Averaging within interrogation windows

(e) Extracting the hue and averaging over time

(f) Sliding median filtering along the $y$-direction
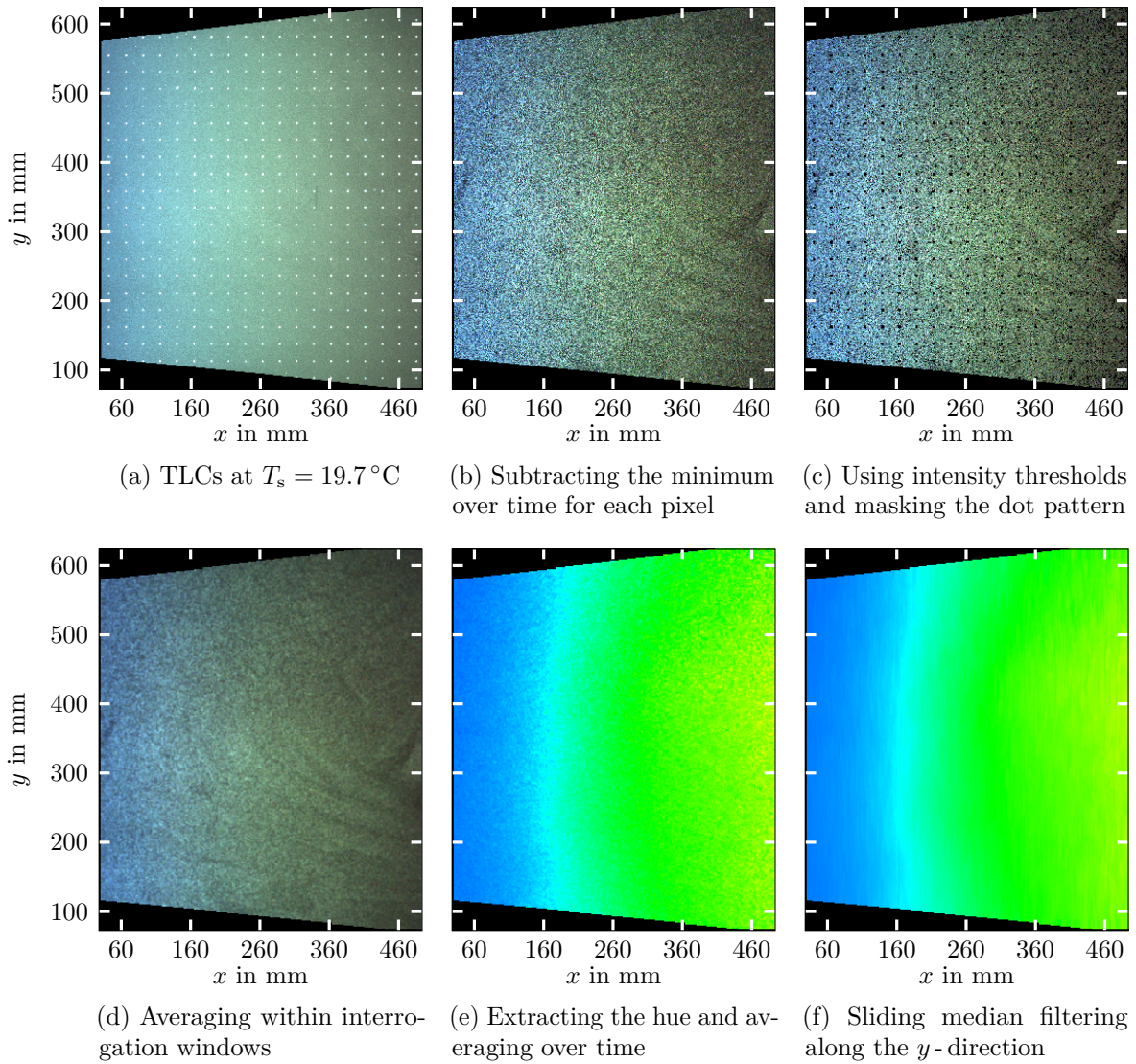
Figure 4.2: Processing of the images for the calibration of the temperature measurements at the example of an image of the TLCs R20C20W for the temperature level $T_\mathrm{s} = 19.7\,^\circ$C recorded in the top horizontal plane of the cell with the aspect ratio $\Gamma = 25$.

bright pixels from the evaluation, meaning that their intensity is not considered as a valid number anymore. Applying those filters, the color of the TLCs can be better evaluated, but the pattern of dots is still not fully removed from the image. Since the determination of exemplary temperature fields has demonstrated, that the footprint of the pattern can be seen, this cannot be neglected. Even though additional filtering approaches, for instance on the basis of the saturation $S$ of the $HSV$-colorspace, might be suited at this point to eliminate the pixels with a high content of white light resulting from the white dots, these are not applied. Considering that the points are small compared to the entire investigated area, a mask has been generated by searching locally for the highest intensities around the center of the dots in an image without TLCs. Thus, the dots are completely excluded as it can be seen in figure 4.2c.

In order to make the calibration measurements more robust, the color signal is not investigated for individual TLC particles, but for a group of particles in small interrogation windows. However, their size is chosen very small, such that the color trend across the image is negligible within the interrogation windows. Since the interrogation windows of

the temperature measurements in RBC will be of the same size as those of the calibration measurements, the smallest length scales of the structures occurring in the temperature fields in RBC, which are estimated based on previous test measurements, are also taken into account for the determination of the size of the interrogation windows. As the length scales of the structures in the temperature fields also depend on the thermal boundary conditions, two different sizes are used for the interrogation windows with a view to the measurements in RBC, which will be presented in section 5. Once the images are processed with interrogation windows having a size of $24 \times 24$ pixel for the measurements with the TLCs R20C20W at small Rayleigh numbers, while another processing is performed with the size of $16 \times 16$ pixel for the measurements with the TLCs R20C20W and R25C50W at larger Rayleigh numbers. Those sizes correspond to physical dimensions of about $4.8\,\text{mm} \times 4.8\,\text{mm}$ and $3.2\,\text{mm} \times 3.2\,\text{mm}$, respectively. Moreover, an overlap of 50% is used for the interrogation windows in each case. In the following the further steps of the image processing are demonstrated at the example of the interrogation windows with the size of $16 \times 16$ pixel, however, it should be mentioned that those steps are applied to the interrogation windows with the size of $24 \times 24$ pixel in the same manner.

Averaging the red, green and blue intensities of all the valid pixels within the interrogation windows, respectively, yields the color appearance depicted in figure 4.2d. However, this color appearance still includes the information of the saturation $S$ and the value $V$, which are not considered as trustworthy indicators for the temperature, as discussed in section 2.2. Therefore, only the hue $H$ is extracted from each interrogation window for the further evaluation based on the time-averaged hue. For the time-averaging all the values of the hue with $H > 0.8$ are reduced by one for the reasons described by means of figure 2.8 in section 2.4. The color shade corresponding to the local hue values, averaged over the 100 images recorded for the temperature level $T_\text{s} = 19.7\,°\text{C}$ of the calibration measurement, is shown in figure 4.2e. As it can be expected on the basis of the previous results in section 2, a distinctive color trend from the left to the right side becomes obvious despite the isothermal conditions, while the color does not considerably vary from the bottom to the top side of the image. Subsequently, the local time-averaged hue values of the calibration data $\langle H \rangle_t$ are processed as it has been demonstrated in figure 2.8 for the measurements in the small experimental setup. This includes that a spatial median filter is applied to the local time-averaged hue for each temperature level. The filter incorporates the 10 adjacent interrogation windows in positive and negative $y$-direction, which approximately corresponds to the physical dimensions of $\pm 16\,\text{mm}$. As the spatial median filter only operates along the $y$-direction, the distinctive physically relevant trend of the hue value in the $x$-direction is not smoothed out, but the filter is still capable of removing local outliers, as it can be seen in figure 4.2f. However, at this point it is emphasized, that the spatial median filter is only used to properly extract the color shade of the calibration measurements. For the following measurements in RBC this type of filter is not applied, so that the temperature field is not affected by a uniaxial operation. With regard to the measurements in convection it should also be noted, that the subtraction of the minimum intensity over time according to figure 4.2b is then performed over sliding time intervals. The width of the sliding intervals is adapted to the flow to cope with the varying displacements of the TLCs over time for the different Rayleigh numbers, such that comparable intensity levels are obtained.

The procedure of the postprocessing, which has just been explained, is applied in the same way to the images for all the temperature levels of each calibration measurement. For a better impression of the results, the color shade of the TLCs R20C20W from figure 4.2f at

the temperature level $T_\mathrm{s} = 19.70\,°\mathrm{C}$ is again depicted in figure 4.3c between the color shades at $T_\mathrm{s} = 19.05\,°\mathrm{C}$, $T_\mathrm{s} = 19.30\,°\mathrm{C}$, $T_\mathrm{s} = 20.20\,°\mathrm{C}$ and $T_\mathrm{s} = 21.35\,°\mathrm{C}$ in the figures 4.3a, 4.3b, 4.3d and 4.3e for comparison. This figure clearly demonstrates the variation of the color shade with temperature and within the field of view due to different observation angles. Besides the transition from the red to the blue color shade with increasing temperature it becomes in particular apparent that the blue color shade sets in much faster for larger observation angles towards the left side of the image.



(a) $T_\mathrm{s} = 19.05\,°\mathrm{C}$   (b) $T_\mathrm{s} = 19.30\,°\mathrm{C}$   (c) $T_\mathrm{s} = 19.70\,°\mathrm{C}$   (d) $T_\mathrm{s} = 20.20\,°\mathrm{C}$   (e) $T_\mathrm{s} = 21.35\,°\mathrm{C}$
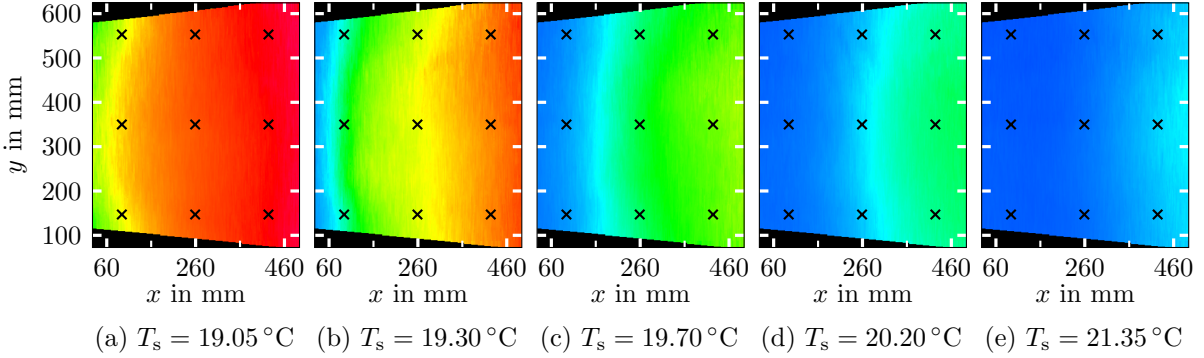
Figure 4.3: Color shade of the TLCs R20C20W for five different temperature levels of the calibration measurement in the top horizontal plane of the cell with the aspect ratio $\Gamma = 25$. The cross signs indicate the position of the interrogation windows, which have been chosen for the exemplary demonstration of the local calibration curves in figure 4.4.

A total of 15 temperature levels in the range $18.70\,°\mathrm{C} \leq T_\mathrm{s} \leq 22.30\,°\mathrm{C}$ and 22 temperature levels in the range $23.80\,°\mathrm{C} \leq T_\mathrm{s} \leq 32.90\,°\mathrm{C}$ have been adjusted during the calibration measurements with the TLCs R20C20W and R25C50W, respectively. On the basis of those measurements the calibration curves have been determined, yielding the local dependency of the time-averaged hue $\langle H \rangle_t$ on the temperature. In each case, only the calibration points from the minimum of the curve towards larger temperatures are considered, in order to obtain an unambiguous correlation between the hue and temperature. For this purpose any local minima in the calibration curves, which might rarely occur due to local imperfections of the seeding with TLCs, are also deleted and replaced by linear interpolation between the two valid neighboring points.

Some exemplary local calibration curves, which show the dependency of the time-averaged hue $\langle H \rangle_t$ on the temperature for the different positions within the field of view indicated in figure 4.3 with the cross signs, are depicted in figure 4.4 for both types of the TLCs. The general characteristics of the calibration curves, as already known from the investigations presented in section 2.2, are confirmed at this point. At the right side of the field of view, where the observation angle is smaller, the red color shade sets in at larger temperatures in comparison to the left side. Furthermore, it is pointed out again, that the color shade undergoes a fast transition for lower temperatures, especially for larger observation angles at the left side of the field of view, but varies more gradually for higher temperatures, when the TLCs slowly become more and more bluish.

Comparing the calibration curves for the TLCs R20C20W in the figure 4.4a with those for the TLCs R25C50W in the figure 4.4b it can be seen that the color changes on a similar way in qualitative terms. However, as it can be expected due to the significant difference of the nominal specification of the TLCs, the red start of the TLCs R25C50W is shifted by about $5\,\mathrm{K}$ towards larger temperatures. Moreover, using the TLCs R25C50W

the transition of the color shade passes over a larger temperature range, such that those are supposed to be useful for measurements over more extended temperature ranges at the expense of the measurement uncertainty. It is not shown in figure 4.4 to maintain the overview, but it should be noted for the sake of completeness, that the calibration curves are linearly extrapolated to cover the total range of the hue $-0.2 \leq H \leq 0.8$. Furthermore, as it has been demonstrated in figure 2.8 for the measurements in the small cylindrical cell, a piecewise cubic interpolation is applied to the total range of each calibration curve with a resolution of the hue of $\Delta H = 0.001$, yielding smooth curves with 1001 points, respectively. In this work those curves are the basis for the temperature measurements by means of linear interpolation of the local hue values between the densely arranged calibration points.
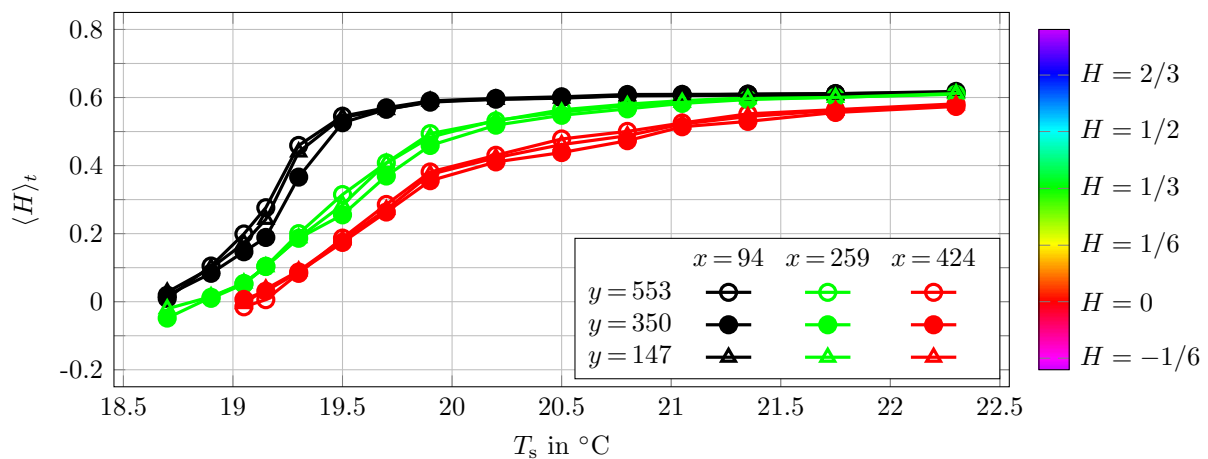


(a) Exemplary calibration curves for the TLCs R20C20W
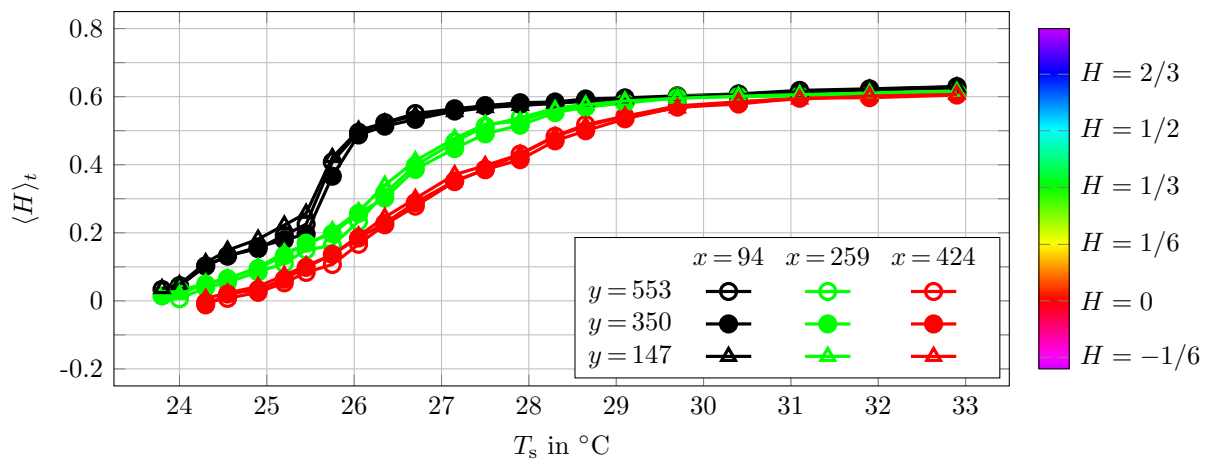


(b) Exemplary calibration curves for the TLCs R25C50W

Figure 4.4: Exemplary calibration curves showing the correlation between the color in terms of the hue $\langle H \rangle_t$ and the set temperature $T_s$ for the two types of TLCs at different positions within the field of view, which are given in millimeters and also marked with the cross signs in figure 4.3. The color bars on the right side of the figures illustrate the color corresponding to the hue values, respectively.

In order to estimate the measurement uncertainty, the same method as introduced in section 2.4 is applied. Thus, the temperature distributions of the calibration measurement are calculated via linear interpolation of the temporally resolved hue values in the local

calibration curves. Afterwards, for each temperature level of the calibration the calculated temperatures are compared with the respective target value given by the temperature measured with the probe inside the Rayleigh-Bénard cell during the calibration. For a better imagination, some exemplary results of the deviations are depicted in figure 4.5. The five different temperature levels correspond to those of figure 4.3, but now the results represent a single instant of time, respectively, whereas the color shades in figure 4.3 result from the time-averaging over the 100 images per temperature level and the additional sliding median filtering. For the determination of the deviations in figure 4.5 based on the instantaneous temperature fields, the only processing step applied to the temporally resolved hue values has been to reduce those by one if $H > 0.8$, as mentioned above. However, one additional condition is that the temperature in each interrogation window is calculated on the basis of a sufficient number of valid pixels. Therefore, the temperatures in the interrogation windows, which incorporate less than a quarter of pixels that are not eliminated by the mask for the dot pattern in the background according to figure 4.2c, are not considered.



(a) $T_s = 19.05\,°C$  (b) $T_s = 19.30\,°C$  (c) $T_s = 19.70\,°C$  (d) $T_s = 20.20\,°C$  (e) $T_s = 21.35\,°C$
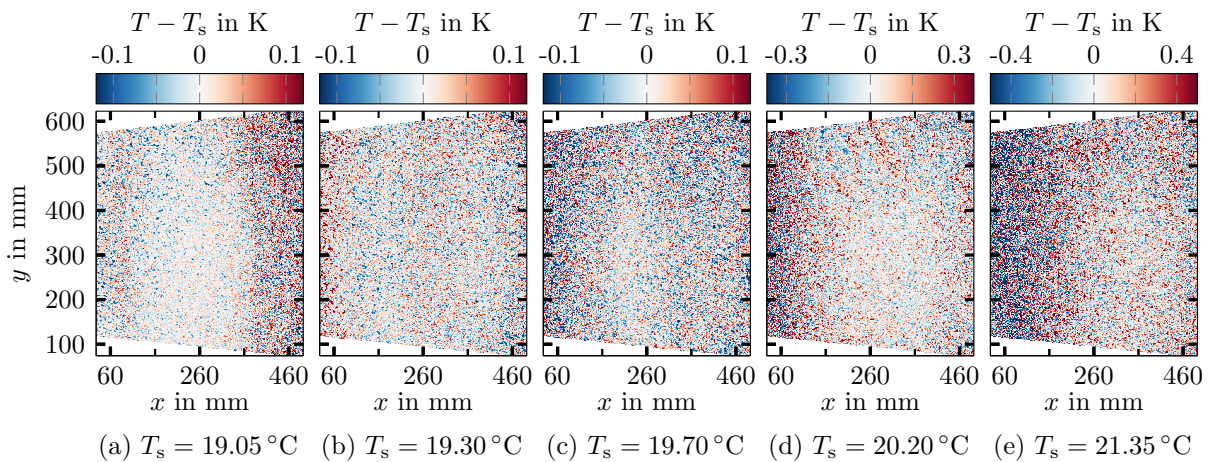
Figure 4.5: Deviation of exemplary instantaneous temperature fields from the respective target value of the calibration measurements.

The results in the figures 4.5a - 4.5c demonstrate that most of the calculated temperatures are close to the target values of $T_s = 19.05\,°C$, $T_s = 19.30\,°C$ and $T_s = 19.70\,°C$. Apart from a few outliers, especially for $T_s = 19.05\,°C$ at the right rim of the image where the TLCs have not yet reached the full brightness level, the maximum absolute deviations amount to about $0.1\,K$, but mostly the absolute deviations are smaller than $0.05\,K$. For the temperature levels of $T_s = 20.20\,°C$ and $T_s = 21.35\,°C$ the absolute deviations are larger, which is why the range of the colorbar at the top of the figures 4.5d and 4.5e has been adapted accordingly. In the main part of the field of view, the absolute deviations for $T_s = 20.20\,°C$ are in most cases still around $0.1\,K$, but when approaching the left rim of the image, the absolute deviations increase, as in this part of the field of view the color appearance of the TLCs does not considerably change with the temperature anymore. This can also be seen in figure 4.4a, in which the calibration curves taken from the left part of the image only have a small slope at $T_s = 20.20\,°C$. It is therefore self-evident, that the deviations further increase from the left side of the field of view when larger temperature levels are considered, as confirmed in figure 4.5e for $T_s = 21.35\,°C$.

Even though the results shown in figure 4.5 enable to roughly estimate the deviations occurring in the temperature measurement, those should be specified more precisely. Hence,

for each temperature level of the calibration measurements with the TLCs R20C20W and R25C50W the absolute deviations of all the 100 image recordings are considered to calculate the average, yielding the mean absolute deviation MAD. For the following investigations of the average, the most extreme outliers are removed by taking into account only those values, which in maximum differ by two times the standard deviation from the median of all the calculated temperatures per temperature level. This is also justified, as significant outliers, which might always appear in the calibration measurements due to a temporary lack of TLCs at a small spot in the field of view, would delusively downgrade the quality of the temperature measurements. With regard to the temperature measurements in RBC, this is not a crucial issue, because the uniformity of the seeding is strongly abetted by the three-dimensional flow. As already outlined in section 2.4.4, it can also be concluded from the results in figure 4.5, that the main local variation of the absolute deviations is apparent in direction of the distinctive color trend of the TLCs, which occurs along the $x$-axis in this case. In order to distinguish between the different deviations in this direction, the average of the absolute deviations is at first only taken along the $y$-axis.

The resulting mean absolute deviation in dependency of the position along the $x$-axis $\mathrm{MAD}_x$ is depicted in figure 4.6 for both types of TLCs. In the figure 4.6a it can be seen that the deviations towards larger observation angles at the left side start to increase strongly at around $T_\mathrm{s} = 21\,°\mathrm{C}$ when the TLCs R20C20W are used. For the lowest temperature level of $T_\mathrm{s} = 18.7\,°\mathrm{C}$, higher deviations become apparent at the right side, because the red start of the TLCs has not fully developed yet. Therefore, only temperatures in the range $18.9\,°\mathrm{C} \le T \le 20.8\,°\mathrm{C}$ should be taken into account for the measurements with the TLCs R20C20W under the present circumstances regarding the large range of observation angles in the camera's field of view, which is necessary to study a wide section with a practicable distance of the camera. Especially the temperatures in between $19.05\,°\mathrm{C} \le T \le 19.9\,°\mathrm{C}$ can be measured precisely, as the deviation does not considerably exceed $\mathrm{MAD}_x = 0.1\,\mathrm{K}$ over the whole field of view. For temperatures in the range $20.2\,°\mathrm{C} \le T \le 20.8\,°\mathrm{C}$, the maximum local deviation close to the left rim of the image amounts to about $\mathrm{MAD}_x = 0.33\,\mathrm{K}$, whereas the average deviation in this range is $\overline{\mathrm{MAD}} \approx 0.17\,\mathrm{K}$.

In the lower half of figure 4.6b a qualitatively similar behavior of the $\mathrm{MAD}_x$ can be seen for the TLCs R25C50W compared to the entire investigated temperature range of the other TLCs, meaning that higher deviations occur at the lowest temperature levels $T_\mathrm{s} = 23.8\,°\mathrm{C}$ and $T_\mathrm{s} = 24\,°\mathrm{C}$ on the right side just before the red start fully sets in, while the deviation first starts to significantly increase at $T_\mathrm{s} = 27.9\,°\mathrm{C}$ on the left side of the image due to the diminishing change of the color with temperature. The latter effect drastically downgrades the quality of the measurements when the temperature is further increased, which is clearly obvious from the large deviations in the upper half of the figure 4.6b for the TLCs R25C50W. In this respect it must be pointed out that for those TLCs the deviations are depicted over a much larger temperature range than for the TLCs R20C20W, as their nominal temperature range is also substantially wider, however, the temperature levels in the upper half of figure 4.6b are not considered for the measurements. Since the deviations in the temperature range starting from $T_\mathrm{s} = 24.3\,°\mathrm{C}$ up to $T_\mathrm{s} = 27.5\,°\mathrm{C}$ are the lowest with a maximum deviation of $\mathrm{MAD}_x \approx 0.34\,\mathrm{K}$ over the whole field of view, this range is most suited for the temperature measurements using the TLCs R25C50W. Hence, the temperatures occurring in the measurements with those TLCs should mainly fall into this range.

It becomes obvious, that the application of the TLCs R25C50W yields larger deviations

for the temperature measurement compared with that of the TLCs R20C20W in the measurement ranges specified above. The reason for the larger deviations is the more gradually passing change of color with temperature from the red towards the blue color shade of the TLCs R25C50W. However, this can be accepted, considering that the TLCs R25C50W are in this work used for measurements over more extended temperature ranges in RBC than the TLCs R20C20W and accordingly the main characteristics of the temperature fields can be studied despite the larger absolute errors. Moreover, it shall be brought into mind again, that all those deviations are obtained from the instantaneous temperature fields of the calibration measurements. Hence, with a view to the investigations based on time-averaged temperature fields, which will be of central importance in section 5, it is further expected that the non systematic errors level out to some extent.
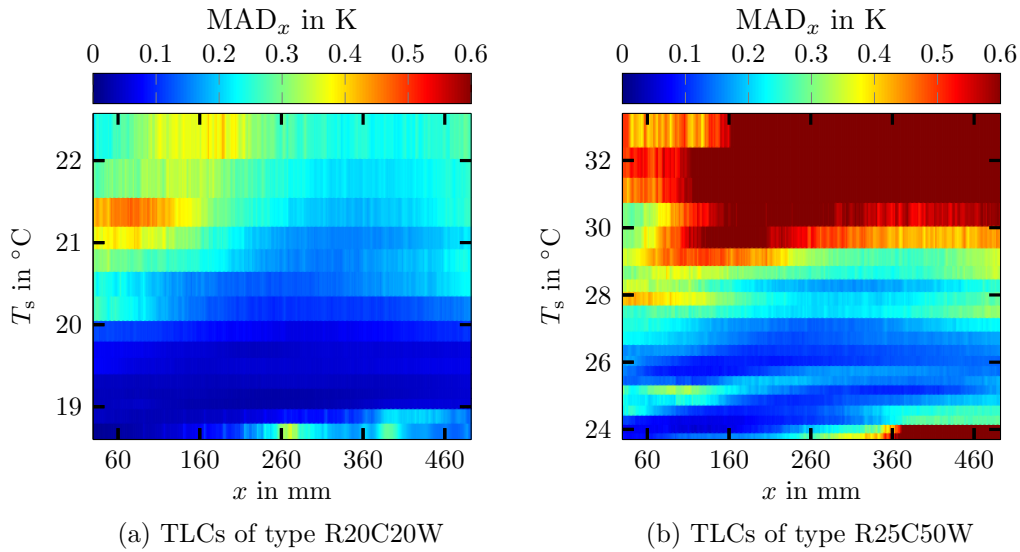


Figure 4.6: The local mean absolute deviation $\mathrm{MAD}_x$ of the temperature measurements in dependency of the $x$-coordinate and the set temperature level $T_\mathrm{s}$ for the two types of TLCs applied in this work.

The mean absolute deviation MAD, averaged over the whole field of view, can be seen in figure 4.7 in dependency of the temperature levels of the calibration measurements. The results for both TLCs, which can also be derived from figure 4.6, affirm the fact that the deviations are the lowest for those temperature ranges with the largest slopes of the local calibration curves. In particular from the minimum MAD at $T = 26.05\,°\mathrm{C}$ for the TLCs R25C50W it gets obvious that the smallest deviations are not necessarily at the lower end of the temperature range, as most of the local calibration curves may have the maximum slope at higher temperatures, which coincides with the curves shown in figure 4.4b. Looking at the mean absolute deviations for both TLCs, the suitability of the respective temperature measuring ranges $18.9\,°\mathrm{C} \leq T \leq 20.8\,°\mathrm{C}$ and $24.3\,°\mathrm{C} \leq T \leq 27.5\,°\mathrm{C}$ as specified above is confirmed. Over all the temperature levels in those ranges an average of $\overline{\mathrm{MAD}} \approx 0.09\,\mathrm{K}$ for the TLCs R20C20W and $\overline{\mathrm{MAD}} \approx 0.16\,\mathrm{K}$ for the TLCs R25C50W is obtained. Of course, the temperature measuring ranges are somehow limiting, but it should already be mentioned at this point, that larger temperature differences between the heating and cooling plate of the Rayleigh-Bénard cell up to nearly $\Delta T = 5\,\mathrm{K}$ are adjusted, because the temperatures occurring in the measurement planes do not reach the values of the boundaries, respectively.

As aforementioned, the processing of the calibration for the TLCs R20C20W is con-

ducted with the two different sizes of the interrogation windows of $16 \times 16$ pixel and $24 \times 24$ pixel for the temperature measurements in RBC at different Rayleigh numbers. All the results regarding the deviations of the measurements using the TLCs R20C20W discussed above have been obtained from the processing with the size of $16 \times 16$ pixel, but the results with $24 \times 24$ pixel have been investigated accurately as well. Qualitatively the results exhibit the same characteristics, such that those are not addressed in detail anymore. Nevertheless, it should be noted that the deviations for the temperature measurements become smaller using the interrogation windows with the size of $24 \times 24$ pixel, since the color shade is specified more reliably based on a larger number of TLC particles. Applying the interrogation window size of $24 \times 24$ pixel, the mean absolute deviation in the temperature range $18.9\,°C \leq T \leq 20.8\,°C$ amounts to about $\overline{\mathrm{MAD}} \approx 0.06\,\mathrm{K}$ and therefore decreases by approximately one third in comparison to the smaller interrogation windows with the size of $16 \times 16$ pixel.

Finally, it should be noted with regard to the measurements in RBC that filtering techniques are applied for the determination of the temperature fields to prevent and also eliminate outliers. First, any hue values, which are obtained from instantaneous images and are larger than the maximum hue of the corresponding local calibration curve, are sorted out, even though each curve is in the postprocessing linearly extrapolated to cover the total range of the hue $-0.2 \leq H \leq 0.8$. Due to the flatness of the calibration curves towards $H = 0.8$, the hue values in the extrapolated range are likely to result in erroneous temperatures and are therefore not considered. Second, if the mask for the dot pattern in the background according to figure 4.2c eliminates more than three quarters of the pixels of an interrogation window, the corresponding temperature is deleted, as the number of valid pixels is too small for a reliable evaluation, having in mind that also intensity thresholds are applied to filter very dark and very bright pixels, respectively. Third, all the local temperatures of the instantaneous temperature fields, which do not fall into the range between the temperatures adjusted at the heating and cooling plate, are deleted in each case, as those temperatures may in general not appear in RBC. In order to fill up the missing values and replace the outliers in the temperature fields, linear interpolation of the temperatures in the neighboring interrogation windows is used.


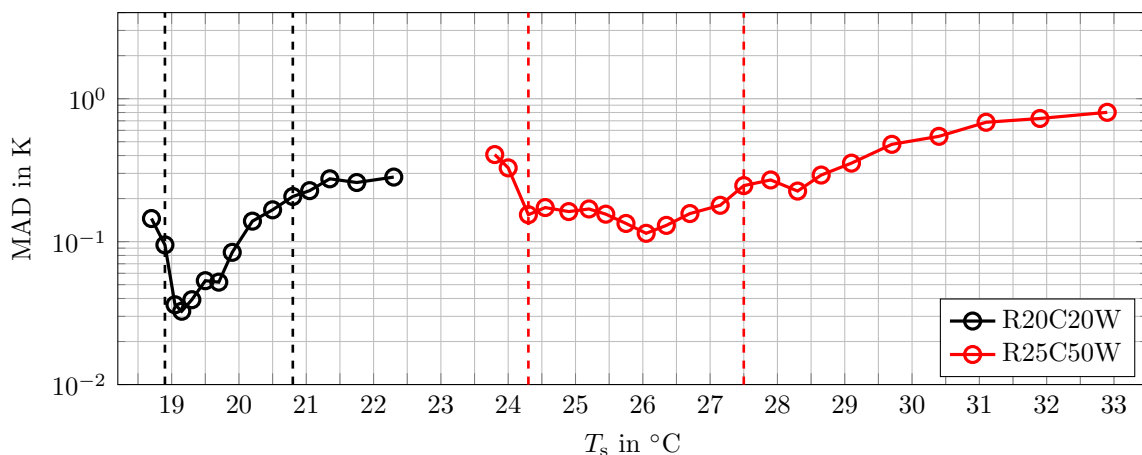
Figure 4.7: The mean absolute deviation MAD of the temperature measurements for the two types of TLCs applied in this work. In addition, the most suitable measuring ranges in consideration of the local deviations depicted in figure 4.6 are delineated with the dashed lines, respectively.

## 4.3    Velocity measuring technique

The velocity measurements are based on the principle, that the temporal displacement of seeding particles dispersed in a flow can be evaluated, thereby offering the possibility to determine local velocities not only at a single point, but simultaneously over a large region of interest. The measuring technique is well known as the Particle Image Velocimetry (PIV), since the motion of the particles is in general captured with cameras on images to study the flow. Due to the technical developments in the last decades, for instance regarding the camera technologies and especially the computing capacities, using PIV has established as one of the most commonly applied methods for the determination of velocity fields in fundamental and industrial research. Thus, the technique has been investigated and optimized thoroughly, which is broadly discussed in the literature. Considering the great variety of the work related to PIV, the content of single studies is not addressed in the following. However, it must be highlighted that details about the concept of PIV and the theoretical background are discussed in the references [153, 154], while a comprehensive overview of practical guidelines and the fundamental theoretical aspects are given in the reference [61].

Nowadays, digital cameras are applied for the recording of the images to enable the processing of the data as well as a fast and precise calculation of the velocity fields on a computer. Therefore, this technique is sometimes also referred to as the Digital Particle Image Velocimetry (DPIV) [153, 155] to distinguish from the early beginnings of PIV, where analog image recordings of tracer particles were used to investigate fluid motion. Compared to many other measuring techniques, that require to insert a probe into the flow, PIV is considered as non-intrusive, since the seeding particles finely dispersed in the flow do not yield local disturbances of the velocity field, which is advantageous in every respect. The components of a standard experimental setup for velocity measurements via PIV are depicted in figure 4.8. For this exemplary illustration a cylindrical Rayleigh-Bénard cell with equal diameter $d$ and height $h$, thus having an aspect ratio of $\Gamma = d/h = 1$, has been chosen as the artificial measurement domain. In a Rayleigh-Bénard cell with an aspect ratio of $\Gamma \approx 1$ usually a large-scale circulation roll spanning the vertical cross-section of the cell with varying orientation emerges, which is sketched in figure 4.8 and can be characterized with PIV measurements. On the basis of this synthesized example, the PIV technique is briefly explained in the following.

As the temporal displacement of the seeding particles, which should be uniformly distributed in the measurement domain, serves as an indicator of the local velocity, it is a fundamental requirement that the particles faithfully follow the flow. This is usually achieved by applying very small particles with a size of only a few microns to reduce effects due to inertia. Furthermore, the mass density of the particles and of the working fluid should match as closely as possible, to impede that the velocity measurements are affected by sedimentation of the particles. In order to cope with slight mismatches, a small size of the particles is advantageous as well, because the settling velocity increases with the diameter of the particles, which can be derived from the balance of the forces of gravity, buoyancy and viscous friction acting on a single particle [156]. However, since the determination of the velocity is based on the light scattered by the seeding particles upon illumination, it must be taken into account, that the scattering intensity decreases with the diameter of the particles and also depends on the ratio of the refractive indices of the particles to that of the fluid [61]. For this reason, a suitable compromise must be found, such that the motion of the particles properly represents the local velocities, but at the
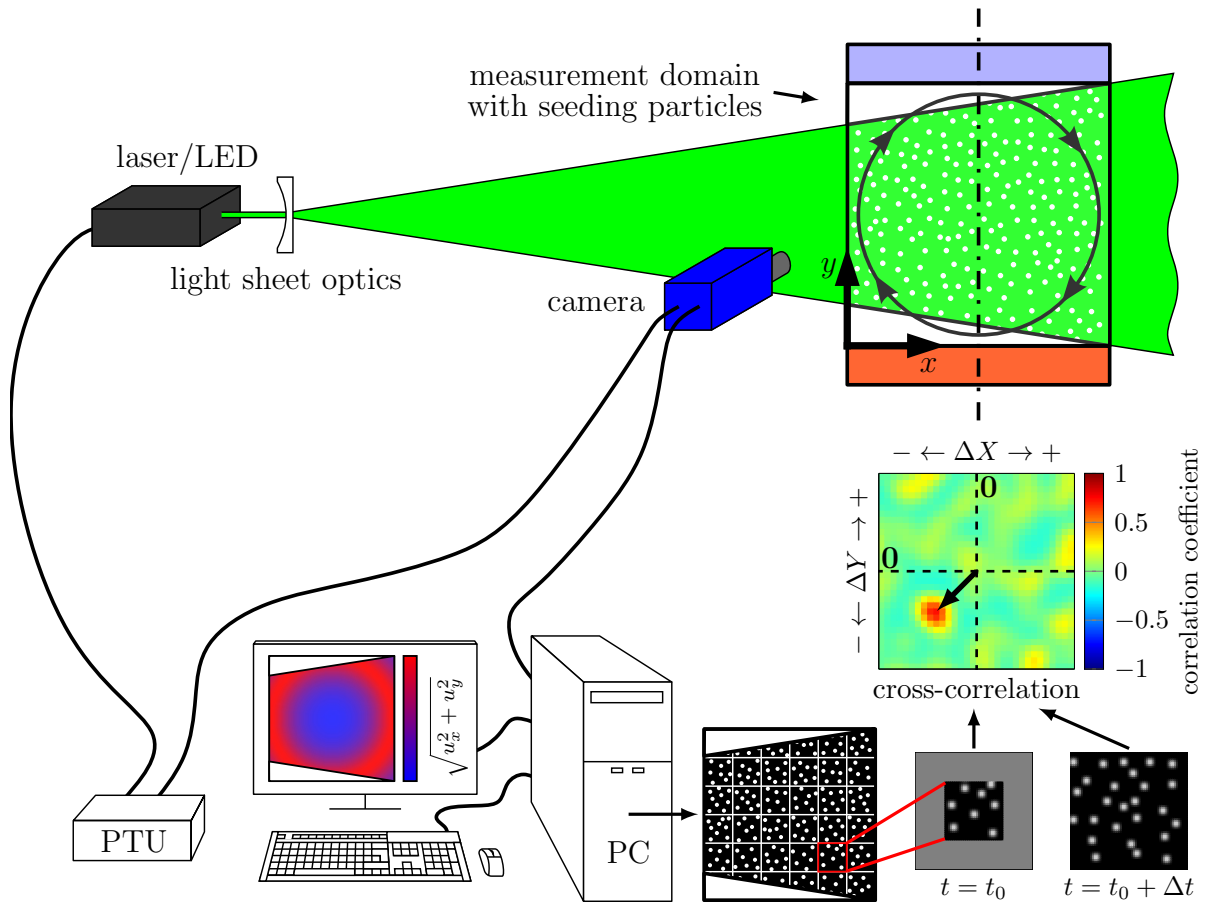
Figure 4.8: Typical components of a standard experimental setup for measuring velocity fields via Particle Image Velocimetry (PIV). The basic principle for the determination of the velocity based on cross-correlation of the particles' images is sketched at the bottom right.

same time the intensity of the scattered light is sufficient for a reliable investigation of the velocity.

Oftentimes the particles are illuminated with intense pulses of monochromatic laser light to obtain high-quality digital images, in which bright particles can clearly be distinguished from the background. For the investigation of the flow in a certain plane, the laser beam must be expanded in one dimension to shape a thin light sheet. For this, at least one cylindrical lens is inserted into the light path as indicated in figure 4.8. However, depending on the specific properties of the laser light and on the desired shape of the light sheet, a combination of different lenses must be used in many cases [61]. The light reflected by the particles upon illumination with two short light pulses of the laser is recorded with a camera on two separate images, which are stored on a computer for the determination of the velocity based on the displacement of the particles in the short time interval between the recording of the images. The illumination with the laser and the recording with the camera is triggered and synchronized with a programmable timing unit (PTU), such that one pulse of the laser is related to one image in each case. The duration of the light pulses and the recording time of the camera must be adapted in the way, that the particles appear bright enough for a reliable evaluation, but are also imaged sharply, meaning that no elongated streaks appear in the camera's image and the particles can be clearly distinguished. Furthermore, both the time delay between the pair of images as well as the

recording time must be adjusted to the velocities occurring in the flow. A large number of image pairs may be recorded successively over time with a certain frequency, such that the temporal evolution of the velocity can be studied on the basis of these image pairs.

In the standard evaluation of PIV measurements, the shift of the particles in a single pair of images is used to determine the velocity field. For this, the whole images are split into many small interrogation windows and the local velocities are calculated by means of cross-correlation of the local particle pattern of the first and second image, as sketched in the bottom right corner of figure 4.8. It should be noted that the depicted particle images are synthesized with uniform shape and gray level distribution against a dark background without image noise for a better visualization. The purpose of the cross-correlation is to find the shift of the particles in the first image, which yields the best match when overlapped with the particle pattern in the second image. In other words, the local particle pattern in the first image can be considered as the template, which is searched for in the second image. In this context it must be mentioned, that no information about possible accelerations or temporal changes of the direction of the fluid motion can be derived from a single image pair, so that a linear shift of the particles between the recording of the two images has to be assumed. Hence, the time delay should be chosen small enough to capture the dynamics of the flow. Moreover, since the direction of fluid motion may significantly vary in space, the size of the interrogation windows should be adjusted to the flow at hand, in order to resolve the smallest flow structures correctly.

Searching for the shift of the particles, which yields the best match when cross-correlating the interrogation windows of the two images, the local sections from the second image can be enlarged compared to the templates extracted from the first image [61]. On this way, it is taken into account that the particles may leave a single interrogation window in the time gap between the recording of the two images. This can be seen in figure 4.8, in which the area for the search of the template within the second image is increased by the half width of the template in each direction. Based on the cross-correlation the so-called correlation map can be composed, which quantifies the match of the particle pattern of the template within the frame of the second image for each shift of the template and is also shown in figure 4.8 on top of the particle images. In the correlation map a distinctive peak becomes apparent, corresponding to the shift of the particles, which results in the best match of the particle pattern. The shifts in the correlation map are usually given in units of pixels in both directions, indicated by $\Delta X$ and $\Delta Y$ at the axis of the figure. Therefore, this shift is used in combination with the dimensional calibration of the image, as explained in the section 4.1, and the time delay between the recording of the images to calculate the local velocity. This procedure is performed for each interrogation window separately, such that the velocity vectors can subsequently be assembled to end up with the entire velocity field.

From the mathematical point of view, the cross-correlation of two digital images is a simple operation, which only requires to sum up all the products of the overlapping pixel intensities of the two images for different shifts. However, in this form the degree of correlation of two images cannot be quickly estimated, since the values of the cross-correlation are arbitrary numbers, depending on the brightness of the particles. Accordingly, usually the normalized cross-correlation coefficient function is applied, to compensate the effect of the absolute intensity level of the images [61]. The resulting normalized cross-correlation coefficient $c_{\mathrm{II}}$, also referred to as the *sample Pearson's correlation coefficient* [157], is in the range $-1 \leq c_{\mathrm{II}} \leq 1$, thereby enabling to assess the degree of correlation already at the first glance. The function for the normalized cross-correlation coefficient

according to equation (4.1), adapted from reference [61], has also been applied in the present case to calculate the correlation map in figure 4.8. The numerator of this equation basically shows the general procedure of cross-correlation, meaning that an interrogation window of the first image, which is here assumed to be squared with a size of $M_U \times M_U$ pixels, is shifted with its pixel intensities $I$ to different positions $(X, Y)$ within the enlarged corresponding interrogation window of the second image with its pixel intensities $I'$ and the products of all the intensities of the overlapping pixels are summed up. However, with regard to the proper normalization the original intensities are reduced by the average values of the template $\mu_I$ and of the respective frame inside the second image $\mu_{I'}(X, Y)$, with the former being the same in each case, whereas the latter has to be computed for every shift separately. The terms in the denominator ensure, that the normalized cross-correlation coefficient may only vary in the range $c_{\mathrm{II}} \in [-1, 1]$.

$$c_{\mathrm{II}}(X, Y) = \frac{\sum_{m,n=0}^{M_U} \left[I(m, n) - \mu_I\right] \left[I'(m + X, n + Y) - \mu_{I'}(X, Y)\right]}{\sqrt{\sum_{m,n=0}^{M_U} \left[I(m, n) - \mu_I\right]^2} \sqrt{\sum_{m,n=0}^{M_U} \left[I'(m + X, n + Y) - \mu_{I'}(X, Y)\right]^2}} \quad (4.1)$$

Having briefly explained the main principle of PIV measurements, it is emphasized that the measuring technique has been and is permanently improved. Besides the technical developments of the hardware components, particularly the ongoing advancements in the processing of the data have contributed to the wide and successful use of PIV. Great attention has also been paid to the aspect, that the processing time can be significantly reduced, if the cross-correlation is not performed in the spatial domain, but in the frequency domain. Applying the Fast Fourier Transformation, the large number of multiplications and summations necessary in the spatial domain can be avoided, thereby decreasing the computational costs. However, when the correlation map is obtained on this way, some specific characteristics of Fourier analysis must be taken into account to impede that a bias error of the tracer particles' shift corresponding to the maximum correlation coefficient is introduced [61]. Nevertheless, due to the enormous advantage regarding the computing time, performing the cross-correlation in the frequency domain is a state-of-the art approach. In order to keep the focus, the special requirements for the evaluation in the frequency domain and other sophisticated techniques applied in the data processing, such as the methods commonly referred to as *window shifting*, *window deformation* and *grid refinement* for the iterative optimization of the results to give only a few keywords, are not discussed in the scope of this work. An overview of these advanced processing techniques is given in the reference [61]. Despite all those possibilities that may be used to considerably improve the results of PIV measurements in the postprocessing, adjusting the hardware settings appropriately and taking care for suitable image recordings of the tracer particles is most important to reliably measure velocity fields via PIV. For instance, if the time delay between the two recordings of an image pair is chosen much too large, such that the dynamics of the investigated flow cannot be captured, those data should not be considered for further analysis. In order to give another example, the seeding concentration can be addressed. If the latter is arbitrarily adjusted, reliable PIV measurements may not be possible at all. In this case, the most one can hope for is that the data can still be evaluated using alternative approaches, such as Laser Speckle Velocimetry (LSV) [158] for a very high seeding concentration or Particle Tracking Velocimetry (PTV) [159] for a very low seeding concentration.

So far, the established measuring technique PIV has been described with respect to the measurement of the velocity components along the plane illuminated with the light

sheet using a single camera. Hence, in a two-dimensional plane the two so-called in-plane components of the velocity are determined, which is why this type of measurement is also known as 2D2C-PIV. However, when using an additional camera in a stereoscopic arrangement, as obvious from figure 3.4 and 3.17b, the third component perpendicular to the plane, known as the out-of-plane component, can also be measured. Therefore, this is referred to as stereoscopic PIV or 2D3C-PIV [145]. When applying more than one camera and illuminating not only a single plane, but a measurement volume, all the three velocity components can be calculated in the three-dimensional space via tomographic PIV, which is then 3D3C-PIV [160]. Typically three or four cameras are used for this measuring technique, however, up to date even two cameras are sufficient in combination with refined reconstruction methods, proposed in the study [161].

If only one camera can be applied, for example due to a strongly limited optical access to the flow domain, but all the three components of the velocity in space are of interest, the Astigmatism Particle Tracking Velocimetry (APTV) [162] might be used. Compared to PIV, a considerably smaller amount of particles is in general inserted into the flow, when a particle tracking approach is applied to reconstruct the trajectories of single particles for the study the flow. In order to determine the position of the single particles in space and all the three velocity components, the APTV technique makes use of the fact, that a varying depth position yields different deformations of a particle's image, when a cylindrical lens is placed in the optical path between the camera and the measurement volume [162]. While the latter approach evaluates the degree of prolate and oblate elliptical deformations of the particles' images, arbitrary deformations may also be utilized to perform 3D3C-PIV with a single camera, using the General Defocusing Particle Tracking (GDPT) [163]. Usually expensive scientific cameras are applied in conjunction with all these measuring techniques, however, those may not always be available or applicable under certain environmental conditions. Therefore, in recent years the concept of using smartphones [164, 165] and low-cost cameras [166] for flow visualization and velocity measurements by means of PIV has been investigated and turned out to be suitable.

In the following some remarks are given on the application of PIV in the present work. At first it should be noted, that the TLCs dispersed in the Rayleigh-Bénard cell are not only used for the temperature measurements via their color appearance, but are the tracer particles for PIV as well. Hence, no additional particles are inserted into the fluid. As the TLCs require to be illuminated with white light, a laser emitting monochromatic light is not used for the illumination. Instead, the white light source presented in section 3.2 is applied to simultaneously determine the temperature and velocity fields, based on the color and the temporal displacement of the TLCs in the white light sheet. Furthermore, in this work all the three velocity components are measured in horizontal planes of the cell via the stereoscopic PIV. The main principle of this technique is, that for each of the two monochrome cameras a 2D2C velocity field is computed, which are subsequently used in combination to derive the 2D3C velocity field. Besides the information of the velocity component out of the measurement plane, the stereoscopic PIV also provides another significant advantage. Due to the stereoscopic imaging of the particles with two cameras, the so-called perspective error [145] is eliminated, meaning that the occurrence of out-of-plane velocity components does not yield a shift of the measured in-plane velocity components, contrary to the standard imaging with only one camera. Further details about the application of this measuring technique in conjunction with the stereoscopic self-calibration, outlined in section 4.1, are explained in the work [152]. As will be shown in section 5, especially the out-of-plane component of the velocity, i.e. the vertical velocity

component in the experimental setup at hand, is very important, because it can be utilized to determine the local heat flux in RBC, which is the main reason for applying the stereoscopic PIV in this case. It should also be noted, that the white light source is not triggered and synchronized for the measurements. The investigated Rayleigh-Bénard flow is slowly evolving, such that light pulses and short exposure times of the cameras are not necessary to sharply image the particles. Thus, during the recording of each image series of the particles, which covers five minutes in most cases for reasons discussed in the following section, the images are taken with a frequency of $f = 5\,\mathrm{Hz}$ and an exposure time of $t_{\mathrm{exp}} = 100\,\mathrm{ms}$, while the white light source is running continuously in this time interval. Using those settings has proven as a suitable choice to capture enough light for the images of the TLCs on the one hand and to obtain the images with an appropriate time delay on the other hand, such that both the temperature and the velocity can be evaluated reliably based on a sufficient color signal and an applicable displacement of the TLCs over time.

Finally, the processing of the images for the determination of the velocity fields should be shortly addressed. In the first step, the minimum intensity of each pixel of the monochrome images is subtracted over sliding time intervals of the recording, respectively, in order to remove disturbances resulting from the background and to improve the contrast of the particles. Subsequently, a standard cross-correlation is applied to the image pairs composed over the time interval of the recording. Since the adjustment of the different Rayleigh numbers in the experiment yields significantly varying velocities, the time gap between the two images of the image pair is adapted to the flow. As mentioned above, a fixed frequency of $f = 5\,\mathrm{Hz}$ is used for the recording, however, this still allows to choose the images used for the cross-correlation. For instance, the evaluation of the flow at low Rayleigh numbers requires not to use images, which directly follow one another, but with a certain time delay in between, such that the velocity can be determined based on a sufficient shift of the TLCs. Furthermore, the size of the interrogation windows for the velocity field is adapted to that of the temperature fields. On this way, each interrogation window incorporates a suitable amount of particles for a reliable evaluation of the particle displacement, but is also small enough to capture the spatial gradients of the velocity. For the optimization of the results, a multi-pass approach with decreasing size of the interrogation windows is utilized, which is advantageous to compute the local velocities most properly. Between each of the passes a refined filtering technique based on *universal outlier detection* [167] is applied to eliminate spurious vectors, while after the final pass the vectors with a significant deviation from the median of the neighboring vectors are rejected in addition. In both cases the spurious vectors might be replaced by a more suitable one corresponding to another peak of the correlation map. If no fitting vector is determined from the correlation map for a specific interrogation window, the vectors of the neighboring windows are used for interpolation. For the entire procedure of the processing the operations implemented in DaVis 8.4 have been used. Moreover, in each case the general recommendations for PIV measurements, as for example given in reference [61], have been considered to figure out appropriate settings for the evaluation of the data.

# Measurements in large aspect ratio Rayleigh-Bénard convection

The measuring techniques described in the previous chapter will now be applied to determine the temperature and velocity fields in large aspect ratio Rayleigh-Bénard convection. After explaining the settings and the procedure of the measurements in section 5.1, the analysis of the temperature and velocity fields, especially with regard to the turbulent superstructures, will be presented in section 5.2.

## 5.1 Settings and procedure of the measurements

As aforementioned, the measurements in the Rayleigh-Bénard cell with the aspect ratio $\Gamma = 25$ have been performed in two different horizontal planes. Besides the horizontal mid plane, another plane close to the top of the cell has been chosen for the measurements, in order to investigate the distribution of the temperature and velocity more deeply. The non-dimensionalized vertical positions of the measurement planes $\tilde{z} = z/h$, which are in the following always denoted as the mid and top plane, are listed in table 5.1. The position of the top plane has been adjusted such that a significant change of the characteristics of the flow can be observed in comparison to the mid plane, however, without extending far into the thermal boundary layer. On this way, the range of the occurring temperatures can be better estimated a priori, because those fluctuate around the average temperature of the heating and cooling plate, when the measurement plane is outside the thermal boundary layer. Since the thickness of the thermal boundary layer in RBC decreases with increasing Rayleigh number, as illustrated in figure 1.2 in the introduction, the vertical position of the top measurement plane has been determined on the basis of the lower limit of the Rayleigh numbers adjustable in the experiments, which is $\mathrm{Ra} \approx 10^5$ for the cell with $\Gamma = 25$. Using water as the working fluid, considerably smaller Rayleigh numbers cannot be achieved in this cell, taking into account that arbitrary small temperature differences between the heating and cooling plate are not applicable from the experimental point of view. The thickness of the thermal boundary layer for $\mathrm{Ra} = 10^5$ can then be estimated by means of the Nusselt number via $\delta_T = h/(2\,\mathrm{Nu})$ [22]. For the Prandtl number $\mathrm{Pr} = 7$, which roughly corresponds to that of water in the temperature range of the experiments, the Nusselt number is around $\mathrm{Nu} = 4.1$ according to the results of the numerical simulations shown in the study [57], yielding $\delta_T \approx 0.12$. Thus, for the Rayleigh number $\mathrm{Ra} = 10^5$ the lower end of the thermal boundary layer at the cooling plate is expected to be at $\tilde{z} = 1 - \delta_T = 0.88$. For the measurements in the top plane the light sheet has been positioned such that its center is about $4\,\mathrm{mm}$ below the cooling plate, resulting in $\tilde{z} \approx 0.86$, as given in table 5.1.

The light sheet is therefore completely outside the thermal boundary layer in most cases or may just slightly extend into it, depending on the Rayleigh number.

The Rayleigh numbers, that have been adjusted for the measurements in the two horizontal planes, can be seen in table 5.1 with the corresponding temperatures of the heating and cooling plate. Those represent the average of the temperatures measured every $10\,\mathrm{s}$ with the sensor elements at both plates during the whole measurements, respectively. However, as explained at the end of section 3.1, not each of the measured values is taken into account for the averaging to cope with the influence of the thermal plumes. The Rayleigh numbers have been varied over one order of magnitude and approximately range in between $2 \times 10^5 \leq \mathrm{Ra} \leq 2 \times 10^6$. This range is on the one hand appropriate to analyze the effect of the Rayleigh number on the turbulent superstructures and is on the other hand also a suitable choice to perform accurate measurements of both the velocity and temperature fields.

| Label | TLCs | $z/h$ | $T_\mathrm{h}$ | $T_\mathrm{c}$ | Ra | $\tilde{x}_\mathrm{fov} \times \tilde{y}_\mathrm{fov}$ | $t_\mathrm{f}$ | $\tilde{t}_\mathrm{total}$ |
|---|---|---|---|---|---|---|---|---|
| $2\mathrm{e}5_\mathrm{m}$ | R20C20W | 0.50 | $19.78\,°\mathrm{C}$ | $19.08\,°\mathrm{C}$ | $2.07 \times 10^5$ | $16.1 \times 16.7$ | $4.51\,\mathrm{s}$ | $5.39 \times 10^3$ |
| $2\mathrm{e}5_\mathrm{t}$ | R20C20W | 0.86 | $19.79\,°\mathrm{C}$ | $19.09\,°\mathrm{C}$ | $2.07 \times 10^5$ | $15.9 \times 16.6$ | $4.51\,\mathrm{s}$ | $5.39 \times 10^3$ |
| $4\mathrm{e}5_\mathrm{m}$ | R20C20W | 0.50 | $20.22\,°\mathrm{C}$ | $18.76\,°\mathrm{C}$ | $4.34 \times 10^5$ | $16.1 \times 16.7$ | $3.12\,\mathrm{s}$ | $7.79 \times 10^3$ |
| $4\mathrm{e}5_\mathrm{t}$ | R20C20W | 0.86 | $20.17\,°\mathrm{C}$ | $18.68\,°\mathrm{C}$ | $4.40 \times 10^5$ | $15.9 \times 16.6$ | $3.09\,\mathrm{s}$ | $7.86 \times 10^3$ |
| $7\mathrm{e}5_\mathrm{m}$ | R20C20W | 0.50 | $20.87\,°\mathrm{C}$ | $18.43\,°\mathrm{C}$ | $7.34 \times 10^5$ | $16.2 \times 16.6$ | $2.40\,\mathrm{s}$ | $1.01 \times 10^4$ |
| $7\mathrm{e}5_\mathrm{t}$ | R20C20W | 0.86 | $20.85\,°\mathrm{C}$ | $18.41\,°\mathrm{C}$ | $7.33 \times 10^5$ | $16.0 \times 16.6$ | $2.40\,\mathrm{s}$ | $1.01 \times 10^4$ |
| $2\mathrm{e}6_\mathrm{m}$ | R25C50W | 0.50 | $28.49\,°\mathrm{C}$ | $23.95\,°\mathrm{C}$ | $2.06 \times 10^6$ | $16.2 \times 16.6$ | $1.53\,\mathrm{s}$ | $1.59 \times 10^4$ |
| $2\mathrm{e}6_\mathrm{t}$ | R25C50W | 0.86 | $28.50\,°\mathrm{C}$ | $23.94\,°\mathrm{C}$ | $2.07 \times 10^6$ | $16.0 \times 16.6$ | $1.53\,\mathrm{s}$ | $1.59 \times 10^4$ |

Table 5.1: Settings for the measurements in the two planes of the Rayleigh-Bénard cell with the aspect ratio $\Gamma = 25$. In the first column a label is specified for each of the measurements, which is also used in the tables 5.2, 5.3 and 5.4. Starting from the second column, the table lists the specifications of the applied TLCs, the non-dimensionalized position of the measurement plane $\tilde{z} = z/h$, the temperature of the heating plate $T_\mathrm{h}$ and cooling plate $T_\mathrm{c}$, the resulting Rayleigh number Ra, the non-dimensionalized size of the field of view $\tilde{x}_\mathrm{fov} \times \tilde{y}_\mathrm{fov} = x_\mathrm{fov}/h \times y_\mathrm{fov}/h$, the free-fall time $t_\mathrm{f}$ and the non-dimensionalized total measuring time $\tilde{t}_\mathrm{total} = t_\mathrm{total}/t_\mathrm{f}$. In the discussion of the results the Rayleigh numbers of the measurements are always given as the rounded values $\mathrm{Ra} = 2 \times 10^5$, $\mathrm{Ra} = 4 \times 10^5$, $\mathrm{Ra} = 7 \times 10^5$ and $\mathrm{Ra} = 2 \times 10^6$.

Regarding the temperature measurements by means of the color shade of the TLCs it should be brought into mind once more, that the measuring range has to match the color characteristics of the TLCs. Accordingly, the temperature of the heating and cooling plate has been adapted carefully for all the measurements. Nevertheless, for some of the measurements it has first turned out in the evaluation, that the measurement should be repeated with slightly shifted temperatures of both the heating and cooling plate, in order to improve the results for a desired temperature difference. Furthermore, as the setup has been disassembled, cleaned and reassembled between each of the measurements, which is very important to ensure optimum conditions for the image recording without deposited TLC particles in the background, obtaining all the experimental results has

been an extensive work. The physical dimensions of the field of view of the cameras, which are listed in table 5.1 in units of the cell's height, are similar in each case, because the distance between the cameras and the two measurement planes does not significantly vary in the present case. Since the fields of view of the three cameras do not completely overlap, the size refers to the intersection area observed by all the three cameras.

A strict procedure was applied for all the measurements. After adjusting the temperatures of the heating and cooling plate at the thermostatic baths, at least 2 h was waited, so that the temperatures of the plates and the sidewalls can reach the stationary state in that period of time. Subsequently, the seeding was inserted into the working fluid through the hose connected to the cell. The working fluid was then thoroughly stirred by slight pressure impulses through the hose until the seeding was uniformly distributed in the cell. However, due to those external pressure impulses, the flow in the cell was strongly disturbed in each case. Hence, after the initial disturbance, another 45 min was waited, respectively, such that its effect decays prior to the actual measurements. The development of the flow structures after the initial disturbance has also been recorded in each case and will be shown at the example of one measurement in section 5.2.5. Immediately after those 45 min many image series with a duration of 5 min have been recorded with a frequency of $f = 5\,$Hz every 20 min. Therefore, each of the image series consists of 1500 images. In the time gap of 15 min between the end of the recording of one image series and the start of the successive one, the light sheet was always switched off and the sidewall, at which the light sheet enters the cell during the measurements, was temporarily covered with a thick insulation aiming for the adiabatic boundary condition. The other three sidewalls were enclosed by insulation all the time.

The measurements have been performed over several hours, respectively. However, especially for the measurements with the TLCs R25C50W a decrease of the seeding concentration could be observed over time, which limits the total measuring time. A possible explanation is that those TLCs are applied at higher temperatures, meaning that the mass density of the water is smaller for those measurements, which might yield a slightly larger mismatch between the mass density of the TLCs and the water. Starting from about 5 h - 6 h after the initial seeding process, accurate temperature measurements become more and more difficult with the TLCs R25C50W, as the measurement plane appears much darker and the background is more present. On the contrary, the measurements with the TLCs R20C20W could be performed over more extended time spans after the seeding process, however, for consistency the same number of image series has been considered in the evaluation of the data. In each case, a total of 19 image series with the duration of 5 min, subsequent to the first image recording of the initial development of the flow over 45 min, is taken into account, yielding a time span of 6 h 50 min between the very first and very last image. This total measuring time $t_{\text{total}}$ is given in table 5.1 in units of the free-fall time $t_{\text{f}} = \sqrt{h/(\alpha\,g\,\Delta T)}$, which is used for the non-dimensionalization of the time-scales in the following and is also listed in the table.

With regard to the sedimentation of the TLCs it should be pointed out, that its effect on the velocity measurements is negligible. Considering that the typical velocities in the experiments with the TLCs R25C50W range from 0.1 mm/s to 1 mm/s, it can be estimated that those exceed the velocity of the sedimentation by a factor between $10^2$ and $10^3$. Even though smaller velocities occur in the experiments with the TLCs R20C20W, especially for the Rayleigh number $\text{Ra} = 2 \times 10^5$ with the maximum velocities in the order of 0.1 mm/s, the effect of the sedimentation is still not relevant, because these TLCs almost fulfill the condition of neutral buoyancy in the given temperature range.

## 5.2    Analysis of the measurements

The heat transport in RBC is in general strongly coupled with the dynamics and the structures occurring in the flow. In large aspect ratio RBC especially the turbulent superstructures may strongly contribute to the heat transport from the bottom to the top of the cell, depending on the Rayleigh number [57]. Therefore, these structures deserve closer attention. In this section, different aspects regarding the turbulent superstructures will be studied on the basis of the simultaneous measurements of the temperature and velocity fields. With the measuring techniques outlined in chapter 4, the temperature and velocity fields have been determined with a spatial resolution, which allows to resolve the fine structures in both fields. The size of the interrogation windows is given in table 5.2 for each of the measurements. Furthermore, the resulting number of grid points is listed, too.

In the explanation of the settings for the calculation of the velocity at the end of section 4.3 it has already been mentioned, that the images have been recorded with a constant frequency of $f = 5\,\mathrm{Hz}$, but the images directly following one another have not been taken for the cross-correlation in most cases. It has turned out in the evaluation, that a time delay of $\Delta t_{\mathrm{PIV}} = 1/f = 0.2\,\mathrm{s}$ between the successive images does not always yield a sufficient shift of the particles for a reliable evaluation of the velocity. Hence, the time delay between the images used for the cross-correlation has been adapted to the flow, respectively. The time delay has been chosen according to table 5.2, which shows that in particular for the smaller Rayleigh numbers a larger time delay is necessary as a result of the lower flow velocities. Aiming for an appropriate shift of the particles between the two images of an image pair it has been taken into account as a rule of thumb, that the largest displacements of the particles should on the one hand not exceed one fourth of the size of the interrogation windows [168]. On the other hand, the relative uncertainty of PIV measurements must also be considered. For carefully performed PIV measurements it is commonly assumed, that the uncertainty in the determination of the particle displacement is in the order of $\sigma_{|\vec{X}|} = 0.1\,\mathrm{pixel}$. Thus, the actual particle displacement should substantially exceed this level of the uncertainty, such that the largest time delay between the images has been applied, which roughly complies with the just described, so-called *one-quarter-rule* [169]. The ratio between the average of the absolute particle displacement $\langle |\vec{X}| \rangle$ and the mentioned level of the uncertainty is listed in table 5.2 for all the measurements. From those ratios it becomes obvious, that the shifts are in average much smaller than the limit given by the *one-quarter-rule*, but are also significantly larger than the level of the uncertainty, thereby allowing for reliable velocity measurements.

Regarding the further investigations it should also be noted that for the evaluation of the data not each of the cameras' images has been processed to keep the computing time in acceptable limits. Starting from the first image of each image series, the temperature and velocity fields have been computed for each fifth image, yielding one temperature and velocity field per second due to the imaging frequency of $f = 5\,\mathrm{Hz}$. With this increment in the evaluation, the temperature and velocity fields are usually determined up to the 1496th image of the entire 1500 images per image series, such that the last fields are available for the time instant $t = 299\,\mathrm{s}$ after the recording of the first image of the respective image series at $t = 0\,\mathrm{s}$. However, for the measurements at the Rayleigh number $\mathrm{Ra} = 2 \times 10^5$, which requires a time delay of $\Delta t_{\mathrm{PIV}} = 1\,\mathrm{s}$ between the successive images for the determination of the velocity field via cross-correlation, the processing cannot be performed anymore for the 1496th image. Hence, for this Rayleigh number the last image considered for the evaluation of both the temperature and the velocity field is the 1491th image, corresponding to the time instant $t = 298\,\mathrm{s}$ after the recording of the first image.

| Label | $M_T/M_U$ | $s_T/s_U$ | $N_T/N_U$ (50% OL) | $t_{\mathrm{avg}}$ | $\Delta t_{\mathrm{PIV}}$ | $\langle|\vec{X}|\rangle/\sigma_{|\vec{X}|}$ |
|-------|-----------|-----------|--------------------|--------------------|---------------------------|----------------------------------------------|
| $2e5_m$ | 24 pixel | 4.8 mm | $191 \times 198$ | 298 s | 1 s | 20.4 |
| $2e5_t$ | 24 pixel | 4.8 mm | $188 \times 197$ | 298 s | 1 s | 24.4 |
| $4e5_m$ | 24 pixel | 4.8 mm | $191 \times 198$ | 205 s | 0.6 s | 18.7 |
| $4e5_t$ | 24 pixel | 4.8 mm | $188 \times 197$ | 206 s | 0.6 s | 23.4 |
| $7e5_m$ | 16 pixel | 3.2 mm | $287 \times 295$ | 159 s | 0.4 s | 17.0 |
| $7e5_t$ | 16 pixel | 3.2 mm | $283 \times 294$ | 159 s | 0.4 s | 20.3 |
| $2e6_m$ | 16 pixel | 3.2 mm | $287 \times 295$ | 102 s | 0.2 s | 14.6 |
| $2e6_t$ | 16 pixel | 3.2 mm | $283 \times 294$ | 102 s | 0.2 s | 16.4 |

Table 5.2: Settings for the evaluation of the temperature and velocity fields. For the measurements, which are labeled according to the first column of table 5.1, the number of pixels in each direction of the squared interrogation windows for the temperature field $M_T$ and the velocity field $M_U$, the corresponding size in physical units $s_T$ and $s_U$, the number of grid points of the temperature and velocity field $N_T$ and $N_U$ in their intersection area, the averaging time for the turbulent superstructures $t_{\mathrm{avg}}$ and the time delay between the images used for the cross-correlation of the PIV measurements $\Delta t_{\mathrm{PIV}}$ are listed. In the brackets of the fourth column the overlap OL of the interrogation windows, which is applied for both fields, is denoted. Furthermore, the column at the right end shows the ratio between the average of the absolute particle displacement $\langle|\vec{X}|\rangle$ and the typically for PIV measurements assumed level of the uncertainty $\sigma_{|\vec{X}|} = 0.1$ pixel.

## 5.2.1 Exposure of the turbulent superstructures

The turbulent superstructures in large aspect ratio RBC can be considered as large-scale structures, which dominate the flow on extended length scales, but when investigating a single instant of time, the Rayleigh-Bénard flow also exhibits many small structures superimposed on the turbulent superstructures. The measurements have shown, that the small-scale structures can particularly be observed in the top plane. Especially in the images recorded with the color camera the small-scale structures can be seen due to the color contrast of the TLCs. For a better impression the color appearance of the TLCs obtained from an exemplary measurement in the top plane at the Rayleigh number $\mathrm{Ra} = 2 \times 10^5$ is depicted in figure 5.1a. It should be noted, that this image has already been processed as it has been demonstrated by means of the figures 4.2a - 4.2d in section 4.2. Thus, single TLC particles cannot be seen, since the average of their color is taken within the interrogation windows. In order to clearly visualize the small-scale structures, the pure color shade in terms of the hue value is shown in figure 5.1b. In the corresponding instantaneous temperature field in figure 5.1c, which is determined from the field of the hue via the local calibration curves, the structures can directly be compared. Strong variations of the temperature on small length scales become apparent in the temperature field, caused by many small thermal plumes rising up from the bottom plate or dropping down from the top plate. Furthermore, some larger areas with similar temperatures can be seen, which already indicates the existence of turbulent superstructures.

In order to fully uncover the turbulent superstructures, the small-scale fluctuations can
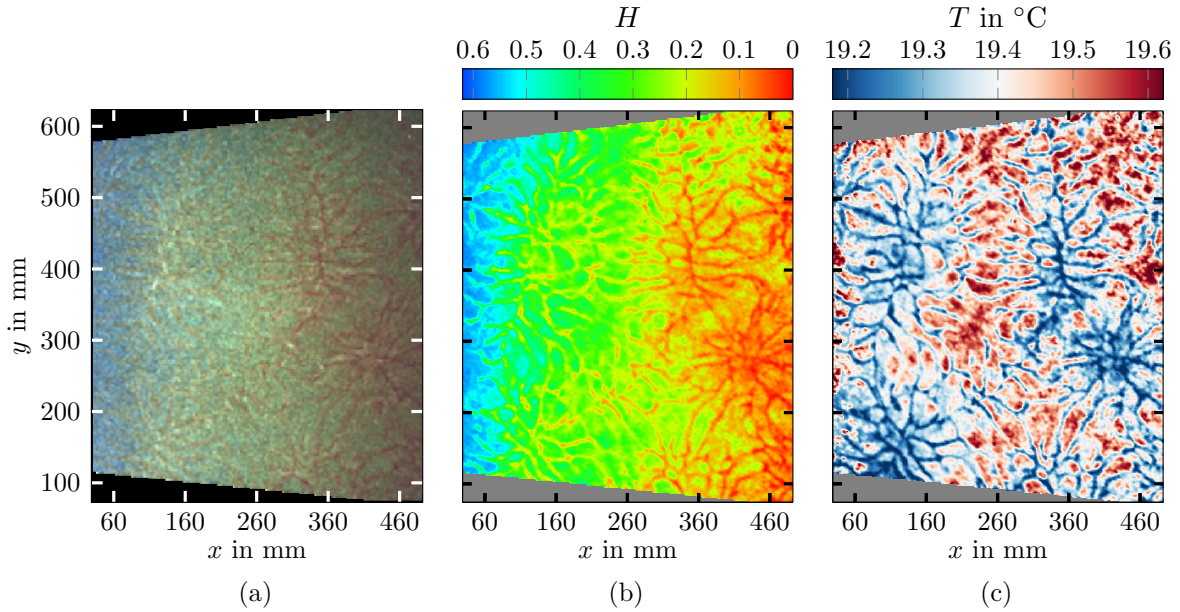
Figure 5.1: Illustration of the color appearance of the TLCs R20C20W (a), the hue field (b) and the corresponding temperature field (c) in RBC for a single instant of time at the example of the measurement in the top plane for the Rayleigh number $\mathrm{Ra} = 2 \times 10^5$.

be removed by time-averaging. As suggested in the study [11], the averaging time should fall into a certain range. Following these suggestions, the small-scale fluctuations are eliminated, but the range of time-averaging is still small enough such that the turbulent superstructures are not smoothed out or even completely removed, considering that those also slowly rearrange over time. However, the limits for the suggested range of the time-averaging can only be used for a very rough estimation, as the lower and upper bound, given by the free-fall time and a diffusive time scale according to the condition (1.16), may significantly differ from each other. As shown in table 5.1, the free-fall time is in the order of seconds, while the diffusive time scale amounts to about $t_\mathrm{d} \approx 1.5\,\mathrm{h}$ for all the measurements. On the basis of these very rough limits and of the results obtained from previous measurements, which have for instance been presented in the study [24], the recording time for each of the single image series has been set to $t_\mathrm{rec} = 5\,\mathrm{min}$, respectively, as it has turned out to be sufficiently long to clearly uncover the turbulent superstructures by time-averaging. This can be seen in figure 5.2, which again shows the instantaneous temperature field at the left side, while the averaging interval increases towards the right side up to the whole time interval considered in the evaluation of this measurement set. By the time-averaging over the successively increasing time intervals, which are given in the captions of the figures 5.2b - 5.2d, the turbulent superstructures are more and more revealed. Due to the relocation of the small-scale structures, those are almost completely removed in the temperature field in figure 5.2d.

Even though the turbulent superstructures are already clearly displayed in the temperature field, the velocity field is also of great importance, since the vertical velocity component $u_z$ is later applied in combination with the temperature field to estimate the local heat flux from the bottom to the top of the Rayleigh-Bénard cell. Therefore, now some fields of the vertical velocity component are shown at the example of the results from the measurement in the top plane at the Rayleigh number $\mathrm{Ra} = 2 \times 10^5$. The same measurement set as for the demonstration of the effect of the time-averaging in figure 5.2
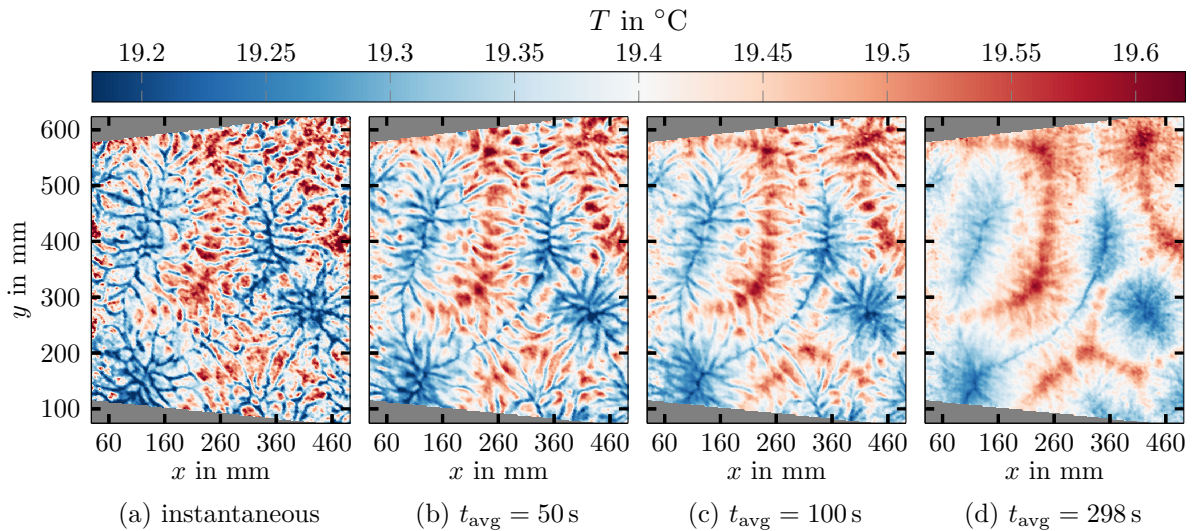
$T$ in °C

Figure 5.2: Successive increase of the averaging time for the exposure of the turbulent super-structures in the temperature field at the example of the measurement in the top plane for the Rayleigh number $\mathrm{Ra} = 2 \times 10^5$ with the heating and cooling plate temperature of $T_\mathrm{h} = 19.79\,°\mathrm{C}$ and $T_\mathrm{c} = 19.09\,°\mathrm{C}$.

is used again. In figure 5.3 the instantaneous and time-averaged fields of the temperature and of the vertical velocity can directly be compared. In this case, the temperature and velocity are still given in their physical units to get a better impression of the measuring ranges of both quantities. Furthermore, the whole horizontal cross-section of the cell is illustrated, so that the measurement area for both fields can be seen. The trapezoidal contour of the temperature field is a result of the inclined arrangement of the color camera, while the contour of the velocity field delineates the intersection of the field of view of the two monochrome cameras. It should also be mentioned, that the transition from blue over white to red in the visualization of the fields is from here on adapted, such that a white area always indicates the average between the heating and cooling plate temperature as well as the absence of vertical fluid motion.

Having a close look to the figures 5.3a and 5.3b, a similar picture of the small-scale structures can be found in both the temperature and velocity field. In this regard especially the fine blue filaments, which demonstrate the form of the structures dropping down from the boundary layer at the cooling plate, are very conspicuous. In such a form the structures are also expected to detach from the heating plate, but on the way to the top the structures are disrupted, so that those small coherent cells cannot be seen for warm and upwelling fluid close to the top of the cell. Moreover, the large-scale structures can be discovered in both fields, but in the velocity field those are not as outstanding as in the temperature field. Hence, for a visual comparison of the large-scale structures the corresponding time-averaged fields in the figures 5.3c and 5.3d should be considered. In those fields the distinctive patterns, which are the footprint of the turbulent superstructures, can easily be identified in each case and it can be seen, that there is a good match between the temperature and the vertical velocity. As it can be expected with regard to the variation of the fluid's mass density, the strongest positive and negative vertical velocity components mostly correspond to the warm and cold parts of the turbulent superstructures, respectively.

The results for the instantaneous and time-averaged fields of the temperature and of the vertical velocity component from the measurement in the mid plane of the cell with
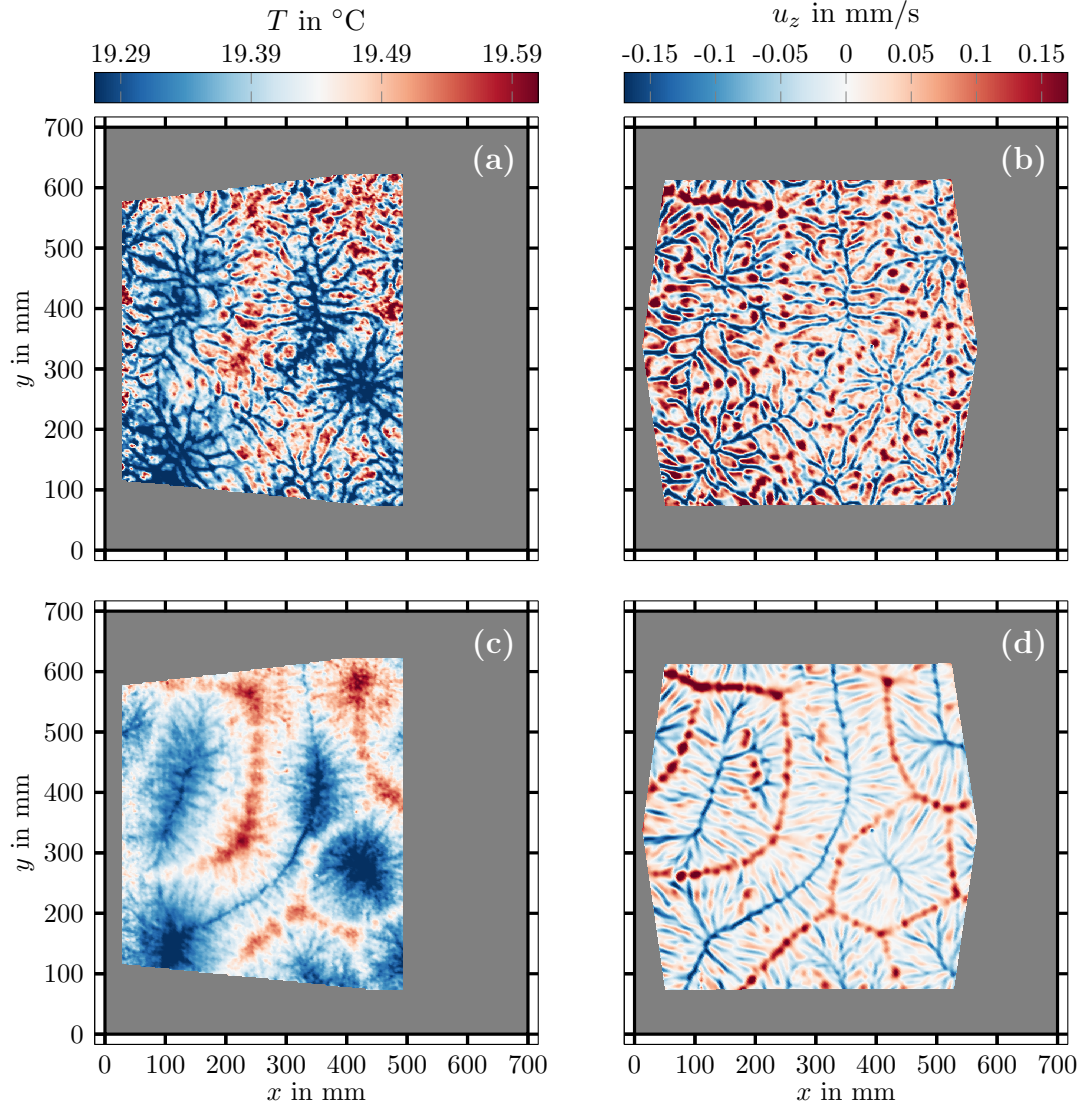
Figure 5.3: Exemplary instantaneous fields of the temperature (a) and of the corresponding vertical velocity component (b) as well as the time-averaged fields (c,d) obtained from the measurement in the top plane of the Rayleigh-Bénard cell at the Rayleigh number $\mathrm{Ra} = 2 \times 10^5$ with the settings according to table 5.1.

almost the same temperatures at the heating and cooling plate can be seen in figure 5.4 for comparison. In the instantaneous fields the structures are here more difficult to compare than in the top plane, since the small coherent cells are not present anymore in the same form. Nevertheless, after time-averaging the turbulent superstructures are clearly uncovered as well. As it has just been seen from the measurements in the top plane, the large-scale structures in the time-averaged temperature and velocity field also provide a good match in the mid plane. However, irrespective of the measurement plane a close look reveals some discrepancies. For example, in the time-averaged velocity field in the mid plane a distinctive upward motion appears in the area around $(x, y) = (400\,\mathrm{mm}, 290\,\mathrm{mm})$, which cannot be found from the temperature field in the form of very warm fluid. At this position only a small streak with a temperature around the mean of the heating and cooling plate temperature can be distinguished, which is surrounded by much colder fluid sinking down and thus driving the upward motion of the fluid embedded in the center due to the continuity of mass. It shall be noted that such differences between the temperature
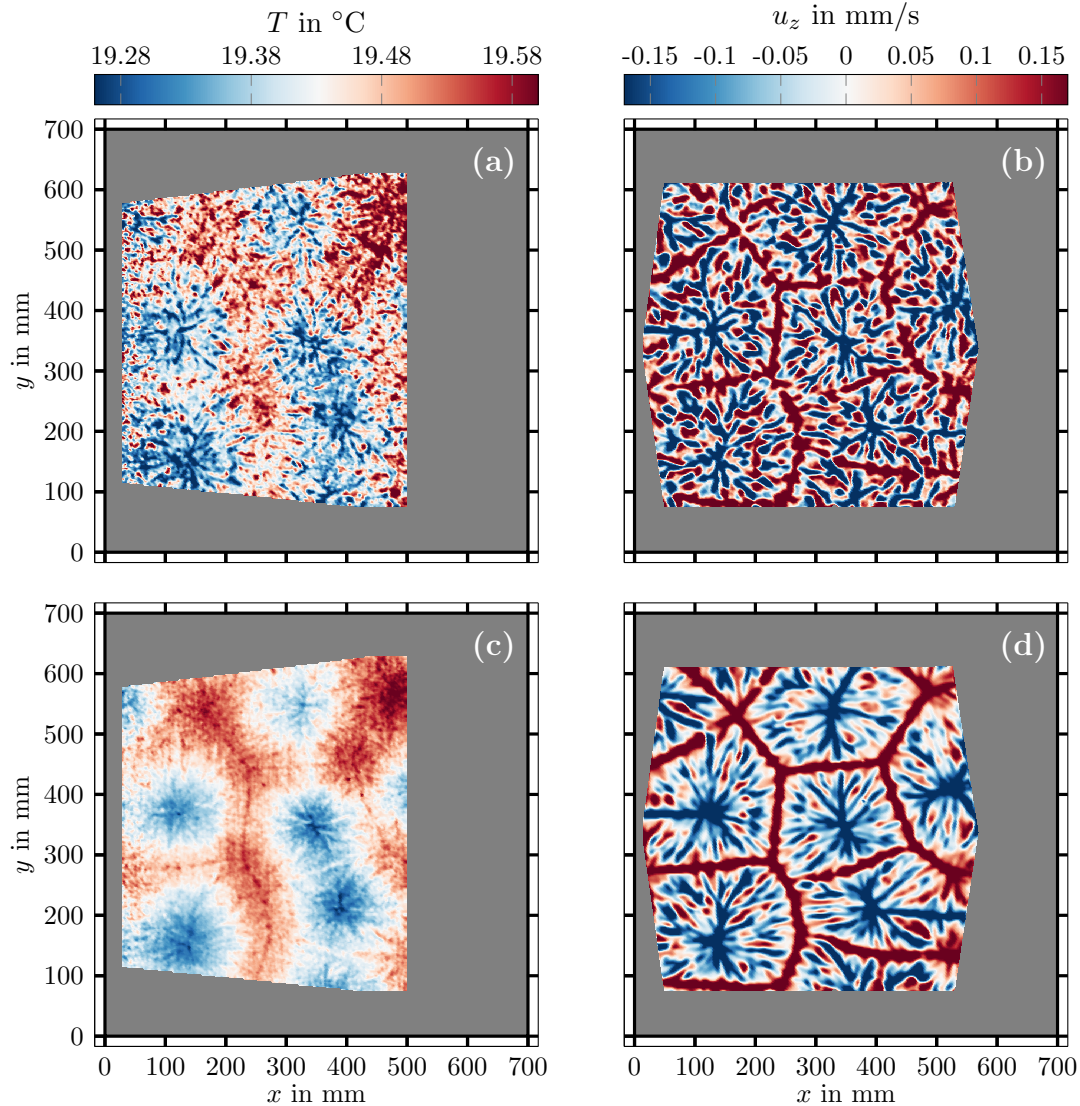
Figure 5.4: Exemplary instantaneous fields of the temperature (a) and of the corresponding vertical velocity component (b) as well as the time-averaged fields (c,d) obtained from the measurement in the mid plane of the Rayleigh-Bénard cell at the Rayleigh number $\mathrm{Ra} = 2 \times 10^5$ with the settings according to table 5.1.

and velocity might be traced back to the experimental boundary conditions to some extent. Despite the great efforts made to achieve isothermal conditions on the heating and cooling plate, small inhomogeneities of the temperature distribution can of course not be impeded, in particular on the side of the transparent cooling plate. Due to the slight increase of the cooling water temperature in flow direction, the measured temperature field also exhibits the trend of higher temperatures along the cooling water flow, which is directed from the bottom to the top edge in all the fields. However, even if this large-scale trend is removed from the temperature field, as it will be demonstrated in the section 5.2.4, some differences regarding the large-scale structures still occur. It might be assumed that this is caused by the time-averaging, but a view to the instantaneous fields suggests that this it not the case. At this point the reader may again have a look at figure 1.6, which shows the results of the numerical simulations from the study [57]. In the numerical results such inequalities between the temperature and velocity field, which would not be expected intuitively, can also be seen, in particular for larger Rayleigh numbers.

It becomes also obvious that the superstructures yield relatively sharp contours in the time-averaged velocity fields, while the transition is rather smooth in the time-averaged temperature fields. This can be explained by the fact, that the temperature is not only transported in the vertical direction, but also in the horizontal direction. As the velocity fluctuations increase with the Rayleigh number, this aspect can especially be seen for larger Rayleigh numbers [11], which is also apparent from the numerical results in the figure 1.6. Furthermore, strong variations on small length scales do usually not occur in the time-averaged temperature fields, while upwelling and downwelling fluid parcels frequently appear in close vicinity within the field of the vertical velocity component despite the time-averaging. It can therefore be concluded that also the small-scale structures persist over some time, such that the variation of the vertical velocity on small length scales is not fully removed by the time-averaging, while the advection of the temperature better levels the variations out. Nevertheless, as the turbulent superstructures are clearly uncovered in each case, it is confirmed that the time-averaging over $5\,\mathrm{min}$ is a suitable choice for the measurements at the Rayleigh number $\mathrm{Ra} = 2 \times 10^5$.

From the results of the time-averaged fields for $\mathrm{Ra} = 2 \times 10^5$ the question arises, if the averaging for the other Rayleigh numbers should be performed over the same time interval. As the variation of the Rayleigh number results in different time scales for the relocation of the small-scale flow structures, this must be considered in the choice of the averaging time. Hence, for the larger Rayleigh numbers the time-averaging is not performed over the whole recording time of each image series, but over the same time interval in units of the free-fall time, since this represents the temporal dynamics of the small-scale structures such as thermal plumes. It has also been shown in the study [11], that for revealing the turbulent superstructures the averaging time in units of the free-fall time does not considerably depend on the Rayleigh number, when the Prandtl number is kept fixed. The averaging time of $t_{\mathrm{avg}} = 298\,\mathrm{s}$, which has turned out to be appropriate for the Rayleigh number $\mathrm{Ra} = 2 \times 10^5$, corresponds to about 66 free-fall times. Therefore, the interval for the time-averaging is adjusted in each case, such that it roughly covers the 66 free-fall times for the specific Rayleigh number. The corresponding averaging times $t_{\mathrm{avg}}$ in physical units are given in table 5.2. However, it should be noted that this very specific choice of the interval length for the time-averaging is not of vital importance, meaning that also a slightly different interval length could have been chosen without having a considerable effect on the results presented in this work.

The turbulent superstructures in the time-averaged fields of the temperature and of the vertical velocity at the different Rayleigh numbers can be seen in figure 5.5 in the non-dimensionalized form for a better comparability. For this exemplary illustration the fields have been obtained from image series recorded in the top plane about $3.5\,\mathrm{h}$ after the initial seeding process, respectively. The temperature fields are made dimensionless with the temperature of the heating and cooling plate according to $\tilde{T} = (T - T_{\mathrm{c}})/(T_{\mathrm{h}} - T_{\mathrm{c}})$, while the velocity fields are made dimensionless with the free-fall velocity via $\tilde{u}_z = u_z/\sqrt{h\,g\,\alpha\,\Delta T}$. Thus, after the non-dimensionalization the thermal boundary conditions are given by the temperature $\tilde{T} = 1$ at the heating plate and $\tilde{T} = 0$ at the cooling plate.

From the temperature fields in the top row of the figure 5.5 several aspects become apparent. The most conspicuous is the deviation of the temperature field at $\mathrm{Ra} = 2 \times 10^5$, since the temperatures are in average shifted towards smaller values. This demonstrates that the measurement plane slightly extends into the thermal boundary layer, which becomes thinner with increasing Rayleigh number, so that the measurement plane is then outside of it for the Rayleigh numbers in the range $4 \times 10^5 \leq \mathrm{Ra} \leq 2 \times 10^6$ and, therefore,

$$\tilde{T} = (T - T_{\mathrm{c}})/(T_{\mathrm{h}} - T_{\mathrm{c}})$$



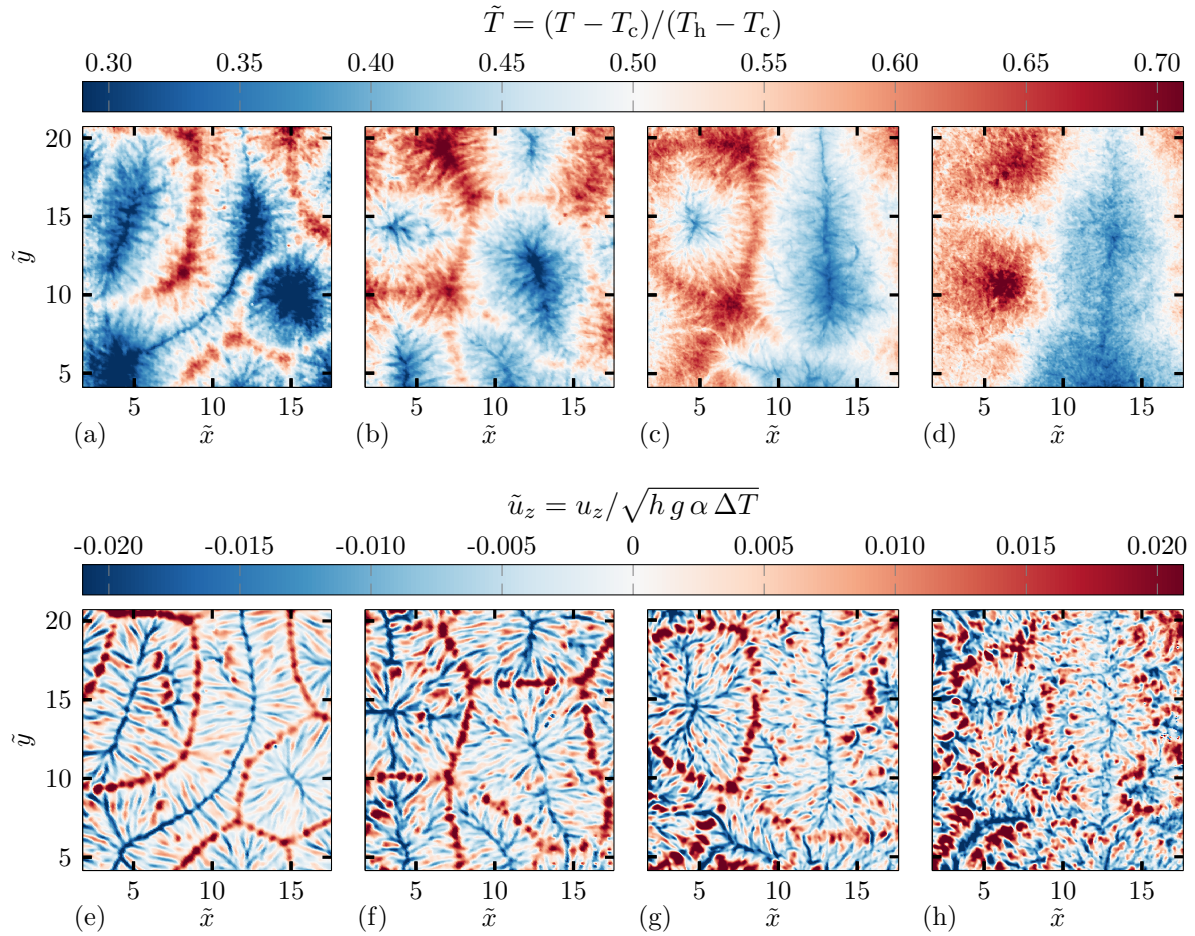$$\tilde{u}_z = u_z/\sqrt{h\,g\,\alpha\,\Delta T}$$



Figure 5.5: The time-averaged fields of the temperature (a-d) and of the corresponding vertical velocity component (e-h) obtained from the independent measurements for the Rayleigh numbers $\mathrm{Ra} = 2 \times 10^5$ (a,e), $\mathrm{Ra} = 4 \times 10^5$ (b,f), $\mathrm{Ra} = 7 \times 10^5$ (c,g) and $\mathrm{Ra} = 2 \times 10^6$ (d,h) in the top plane of the Rayleigh-Bénard cell. The time-averaging was performed over 66 free-fall times, respectively.

the average temperature is closer to $\tilde{T} = 0.5$. Another point, which is in particular obvious from the temperature fields, is the variation of the size of the turbulent superstructures. Comparing the figures 5.5a - 5.5d it can be seen that the superstructures grow with the Rayleigh number. While several superstructures, which are composed of adjacent warm and cold regions, appear for the smaller Rayleigh numbers, a large superstructure spans almost the whole field of view at $\mathrm{Ra} = 2 \times 10^6$.

As outlined before, the turbulent superstructures can be found in the field of the vertical velocity component as well. For the Rayleigh numbers $\mathrm{Ra} = 2 \times 10^5$, $\mathrm{Ra} = 4 \times 10^5$ and $\mathrm{Ra} = 7 \times 10^5$ the distinctive patterns occur in a similar arrangement in both fields, however, it becomes apparent that a local breakup of the contours of the superstructures is more likely to happen with increasing Rayleigh number. For the largest Rayleigh number $\mathrm{Ra} = 2 \times 10^6$ the turbulent superstructures can still be seen in the velocity field, but it is much more difficult to distinguish the contours and to retrace the patterns from the temperature field. Since for this Rayleigh number the time-averaging only covers about one third of each image series according to table 5.2, the averaging interval has also been enlarged for test purposes, yielding no considerable improvements. In general, all the velocity fields in the bottom row demonstrate that the time-averaging does not fully

remove the small-scale structures. Hence, with regard to the determination of the size of the turbulent superstructures an additional filter will be introduced in the section 5.2.4.

Some exemplary results of the time-averaged fields in the mid plane for the different Rayleigh numbers will be shown in section 5.2.3, where the possibility of using the combined temperature and velocity field measurements for the estimation of the local heat flux will be demonstrated. Nevertheless, at this point the results of the measurement in the mid plane at the Rayleigh number $Ra = 2 \times 10^5$ are again illustrated in the figures 5.6a and 5.6b in the non-dimensionalized form to allow for a visual comparison with the results of the numerical simulations in the figures 5.6c and 5.6d. These depict the time-averaged fields of the temperature and of the vertical velocity component for $Ra = 10^5$ from the study [57]. It should also be noted, that in this numerical study a time-averaging over 207 free-fall times has been applied for the case $Ra = 10^5$, while the time interval for the averaging covers 66 free-fall times in the present experimental work. However, based on the results in the supplementary material of the study [11] it can be estimated that such a variation of the averaging time does not have a significant effect on the main characteristics of the fields. Thus, the numerical results for $Ra = 10^5$ and the experimental results for $Ra = 2 \times 10^5$ can be considered for a first comparison.



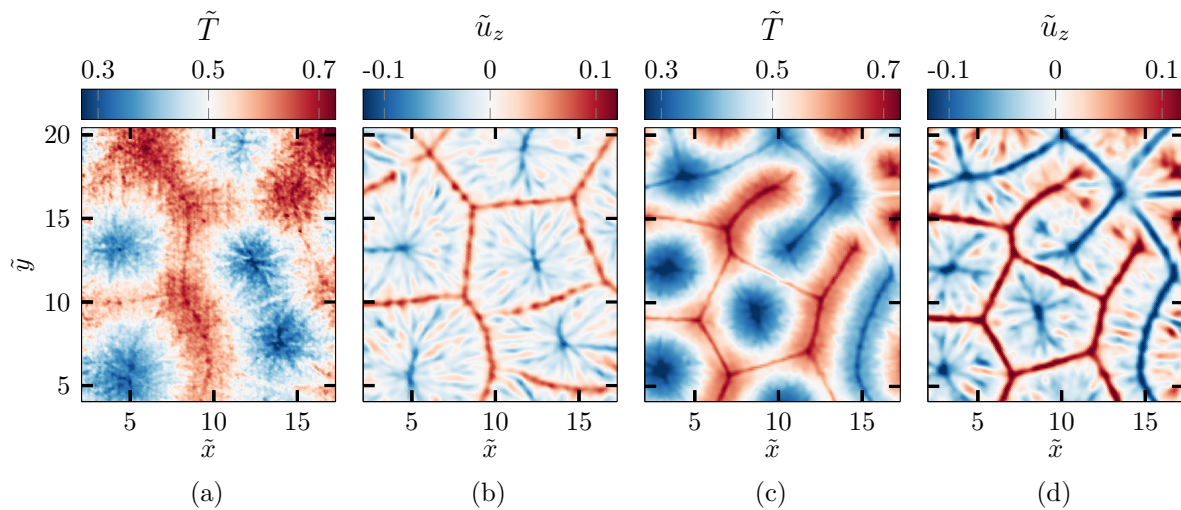(a)                    (b)                    (c)                    (d)

Figure 5.6: Visualization of the time-averaged fields of the temperature (a,c) and of the vertical velocity component (b,d) in the mid plane, obtained from the experiments (a,b) for the Rayleigh number $Ra = 2 \times 10^5$ and from the numerical simulations (c,d) for the Rayleigh number $Ra = 10^5$, respectively. The results of the numerical simulations for $Pr = 7$ and aspect ratio $\Gamma = 25$ have peen published in the work [57] and the data have been provided by the authors. However, here the style of the representation has been changed and the fields have been trimmed to show the same section of the mid plane for this comparison.

The temperature and velocity fields in the figure 5.6 reveal some similarities and dissimilarities of the experimental and numerical results. As aforementioned, it is seen in each case that the turbulent superstructures yield sharp contours in the field of the vertical velocity component, while those leave a broader footprint in the temperature field. Furthermore, in both the experimental and the numerical results a good match of the turbulent superstructures in the temperature and velocity field can be found, however, again the occurrence of local discrepancies is pointed out. At the position of such discrepancies, which for instance appear around $(\tilde{x}, \tilde{y}) = (14, 10)$ in the experiment and around $(\tilde{x}, \tilde{y}) = (15, 14)$ in the simulation, the temperature is oftentimes close to

$\tilde{T} = 0.5$ despite a strong vertical fluid motion in upward or downward direction. Regarding the occurring temperatures and velocities it becomes obvious, that those are similarly distributed, but in the center of the upwelling and downwelling parts of the turbulent superstructures the temperature and velocities are more extreme according to the numerical results. A possible explanation for this is the higher spatial resolution of the numerical simulations. Considering that the entire horizontal dimension of the flow domain is resolved with $1024 \times 1024$ grid points in the simulations for $\mathrm{Ra} = 10^5$, it can be determined that the spatial resolution is more than six times higher compared to that of the experiment for $\mathrm{Ra} = 2 \times 10^5$, when the overlapping interrogation windows are not taken into account. Hence, even though the experiments allow to resolve most of the small-scale structures, as shown by means of the instantaneous fields in the figures 5.3 and 5.4, the peak velocities and temperatures embedded in the fine structures are less resolved, so that the extreme values of the temperature and of the velocity are slightly smoothed out. Moreover, the visual comparison of the turbulent superstructures already indicates that those span larger horizontal dimensions in the experiments, which is quantitatively confirmed in the section 5.2.6.

## 5.2.2   Statistics of the temperature and velocity distribution

In order to gain deeper insights into the measurements, it is also of interest to study the distribution of the temperature and of all three velocity components. The probability density functions (PDFs) of the temperature and of the velocity components are depicted in figure 5.7 for the measurements in the mid and top plane at the example of the Rayleigh numbers $\mathrm{Ra} = 2 \times 10^5$ and $\mathrm{Ra} = 7 \times 10^5$. In each case, the PDFs incorporate all the temporally and spatially resolved data in the intersection area of the temperature and velocity fields obtained from all the image series with the duration of $5\,\mathrm{min}$, subsequent to the first recording over $45\,\mathrm{min}$ immediately after the initial seeding process. It should be noted that each probability $< 10^{-3}$ has been cut off, as the corresponding temperatures and velocities can be neglected due to their rareness and the main part of the PDFs is better distinguishable. The PDFs in the figures 5.7a and 5.7d show that the two non-dimensionalized horizontal velocity components $\tilde{u}_x$ and $\tilde{u}_y$ are in the mid plane similarly distributed as the non-dimensionalized vertical velocity component $\tilde{u}_z$, confirming the three-dimensionality of the Rayleigh-Bénard flow in the bulk area. As it can be expected, the vertical velocity component strongly differs from the horizontal velocity components in the top plane, since the upstreaming fluid is redirected into the horizontal direction in close vicinity to the cooling plate. This results in a more pronounced peak for the vertical velocity components around $\tilde{u}_z = 0$, while the probability for vanishing horizontal velocity components is decreased. It is also conspicuous that the vertical velocity component is asymmetrically distributed in the top plane. The distribution is more extended towards positive values of the vertical velocity component, as the upstreaming fluid still has a certain momentum, while the downstreaming fluid accelerates in the top measurement plane.

The PDFs of the temperature in the figure 5.7c, which result from the measurement at $\mathrm{Ra} = 2 \times 10^5$, demonstrate that the top plane is in this case not fully embedded in the bulk area, but extends into the thermal boundary layer at the upper side, because the distribution of the temperature is clearly shifted towards lower values in comparison to that of the mid plane. This is also confirmed by the average values of the temperature given in table 5.3. The strongest deviation from the theoretically expected average value in the bulk area of $\langle \tilde{T} \rangle = 0.5$ can be found for the measurement in the top plane at $\mathrm{Ra} = 2 \times 10^5$ with

the average temperature of $\langle \tilde{T} \rangle = 0.44$. This deviation is large enough to assume an effect of the thermal boundary layer. The average temperature also differs from $\langle \tilde{T} \rangle = 0.5$ for the other measurements, but the deviations are smaller and are not caused by the thermal boundary layer. In this context it should be noted, that the measurement area does not cover the whole horizontal cross-section of the cell, which is a reasonable explanation for the deviations, having in mind that the turbulent superstructures yield a local shift of the temperatures. Furthermore, also the measurement uncertainty contributes to the deviations. However, for example the average temperature of $\langle \tilde{T} \rangle \approx 0.53$ in the mid plane at $\mathrm{Ra} = 2 \times 10^5$ corresponds to a deviation of about $0.02\,\mathrm{K}$ from the expected value, given by the mean of the heating and cooling plate temperature. Thus, the deviations are very small and do not need to be further investigated.

While the PDFs for the temperature at $\mathrm{Ra} = 2 \times 10^5$ in the figure 5.7c remind of a Gaussian distribution, the PDFs of the temperatures measured at $\mathrm{Ra} = 7 \times 10^5$, which are depicted in the figure 5.7f, do not exhibit such a smooth form. Furthermore, in particular the asymmetric distribution of the extreme temperatures is outstanding, since larger temperatures towards $\tilde{T} = 1$ occur more often than temperatures towards the lower end at $\tilde{T} = 0$. However, this should not be interpreted physically, as the thermal boundary conditions have always been adapted to enable the most reliable measurement of the temperature around $\tilde{T} = 0.5$. Therefore, considering the specifications of the TLCs R20C20W, which have been applied for these measurements, the measurement uncertainty increases for the extreme temperatures. Of course this is undesirable, but it can be accepted, as the occurring temperatures mainly fall into the range $0.2 \leq \tilde{T} \leq 0.8$, in which the measurements yield accurate results. On the contrary, such an increase of the measurement uncertainty does not occur for the other measurements with the TLCs R20C20W at $\mathrm{Ra} = 2 \times 10^5$ and $\mathrm{Ra} = 4 \times 10^5$, since the range of the occurring temperatures is smaller.

The results of the statistical analysis of the temperature and velocity data from the measurements in the mid and top plane are summarized in table 5.3 for all the Rayleigh numbers. The mean absolute values and the standard deviations of the three velocity components and of the temperature as well as the root-mean-square velocity $\tilde{U}_{\mathrm{rms}} = \langle \tilde{u}_x^2 + \tilde{u}_y^2 + \tilde{u}_z^2 \rangle^{(1/2)}$ of the measurements with the TLCs R20C20W at the Rayleigh numbers $\mathrm{Ra} = 2 \times 10^5$, $\mathrm{Ra} = 4 \times 10^5$ and $\mathrm{Ra} = 7 \times 10^5$ have been determined from all the 19 image series with the recording time of $5\,\mathrm{min}$, respectively. As already mentioned above, accurate measurements could not be performed over the whole duration of the experiments for the Rayleigh number $\mathrm{Ra} = 2 \times 10^6$ due to the strongly decreasing seeding density of the TLC R25C50W. Even though the color shade of the TLCs is not directly affected by the seeding density, especially the uncertainty of the temperature measurement could not be kept on the same level towards the end of these experiments. Hence, for the determination of the statistical quantities in table 5.3 both the temperature and velocity data of the last five image series recorded at $\mathrm{Ra} = 2 \times 10^6$ have not been considered.

Due to the non-dimensionalization of the velocity components, a significant change of their magnitude with the Rayleigh number is not obvious from table 5.3. Nevertheless, the root-mean-square velocity $\tilde{U}_{\mathrm{rms}}$ exhibits an increasing trend for the measurements in the mid and top plane, respectively. The root-mean-square velocities in the order of $\tilde{U}_{\mathrm{rms}} = 0.1$ are similar to that of the numerical simulations in the study [57], where $\tilde{U}_{\mathrm{rms}} = 0.089$ for $\mathrm{Ra} = 10^5$ and $\tilde{U}_{\mathrm{rms}} = 0.102$ for $\mathrm{Ra} = 10^6$ was obtained. Those values cannot be compared one-to-one, since the results of the numerical simulations are based on the entire flow domain, however, the slightly smaller root-mean-square velocities in the experiments are
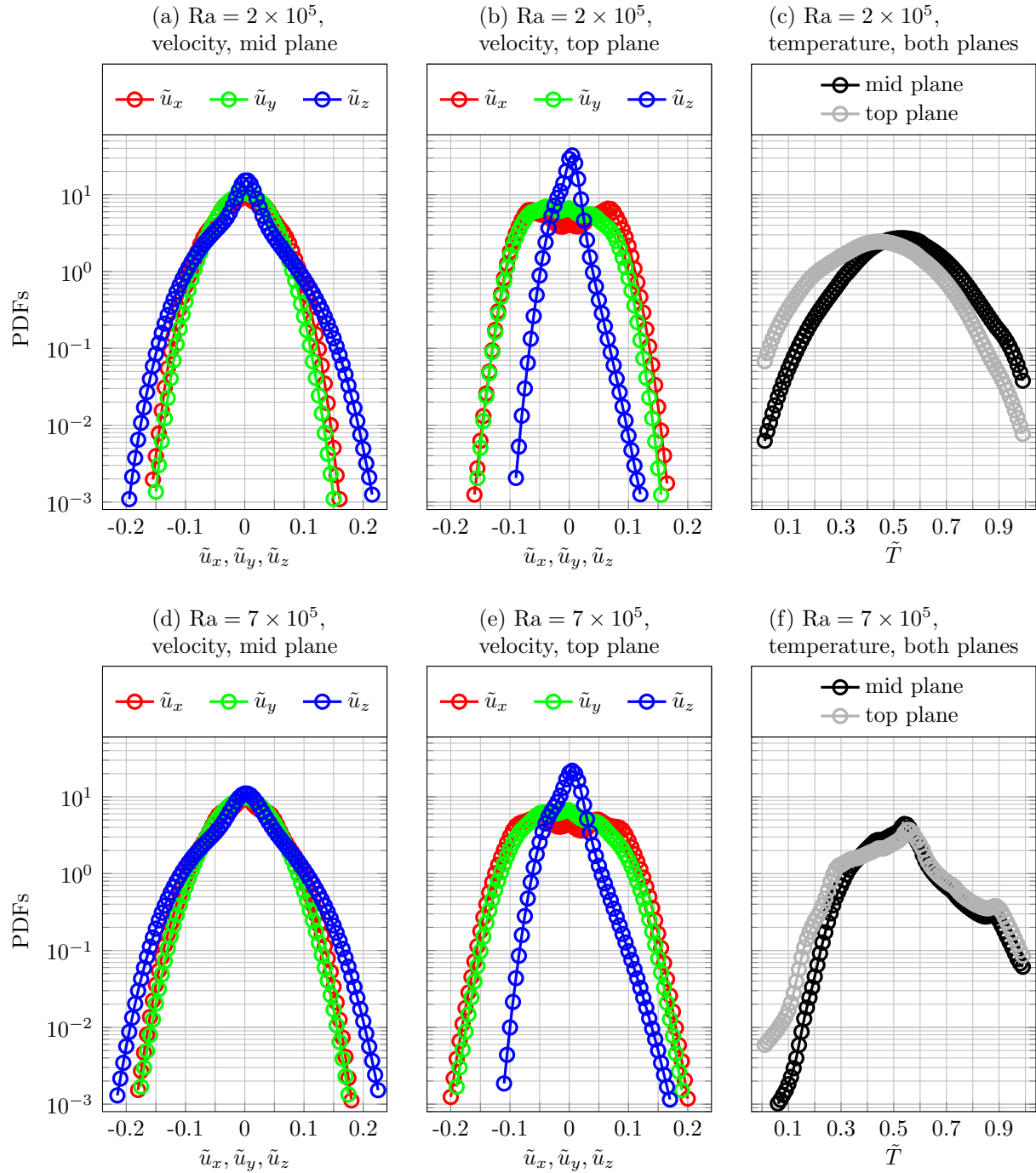
Figure 5.7: Probability density functions (PDFs) of the three velocity components and of the temperature for two different Rayleigh numbers considering the full data sets of the long-time measurements in the mid and top plane of the cell, respectively. The Rayleigh numbers are given at the top of each plot.

probably caused by the fact, that the peak velocities are decreased due to the smaller spatial resolution of the measurements. As already discussed by means of the PDFs in figure 5.7, the results in table 5.3 confirm the predominance of the horizontal velocity components in the top plane, while the mean absolute values of the velocity components do not considerably differ from each other in the mid plane. Despite the smaller vertical velocity components in the top plane, the root-mean-square velocity exceeds that of the

measurements in the mid plane in each case because of the larger magnitude of the horizontal velocity components. It can also be seen, that the standard deviation of the velocity components is always larger than the corresponding mean absolute value, showing that the velocity components considerably vary across the measurement area.

The mean values of the temperatures listed in the table 5.3 have already been addressed before. Except for the measurement in the top plane at $2 \times \text{Ra} = 10^5$, where the measurement area slightly extends into the thermal boundary layer at the cooling plate, the mean value does not substantially differ from the theoretically in the bulk area expected average $\langle \tilde{T} \rangle = 0.5$. The standard deviation of the temperature, which is given in the last column of the table 5.3, is typically around $\sigma_{\tilde{T}} = 0.15$ for the measurements conducted with the TLCs R20C20W at the Rayleigh numbers $\text{Ra} = 2 \times 10^5$, $\text{Ra} = 4 \times 10^5$ and $\text{Ra} = 7 \times 10^5$. It is therefore quantitatively confirmed that extreme temperatures, which are close to $\tilde{T} = 0$ or $\tilde{T} = 1$ and cannot be measured as precisely anymore, do not strongly affect the results. However, one exception becomes apparent, since the standard deviation of the temperature resulting from the measurement in the top plane at $\text{Ra} = 4 \times 10^5$ amounts to about $\sigma_{\tilde{T}} = 0.21$. During this measurement experimental problems have occurred after several hours of operation, so that the measurement had to be restarted with some additionally inserted TLCs. Because of the larger amount of TLCs deposited on the heating plate the imaging conditions were not optimal anymore, causing the increase of the standard deviation of the measured temperatures. Nevertheless, the results of this experiment can still be considered as accurate and do not alter the main conclusions of the further investigations. It becomes also obvious from the table 5.3, that the standard deviation of the temperature at $\text{Ra} = 2 \times 10^6$ is around $\sigma_{\tilde{T}} = 0.2$ in both measurement planes, but this cannot be considered as an effect of the Rayleigh number, since an increasing Rayleigh number yields a better equalization of the occurring temperatures due to the stronger fluctuations. Thus, the larger standard deviation is related to the measuring technique, since for these experiments the TLCs R25C50W have been used, resulting in a larger measurement uncertainty as shown in section 4.2.

| Label | $\langle|\tilde{u}_{\text{x}}|\rangle$ | $\sigma_{\tilde{u}_{\text{x}}}$ | $\langle|\tilde{u}_{\text{y}}|\rangle$ | $\sigma_{\tilde{u}_{\text{y}}}$ | $\langle|\tilde{u}_{\text{z}}|\rangle$ | $\sigma_{\tilde{u}_{\text{z}}}$ | $\tilde{U}_{\text{rms}}$ | $\langle\tilde{T}\rangle$ | $\sigma_{\tilde{T}}$ |
|---|---|---|---|---|---|---|---|---|---|
| $2e5_{\text{m}}$ | 0.035 | 0.043 | 0.030 | 0.038 | 0.032 | 0.044 | 0.073 | 0.531 | 0.151 |
| $2e5_{\text{t}}$ | 0.053 | 0.060 | 0.044 | 0.051 | 0.013 | 0.017 | 0.081 | 0.440 | 0.163 |
| $4e5_{\text{m}}$ | 0.035 | 0.044 | 0.032 | 0.041 | 0.036 | 0.049 | 0.077 | 0.498 | 0.146 |
| $4e5_{\text{t}}$ | 0.059 | 0.068 | 0.045 | 0.054 | 0.017 | 0.023 | 0.090 | 0.507 | 0.211 |
| $7e5_{\text{m}}$ | 0.037 | 0.046 | 0.034 | 0.043 | 0.038 | 0.051 | 0.081 | 0.520 | 0.131 |
| $7e5_{\text{t}}$ | 0.058 | 0.067 | 0.047 | 0.056 | 0.018 | 0.025 | 0.091 | 0.516 | 0.157 |
| $2e6_{\text{m}}$ | 0.042 | 0.053 | 0.037 | 0.047 | 0.039 | 0.051 | 0.087 | 0.498 | 0.193 |
| $2e6_{\text{t}}$ | 0.056 | 0.067 | 0.049 | 0.061 | 0.022 | 0.030 | 0.095 | 0.506 | 0.213 |

Table 5.3: Mean absolute value and standard deviation of the velocity components and of the temperature obtained from the data sets of the measurements in the mid and top plane. Furthermore, the root-mean-square velocity $\tilde{U}_{\text{rms}}$ is listed for each of the measurements.

## 5.2.3   Estimation of the local heat flux

So far the temperature and velocity fields have been considered separately to visualize the turbulent superstructures. However, the fields can also be used in combination to investigate the local heat flux in RBC, which is one of the most important benefits of the presented measuring technique. Since the focus of this experimental study is on clearly uncovering the turbulent superstructures in large aspect ratio RBC from the experimental point of view for the first time, which has required many preliminary works as demonstrated in the previous sections, the experiment has not yet been optimized with regard to studying the local heat flux. Very precise measurements of the local heat flux will require further upgrades of the experiment. Nevertheless, the data from the experiments are applied to show that simultaneous measurements of the temperature and velocity fields are useful to characterize the heat flux associated with the superstructures. With a view to future studies the main issues are addressed in this section, so that it can be viewed as proof of concept and may help to perform accurate measurements of the local heat flux.

Since the estimation of the local heat flux in RBC requires the information of the vertical velocity component, it is from the experimental point of view advantageous to conduct those investigations in the mid plane in the present case, as the vertical velocity in the top plane is dampened by the adjacent cooling plate, resulting in a larger relative measurement uncertainty. Therefore, the possibility to analyze the local heat flux is demonstrated by means of the simultaneous measurements of the temperature and velocity fields in the mid plane.

Some exemplary time-averaged fields of the temperature and of the vertical velocity component in the mid plane are depicted in the left and central column of the figure 5.8. Those results for the Rayleigh numbers ranging from $\mathrm{Ra} = 2 \times 10^5$ up to $\mathrm{Ra} = 2 \times 10^6$ have again been determined on the basis of an image series, which has been recorded about 3.5 h after the initial seeding process, respectively. Contrary to the measurements in the top plane, which have been shown in figure 5.5, no significant deviation of the average temperature from $\tilde{T} = 0.5$ can be seen, since the mid plane is fully embedded in the bulk area of the cell. Moreover, with regard to the size of the turbulent superstructures the same trend as observed in the top plane can be seen, meaning that the superstructures grow with the Rayleigh number.

Here, the local heat flux is quantified with the local Nusselt number, which represents the increase of the heat flux from the bottom to the top plate of the cell due to the convective motion in comparison to the state of rest. In general, the estimation of the local Nusselt number requires to know the gradient of the temperature along the vertical axis $\partial \tilde{T}(x,y)/\partial \tilde{z}$ to incorporate also the diffusive contribution to the total heat flux, but this gradient cannot be determined from a measurement in a single plane. Therefore, the local Nusselt number, which can be obtained from the experiment at hand based on the measurement of the temperature and the vertical velocity in the mid plane, can only represent the convective heat flux in spatial resolution. However, in the bulk area of the Rayleigh-Bénard cell the gradient of the temperature along the vertical axis vanishes, if the average over the horizontal plane is taken, as illustrated in figure 1.2. Hence, the diffusive heat flux cancels out in the horizontal average. Aiming to determine the average of the local Nusselt number in the mid plane for the comparison with numerical results, knowledge of the spatially resolved gradient of the temperature along the vertical axis is thus not necessary. As for instance shown in the study [57], the local Nusselt number can then easily be calculated via $\mathrm{Nu}_{\mathrm{loc}} = \sqrt{\mathrm{Ra}\,\mathrm{Pr}}\,\Theta_{\mathrm{lin}}\,\tilde{u}_z$, where $\Theta_{\mathrm{lin}}$ denotes the dimensionless temperature difference between the local temperature $\tilde{T}(x,y)$ and the temperature, that
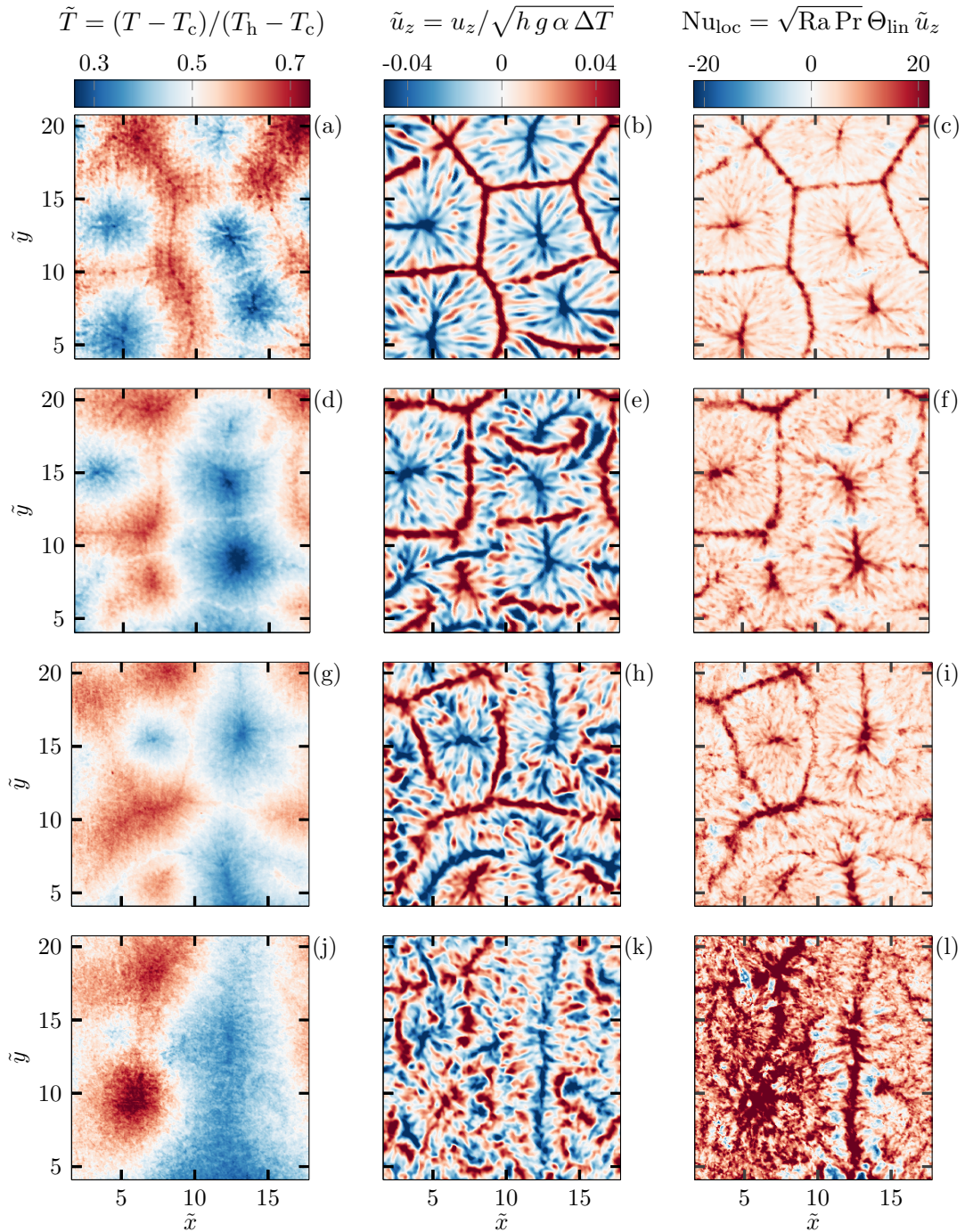
Figure 5.8: Exemplary time-averaged fields of the temperature (left column), of the vertical velocity component (mid column) and of the local Nusselt number (right column) showing the turbulent superstructures for the measurements in the mid plane with the settings according to table 5.1. From the top to the bottom row the Rayleigh number amounts to $\mathrm{Ra} = 2 \times 10^5$ (a-c), $\mathrm{Ra} = 4 \times 10^5$ (d-f), $\mathrm{Ra} = 7 \times 10^5$ (g-i) and $\mathrm{Ra} = 2 \times 10^6$ (j-l), respectively.

would result without convective motion at the height of the measurement plane, i.e. $\Theta_{\mathrm{lin}} = \tilde{T}(x, y) - (1 - \tilde{z})$ [24]. Thus, in the mid plane this difference is $\Theta_{\mathrm{lin}} = \tilde{T}(x, y) - 0.5$. The product $\Theta_{\mathrm{lin}} \tilde{u}_z$ for the determination of the local Nusselt number is calculated from the temporally resolved data of the temperature and of the vertical velocity component. Although the evaluation of both quantities has been performed with the same spatial resolution according to table 5.2, the grid points are slightly shifted due to the approach of

the dimensional calibration outlined in section 4.1. However, the temperature and velocity data must be available for the same grid points to determine the local heat flux. Therefore, the vertical velocity has been computed at the grid points of the temperature fields via linear interpolation. The resulting time-averaged fields of the local Nusselt number for the different Rayleigh numbers can be seen at the right side of figure 5.8.

The comparison of the time-averaged fields of the temperature with that of the vertical velocity component and of the local Nusselt number in figure 5.8 demonstrates the effect of the turbulent superstructures on the local heat flux. The maximum values of the latter are clearly obvious from the fields of the local Nusselt number. Especially the results for the Rayleigh numbers $Ra = 2 \times 10^5$, $Ra = 4 \times 10^5$ and $Ra = 7 \times 10^5$ show, that the local maxima occur in the regions, where the time-averaged temperature reaches its extreme values, corresponding to the updrafts and downdrafts of the turbulent superstructures. Hence, it is confirmed that the superstructures strongly drive the heat flux from the bottom to the top of the Rayleigh-Bénard cell. In the fields of the local Nusselt number it can be seen, that the turbulent superstructures are most outstanding for the smaller Rayleigh numbers. For the Rayleigh number $Ra = 2 \times 10^5$ the time-averaged local Nusselt number in the area between the contours of the superstructures is almost uniform and much smaller than the maximum local Nusselt numbers. A close look to the fields for $Ra = 4 \times 10^5$ and $Ra = 7 \times 10^5$ in the figures 5.8f and 5.8i reveals that the nonuniformities of the local Nusselt number in the area between their contours become larger, which indicates the increasing effect of the turbulent fluctuations on the heat flux. The enhancement of the heat transport by the superstructures can still be observed in the field of the local Nusselt number for $Ra = 2 \times 10^6$, but in this case the dominance of the superstructures is decreased.

For a better impression of the analysis regarding the local heat flux, the PDFs of the temporally resolved values of the local Nusselt number are shown in figure 5.9. In this case, the PDFs are normalized with the respective maximum for a better comparability. It can be seen, that the range of the local Nusselt numbers is much larger, when the instantaneous fields are considered. Very conspicuous is that strongly negative values of the local Nusselt number frequently occur, meaning that the upward motion of cold fluid and the downward motion of warm fluid due to the interaction of the flow structures are not rare events. Nevertheless, the PDFs are more extended towards positive values of the local Nusselt number, as it can be expected considering the effect of thermal buoyancy.

Since the Nusselt number is the key quantity to describe the heat flux in RBC, the experimental results should be assessed by a comparison with numerical results. For the comparison the average of the local Nusselt number is most suited, as this single value represents the magnitude of the heat flux across the investigated area. Considering that not the whole horizontal cross-section of the Rayleigh-Bénard cell is analyzed in the present case, the average of the local Nusselt number, which is denoted as the Nusselt number $Nu := \langle Nu_{loc} \rangle$, is not referred to as the global Nusselt number. The Nusselt number is given in the table inserted in figure 5.9 for each Rayleigh number. For the comparison the results from the numerical study [57] are used, because in this study RBC has been investigated for the Prandtl number $Pr = 7$ and the aspect ratio $\Gamma = 25$. Hence, the results can almost directly be compared, as the adjusted Rayleigh numbers are also similar. From the numerical simulations the Nusselt numbers of $Nu_{sim,1} = 4.1$, $Nu_{sim,2} = 8.3$ and $Nu_{sim,3} = 16.2$ have been obtained for the Rayleigh numbers $Ra_{sim,1} = 10^5$, $Ra_{sim,2} = 10^6$ and $Ra_{sim,3} = 10^7$, so that the Nusselt number can be expressed by the exponential fit $Nu = 0.133 \, Ra^{0298}$. The Nusselt numbers, which result from applying this exponential fit

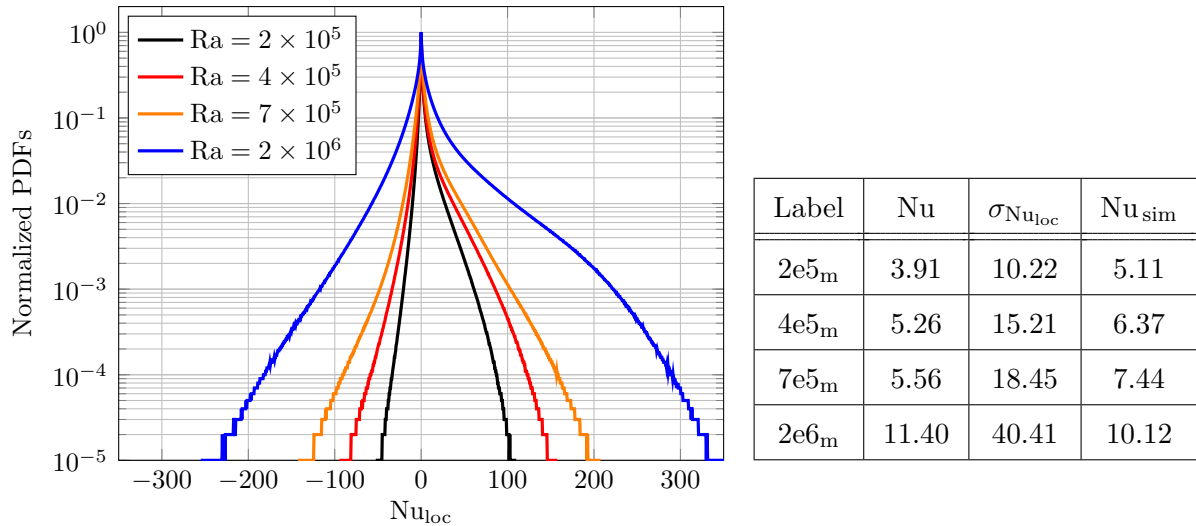| Label | Nu | $\sigma_{\mathrm{Nu_{loc}}}$ | $\mathrm{Nu_{sim}}$ |
|-------|------|-------|-------|
| $2\mathrm{e}5_\mathrm{m}$ | 3.91 | 10.22 | 5.11 |
| $4\mathrm{e}5_\mathrm{m}$ | 5.26 | 15.21 | 6.37 |
| $7\mathrm{e}5_\mathrm{m}$ | 5.56 | 18.45 | 7.44 |
| $2\mathrm{e}6_\mathrm{m}$ | 11.40 | 40.41 | 10.12 |

Figure 5.9: The normalized probability density functions of the temporally resolved local Nusselt number resulting from the measurements in the mid plane at the different Rayleigh numbers. The average of the local Nusselt number $\mathrm{Nu} := \langle \mathrm{Nu_{loc}} \rangle$ and the corresponding standard deviation are given in the inserted table on the right side. Furthermore, the Nusselt numbers $\mathrm{Nu_{sim}}$ determined from the results presented in the numerical study [57] via an exponential fit are listed in the table for each Rayleigh number adjusted in the experiment.

to the Rayleigh numbers adjusted in the experiment, are listed in the right column of the table included in figure 5.9. For this estimation the accurately determined Rayleigh numbers of the experiments according to table 5.1 have been used. It can be seen that the Nusselt numbers for the Rayleigh numbers $\mathrm{Ra} = 2 \times 10^5$, $4 \times 10^5$ and $7 \times 10^5$ are smaller than the values calculated with the exponential fit based on the numerical results. Even though an overestimation of the Nusselt number in the numerical simulations might be possible, there are several points, which suggest an underestimation in the experiments. These shall be addressed in the following.

One aspect, which explains the underestimation of the Nusselt number in the experiments, is the smaller spatial resolution compared to the numerical investigations. In the evaluation of the measurements the spatial resolution given in table 5.2 has been adjusted in the way, that the small-scale structures can be resolved, while the measurement uncertainty of both the temperature and the velocity is kept as low as possible. With this tradeoff it has been accepted that the peak temperatures and velocities embedded within the structures are not fully resolved. In order to evaluate the effect of the spatial resolution of the measurements, exemplary instantaneous fields of the temperature and of the vertical velocity from the numerical simulations conducted for the study [57] are considered now. The full three-dimensional fields for one instant of time at $\mathrm{Ra} = 10^6$ have been provided by the authors of this numerical study, but here only a small section in the horizontal mid plane is shown. This section covers $150 \times 150$ grid points and is located in the center of the horizontal plane with its $1024 \times 1024$ grid points, which ensure that the spatial resolution is sufficiently high. The central section of the non-dimensionalized temperature and velocity field can be seen in the figures 5.10a and 5.10b. The resulting field of the local Nusselt number is depicted in figure 5.10c, in which the local peaks can clearly be observed due to the high spatial resolution.

For demonstrating the effect of the smaller spatial resolution of the experimental analysis, the data at the grid points in the temperature and the velocity field are averaged

$$\tilde{T} = (T - T_c)/(T_h - T_c) \qquad \tilde{u}_z = u_z/\sqrt{h\,g\,\alpha\,\Delta T} \qquad \mathrm{Nu_{loc}} = \sqrt{\mathrm{Ra\,Pr}}\,\Theta_{\mathrm{lin}}\,\tilde{u}_z$$
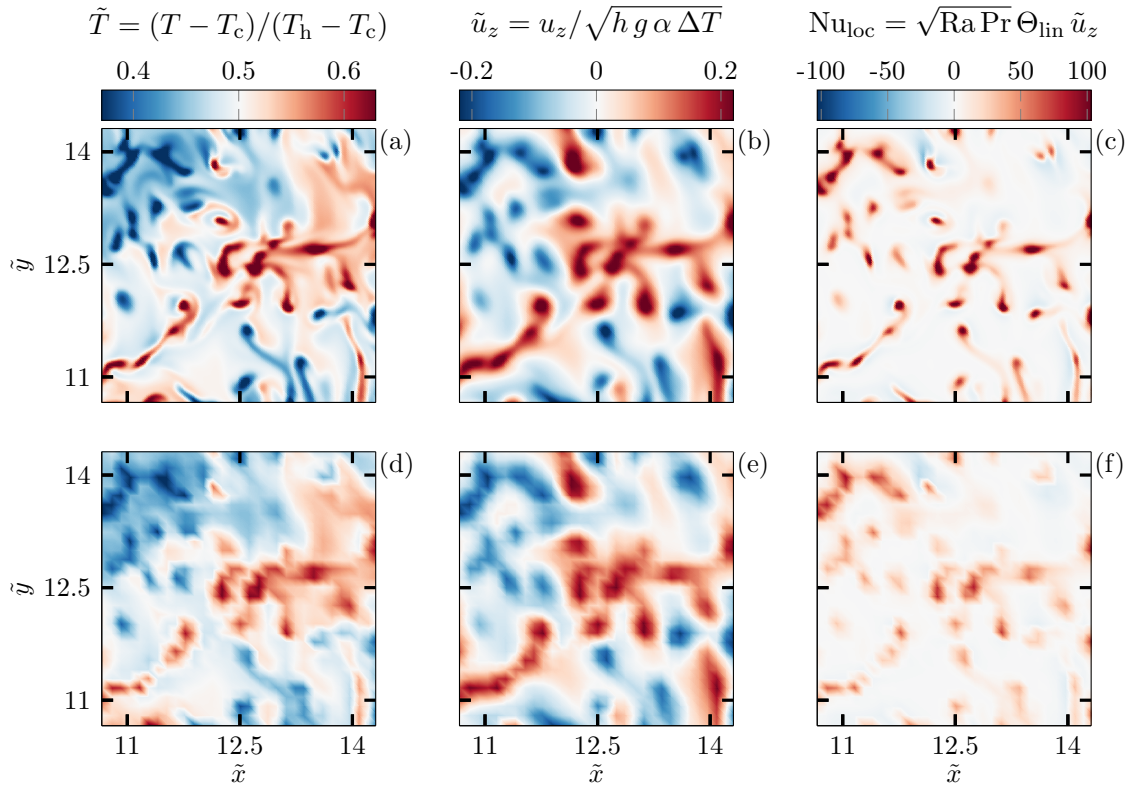


Figure 5.10: Visualization of the effect of a decreasing spatial resolution on the determination of the instantaneous fields of the temperature (a,d), of the vertical velocity component (b,e) and of the local Nusselt number (c,f). The instantaneous fields in the upper row show the results of the numerical simulations for $\mathrm{Ra} = 10^6$, which have been performed for the study [57]. The full three-dimensional fields of the temperature and of the velocity for this instant of time have been provided by the authors of this numerical study. For the visualization only a central section of the horizontal mid plane of the flow domain is depicted here. The lower row shows the corresponding fields of the temperature and of the vertical velocity component after taking the average in interrogation windows with the size of $5 \times 5$ grid points, yielding the field of the local Nusselt number at the bottom right side.

within small kernels. Considering the spatial resolution of the numerical simulation, which is $1024/25 \approx 41$ grid points per height of the cell, and that of the measurement in the mid plane for $\mathrm{Ra} = 7 \times 10^5$, which is $295/16.6 \times 0.5 \approx 8.9$ grid points per height of the cell, it can be estimated that the kernels should cover $5 \times 5$ grid points to represent the effect of the averaging in the measurements. The spatial resolution of the measurement for the Rayleigh number $\mathrm{Ra} = 7 \times 10^5$ has been chosen due to the largest deviation of the average of the local Nusselt number according to the table in figure 5.9. Using the kernel size of $5 \times 5$ grid points for the averaging yields the field of the temperature and of the vertical velocity component in the figures 5.10d and 5.10e. From the comparison with the highly resolved fields it becomes obvious that the structures are noticeably smeared out, but can still be distinguished. If the field of the local Nusselt number is then determined from the fields with the smaller spatial resolution, which is not the same as directly averaging within the kernels of the original field of the local Nusselt number, the peak intensities decrease as expected. This can be seen in figure 5.10f. The average of the local Nusselt across the whole horizontal mid plane amounts to approximately $\mathrm{Nu} = 8.35$ in the original

field of the simulation for $Ra = 10^6$ and is about $Nu = 7.52$, when the averaging within the kernels is applied. It is therefore confirmed, that the smaller spatial resolution of the measurement data contributes to the underestimation of the Nusselt numbers in the experiments for the Rayleigh numbers $Ra = 2 \times 10^5$, $Ra = 4 \times 10^5$ and $Ra = 7 \times 10^5$ according to the results in figure 5.9.

This effect of the smaller spatial resolution has also exemplarily been checked on the basis of the measurement data itself. However, as the spatial resolution of the measurements at $Ra = 7 \times 10^5$ and $Ra = 2 \times 10^6$, as given in the table 5.2, is already close to the upper possible limit in consideration of the measurement uncertainty, this has only been tested for the measurements at $Ra = 2 \times 10^5$ and $Ra = 4 \times 10^5$. For this, three out of the nineteen image series have been used, respectively, with one being taken from the beginning, another from the middle part and the last from the end of each measurement. Changing the spatial resolution from $24 \times 24$ pixel to $16 \times 16$ pixel, the average of the local Nusselt number obtained from these three image series has increased from $Nu = 3.91$ to $Nu = 4.06$ at $Ra = 2 \times 10^5$ and from $Nu = 5.31$ to $Nu = 5.58$ at $Ra = 4 \times 10^5$. In figure 5.9 it can be seen that this is already a noteworthy change of the Nusselt number towards the value expected from the simulations, even though the spatial resolution is still much smaller.

In addition to the averaging within the kernels, an averaging over several horizontal layers around the mid plane has been applied to the simulation data for $Ra = 10^6$ to figure out, whether the thickness of the white light sheet may have an effect on the determination of the Nusselt number. The number of horizontal layers for the averaging has been adjusted considering the ratio between the light sheet thickness and the height of the measurement cell. Due to the averaging across the horizontal layers of the simulation domain the Nusselt number has further reduced to $Nu = 7.34$. Hence, because of the averaging within the kernels and across the layers the Nusselt number has decreased from $Nu = 8.35$ to $Nu = 7.34$, which is about 12% less. From the table in figure 5.9 it becomes obvious that this already explains a large percentage of the occurring deviations between the experimental and numerical results. Another point, that cannot be omitted is the approach applied for the dimensional calibration, which has been described in section 4.1. This method has been used, as it allows to derive the physical dimensions from the cameras' images of different horizontal planes within the cell without the necessity to accurately place a calibration target at the height of each measurement plane separately. Due to the capabilities of the applied stereoscopic self-calibration it was possible to dewarp and correct the cameras' images with a remaining disparity of about 0.3 mm in average. Even though this disparity is very small compared to the size of the interrogation windows for the temperature and the velocity field, it is likely to decrease the Nusselt number, as the peak values of both fields are in the evaluation not determined at exactly the same position. Furthermore, the aforementioned correction of the velocity data from the grid points of the velocity field to those of the temperature field via linear interpolation should be addressed. This method has been implemented in the program code to enable the estimation of the local Nusselt number even in the case that the temperature and velocity fields are given with different spatial resolutions, as for instance shown in the study [24], but if the fields are calculated with the same spatial resolution as in the present case, a window shifting in one of the two fields prior to the processing would be more suitable. However, due to the overlap of the interrogation windows of 50% in both fields, the maximum shift in each direction could have been about one fourth of their size in the worst case, which has not occurred. As the change of the velocity data over a few tenth millimeter by means

of linear interpolation is very small, this is also not expected to significantly affect the results. Nevertheless, for further optimizations this can be considered.

It is apparent from the table inserted in figure 5.9, that the results for the Rayleigh number $Ra = 2 \times 10^6$ constitute an exception, as the Nusselt number determined from the measurements is larger than expected from the exponential function fitted through the Nusselt numbers given in the study [57]. The field of the local Nusselt number depicted in figure 5.8l has already indicated, that its average is considerably larger. A possible explanation is that the turbulent superstructures span wider horizontal dimensions at the Rayleigh number $Ra = 2 \times 10^6$, so that the average of the local Nusselt number depends on the position of the measurement section to an increasing extent. In other words, shifting the field of view of the cameras has an effect on the Nusselt number, which is not negligible. However, it should be brought into mind once more, that the experiments for the Rayleigh number $Ra = 2 \times 10^6$ have been performed with the TLCs R25C50W to determine the temperature over larger measuring ranges, thereby increasing the measurement uncertainty. As the experiments with these TLCs were in general much more challenging, especially due to the gradually decreasing seeding concentration, the degree of uncertainty in the determination of the Nusselt number is larger. Nevertheless, both the average of the local Nusselt number and the standard deviation, which is also listed in the table within figure 5.9, follow the well-known trend and accordingly show that the importance of convection for the heat flux increases with the Rayleigh number.

It can finally be stated, that the results in this section have demonstrated the possibility of measuring the local heat flux in RBC by means of simultaneous measurements of temperature and velocity fields using TLCs. The deviations between the experimental and numerical results can at least to some extent be traced back to the limited spatial resolution in the evaluation of the experimental data and in general to the experimental approach, such as using a light sheet with a certain thickness for the illumination of the tracer particles. In order to improve the measurements of the local heat flux it is suggested to upgrade the experimental facility by using a larger number of cameras, thereby allowing for increased spatial resolution of the measurements. Furthermore, the averaging across the thickness of the light sheet can be avoided by performing simultaneous volumetric measurements of the temperature and velocity fields, which are desirable in any respect, but their implementation still requires a lot of work.

### 5.2.4   Illustration of the two-dimensional Fourier analysis

For the analysis of many scientific and engineering problems it is in many cases of importance to investigate typical frequencies of a quantity within time series of data. A very common approach to analyze the frequencies is the so-called Fast Fourier Transform (FFT), which is broadly explained in the literature, as for example in the reference [170]. However, since the FFT in general enables to detect repetitively occurring events, its use is not restricted to the study of time series. For instance, it can also be applied to investigate the iterative appearance of certain intensity levels in images, which is very useful in many applications, such as for the determination of velocity fields in fluid flows via PIV [61] as already mentioned in the section 4.3. In the present work the FFT is utilized to characterize the turbulent superstructures in Rayleigh-Bénard convection. As it has been demonstrated, the emergence of those structures yields typical patterns in the temperature and velocity field depending on the experimental boundary conditions. Since the patterns feature repeating magnitudes of the temperature and velocity, respectively,

the FFT is applied to specify the characteristic wavelength of the turbulent superstructures in this case. This method has already been applied in the numerical study [11] about turbulent superstructures in Rayleigh-Bénard convection.

Due to the fact that the FFT is a more efficient way to compute the Discrete Fourier Transform (DFT), it is oftentimes used to reduce the computational costs for the evaluation of large data sets. For the Fourier analysis in this work the FFT algorithm implemented in the software *Matlab R2020b* has been used. Since the FFT is a common mathematical operation, the theoretical background is not addressed now, however, some explanations are given in the following to get a better idea of the analysis conducted for this work. As the FFT can be considered as a modified version of the DFT, but the latter is the basic mathematical operation, the approach is explained on the basis of the DFT.

First of all, the result of a two-dimensional DFT applied to an image is a matrix with the number of entries corresponding to the resolution of the image. Each of the entries represents the intensity of the match between the image and a two-dimensional plane wave with sinusoidal form and a certain wavelength, which is varied in both directions of the grid. Thus, the two-dimensional DFT is a quantitative comparison of sinusoidal plane waves having different wavelengths and orientations with a given image. For this, each wave is discretized such that it has data points at the same positions as the image itself. Quantitatively comparing means that the image is overlaid with the discretized wave, the overlapping data points are multiplied and summed up. This operation is conducted for each of the waves separately. However, each of the multiplications is performed in the complex domain, yielding a real and imaginary part, which represent the match of the image with a certain wave on the one hand, but also the match with the wave phase-shifted by a quarter of the wavelength, corresponding to sine and cosine. Hence, the sum of the products of the overlapping data points is always a complex number, known as the Fourier coefficient. Since the absolute value of the Fourier coefficient is not affected by a phase shift of the wave compared to the image, this method is suited to study the similarity of the image and the wave, without having to consider at which point the wave starts. The Fourier coefficients are determined according to equation (5.1) [170]. In this equation, $\hat{F}$ denotes the discrete Fourier transform of the image $F$ consisting of $M \times N$ data points. The indices $m$ and $n$, which run in between $0 \leq m \leq M-1$ and $0 \leq n \leq N-1$ represent the position of the data points within the image, while the indices $q$ and $r$ stand for the varying wavelength and orientation of the sinusoids and also run in between $0 \leq q \leq M-1$ and $0 \leq r \leq N-1$. The symbols $\omega_M$ and $\omega_N$ are the basic terms for the complex sinusoids, that read $\omega_M = e^{-2\pi i/M}$ and $\omega_N = e^{-2\pi i/N}$.

$$\hat{F}_{q,r} = \sum_{m=0}^{M-1} \sum_{n=0}^{N-1} \omega_M^{mq}\, \omega_N^{nr}\, F_{m,n} \tag{5.1}$$

The procedure for the processing of the data for the Fourier analysis in this work can be seen in the flowchart in figure 5.11. For a better impression the main steps of the processing are demonstrated in figure 5.12 by means of a series of temperature fields obtained from the measurement in the mid plane of the cell with aspect ratio $\Gamma = 25$ for the Rayleigh number $\mathrm{Ra} = 2 \times 10^5$. An instantaneous temperature field of this series can be seen in figure 5.12a. As the Fourier analysis are in this work applied to determine the characteristic wavelength of the turbulent superstructures, initially the average over a certain time interval is taken, so that the small scale fluctuations are already removed. The choice of the averaging time has been discussed in the section 5.2.1 and is listed in the table 5.2. Subsequently, the temperature is non-dimensionalized with the temperature difference between the heating
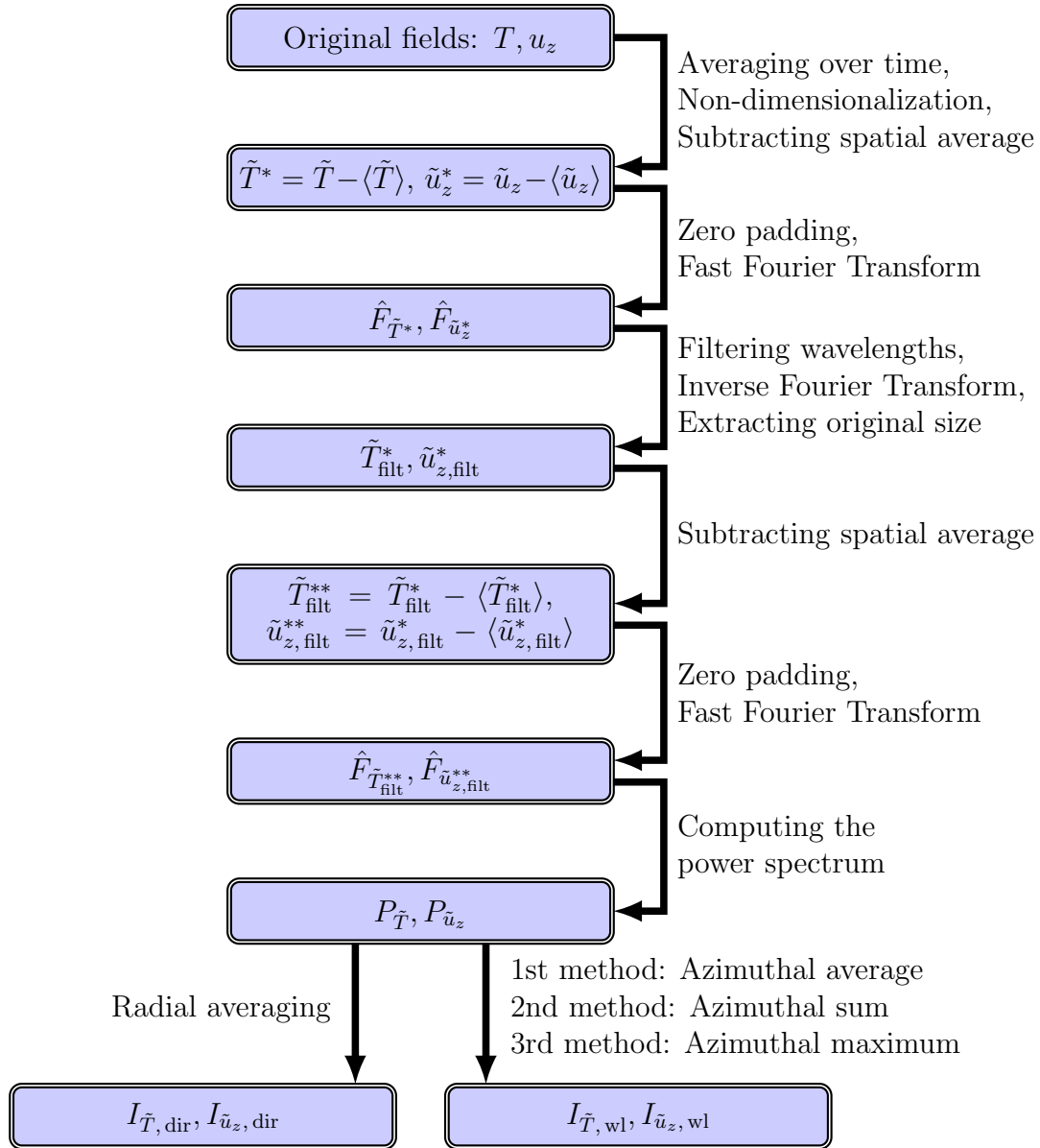
Figure 5.11: Flowchart of the data processing for the Fourier analysis.

and cooling plate, while the spatial coordinates are non-dimensionalized with the height of the Rayleigh-Bénard cell. Afterwards the spatial average of the temperature is subtracted from each data point, since only the variation of the temperature is of interest, but not its offset. As it can be seen in figure 5.12b, the shifted non-dimensionalized temperature does therefore not fluctuate around $\tilde{T}^* = 0.5$, but around $\tilde{T}^* = 0$. Analogously, the vertical velocity non-dimensionalized with the free-fall velocity would at this point fluctuate around $\tilde{u}_z^* = 0$, however, this is more or less the case a priori, as the upward and downward motion of the fluid is usually well-balanced. Because the absolute values of the Fourier coefficients are later used to specify the wavelength of the turbulent superstructures, subtracting the spatial average is advantageous to eliminate the coefficient corresponding to $q = 0$ and $r = 0$ from equation (5.1), which is only the sum of all data points of the image and does not provide any information about the local variation of the temperature.

In the next step, zeros are padded around the temperature field, until it reaches the size of $2048 \times 2048$ grid points, which is much larger than the original size given in table 5.2.
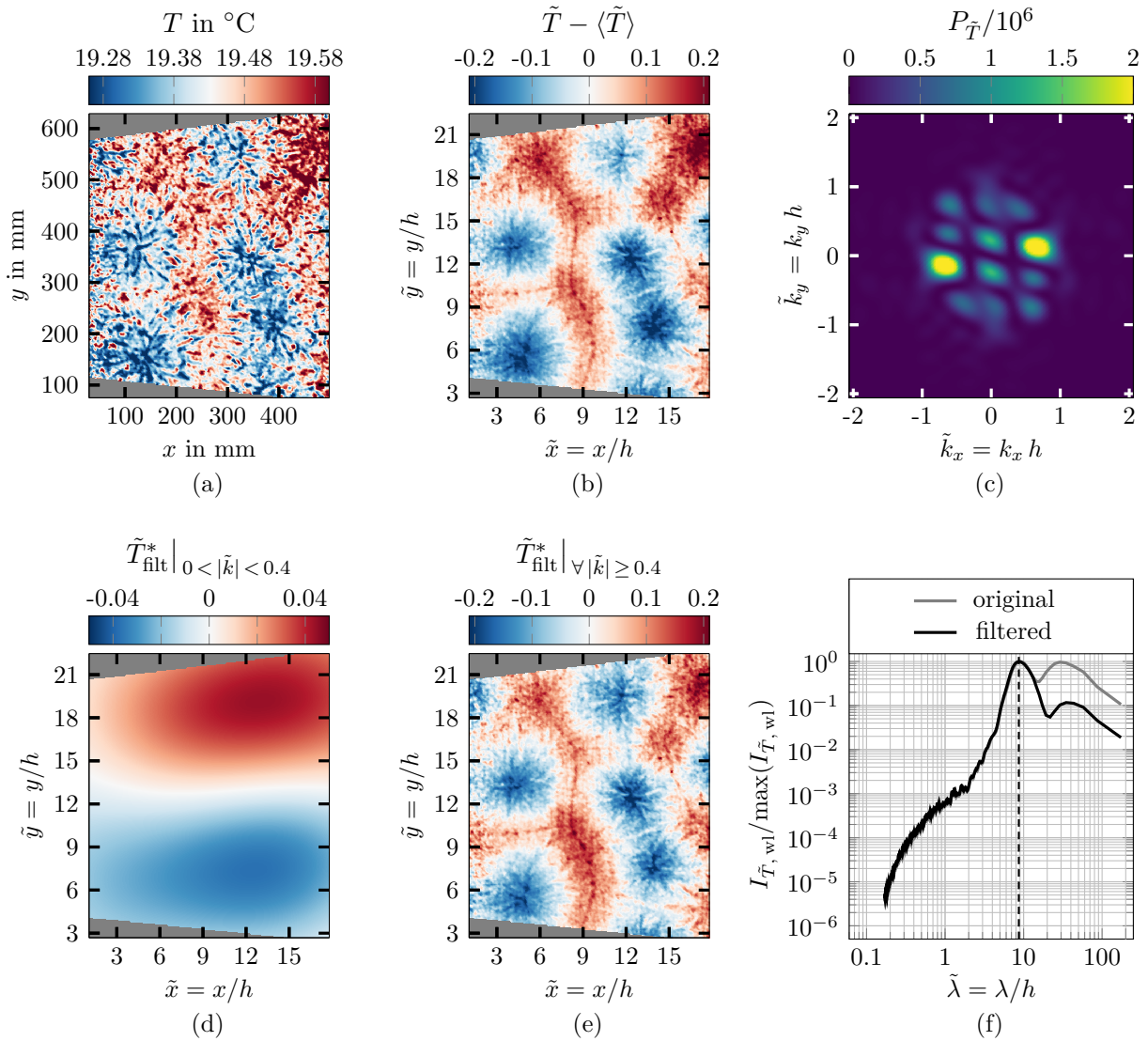
Figure 5.12: Procedure for the determination of the characteristic wavelength of the turbulent superstructures at the example of a series of temperature fields obtained from the measurement in the mid plane at the Rayleigh number $\mathrm{Ra} = 2 \times 10^5$. (a) Exemplary instantaneous temperature field of this series, (b) Non-dimensionalized time-averaged temperature field after subtraction of the spatial average, (c) Power spectrum, (d) Inverse Fourier Transform of the temperature field in figure 5.12b including the wavenumbers in the range $0 < |\tilde{k}| < 0.4$, (e) Inverse Fourier Transform of the temperature field in figure 5.12b including the wavenumbers $\forall |\tilde{k}| \geq 0.4$, (f) Normalized wavelength intensities of the power spectrum determined from the temperature fields in the figures 5.12b and 5.12e.

On this way, the wavelengths in the temperature field can be studied in finer steps. For a better understanding of this reason for the zero padding it might be helpful to think of the sinusoids superimposed on the temperature field. In the non zero-padded temperature field, for example, the combination of the indices $q = 0$ and $r = 1$ from equation (5.1) stands for a wave in the horizontal direction with a wavelength covering the whole temperature field. The successive pair of indices $q = 0$ and $r = 2$ represents the horizontal sinusoidal plane wave with a wavelength that covers already just one half of the temperature field, which is a significant decrease. Due to the enlarging of the temperature field by zero

padding, the difference between the wavelength of successive sinusoids becomes smaller, considering only the wavelengths that do not exceed the size of the temperature field. The specific size of $2048 \times 2048$ grid points has been chosen, because this allows to determine the Fourier coefficients with a suitable resolution of the wavelength, while the number of grid points in each direction is a power of two, which improves the performance of the Fourier analysis [171].

On the basis of the zero-padded temperature field, the Fourier coefficients are computed according to the equation (5.1), yielding $2048 \times 2048$ entries. It gets obvious from the multiplication in this equation, that all the additional zeros do not affect the coefficients. Squaring the absolute values of the Fourier coefficients yields the power spectrum depicted in figure 5.12c, where the wavenumbers in both directions $\tilde{k}_x$ and $\tilde{k}_y$ are indicated at the axis, respectively. In this case, the wavenumber is non-dimensionalized with the height of the Rayleigh-Bénard cell $h$ and accordingly represents the number of wave periods on the length scale $2\pi h$. Only the power spectrum corresponding to a central section of the Fourier transform is depicted for a better illustration, because this part with $115 \times 115$ entries is sufficient to show the largest values around the center with the main information about the temperature field. It should also be noted, that for the representation of the power spectrum in figure 5.12c the upper right and the lower left quadrant as well as the upper left and the lower right quadrant of the original Fourier transform have been interchanged, which is a common procedure when performing two-dimensional Fourier analysis. Therefore, the Fourier coefficients representing the sinusoids with the smallest wavenumbers and thus the largest wavelengths are in the center of the matrix, considering the characteristic of the wavenumbers above the limit given by Nyquist's theorem, which is in the center of the original Fourier transform. The sinusoids with wavenumbers larger than this limit do not indicate small wavelengths in the temperature field, but correspond to a larger wavelength complying with Nyquist's theorem. For this correspondence, the wavenumber at the Nyquist limit is the point of symmetry in the original Fourier transform, i.e. the larger the wavenumber above the Nyquist limit, the smaller the wavenumber represented by the respective Fourier coefficient. Both of the corresponding wavenumbers yield the same absolute value of the Fourier coefficient, which is the reason for the overall symmetry of the power spectrum, which is clearly obvious from figure 5.12c. However, since the Fourier coefficients are conjugate complex in each case, meaning that the real part is the same, but the imaginary part has the contrary sign, the absolute values stemming from the range above the Nyquist limit are indicated with a mathematically equivalent negative wavenumber in figure 5.12c.

Due to the adjusted arrangement of the Fourier Transform, the entries on a circumference around the center of the corresponding power spectrum basically represent the intensity of the waves with the same wavelength, but a varying orientation. In this case, the power spectrum exhibits two distinctive maxima, which are related to the characteristic wavelength of the turbulent superstructures in the temperature field, however, also close to the center of the power spectrum some larger values appear. Those do not correspond to specific flow structures, but result from the experimental boundary conditions. As already addressed in the section 5.2.1, the slight warming of the cooling water in its flow direction from the bottom to the top edge in figure 5.12b yields the trend of the increasing temperatures in this direction of the temperature field. With regard to the reliable investigation of the size of the turbulent superstructures, this large scale trend should be removed. For the demonstration of the large-scale trend all the Fourier coefficients in the Fourier Transform, except for those close to the center, are set to zero. Thus, utilizing the

inverse Fourier Transform according to its general definition in equation (5.2) [170], in which $F$ can be understood as the temperature field obtained from the Fourier Transform $\hat{F}$, reveals the trend in figure 5.12d. In this case, the total wavenumbers $\tilde{k} = (\tilde{k}_x^2 + \tilde{k}_y^2)^{1/2}$ included in the inverse Fourier Transform are in the range $0 < |\tilde{k}| < 0.4$, considering that the Fourier coefficient for $\tilde{k} = 0$ has already been removed by subtracting the spatial average from the temperature field. Thus, all the corresponding wavelengths are larger than $\tilde{\lambda} = 2\,\pi/0.4 \approx 15.7$. It becomes obvious from figure 5.12d, that those wavelengths span much wider horizontal dimensions compared to the turbulent superstructures. Hence, the corresponding entries in the Fourier Transform are set to zero for the determination of the characteristic wavelength of the turbulent superstructures, while all the entries for the smaller wavelengths in the range $\tilde{\lambda} \leq 15.7$ of the original Fourier Transform are taken into account. If then the inverse Fourier Transform is calculated again and only the original size of the temperature field is extracted from the matrix with the $2048 \times 2048$ entries, the large-scale trend of the temperature is considerably reduced in the field of the filtered temperature $\tilde{T}_{\text{filt}}^*$ in figure 5.12e. Therefore, the suitability of this kind of wavelength filtering is confirmed.

$$F_{m,n} = \frac{1}{M\,N} \sum_{q=0}^{M-1} \sum_{r=0}^{N-1} \omega_M^{-m\,q}\, \omega_N^{-n\,r}\, \hat{F}_{q,r} \qquad (5.2)$$

Since the average of the filtered temperature field is $\langle \tilde{T}_{\text{filt}}^* \rangle \neq 0$ due to the removal of some wavelengths prior to the inverse Fourier Transform, the average is again subtracted to get rid of the offset. Once more zero padding is applied to the resulting temperature field $\tilde{T}_{\text{filt}}^{**} = \tilde{T}_{\text{filt}}^* - \langle \tilde{T}_{\text{filt}}^* \rangle$), resulting in the grid with $2048 \times 2048$ entries. Subsequently the Fast Fourier Transform is computed for this temperature field with additional zeros, so that the wavenumbers contained in the temperature field can be investigated with increased resolution based on the resulting power spectrum. The latter is not depicted again, because it looks very similar to that in figure 5.12c, however, the values in the center are now significantly decreased due to the filtering approach. Since the entries on the discrete circumferences around the center of the power spectrum represent the intensity of the waves with the same wavelength, the average can be taken along the circumferences to quantify the presence of each wavelength in the temperature field. Alternative approaches to using the azimuthal average will be discussed further below. The intensities obtained from the azimuthal averaging of the power spectrum of this exemplary temperature field are given along the black curve in figure 5.12f. Here, those are not depicted in dependency of the non-dimensionalized wavenumber $\tilde{k}$, but of the non-dimensionalized wavelength $\tilde{\lambda} = 2\,\pi/\tilde{k}$, because this allows for a better imagination of the length scales. Furthermore, all the averages of the single circumferences are normalized with the maximum average, respectively. Hence, such a curve is in the following always referred to as the normalized wavelength intensity. It becomes obvious, that a pronounced peak occurs in this curve, resulting from the distinctive maxima in figure 5.12c. The corresponding wavelength of about $\tilde{\lambda} = 8.7$ is considered to be characteristic for the turbulent superstructures in this case. Having a look at figure 5.12e this proves to be plausible, as the typical distance between the most dominant patterns with similar temperature can approximately be estimated to this value. The direction, which most strongly contributes to this estimation of the characteristic wavelength of the turbulent superstructures, can be derived from the line connecting the two outstanding maxima in figure 5.12c. Especially along this line the sinusoids with a wavelength of around $\tilde{\lambda} = 8.7$ provide a good match for the temperature field. For comparison, the normalized wavelength intensity determined from the original

temperature field with the large scale trend in figure 5.12b is shown in figure 5.12f as well. It can be seen, that the global maximum cannot clearly be distinguished in this case, as a second distinctive peak occurs at around $\tilde{\lambda} = 29$, which is far away from the real wavelength of the turbulent superstructures. Hence, it is proven that the experimental data must be evaluated carefully with an additional filtering, if the intensities of the power spectrum are used to find out the wavelength of the turbulent superstructures.

Having demonstrated the method for determination of the characteristic wavelength of the turbulent superstructures by means of a temperature field, the procedure for identifying their wavelength in the velocity field should be addressed as well. In principle the method is the same, so that it is not discussed in detail again. However, as the velocity field contains some regular variations on smaller length scales despite the time-averaging, the filtering in the wavelength domain is modified in comparison to the temperature field. This is briefly shown in the following at the example of the field of the vertical velocity component corresponding to the temperature field, which has just been considered to explain the analysis depicted in figure 5.12. The non-dimensionalized time-averaged velocity field with subtracted average can be seen in figure 5.13a. Even though the turbulent superstructures are dominant, it becomes apparent that also the change of the velocity on smaller length scales is not negligible. But since these should not affect the determination of the characteristic wavelength of the superstructures, the filter applied to the Fourier Transform of the velocity field removes variations on small length scales on the one hand and, on the other hand, any trends of the velocity on very large length scales, even though the latter are obviously less present than in the temperature field. The lower threshold of the wavenumber has again been set to $|\tilde{k}| = 0.4$, which is equivalent to the wavelength $\tilde{\lambda} = 15.7$, thereby ensuring that a significant large-scale trend beyond the size of the superstructures does not occur. The determination of an appropriate upper threshold of the wavenumber is more challenging, since the length scales of the smaller structures in the velocity field strongly depend on the Rayleigh number. Hence, the approach is to apply a very strict filter, which is capable of removing the small-scale variations in any case, thereby revealing the turbulent superstructures more clearly. Looking at the velocity field in figure 5.13a it can be estimated, that their characteristic wavelength typically spans horizontal dimensions of $\tilde{\lambda} \approx 8$ in this case, such that the wavelengths around $\tilde{\lambda} = 8$ should not be affected by the filtering. On the basis of this estimation and with a view to the velocity fields at the other Rayleigh numbers the upper threshold of the wavenumber has been set to $|\tilde{k}| = 1.3$. Therefore, the filter restricts the wavenumbers to the range $0.4 \leq |\tilde{k}| \leq 1.3$, which corresponds to the wavelengths in the range $4.8 \leq \tilde{\lambda} \leq 15.7$. Using this range of wavenumbers the main characteristic of the pattern of the turbulent superstructures is not altered for each of the applied Rayleigh numbers.

The effect of the filter is demonstrated in figure 5.13b, which shows the velocity field determined from the filtered Fourier Transform of the original velocity field in figure 5.13a. It is clearly apparent that the undesirable wavelengths have successfully been eliminated, but still the contours of the superstructures are properly displayed. The only difference worth mentioning is that the updrafts in the areas around $(\tilde{x}, \tilde{y}) = (14, 5)$ and $(\tilde{x}, \tilde{y}) = (14, 10)$ are weakened by the filtering. Looking at figure 5.12e it can be seen that this is in good agreement with the corresponding temperature field, which indicates that the temperature in these areas is not noticeably above the average. Furthermore, the normalized wavelength intensity determined via the azimuthal averaging of the power spectrum of the velocity field is depicted in figure 5.13c. The expected decrease of the intensity on both sides of the peak is confirmed, however, the location of the peak itself

is not shifted by the filter in this exemplary case. Nevertheless, the filter is consistently applied, which has turned out to be especially important for the measurements at the larger Rayleigh numbers. This can be seen in figure 5.14 at the example of a temperature field and the corresponding velocity field resulting from the measurement in the mid plane at the Rayleigh number $Ra = 7 \times 10^5$. The results in the top row for the temperature field and in the lower row for the velocity field demonstrate that in both cases the filtering is necessary to impede that the characteristic wavelength of the superstructures is either strongly overestimated because of a large-scale trend in the temperature field or strongly underestimated due to variations on smaller length scales in the velocity field.
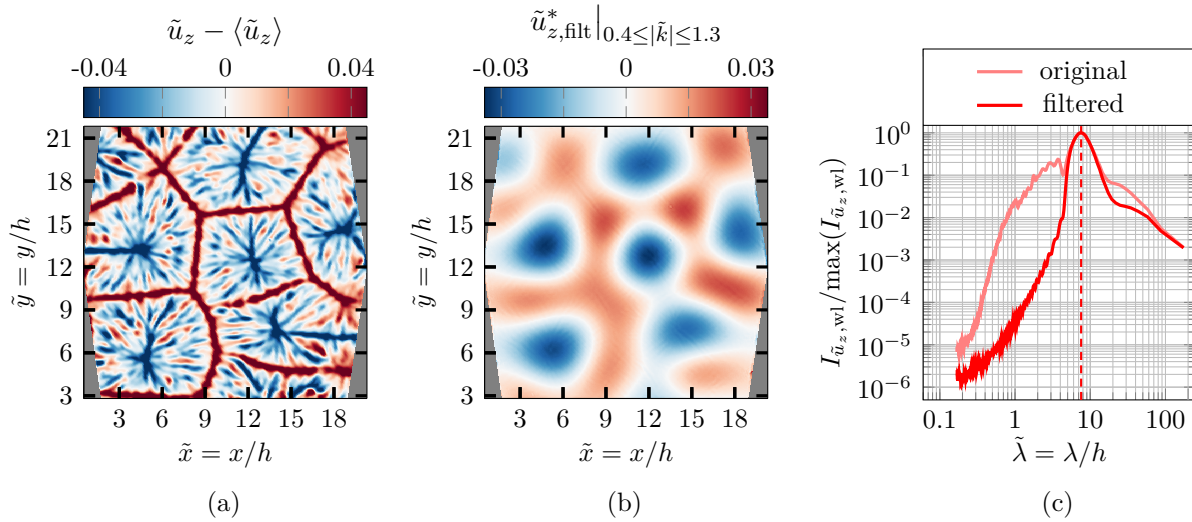


Figure 5.13: Illustration of the filter in the wavenumber domain for the determination of the characteristic wavelength of the turbulent superstructures in the field of the vertical vertical component. (a) Exemplary time-averaged field obtained from the measurement in the mid plane at the Rayleigh number $Ra = 2 \times 10^5$, (b) The field of the vertical velocity component after applying the filter, (c) The normalized wavelength intensities of the corresponding power spectra.

A close look to all the figures, which show the normalized wavelength intensities obtained from the power spectrum of the temperature and velocity fields, reveals that the peak is not located at the same wavelength. In each case, the peak in the velocity field is shifted towards smaller wavelengths, which would not be expected intuitively. However, when reviewing the studies about turbulent superstructures in RBC, it becomes obvious that this point remains puzzling. For instance, this aspect has already been reported in the work [53], where the characteristic wavelength of the superstructures has been determined from the time-averaged spectra of the thermal variance and the turbulent kinetic energy. Furthermore, the wavelength of the turbulent superstructures uncovered by time-averaging of the temperature and the velocity field has been analyzed deeply by means of numerical simulations in the work [11] and it has been found, that the wavelengths corresponding to the size of the superstructures in the temperature field $\hat{\lambda}_{\tilde{T}}$ tends to be larger than their size in the velocity field $\hat{\lambda}_{\tilde{u}_z}$. This difference has especially occurred for large Rayleigh numbers and Prandtl numbers, since the temperature in this case gets rather advected by the horizontal velocity than diffused by thermal diffusivity. In the numerical study [57] for $10^5 \leq Ra \leq 10^7$ and $Pr = 7$ it can also be seen that larger dimensions of the superstructures have been determined from the time-averaged temperature fields. However, recently it has explicitly been pointed out in the reference [58], that superstructures of the same size exist in both fields, but in the velocity field these are more covered by structures on smaller
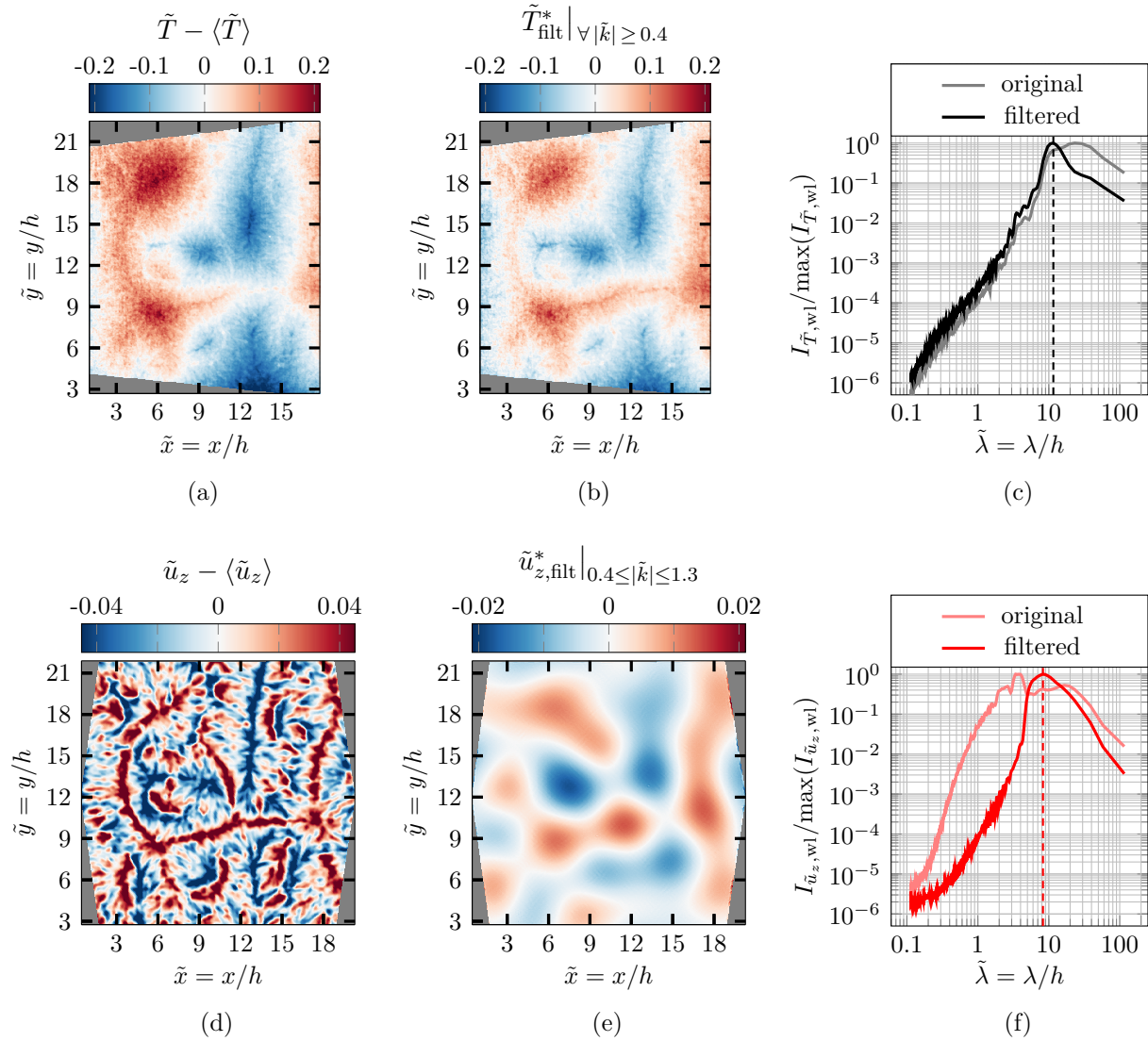
Figure 5.14: Illustration of the filtering approach applied to an exemplary measurement at the Rayleigh number $Ra = 7 \times 10^5$. The top row shows the non-dimensionalized time-averaged temperature field with subtracted spatial average (a), the filtered temperature field (b) and the corresponding normalized intensities of the wavelengths (c). Analogously, for the velocity field these results are depicted in the figures in the bottom row (d-e).

scales. By applying a low-pass filter in the wavenumber domain to the instantaneous fields the variation of the velocity on smaller length scales has been removed, such that the coherence of the structures in both fields has been shown in this numerical study. Hence, as it has just been shown, in the present work a filter in the wavenumber domain is in addition applied after the time-averaging to fully remove the variations of both the temperature and the velocity on small length scales, but still there is a little discrepancy.

In order to figure out, whether the method for the determination of the characteristic wavelength of the superstructures may affect the results, alternative approaches to using the azimuthal average of the power spectrum have exemplarily been applied to the filtered temperature and velocity field from measurement in the mid plane at the Rayleigh number $Ra = 2 \times 10^5$, which are depicted in the figures 5.12e and 5.13b. The approaches can be compared in figure 5.15. On the left hand side the normalized intensities resulting from the

azimuthal averaging of the power spectrum are shown again. Even though the azimuthal averaging is the most obvious method to quantify the intensity of the wavelengths in the temperature and velocity field, it might be the case, that smaller wavelengths away from the center of the power spectrum are underestimated, since a local maximum is less weighted due to the averaging over a larger number of entries. In order to impede that local peaks of the power spectrum are covered by the averaging, the azimuthal sum can be used instead. Since most of the entries towards the rim of the power spectrum are almost equal to zero, small wavelengths are not significantly overestimated, but of course their intensity increases due taking the sum over more entries of the power spectrum. In return the largest wavelengths are decreased, so that the peak at the wavelength of the superstructures can in many cases be distinguished more clearly, which is apparent from figure 5.15b. Since the power spectrum in figure 5.12c has demonstrated that a sinusoidal plane wave with a specific orientation may provide an outstanding match for the turbulent superstructures, it is also an option to directly determine the wavelength corresponding to the maximum of the power spectrum. The maxima of the circumferences around the center of the power spectrum of the investigated example are depicted in figure 5.15c. It can be seen that each of the three approaches yields a slightly smaller characteristic wavelength of the superstructures in the velocity field, respectively. Hence, this discrepancy is not supposed to be caused by the azimuthal averaging. In section 5.2.6 it will again be addressed based on a larger number of data sets. As the three methods illustrated in figure 5.15 yield similar results regarding the position of the peak, all of them are taken into account and the median of the wavelengths at the peaks is taken separately for the temperature and the velocity field in each case, in order to determine the wavelength of the superstructures most reliably.
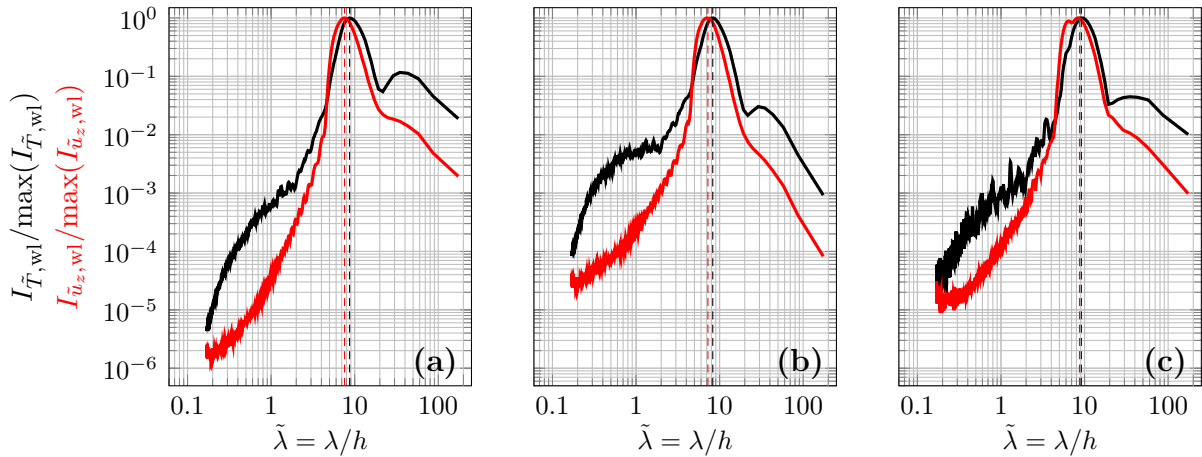


Figure 5.15: Illustration of different methods for the estimation of the normalized wavelength intensities in the time-averaged fields of the temperature and of the vertical velocity component shown in the figures 5.12e and 5.13b, determined from the power spectrum via the azimuthal average (a), the azimuthal sum (b) and the maximum in azimuthal direction (c).

As the typical wavelength of the turbulent superstructures is in the end described with a single value, it should also be shown that this is reasonable. For this, different filter ranges in the wavenumber domain are applied to the temperature field obtained from the measurement in the mid plane at the Rayleigh number $\mathrm{Ra} = 2 \times 10^5$. The temperature field resulting from the filtering of the large-scale trend can be seen in figure 5.16a again. Contrary to the corresponding velocity field depicted above in figure 5.13a, this field only includes some negligible variations on small length scales. Nevertheless, at first the

effect of using the same filtering range as for all the velocity fields, which incorporate the wavenumbers in the range $0.4 \leq |\tilde{k}| \leq 1.3$ after the filtering, should be visualized. The result in figure 5.16b demonstrates, that the pattern of the turbulent superstructures is maintained. Thus, the filtering range is now increased, such that only the wavenumber determined from the peak of the normalized wavelength intensity remains. In this example the three methods according to figure 5.15 yield a median wavenumber of $\tilde{k} = 0.72$ for the peak, corresponding to the wavelength $\tilde{\lambda} = 8.7$. After this very strict filtering some changes are obvious from the resulting temperature field in figure 5.16c, which is not surprising, considering that in this case only 114 entries of the total of $2048 \times 2048$ entries are not removed from the Fourier Transform. However, comparing all the results in figure 5.16 it is seen that the temperature field based on only one wavenumber still represents a good approximation to the other temperature fields. It can therefore be concluded, that the characterization of the wavelength of the turbulent superstructures via the peak of the normalized wavelength intensity is a suitable approach.
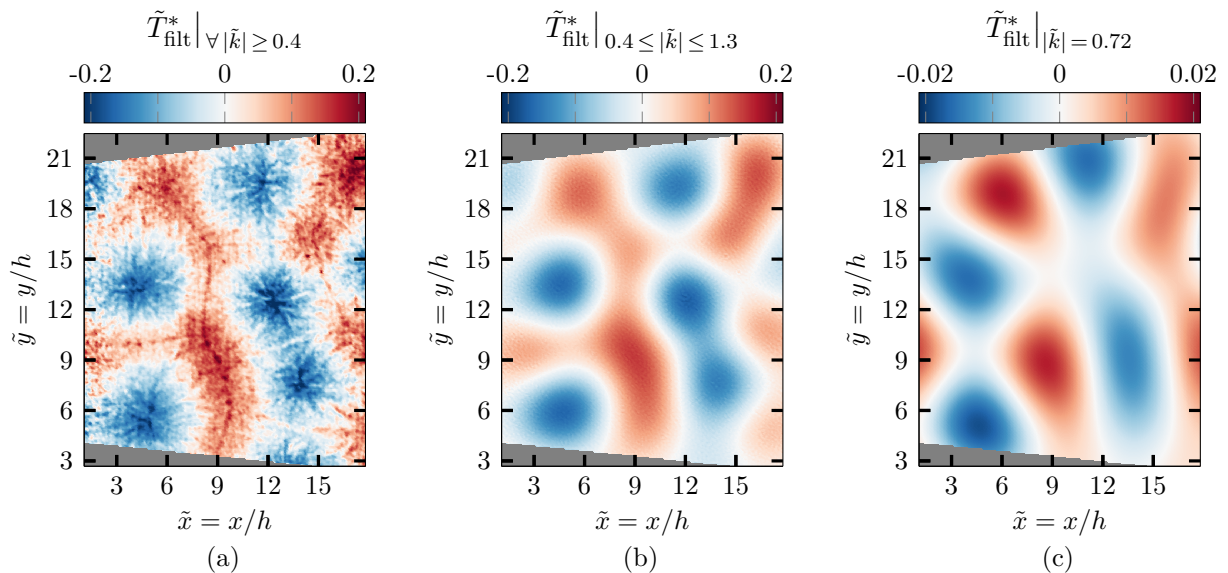


Figure 5.16: Application of different filters in the wavenumber domain to an exemplary time-averaged temperature field obtained from the measurement in the mid plane at the Rayleigh number $\mathrm{Ra} = 2 \times 10^5$. The range of the wavenumbers, which are not removed by the filter, are given at the top of each field.

So far the procedure of the Fourier analysis conducted in this work has been illustrated with regard to clearly revealing the superstructures in both the temperature and the velocity field, which enables to determine their characteristic wavelength more reliably. However, as the measurements have been performed over extended time intervals, it is possible to observe the reorganization of the turbulent superstructures as well. Since their reorganization can also be characterized with the Fourier analysis, the procedure shall also be shortly explained. The reader may again have a look at the flowchart in figure 5.11, where it can be seen that nearly all the processing steps of the measurement data are the same as for the Fourier analysis demonstrated heretofore except for the last step. The power spectrum is then not evaluated via azimuthal operations, but via radial averaging of the entries. Taking the average of the entries along the discrete lines from the center of the power spectrum towards the rim for different azimuthal angles $\phi$ allows to quantify the arrangement of the turbulent superstructures. Based on the exemplary

filtered temperature field from the measurement in the mid plane at the Rayleigh number $Ra = 2 \times 10^5$ in figure 5.17a, the radial averaging of the corresponding power spectrum is sketched in figure 5.17b. The resulting radial average, which is in the following also referred to as the directional intensity $I_{\tilde{T}, \text{dir}}$, is depicted in figure 5.17c in dependency of the azimuthal angle $\phi$. Due to the symmetry of the power spectrum around the center the directional intensities are restricted to the angles in the range $0 \leq \phi \leq \pi$. From the radial average the arrangement of the turbulent superstructures becomes clearly obvious, since the peak at about $\phi = \pi/16$ indicates the outstanding maximum of the power spectrum. By means of these analysis it will be seen in section 5.2.6, that the superstructures relocate over time. It shall finally be noted that for the radial averaging only a central section of the power spectrum is used in each case, because the entries strongly decrease for large wavenumbers. As those are not of interest for the investigation of the superstructures, only the wavenumbers in the range $|\tilde{k}| < 2\pi/3$ are considered for the radial averaging, thereby ensuring that the relevant entries are incorporated. This is confirmed by the power spectrum in figure 5.17b, which is restricted to this range of the wavenumbers.
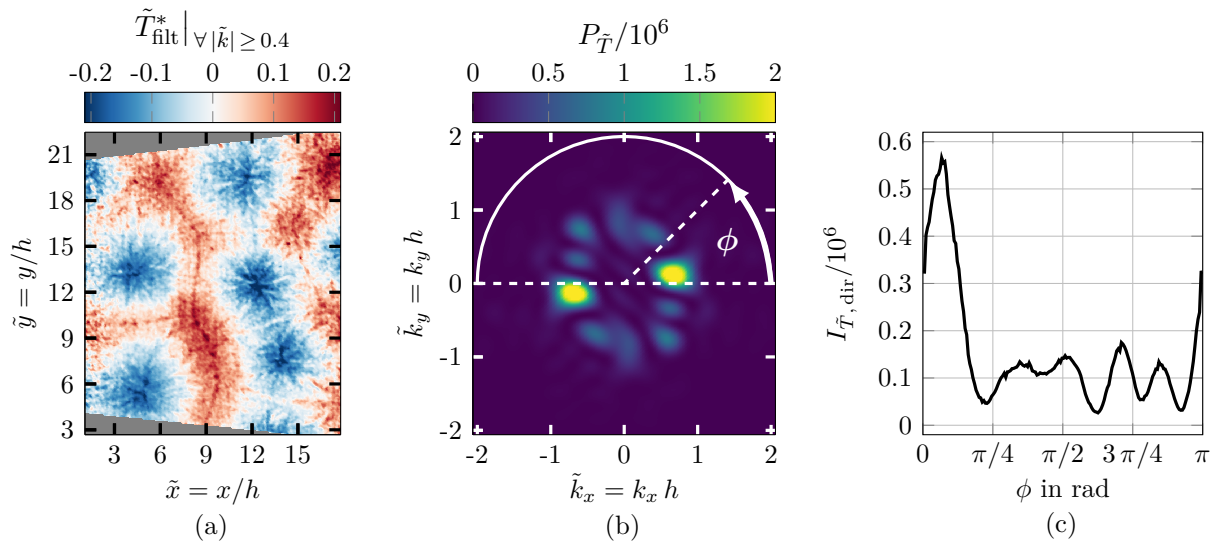


Figure 5.17: Procedure for the determination of the organization of the turbulent superstructures, visualized by means of a time-averaged temperature field in the mid plane at the Rayleigh number $Ra = 2 \times 10^5$ (a). The organization can already be seen in the power spectrum (b) and is additionally shown with the corresponding radial average of the latter in dependency of the azimuthal angle $\phi$ (c).

## 5.2.5   Initial formation of the turbulent superstructures

As it has been described in section 5.1, the tracer particles for the measurements are inserted into the working fluid with slight pressure impulses and the flow is strongly disturbed by that, such that the turbulent superstructures cannot be seen from the beginning of each measurement. However, already a short time after the external disturbance, many thermally induced flow structures start to evolve and assemble to larger structures, that indicate the turbulent superstructures. Even though the arrangement of the small convective flow structures is not replicable, because it depends on the initial conditions as for example the arrangement of the flow structures prior to the disturbing and the seeding process itself, the continuous growth of the flow structures could be observed in

each of the initial recordings with the duration of 45 min. As the process of the growing exhibits similar features, respectively, it is exemplarily demonstrated in this section for the measurement in the mid plane of the Rayleigh-Bénard cell at Ra $= 4 \times 10^5$ with the temperature settings according to table 5.1. In a similar manner this has already been presented in the study [24] for another measurement in the top plane.



$$\tilde{T} = (T - T_c)/(T_h - T_c)$$

(a) $t = 100\,\text{s}$     (b) $t = 300\,\text{s}$     (c) $t = 500\,\text{s}$     (d) $t = 800\,\text{s}$

(e) $t = 1200\,\text{s}$     (f) $t = 1700\,\text{s}$     (g) $t = 2300\,\text{s}$     (h) $t = 2690\,\text{s}$
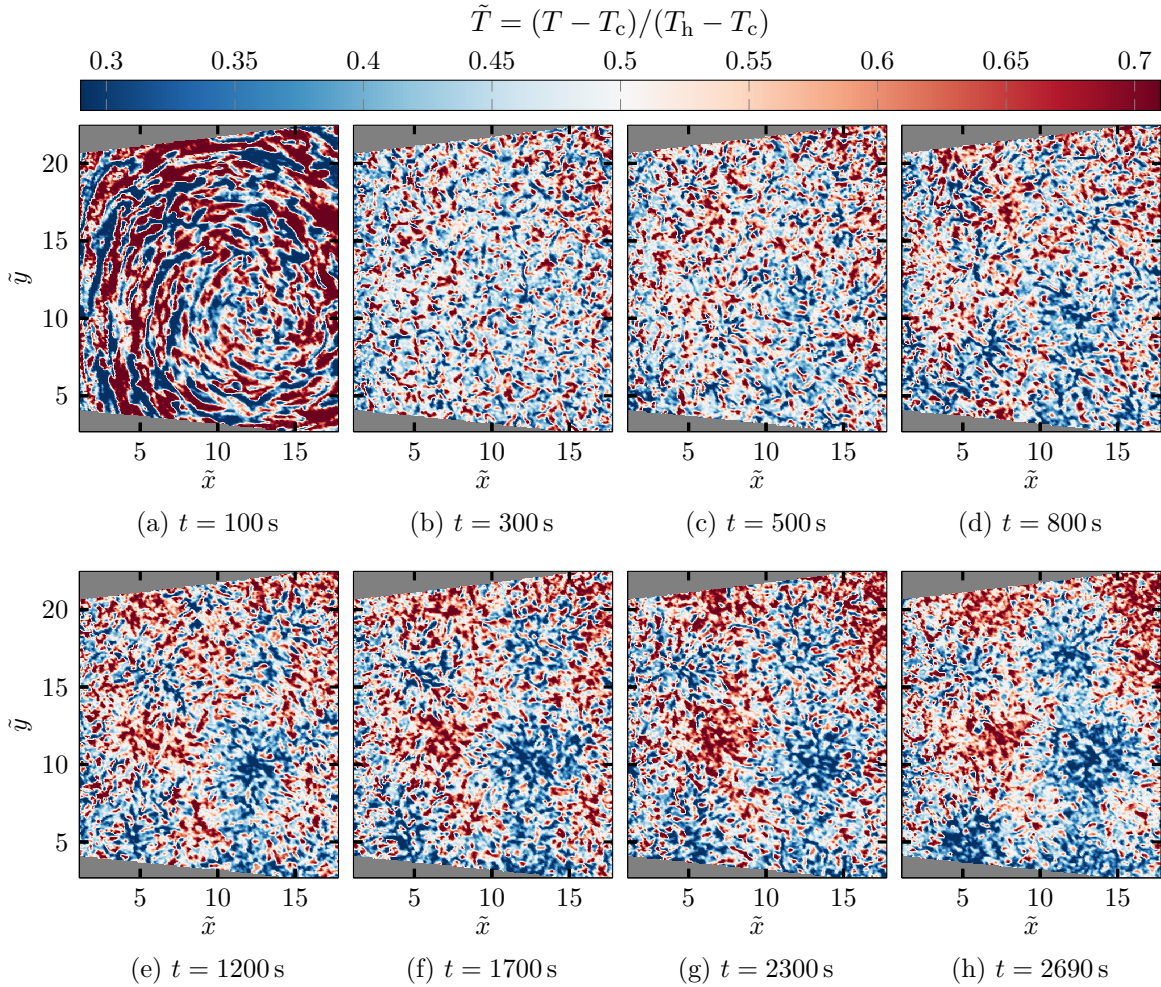
Figure 5.18: Instantaneous temperature fields for different instants of time, showing the initial growth of the flow structures subsequent to the end of the stirring process at $t = 0\,\text{s}$ for the measurement in the mid plane at the Rayleigh number Ra $= 4 \times 10^5$. The settings of the measurement are listed in table 5.1.

Aiming to show this development of the flow structures, which are correlated to the temperature field, only the images recorded with the color camera have been applied to determine the temperature field for different points in time. Some successive temperature fields for the measurement at Ra $= 4 \times 10^5$ are shown in figure 5.18 together with the corresponding time instants, starting from $t = 100\,\text{s}$ subsequent to the first image recording at $t = 0\,\text{s}$ immediately after the stirring process. From the shape and the arrangement of the structures in temperature field at $t = 100\,\text{s}$ depicted in figure 5.18a the disturbance of the flow via the pressure impulses is clearly obvious, as these impulses have caused the noticeable large-scale swirl in the cell. However, already in the temperature field at $t = 300\,\text{s}$ shown in figure 5.18b this distinctive large rotating motion cannot be observed visually anymore and smaller structures induced by thermal buoyancy become apparent. Those small structures further assemble over time from $t = 500\,\text{s}$ up to $t = 2690\,\text{s}$ in the

figures 5.18c - 5.18h. Such a growth of the structures has also been reported based on the results of numerical simulations [51]. In the course of time the larger patterns of warm and cold fluid can already be identified, which is the footprint of the turbulent superstructures.

In order to further confirm the initial growth of the structures in the instantaneous temperature fields, the procedure for the Fourier analysis demonstrated in the previous section is used. However, in this case no time-averaging is performed, so that the processing according to the flowchart in figure 5.11 is directly applied to the exemplary instantaneous temperature fields in figure 5.18. Hence, the normalized wavelength intensities are obtained from each of the instantaneous temperature fields via the power spectrum, respectively. Different methods for the determination of the normalized wavelength intensities have been discussed based on figure 5.15, but for this demonstration only the azimuthal average of the power spectrum is considered. The resulting normalized wavelength intensities can be seen in figure 5.19 for the different instants of time. Since the effect of the initial stirring process is strongly pronounced at the beginning of the image recording, the intensity profiles in figure 5.19 are shown starting from $t = 500\,\mathrm{s}$.
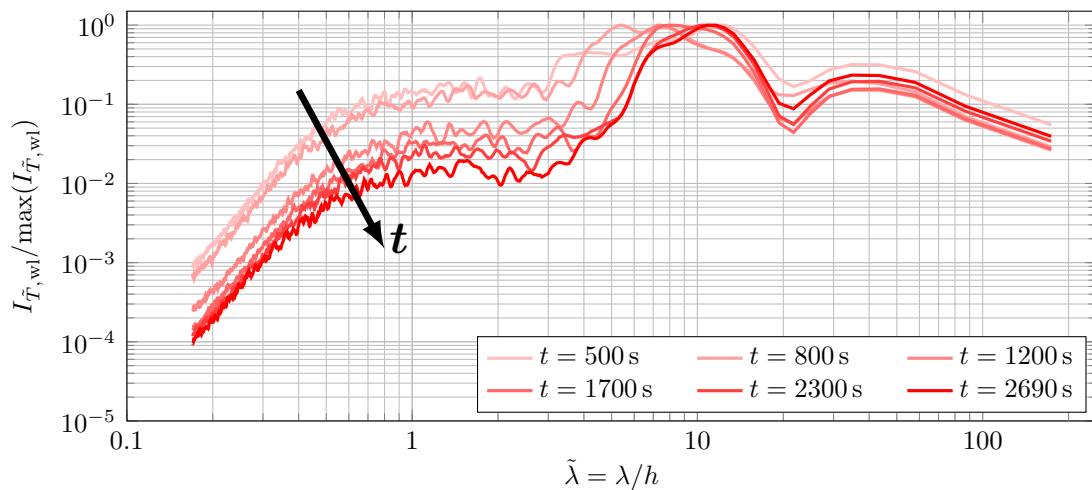


Figure 5.19: Temporal variation of the normalized wavelength intensities after the initial disturbance of the flow at $\mathrm{Ra} = 4 \times 10^5$. The results starting from $t = 500\,\mathrm{s}$ have been obtained from the instantaneous temperature fields in the mid plane depicted in figure 5.18.

It can clearly be seen that the intensities of small wavelengths decrease over time and that the peaks at larger wavelengths change their position. This demonstrates that small structures in the temperature field assemble to larger structures, which need some time to reach a typical pattern size. While the curve of the normalized wavelength intensity for the time instant $t = 500\,\mathrm{s}$ still has a different form close to the peak due to the influence of the initial disturbance, the other curves reveal that the wavelength corresponding to the peak increases. Approaching the end of the investigated time range the curves become very similar and the peaks nearly coincide with each other, showing that the size of the structures does not considerably change anymore between those time instants. The normalized wavelength intensity for the last time instant at $t = 2690\,\mathrm{s}$ has its maximum at approximately $\tilde{\lambda} = 10.2$, which roughly matches the corresponding temperature field in figure 5.18h, since the mean distance of the most dominant patterns with similar temperature can rouhgly be estimated to this value.

From the results of the other experiments in the mid plane for the different Rayleigh numbers a similar behavior has been found. Hence, in each case the normalized wavelength

intensities corresponding to the small-scale structures decrease over time, while the maximum at larger wavelengths shifts until the influence of the initial disturbance has fully decayed. After this initial transient, a clear maximum occurs in the intensity of the wavelengths, as it can be seen in figure 5.20. It has turned out, that the initial transient passes off on smaller time scales with increasing Rayleigh number, because thermal buoyancy is more dominant and forces the effect of the external disturbance to abate more quickly. Hence, while the transient process for the Rayleigh numbers $\mathrm{Ra} = 2 \times 10^5$ and $\mathrm{Ra} = 4 \times 10^5$ has just come to the end after the initial recording covering $45\,\mathrm{min}$, the intensity profiles of the wavelength reach the desired form with one distinctive maximum representing the characteristic wavelength of the turbulent superstructures already at earlier instants of time, if the Rayleigh number is larger. This maximum does not anymore continuously shift towards larger wavelengths over time, however, due to the gradual relocation of the turbulent superstructures temporary changes of the determined characteristic wavelength still occur within the investigated area, as it will be shown in the next section.
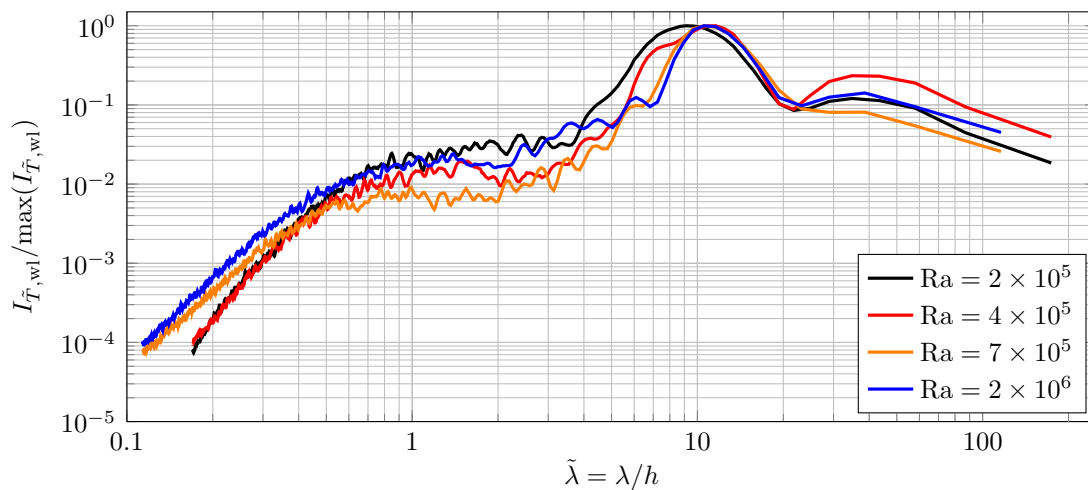


Figure 5.20: The normalized wavelength intensities for the different Rayleigh numbers obtained from the last instantaneous temperature field of each recording in the mid plane after the initial disturbance of the flow.

## 5.2.6 Long-term investigations of the turbulent superstructures

Since the evaluation of all the measurement data requires several processing steps, it is computationally expensive to determine both the temperature and the velocity fields over extended time spans. However, compared to direct numerical simulations (DNS), which are oftentimes are applied to investigate turbulent flows, the computing time is much smaller. The high computational costs of the DNS are still a significant drawback, but as the equations of motion are solved with a very high spatial resolution to capture the variation of the physical quantities on the smallest length scales, the numerical data provide the possibility to analyze the flow in great detail. Based on results of the numerical simulations it has been shown in section 5.2.3, that the high spatial resolution in the determination of the temperature and the velocity allows to accurately investigate the local heat flux in RBC. Of course, this is also possible in the experimental facility at hand, but it has been demonstrated that the spatial resolution must be further enhanced,

such that the local peaks of the heat flux are not smeared out. For this purpose a larger number of cameras would have to be applied to study the flow with the presented optical measuring technique, as the decrease in the size of the field of view is not a suitable option, if turbulent superstructures are of interest. Using more cameras to achieve a spatial resolution comparable to that of the DNS would then also yield a substantial increase of the computational costs in the evaluation of the measurement data. Irrespective of the computational efforts, it is not the aim of the present work to push the spatial resolution to the experimentally achievable limit, but to get a more general impression of large aspect ratio RBC. Hence, the limited spatial resolution, which still allows to capture the small-scale structures in the flow, has been accepted with a view to the possibility of the long-term investigation of the flow without excessively increasing the computation time. This can be considered as the complementary part to the numerical simulations, as those do usually not cover such extended time spans. Therefore, the last section of this work shall give some insights into the behavior of turbulent superstructures on the long run.

In order to show that the turbulent superstructures reorganize over time, again the measurement performed in the mid plane at the Rayleigh number Ra $= 2 \times 10^5$ is considered at first. Three time-averaged temperature fields are depicted in the figures 5.21a - 5.21c, which show the arrangement of the turbulent superstructures for the time instants $\tilde{t}_1 = 1398$, $\tilde{t}_2 = 3529$ and $\tilde{t}_3 = 5393$, respectively. The given time instants are here and in the following always understood as the start of each recording of the image series, which are used for the time-averaging. The reference at $\tilde{t} = 0$ is the end of the initial seeding process. Just for a better imagination it should be noted that the time instant $\tilde{t}_3 = 5393$ in the demonstrated case corresponds to the last of the evaluated image series, which has been recorded 6 h 45 min after the end of the initial seeding process. From the comparison of the temperature fields it becomes clear that the pattern of the turbulent superstructures varies slowly. For example, comparing the temperature fields in the figures 5.21a and 5.21b many similarities can be seen, but there are also some remarkable changes, as for instance the merging of the two cold areas at the bottom right side. In the temperature field for the last time instant the elongated cold area from the second time instant is divided again. The fact, that the relocation of the superstructures in the time gap of more than 2 h between each of the temperature fields can be followed, confirms that the reorganization is a very slow process.

Even though the variation of the pattern left by the turbulent superstructures can be seen with the naked eye, this should also be quantified. The method for quantitatively estimating the reorganization, as it has been explained at the end of the section 5.2.4, is based on the power spectrum of the temperature fields. The power spectra, which are depicted in the figures 5.21d - 5.21f, visualize the rearrangement of the superstructures at the first glance. For the first time instant the power spectrum exhibits two outstanding maxima, which have already been seen in a similar form in figure 5.17b. The line connecting the two maxima indicates the direction, in which a sinusoidal plane wave with the corresponding wavenumber yields a good match to the temperature field in figure 5.21a. A close look to this figure also reveals that the variation of the temperature along this direction can be expressed with a wave in good approximation. The relocation of the turbulent superstructures is apparent from the power spectra in the figures 5.21b and 5.21c. While the two peaks are decreased at the second time instant, there is an even more uniform distribution of the power spectrum around the center at the third time instant. The reader may again look at the corresponding temperature fields, where the change of the power spectrum can be recognized. Especially from the temperature field in figure
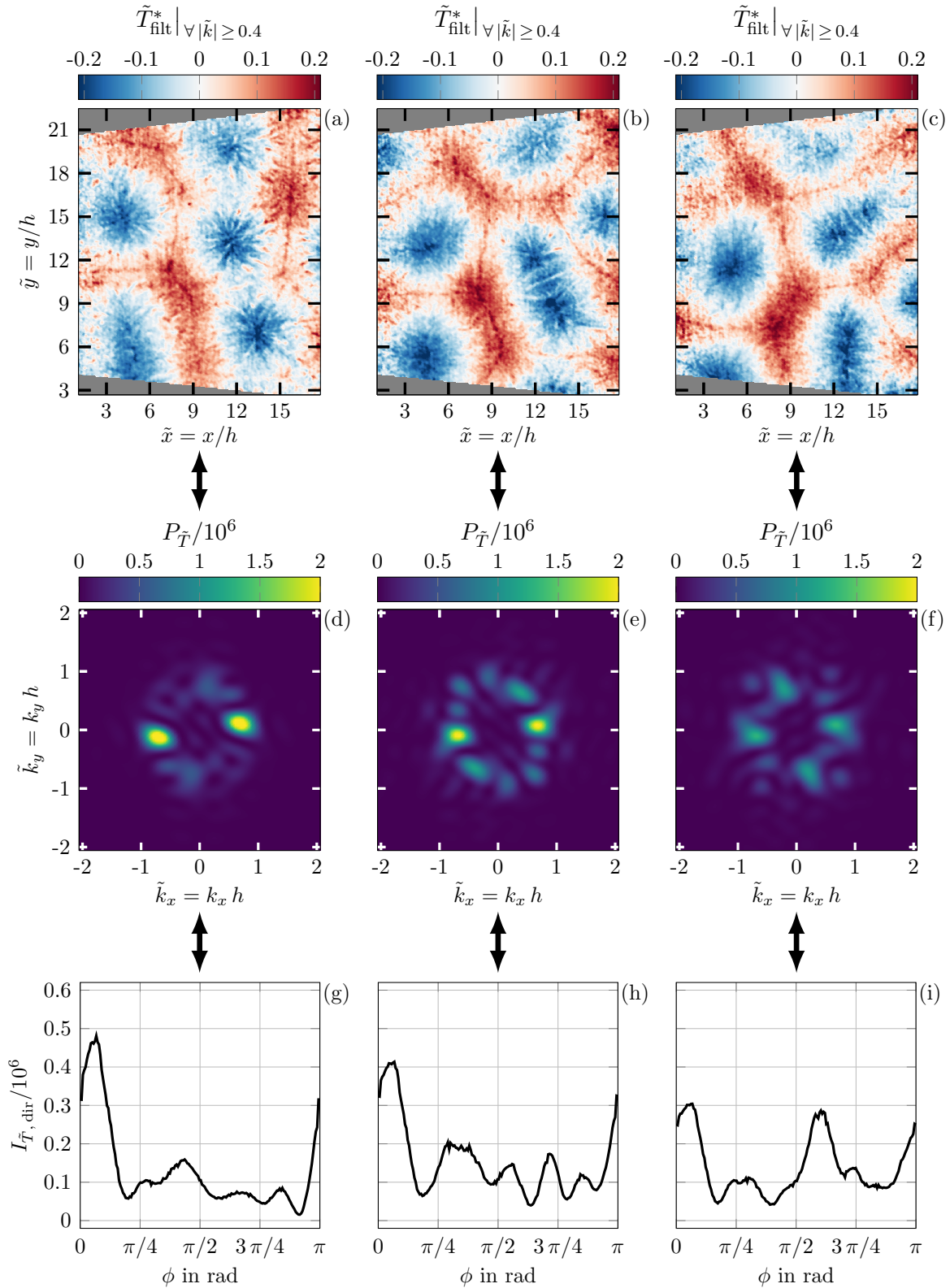
Figure 5.21: Exemplary demonstration of the reorganization of the turbulent superstructures by means of the time-averaged temperature field in the mid plane at the Rayleigh number $\mathrm{Ra} = 2 \times 10^5$. In the upper row the temperature fields with the averaging interval beginning at the time instants $\tilde{t}_1 = 1398$, $\tilde{t}_2 = 3529$ and $\tilde{t}_3 = 5393$ are shown. These have been processed with the filtering approach explained in the section 5.2.4. In the mid row the central section of the corresponding power spectrum is depicted, while the directional intensities of the entries in these sections of the power spectra are given in dependency of the azimuthal angle $\phi$ in the lower row.

5.21c a typical size of the superstructures can be found without a noticeably preferential orientation, which explains the stronger pronounced uniformity of the power spectrum. All these findings are additionally confirmed in the figures 5.21g - 5.21i. These show the directional intensities obtained from the radial averaging of the power spectrum, which clearly reveal the transition towards the more uniform distribution of the power spectrum by means of the ratio of the peaks. As it has been sketched in figure 5.17b, the azimuthal angle $\phi$ for the radial averaging starts between the lower and the upper half on the right side of the power spectrum and increases in counterclockwise direction.

Since the results illustrated in figure 5.21 only show the arrangement of the superstructures at the example of three time-averaged temperature fields measured in the mid plane at the Rayleigh number Ra $= 2 \times 10^5$, their reorganization should be further discussed. Hence, the directional intensities $I_{\tilde{T},\mathrm{dir}}$ determined from all the time-averaged temperature fields in the mid plane are depicted in the figure 5.22 for the different Rayleigh numbers. In this case, the directional intensities are shown in dependency of the azimuthal angle $\phi$ and the non-dimensionalized time $\tilde{t}$, so that the reorganization of the superstructures becomes obvious. Furthermore, the directional intensities are normalized with the maximum occurring value at each Rayleigh number, respectively. In this manner the reorganization has already been addressed in the numerical study [11], but in the present work the investigated time interval is larger. However, since the measurements for the different Rayleigh numbers cover the same time interval in physical units, the non-dimensionalized time-interval varies, as it can be seen in figure 5.22. It should also be noted, that the results for the Rayleigh number Ra $= 2 \times 10^6$ are considered trustworthy up to $\tilde{t} \approx 12000$, because the measurement data for later points in time are in this case affected by the decreasing concentration of the TLCs R25C50W in the measurement plane.

The results of the directional intensities conspicuously demonstrate, that the maximum values are mostly at the left or right margin, showing that the turbulent superstructures are oftentimes arranged in a similar way. It has already been seen before that two distinctive peaks may occur in the power spectrum. Now it is confirmed that these peaks mostly appear in a narrow range, corresponding to a wavelike variation of the temperature along the $x$-direction rather than the $y$-direction. This suggests that the turbulent superstructures do not freely move in the experiment. It can therefore be assumed that the slight temperature inhomogeneities on the heating and cooling plate influence the organization of the superstructures. However, in this context it should be mentioned that an almost persisting arrangement of the superstructures has in some cases also been found in reference [11], though the investigated time interval is smaller in that study. Therefore, this must not necessarily result from the experimental boundary conditions, but as the two maxima frequently occur at a similar position for each Rayleigh number, a relation to the deviations from the isothermal boundary condition is not unlikely. Despite this the flow is not strictly predetermined, so that the relocation of the superstructures can be observed, respectively.

Comparing the results in figure 5.22, a clear variation with regard to the dynamic of the reorganization does not become obvious in this range of the Rayleigh number. Nevertheless, a few differences can be seen. For their discussion it is helpful to select some temperature fields, which most clearly show the reorganization of the superstructures at the different Rayleigh numbers. A suitable selection is possible on the basis of the figures 5.22a - 5.22d. The temperature fields for the chosen time instants marked with an arrow at the right side of each plot of the directional intensities are depicted in figure 5.23. One aspect, which is noticeable in the figures 5.22c and 5.22d obtained from the measurements at the two largest

$$I_{\tilde{T},\,\text{dir}}/\max(I_{\tilde{T},\,\text{dir}})$$

(a) Ra $= 2 \times 10^5$

(b) Ra $= 4 \times 10^5$

(c) Ra $= 7 \times 10^5$
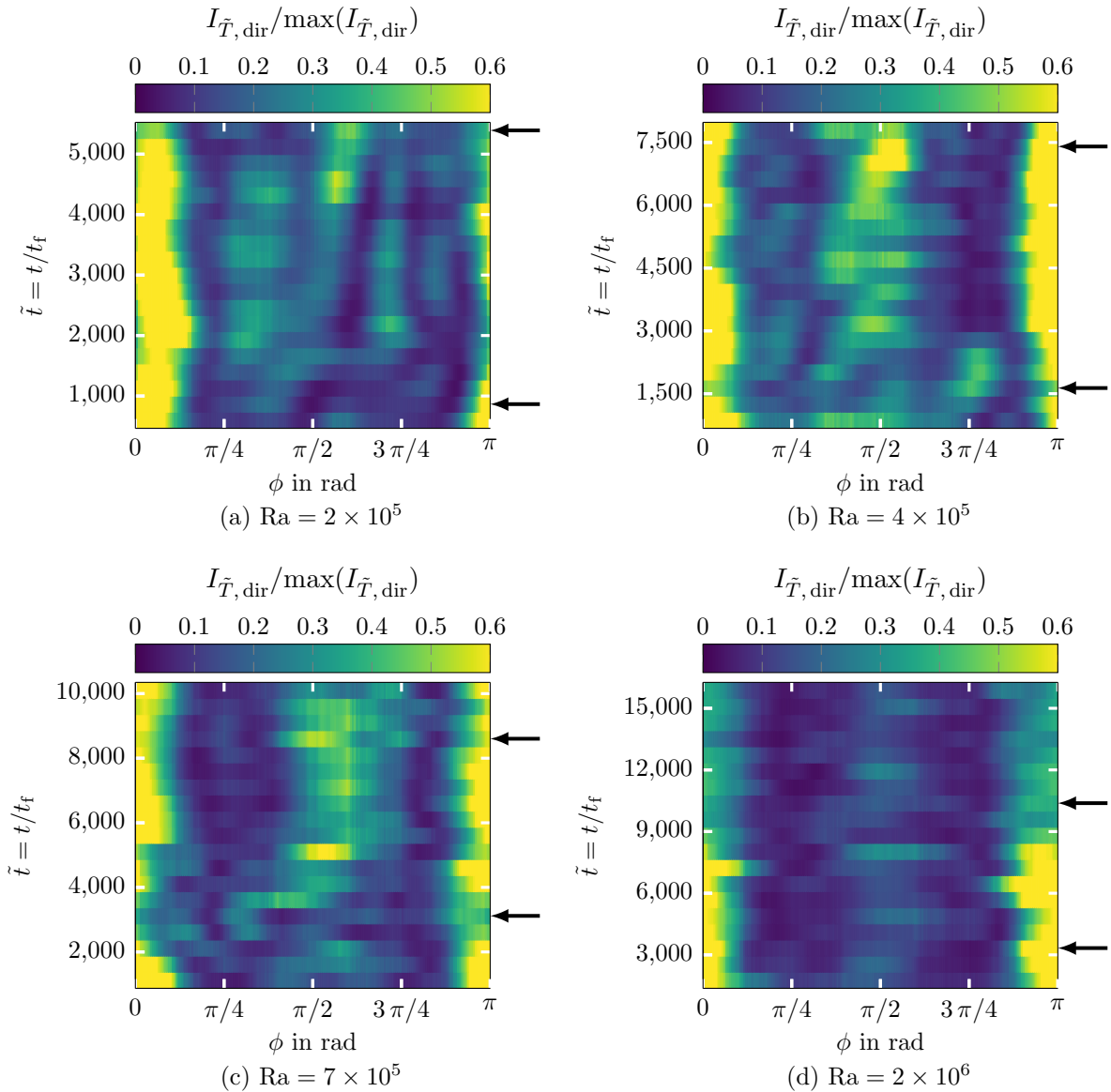
(d) Ra $= 2 \times 10^6$

Figure 5.22: Visualization of the reorganization of the turbulent superstructures in the temperature fields in the mid plane for the different Rayleigh numbers. The reorganization over time is illustrated by the directional intensities $I_{\tilde{T},\,\text{dir}}$, which represent the radial average of the power spectra in dependency of the azimuthal angle $\phi$, respectively. The arrows at the right side of each plot indicate the time instants for the temperature fields shown in figure 5.23.

Rayleigh numbers, is that small values of the directional intensities appear around $\phi = \pi/4$ and $\phi = 3\pi/4$, in particular for Ra $= 2 \times 10^6$. This indicates, that for larger Rayleigh numbers wavelike variations of the temperature preferentially occur along the $x$-direction and $y$-direction, but not along the diagonals of the Rayleigh-Bénard cell. However, for Ra $= 7 \times 10^5$ this is not always the case, as apparent from the selected temperature fields with and without a preferential orientation of the turbulent superstructures. At the first time instant in figure 5.23c the orientation of the superstructures is manifold, while their contours at the second time instant in figure 5.23g have the preference for aligning parallel to the sidewall of the cell. Hence, despite the large aspect ratio $\Gamma = 25$ the influence of the sidewalls seems not fully suppressed, when the turbulent superstructures grow larger with the Rayleigh number. Nevertheless, the reorganization still takes place, as the figures

5.22c and 5.22d confirm. For the case $\mathrm{Ra} = 2 \times 10^6$ it is less obvious, but this can also be explained by means of the selected temperature fields. In figure 5.23d it can be seen that the pattern of the superstructures is in this case distinguished by an outstandingly wavelike variation of the temperature in $x$-direction and almost uniform temperature in $y$-direction. As this pattern can thus be described with a sinusoidal plane wave in a very good approximation, the directional intensities for the azimuthal angles around $\phi = 0$ and $\phi = \pi$ are very high, such that the normalization with the overall maximum yields considerably smaller values for the other entries in the plot in figure 5.22d.
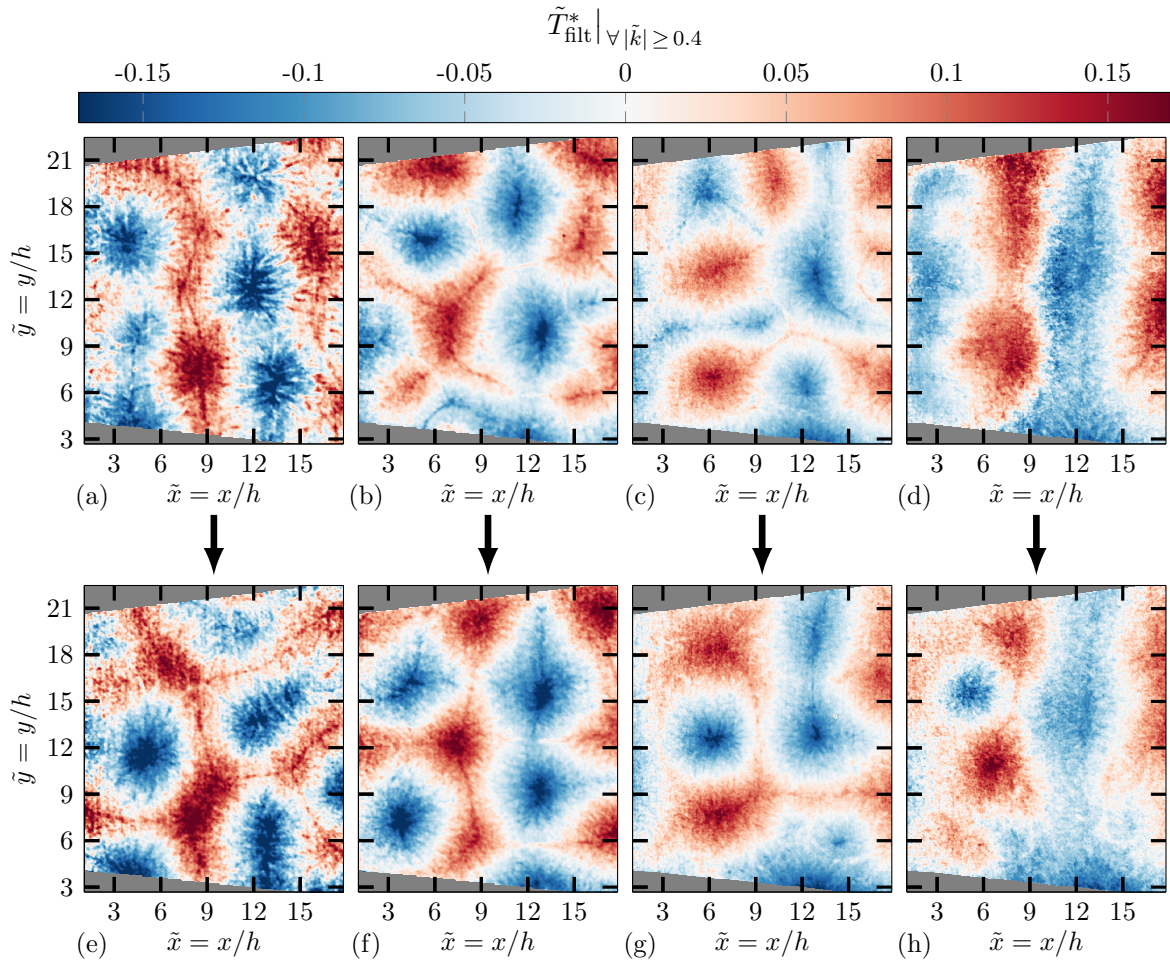


Figure 5.23: Demonstration of the reorganization of the superstructures by means of selected temperature fields in the mid plane at the Rayleigh numbers $\mathrm{Ra} = 2 \times 10^5$ (a,e), $\mathrm{Ra} = 4 \times 10^5$ (b,f), $\mathrm{Ra} = 7 \times 10^5$ (c,g) and $\mathrm{Ra} = 2 \times 10^6$ (d,h). The corresponding time instants are marked in figure 5.22 with the arrows at the right side of each plot.

For the Rayleigh number $\mathrm{Ra} = 2 \times 10^5$ the preferential alignment of the superstructures cannot be found to that extent, but for $\mathrm{Ra} = 4 \times 10^5$ it can also be seen in some cases. For instance, the temperature field in figure 5.23f, which corresponds to the second time instant marked in figure 5.22b, demonstrates that areas with similar temperatures are mainly located at the same positions in $x$-direction and $y$-direction, respectively. Hence, the variation of the temperature better follows a wavelike form in these directions.

The temperature fields in figure 5.23 also show that the size of the turbulent superstructures depends on the Rayleigh number. Within the scope of the present work their wavelength has already been investigated at the example of selected time-averaged temperature and velocity fields. In order to specify their wavelengths more reliably, those

are now studied over the entirety of the evaluated image series recorded at each Rayleigh number in both measurement planes. The characteristic wavelengths of the superstructures in the time-averaged fields of the temperature and of the vertical velocity component are denoted as $\hat{\lambda}_{\tilde{T}}$ and $\hat{\lambda}_{\tilde{u}_z}$, respectively. For the determination of $\hat{\lambda}_{\tilde{T}}$ and $\hat{\lambda}_{\tilde{u}_z}$ the approach thoroughly explained in section 5.2.4 has been applied, meaning that the power spectra of the time-averaged fields have been considered to obtain the wavelength, which yields the best match to these fields. The temporal average of the wavelengths corresponding to the large-scale structures are given in table 5.4 for each of the measurements. As mentioned above, the measurements at the Rayleigh number Ra $= 2 \times 10^6$ are affected by the temporally decreasing concentration of the tracer particles. Starting from about $\tilde{t} \approx 12000$ the effect has become more and more pronounced. Even though this time instant cannot be considered as a strict limit, the image series obtained in the time interval $\tilde{t} > 12000$ have not been taken into account for the average values shown in table 5.4. Furthermore, it has to be pointed out again that all the eight measurements are independent, meaning that the results from the mid plane and the top plane are obtained from different flows.

From the results in table 5.4 it becomes obvious that the characteristic wavelengths of the superstructures determined on the basis of the temperature fields are larger in each case, as it has already been noticed in section 5.2.4. There it has been shown, that a strict filter in the wavenumber domain must be applied to the velocity field, in order to remove the small-scale structures, which still remain after the time-averaging. With this filtering approach the structures on much smaller length scales compared to that of the turbulent superstructures are successfully eliminated. However, as it has been addressed several times in the course of this work, the velocity field exhibits some structures on larger length scales, which do not occur in the temperature field in a comparable intensity. Hence, a strong updraft or downdraft does frequently appear, even though at the same position the temperature does not considerably deviate from the average. In many cases these distinctive updrafts or downdrafts are embedded in the center of large areas with almost uniform temperature in the time-averaged temperature field. These additionally appearing structures in the velocity field are decreased by the filtering approach, but cannot anymore be completely removed, in order to preserve the pattern of the structures on the largest length scales. This causes the smaller characteristic wavelengths in the field of the vertical velocity component according to table 5.4. In this table the results obtained from both fields are referred to as the characteristic wavelength of the turbulent superstructures to impede confusion by different denotations, but the discrepancy suggests that the wavelengths resulting from the velocity field should rather be considered representative for large-scale structures than specifically for the turbulent superstructures. The latter, which are the most outstanding large-scale structures, are more clearly revealed in the time-averaged temperature fields. Thus, the results in the upper row of table 5.4 better represent the characteristic wavelength of the turbulent superstructures, such that the results in the lower row are not further discussed to keep the focus.

Even though the measurements in the mid and top plane have been performed independently from each other, the results determined from the temperature fields should be compared. It can be seen that the wavelength of the turbulent superstructures are close to each other in most cases. This shows that the superstructures almost span the whole height of the Rayleigh-Bénard cell, which has also been demonstrated based on the results of numerical simulations [53, 58]. However, one exception is apparent from table 5.4. At the Rayleigh number Ra $= 4 \times 10^5$ the characteristic wavelengths of the turbulent superstructures in the mid and top plane do not just slightly differ from each other. In

|                          | $2e5_m$ | $2e5_t$ | $4e5_m$ | $4e5_t$ | $7e5_m$ | $7e5_t$ | $2e6_m$ | $2e6_t$ |
|--------------------------|---------|---------|---------|---------|---------|---------|---------|---------|
| $\langle\hat{\lambda}_{\tilde{T}}\rangle_t$ | 8.87 | 8.99 | 9.82 | 8.62 | 10.95 | 10.41 | 10.94 | 10.92 |
| $\langle\hat{\lambda}_{\tilde{u}_z}\rangle_t$ | 7.23 | 6.80 | 7.72 | 8.28 | 7.03 | 8.01 | 8.56 | 7.35 |

Table 5.4: Temporal average of the characteristic wavelength of the turbulent superstructures in the field of the temperature $T$ and of the vertical velocity component $u_z$ for the measurements at the different Rayleigh numbers in the mid and top horizontal plane. The labels in the top row indicate all the independent measurements and refer to the tables 5.1 and 5.2, in which the settings of the measurements and of the evaluation are listed.

this case the wavelength $\hat{\lambda}_{\tilde{T}}$ is about 12% smaller in the top plane. Since the temperatures adjusted at both the heating and cooling plate almost coincide, this difference is not supposed to have its origin in the thermal boundary conditions. Most likely it can be explained by the fact, that the measurements have not been performed over the entire horizontal cross-sectional area of the cell due to issues related to the measuring technique. It can therefore be assumed, that the specific arrangement of the turbulent superstructures in the investigated area yields a considerable difference in the determination of their wavelength, which might become smaller, when the measurement section is enlarged. This cannot be verified at this point, though there is further evidence for this assumption, which can be derived from figure 5.24.

In figure 5.24 the characteristic wavelength of the turbulent superstructures, as determined from all the time-averaged temperature fields, can be seen in dependency of the time instant for both measurement planes. A mentionable time dependency of the wavelength of the superstructures is usually not expected in the classical Rayleigh-Bénard system with isothermal boundary conditions, if the whole horizontal plane of the cell is analyzed. However, here it is seen that the characteristic wavelength of the superstructures undergoes some variations. It should be noted that the variation of the wavelength between discrete values is just due to the evaluation via the Fourier analysis with discrete wavenumbers. In order to get back to the difference of the average size of the superstructures for $Ra = 4 \times 10^5$ obtained from the mid and top plane, the time-dependent results in the figures 5.24a and 5.24b are considered. The comparison confirms that the wavelength of the superstructures is on average larger in the mid plane for this Rayleigh number, but it becomes obvious, that towards the end of the measurement in the mid plane the wavelength gets smaller. For the last three time instants the wavelength is in between $8 \leq \hat{\lambda}_{\tilde{T}} \leq 9$, which is also the typical range in the top plane. This shows, that the superstructures are not in general larger in the mid plane for this Rayleigh number, as only their reorganization has proceeded on a different way in this particular case. Hence, when investigating a larger measurement area such a difference of the wavelength of the superstructures at $Ra = 4 \times 10^5$ would probably not be noticeable. If in future studies the measurement area must also be restricted, for whatever reason it may be, it is recommended to further increase the measurement time, such that the determination of the characteristic wavelength of the superstructures is less affected by their temporary arrangement. In particular also the results in figure 5.24b for the measurement at $Ra = 2 \times 10^5$ in the top plane demonstrate, that the effect of the momentary arrangement is not negligible in the present case, since the wavelength considerably varies around the average. However, concerning the measuring time it should be noted, that the measurements have already been performed over several hours. Especially the measurements with the TLCs R25C50W at $Ra = 2 \times 10^6$ have shown, that the
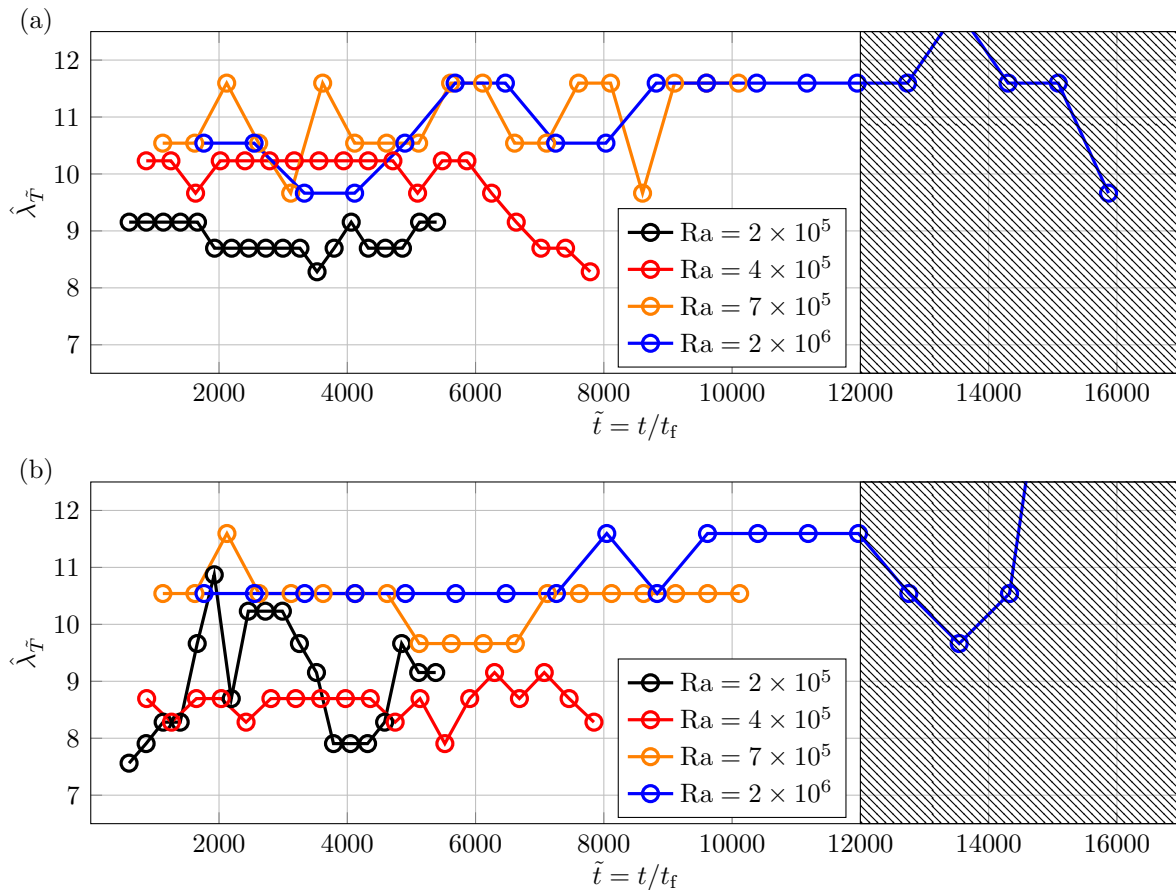
Figure 5.24: The characteristic wavelength of the turbulent superstructures in the temperature field in the mid plane (a) and top plane (b) for the different Rayleigh numbers in dependency of the time, which is given in units of free-fall times. The time interval in the shaded area on the right side is not considered in the evaluation due to the decreasing concentration of the tracer particles in the measurement planes.

experimental results may be affected by the decreasing seeding concentration, such that a further significant increase of the measuring time is challenging. If pure water shall be the working fluid, this might require to use customized TLCs with a smaller diameter of the encapsulation, but this would yield other difficulties due to the decreasing intensity of the reflected light. Otherwise, a properly adjusted mixture of water and another fluid as for instance glycerin could be used to adapt the mass density, thereby retarding the sedimentation.

Finally, the experimental results regarding the characteristic wavelength of the superstructures should also be compared to the results from the numerical simulations for $Pr = 7$ and $\Gamma = 25$, which have been presented in the study [57]. The wavelengths resulting from the numerical simulations for the Rayleigh numbers $Ra_{sim,1} = 10^5$, $Ra_{sim,2} = 10^6$ and $Ra_{sim,3} = 10^7$ are given in the table 5.5. Since these Rayleigh numbers are not exactly the same as those of the experiments, a one-to-one comparison is not possible, however, at least for $Ra_{sim,1} = 10^5$ and $Ra_{sim,2} = 10^6$ the results can be compared due to the same order of magnitude. It gets obvious at the first glance that according to the numerical results the characteristic wavelength of the turbulent superstructures in the velocity field is in each case smaller than that in temperature field, too. Moreover, comparing the tables 5.4 and 5.5 it can be seen that the wavelengths determined from the experiments are in general larger. If again only the results obtained from the temperature field are taken

into account, as those have turned out to be better suited for specifying the wavelength of the turbulent superstructures in the experiments, a decrease of the wavelength of about one third can be found from the numerical data. Furthermore, the wavelength of the superstructures based on the experimental data by trend increases with the Rayleigh number, while it is almost constant according to the numerical results.

|  | $\mathrm{Ra\,sim,1} = 10^5$ | $\mathrm{Ra\,sim,2} = 10^6$ | $\mathrm{Ra\,sim,3} = 10^7$ |
|---|---|---|---|
| $\hat{\lambda}_{\tilde{T}}$ | 6.3 | 6.3 | 6.2 |
| $\hat{\lambda}_{\tilde{u}_z}$ | 5.4 | 5.7 | 4.3 |

Table 5.5: The characteristic wavelength of the turbulent superstructures in the field of the temperature $T$ and of the vertical velocity component $u_z$ according to the results of the numerical simulations published in the work [57].

As the cause of the differences between the experimental and numerical results for the wavelengths of the superstructures different aspects may come into question. First of all, the influence of the controlling parameters given by the Rayleigh number, the Prandtl number and the aspect ratio should be addressed. Even though the discrete values of the Rayleigh numbers adjusted in the experiment differ from that of the numerical simulations, the overall range of about $2 \times 10^5 \leq \mathrm{Ra} \leq 2 \times 10^6$ is fully covered by the range $10^5 \leq \mathrm{Ra\,sim} \leq 10^7$ of the simulations. It can be seen that small deviations of the Rayleigh numbers within these ranges are not a reasonable explanation for this difference of the wavelength of the superstructures. Furthermore, the Prandtl number calculated from the average temperature of the working fluid is very close to $\mathrm{Pr} = 7$ for the measurements at $\mathrm{Ra} = 2 \times 10^5$, $\mathrm{Ra} = 4 \times 10^5$ and $\mathrm{Ra} = 7 \times 10^5$, while it amounts to about $\mathrm{Pr} = 6$ for the measurements at $\mathrm{Ra} = 2 \times 10^6$ due to the shift of the average temperature. However, the influence of the Prandtl number on the wavelength of the superstructures has been investigated in the work [11] and on the basis of the results it can be concluded, that such a deviation of the Prandtl number is not expected to have a significant effect. With regard to the aspect ratio it should be noted, that small deviations from $\Gamma = 25$ occur due to manufacturing tolerances and an additional thin sealing between the Rayleigh-Bénard cell and the heating plate inserted for the watertightness. While the former is negligible, the latter yields a decrease of the aspect ratio towards $\Gamma \approx 24$. However, this change of the aspect ratio is not supposed to have a large effect. The small deformation of the cooling plate due to the pressure in the cooling circuit, which is estimated in the appendix B.2, does also not remarkably affect the aspect ratio. Therefore, the three controlling parameters Ra, Pr and $\Gamma$ are suited for the comparison and do most likely not cause the difference of the wavelength of the superstructures.

Besides the controlling parameters Ra, Pr and $\Gamma$ the boundary conditions should be discussed with respect to the occurring differences of the results. In the numerical simulations for the study [57] thermally insulated sidewalls have been applied to comply with the adiabatic boundary condition of the Rayleigh-Bénard model. This condition is fulfilled in the experiment in a good approximation, so that the sidewalls are not suspected to be the main cause of the differences regarding the wavelength of the superstructures. Therefore, it seems probable that these can be traced back to the thermal boundary conditions at the heating and cooling plate. It should be pointed out, that the real wavelength of the superstructures, as these would occur in RBC with ideal boundary conditions, can neither be determined from the present experiment nor from numerical simulations with absolute

certainty. However, possible issues resulting from the numerical methods are not outlined here, as the focus should be on the question, if the wavelength of the superstructures is overestimated due to the thermal boundary conditions of the experiment.

An overestimation of the horizontal extent of the superstructures is possible, considering that the thermal diffusivity of both the bottom and top plate are limited in practice. Especially for the cooling plate at the top side a low thermal diffusivity had to be accepted to provide the optical access through the transparent plate made of glass. According to the theoretical considerations in reference [172], the limited thermal diffusivity of the plates enclosing the fluid layer at the bottom and top side strongly changes the situation known from the classical RBC with isothermal boundary conditions. As shown at the end of section 3.1, the impact of the turbulent superstructures on the plates yields some temperature inhomogeneities, which cannot be circumvented due to the limitation of the thermal diffusivity. It can therefore also be expected, that the size of the flow structures does not remain unaffected.

The influence of the limited thermal diffusivity of the plates is in particular noticeable, if the thermal diffusivity of the working fluid $\kappa_{\mathrm{f}}$ is much larger compared to that of the solid plates $\kappa_{\mathrm{s}}$, yielding a ratio $\kappa_{\mathrm{f}}/\kappa_{\mathrm{s}} \gg 1$ and thus a shift from constant temperature for $\kappa_{\mathrm{f}}/\kappa_{\mathrm{s}} \to 0$ towards constant heat flux for $\kappa_{\mathrm{f}}/\kappa_{\mathrm{s}} \to \infty$ at the boundaries. At the heating plate this governing ratio is $\kappa_{\mathrm{f}}/\kappa_{\mathrm{s}} \ll 1$ due to the excellent thermal conductivity $\lambda_{\mathrm{s}}$ of aluminum, so that strong deviations from the isothermal temperature distribution do not occur, as seen in section 3.1. However, at the cooling plate the ratio roughly amounts to $\kappa_{\mathrm{f}}/\kappa_{\mathrm{s}} \approx 1$, taking into account that the effective thermal conductivity of the working fluid, which is increased due to the convective motion as quantified by the Nusselt number, is used to determine this ratio [173]. Hence, the boundary condition at the cooling plate can be considered as intermediate between constant temperature and constant heat flux. For each of these conditions the results of numerical simulations for $\mathrm{Pr} = 1$ in a Rayleigh-Bénard cell with $\Gamma = 60$ have been presented in the study [174]. Applying the so-called Neumann boundary condition instead of the Dirichlet boundary condition, thereby specifying the gradient of the temperature at the plate and accordingly the heat flux instead of the temperature itself, an impressive difference is seen in this numerical work. The Dirichlet boundary condition with constant temperature yields the turbulent superstructures with an horizontal extent, which is larger than the cell's height, but much smaller than the structures resulting from the Neumann boundary condition with constant heat flux. In the latter case it is observed, that the small scale structures gradually aggregate on extended time scales and in the end even span the whole flow domain, such that these structures are referred to as supergranules to distinguish from the superstructures. Thus, as the cooling plate in the experimental setup at hand does not exhibit a perfectly uniform temperature distribution, it is reasonable that the size of the superstructures is shifted towards larger values. However, as the cooling plate does also not provide a constant heat flux and the temperature distribution at the heating plate can be considered as isothermal, the large-scale structures occurring in the experiments do not continuously grow over time and can therefore still be classified as turbulent superstructures.

# Summary and outlook

In the present work an experimental facility for the investigation of large aspect ratio Rayleigh-Bénard convection has been designed and set up. It is known from numerical simulations that characteristic large-scale structures, also referred to as turbulent super-structures, emerge in Rayleigh-Bénard convection when the flow domain has a large aspect ratio. The aim of this work was to clearly uncover these structures in an experimental setup and to get an impression of their main characteristics from the experimental point of view.

For the investigation of the turbulent superstructures a Rayleigh-Bénard cell with the dimensions of $l \times w \times h = 700 \, \text{mm} \times 700 \, \text{mm} \times 28 \, \text{mm}$ has been used. In the design of the setup those dimensions of the cell have turned out as a suitable choice, since the aspect ratio $\Gamma = l/h = 25$ provides the possibility to clearly observe the turbulent superstructures according to the results of numerical simulations, while the entire experimental facility can still be handled under common laboratory conditions. Furthermore, using water as the working fluid Rayleigh numbers in the order of $\text{Ra} = 10^5$ and $\text{Ra} = 10^6$ can be achieved with moderate temperature differences between the bottom and top plate of this cell, which allows for a comparison of the experimental results with that of previous numerical simulations for $\Gamma = 25$ and $\text{Pr} = 7$ [57].

One of the main challenges in the design of the experimental facility was to provide the optical access to the flat Rayleigh-Bénard cell with regard to the application of established optical measuring techniques. For this, the sidewalls of the cell and the cooling plate at the top are made of glass. As the transparent cooling plate is cooled by water flowing above it through a specially designed frame with a large cutout, so that the whole cell is optically accessible from the top side without hindrance, the cooling circuit had to be designed accurately for keeping the pressure in the circuit on a low level with respect to the mechanical stability of the glass plate. By means of numerical simulations the mechanical stability has been proven. Furthermore, the uniform flow of the cooling water above the glass plate was an important aspect in the design, in order to impede strong temperature inhomogeneities on its lower surface inside the Rayleigh-Bénard cell. Hence, the frame on top of the cooling plate has been designed on the basis of numerical simulations of the cooling water flow with the focus on its uniformity, meaning that the flow does not exhibit recirculation zones, which would yield a local increase of the temperature on the cooling plate. From the results of additional infrared measurements it can be concluded, that considerable local discontinuities do not occur in the cooling water flow.

Besides the design of the experimental facility, another key point of this work was to enable the simultaneous measurements of the temperature and velocity fields in horizontal

planes of the Rayleigh-Bénard cell using thermochromic liquid crystals. Applying those as tracer particles dispersed in the flow allows to determine the velocity field with the established Particle Image Velocimetry, while the temperature can be measured via their temperature-dependent color appearance upon illumination with white light. Whereas for the evaluation of the velocity a commercial software solution has been used, the determination of the temperature based on the color of the thermochromic liquid crystals has required a detailed characterization of this measuring technique and a lot of progamming work. The investigations in another smaller experimental setup, which has specifically been built for the characterization of the measuring technique, have clearly shown that the spectral power distribution of the white light source used for the illumination of the thermochromic liquid crystals is of great importance for the dynamic range of the color. It has been found that an unevenly distributed spectral power may yield a very narrow dynamic range of the color, while similar intensitites in the red, green and blue wavelength range of the illumination source result in a significant color change of the thermochromic liquid crystals with temperature, which is advantageous for precise temperature measurements. With regard to the measurements in the large Rayleigh-Bénard facility the influence of the angle between illumination and observation with a color camera on the color appearance of thermochromic liquid crystals has been anaylzed, too. The most important outcome is that the main color change passes off in a very narrow temperature range, when a perpendicular arrangement of the axis of the camera to that of the illumination is applied, while the color changes more gradually with temperature for smaller angles between illumination and observation. Moreover, these studies have shown that the angles between the illumination and the color camera in the range $50° \leq \varphi_{cc} \leq 70°$ are appropriate to achieve a low measurement uncertainty. However, in general the best suited angle depends on the desired temperature measuring range as well as on the specifications of the applied TLCs.

For the simultaneous measurements of the temperature and velocity fields in the large Rayleigh-Bénard facility two monochrome cameras and one color camera were used to study the flow in horizontal planes through the transparent cooling plate. Via the Stereoscopic Particle Image Velocimetry performed with the two monochrome cameras, both the velocity in the horizontal and vertical direction could be determined. The color camera, which has been arranged with an angle of $\varphi_{cc} = 65°$ according to the findings from the preliminary experiments in the smaller setup, was used for the temperature measurements based on the color of the thermochromic liquid crystals. For the illumination of the TLCs in the large horizontal cross-sectional area of the cell, a white light source consisting of many horizontally aligned white LEDs and a light sheet optic has been set up. In order to reliably measure the temperature fields, different calibration techniques have already been tested a priori by means of the measurements in the small setup. All the calibration techniques are solely based on the chromaticity of the thermochromic liquid crystals, represented by the hue $H$ of the $HSV$-colorspace, since this variable has shown the most robust temperature dependency. For the final temperature measurements in Rayleigh-Bénard convection a calibration technique based on linear interpolation of the measured hue values in local calibration curves has been chosen. Using this calibration technique, a mean absolute deviation across the whole temperature field of $\overline{MAD} < 0.1\,\mathrm{K}$ is obtained for temperature differences between the heating and cooling plate up to about $\Delta T = 3\,\mathrm{K}$. For larger temperature differences up to $\Delta T \approx 5\,\mathrm{K}$ the mean absolsute deviation does not exceed $\overline{MAD} = 0.2\,\mathrm{K}$.

For the characterization of the superstructures the Rayleigh numbers of approximately $\mathrm{Ra} = 2 \times 10^5$, $\mathrm{Ra} = 4 \times 10^5$, $\mathrm{Ra} = 7 \times 10^5$ and $\mathrm{Ra} = 2 \times 10^6$ have been adjusted. At these

Rayleigh numbers the Rayleigh-Bénard flow has been studied in independent measurements in the horizontal mid plane and in another horizontal plane closer to the cooling plate. Based on the simultaneous measurements of the temperature and velocity fields the turbulent superstructures could be investigated in greater detail from the experimental point of view for the first time. It has been seen that a time-averaging of the temperature field and of the velocity field reveals the large-scale structures in both fields. However, while the time-averaging nearly removes all the structures on small length scales from the temperature field, the structures with a smaller horizontal extent compared to that of the superstructures are not fully eliminated in the velocity field. This was especially obvious for larger Rayleigh numbers. Even the application of a strict filter in the wavenumber domain was not capable of removing all the smaller structures, as the filtering range of the wavenumber could not be chosen too large, in order to preserve the pattern of the turbulent superstructures. Due to these additionally occurring structures in the velocity field, the main characteristics of the superstructures have been studied by means of the time-averaged temperature fields. As the measurements have been performed over several hours in each case, it could be shown that the superstructures gradually rearrange on extended time intervals. Furthermore, the measurements have demonstrated that the turbulent superstructures grow with the Rayleigh number. Considering all the applied Rayleigh numbers, their characteristic wavelength has been estimated to fall into the range $8 < \hat{\lambda}_{\tilde{T}} < 11$ in the horizontal mid plane and in the horizontal plane closer to the top of the cell. Hence, the superstructures in RBC nearly span the entire height of the flow domain without changing their horizontal extent.

The application of the combined measuring technique also allows to study the local heat flux in RBC, which requires knowledge of the temporally and spatially resolved temperature and vertical velocity component. It has been shown, that this approach is suited to capture the large impact of the turbulent superstructures on the local heat flux. However, by a comparison of the experimental results with that of numerical simulations it has been found, that the measurement data must be available at a higher spatial resolution, such that the local peaks of the heat flux can be determined more accurately. Due to the decreased spatial resolution of the measurements compared to the numerical simulations, the heat flux quantified with the Nusselt number was typically underestimated by about one fourth. Besides the results of the analysis regarding the local heat flux, the typical magnitude of the velocities occurring in the experiment and the wavelengths of the superstructures have been compared to the outcomes of the numerical simulations presented in the study [57]. While the magnitude of the velocity is in good agreement, since the root-mean-square velocity amounts to about $\tilde{U}_{\mathrm{rms}} = 0.1$ in both cases, the superstructures have a larger horizontal extent in the experiments. According to the numerical simulations, the wavelength of the superstructures is on average about one third smaller. The review of all the possible reasons for this difference suggests, that the inevitable deviations from the isothermal boundary conditions in the experiment are the most probable explanation. Despite the great effors made in the design of the heating and cooling circuit, some inhomogeneities on the heating and cooling plate cannot be impeded due to the impact of the turbulent superstructures, especially on the latter because of its lower thermal conductivity.

It should finally be stated, that the present work has demonstrated the possibility of gaining experimental access to the turbulent superstructures in RBC, which have mainly been investigated in numerical simulations so far. However, due to the rareness of the experimental studies in this field many questions remain still open, and the present work

can only be considered as a starting point for future investigations. In particular the discrepancy of the size of the turbulent superstuctures in the experiment compared to that in numerical simulations should be analyzed with the focus on the effect of the inevitable deviations from the isothermal and adiabatic boundary condition. In this regard it must be mentioned that the large horizontal dimension of the superstructures in water was not expected to this extent. For further experimental studies with this cell and water as the working medium it would be of advantage to enlarge the field of view. At best, the full horizontal cross-sectional area is analyzed, which has turned out be very challenging due to the scattering behavior of the thermochromic liquid crystals and the resulting diffusive reflection on the heating plate in the background of the cameras' images. In order to circumvent this problem, using a Rayleigh-Bénard cell with a larger aspect ratio could be taken into account as well, thereby decreasing the physical dimensions of the turbulent superstructures. However, this would further limit the maximum achievable Rayleigh number. Furthermore, in conjunction with optical measuring techniques other transparent fluids or gases might be applied as the working medium to experimentally assess the effect of the Prandtl number. Since the simultaneous measurements of the temperature and velocity fields have been performed in horizontal planes in this work, the measuring technique should in the future also be adapted to volumetric measurements, such that the turbulent superstructures can be studied in their full three-dimensional complexity.
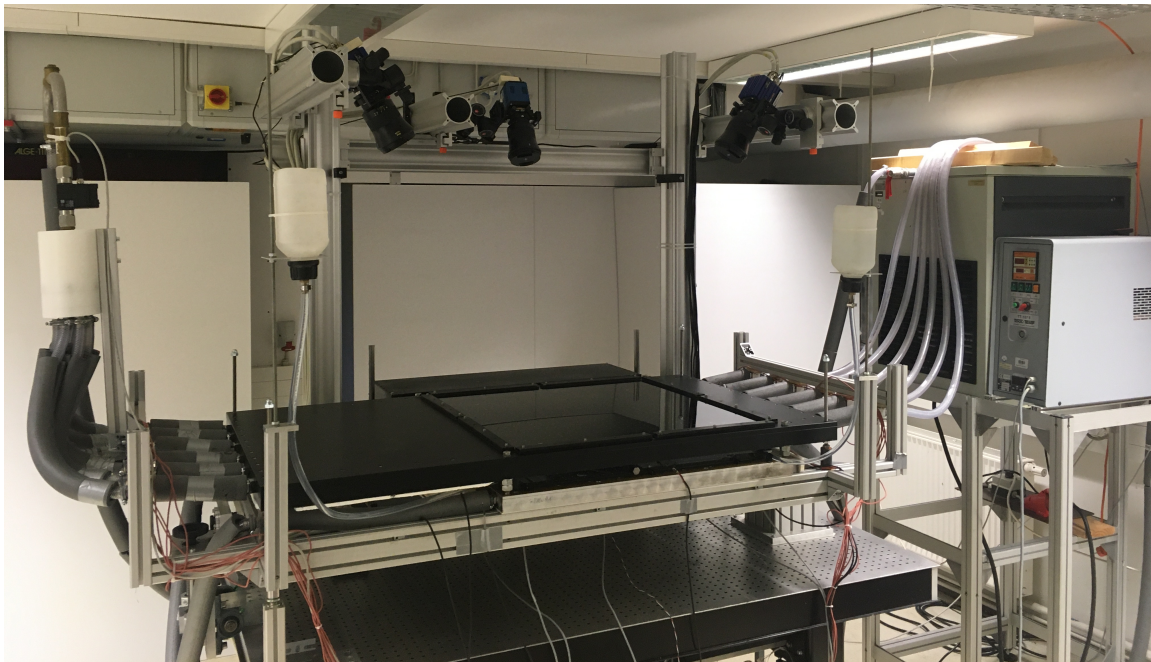
# Photographs of the experimental facility



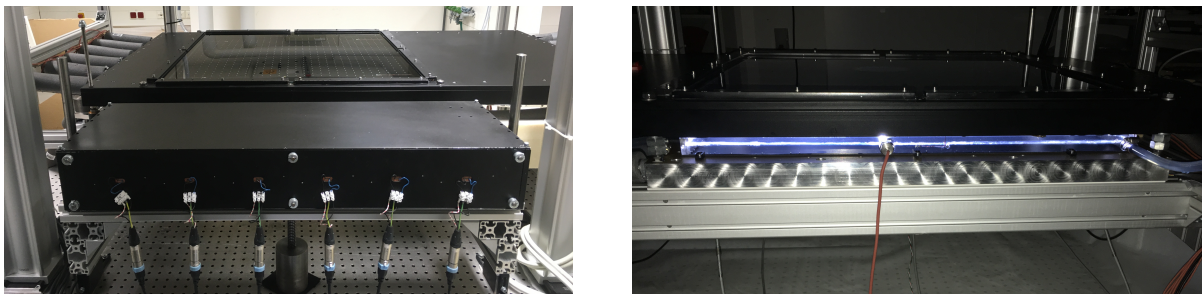Figure A.1: The experimental facility without the insulation at the heating and cooling plate.



Figure A.2: The arrangement of the white light source for the illumination of the thermochromic liquid crystals in horizontal planes of the Rayleigh-Bénard cell (left) and an impression of the white light sheet at the opposite side of the cell (right). The threaded spindle at the bottom side of the light source is used for adjusting its vertical position.
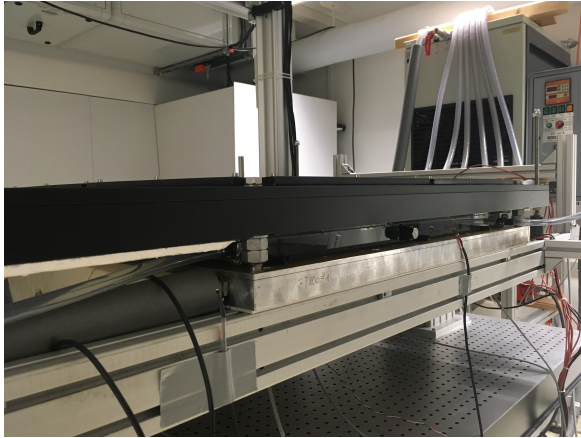
Figure A.3: A side view of the flat Rayleigh-Bénard cell with the aspect ratio $\Gamma = 25$ mounted between the heating plate and the frame of the cooling circuit. During the measurements, the mounting frame, the heating plate, the sidewalls of the Rayleigh-Bénard cell as well as the frame of the cooling circuit is covered with insulation, as it can be seen in the figures A.4, A.6 and in the figure 3.5 within the section 3. Therefore, the heat loss to the surroundings or the heat absorption from the surroundings is reduced to a minimum.



Figure A.4: The insulation at the sidewall with foam material. During the measurements the foam permanently covers the sidewalls except for that, at which the white light sheet enters the cell. At this sidewall the foam material is temporarily removed for the duration of the recording of each image series. Due to the fact, that the temperature in the lab environment is adapted to the average temperature of the working fluid in the cell and the sidewalls are made of glass, this insulation can be considered as an add-on, in order to minimize the heat flux through the sidewalls with regard to the adiabatic boundary condition.
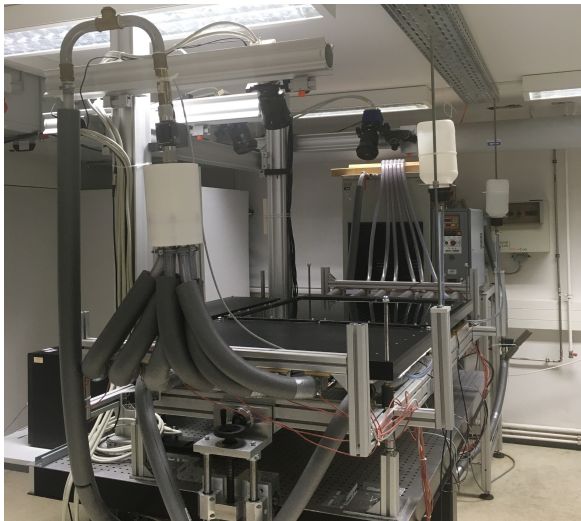


Figure A.5: A view of the experimental facility showing the flow distributor in the cooling circuit from the front. Inside the distributor the flow area of the downward streaming cooling water is gradually widening up to impede large pressure losses. Furthermore, its geometry is axisymmetric to obtain equal flow rates through each of the connected hoses.
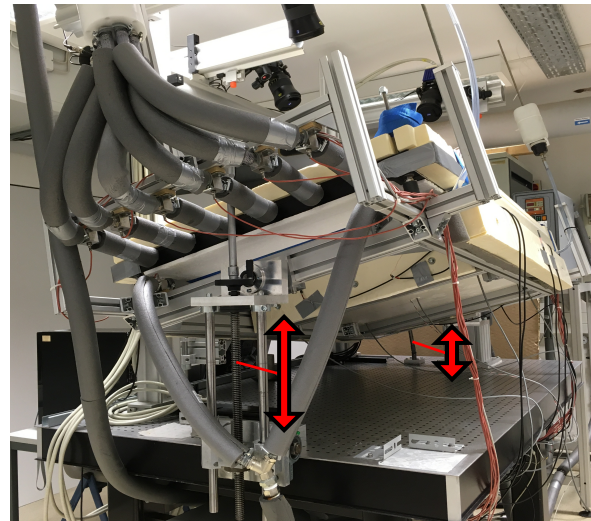


Figure A.6: The inclined setup during the venting of the cell and of the cooling circuit. In order to completely remove the air, the venting is repeated several times for different inclined positions of the setup, which can be turned around two axis continuously. The mechanisms used for the adjustment of the inclination are marked in the photo, respectively.
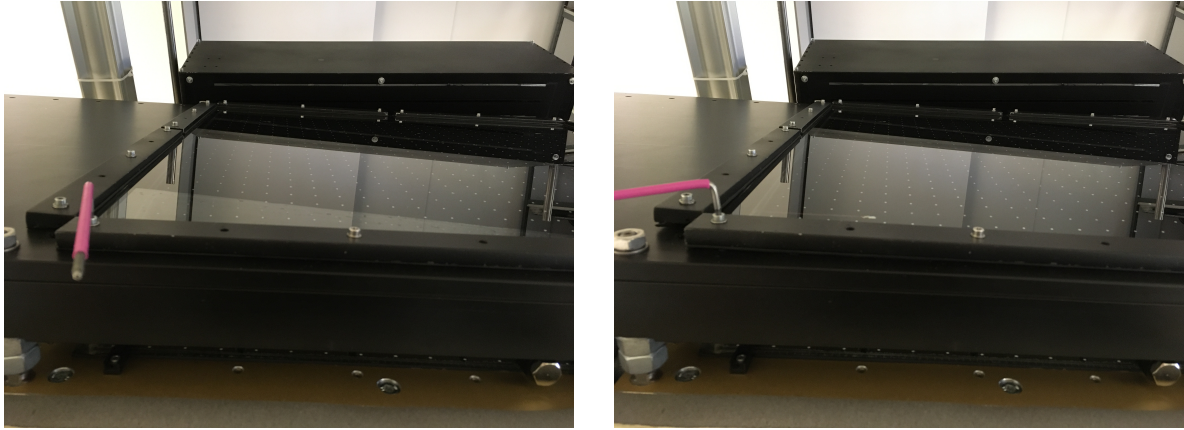
Figure A.7: Removal of the air in the cooling circuit for the optical accessibility of the Rayleigh-Bénard cell without hindrance. Since the mounting frame of the Rayleigh-Bénard cell can be inclined around two axis, the air can be fully removed by successively loosening and tightening the screws at the different edges of the covering glass plate. This is exemplarily demonstrated for one edge in the two images, with the left one showing a large air bubble in the corner, which is not present anymore in the right one.
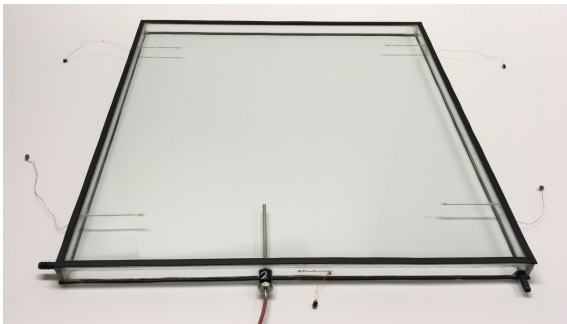


Figure A.8: The demounted Rayleigh-Bénard cell with the aspect ratio $\Gamma = 25$ and the cooling plate at the top side. The temperature measuring lance inserted through the side wall is used for the calibration of the temperature measurements via the color signal of the TLCs. In order to prevent an effect on the flow during the measurements in RBC, the lance can also be replaced by a simple plug, which can for example be seen in figure A.3 and A.4. Furthermore, this image shows the small PT100 sensor elements for the measurement of the temperature at the cooling plate and at the cell's sidewall.
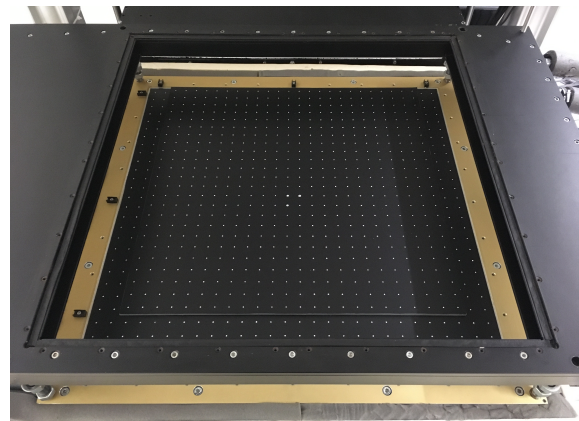


Figure A.9: A view of the flat calibration target, which is temporarily placed on the heating plate of the Rayleigh-Bénard cell for the dimensional calibration. As explained in section 4.1, images of the dot pattern on the calibration target and on the heating plate are separately taken with the applied cameras. In each case, the Rayleigh-Bénard cell is inserted, both the cell as well as the cooling circuit are filled with water and the latter is cooled with the same flow rate of the cooling water as in the actual measurements, in order to ensure that the conditions for the imaging do not vary, respectively. Further details about the calibration procedure with the so-called stereoscopic self-calibration are described in section 4.1.
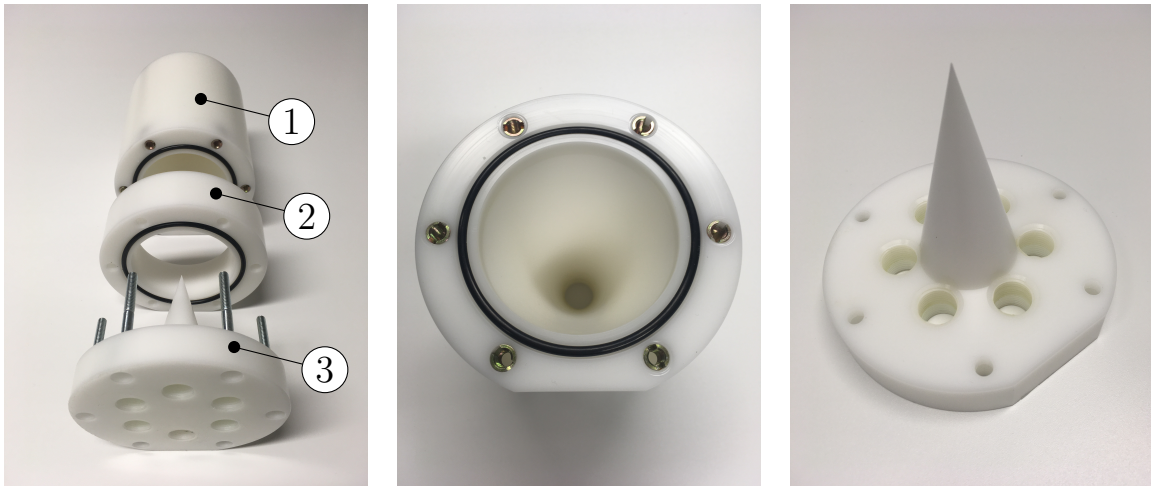
Figure A.10: The demounted flow distributor of the cooling water circuit (left), consisting of ① - the main body with a conical diffuser, ② - the distance ring and ③ - the diffuser plate with a cone. Larger views of the main body and the diffuser plate are depicted in the middle and at the right side of the figure. As it can be seen in figure A.5, the cooling water enters the main body from the top side and streams out at the bottom side of the diffuser plate into the six hoses connected to the frame above the Rayleigh-Bénard cell. The distance ring is mounted in front of the diffuser plate to further equalize the cooling water flow streaming out of the main body, in which the flow area is gradually widened by the conical diffuser. In order to impede the impinging of the cooling water flow in the center of the diffuser plate, it has a pointed cone at the top side, which reduces the pressure loss considerably. Aiming for the same flow rate through each of the six outlets in the diffuser plate, the whole flow area inside the flow distributor is axisymmetric. In addition, the flow distributor is mounted vertically at a profile bar as obvious from figure A.1, thereby preventing a preferential flow direction due to the influence of gravity.

# Numerical simulations for the design of the experimental facility

During the design of the experimental facility, several numerical simulations have been performed to estimate the cooling water flow through the frame on top of the Rayleigh-Bénard cell and the mechanical stress of the glass plates enclosing the cooling water flow. The numerical simulations and the main results are described in the two following sections B.1 and B.2.

## B.1   The cooling water flow

With regard to the ideal boundary conditions of the Rayleigh-Bénard experiment, the temperature distribution on the heating and cooling plate should be as homogeneous as possible. The heating and the cooling circuit as well as the measures taken to minimize the temperature inhomogeneities on the plates are explained in the sections 3.1.2 and 3.1.3, but since the cooling circuit was specially designed for providing the optical access to the measurement cell, the cooling water flow deserves closer attention. This is in particular important due to the low thermal conductivity of the cooling plate made of glass, which would not equalize considerable temperature differences of the water streaming above the plate. Even though measuring the temperature in the inlet and outlet of the frame on top of the Rayleigh-Bénard cell has assured that the temperature increase of the cooling water in flow direction is small on average, strong local temperature inhomogeneities on the cooling plate cannot be completely ruled out by those measurements. For example, stagnation zones and flow reversals of the cooling water would result in distinctive deviations from the isothermal boundary condition, which might not always be detected by means of the temperature sensors in the inlet and outlet. However, as it can be seen in figure 3.9 of the section 3.1.3, the flow guiding frame has a purpose-built geometry with large diffusers and nozzles, in order to obtain a uniform flow without such discontinuities.

The geometry of the frame has been designed by means of numerical simulations with *Ansys Fluent 16.2*. It should be emphasized, that the simulations were not performed to precisely determine the velocity field, since this is not of interest in the scope of this work. Here, the main goal was to confirm the suitability of the flow guiding frame designed on the basis of earlier studies about diffusers [138, 139], aiming for a cooling water flow, which does not separate from the contour of the surrounding frame to impede flow reversals. Moreover, the simulations allow to easily check different angles of the diffusers and nozzles, thereby figuring out the possibilities to reduce their length with respect to the practical

suitability of the experimental setup. In the present case two-dimensional models were used for the numerical simulations, as those are computationally less expensive, but also allow to study the basic characteristics of the cooling water flow, which is expected to mainly stream in the horizontal direction between the two enclosing glass plates due to their small distance of about 4 cm.

For computing the velocity field of the cooling water flow, a constant velocity has been assumed at all the six inlets, while the ambient pressure has been set as the constant pressure at the six outlets of the frame. Furthermore, the no-slip condition has been imposed at all the boundaries between the cooling water and the frame. The fixed velocity at the inlets was specified based on the cooling water flow of $\dot{V}_{\mathrm{cw}} = 30\,\mathrm{l/min}$, which was adjusted during all the flow measurements in RBC. Assuming that the total flow rate is equally split up, yielding the same flow rate through each of the six inlet hoses with a diameter of $d_{\mathrm{in}} = 16\,\mathrm{mm}$, the velocity at the inlet of $v_{\mathrm{in}} = 0.41\,\mathrm{m/s}$ is obtained. Thus, the Reynolds number at the inlet $\mathrm{Re}_{\mathrm{in}}$ amounts to about $\mathrm{Re}_{\mathrm{in}} = 7000$, indicating that the flow in the hoses is already turbulent, as the Reynolds number is larger than the corresponding critical Reynolds number $\mathrm{Re}_{\mathrm{c}} = 2300$ of a pipe flow. In order to meet these conditions, the very common $\kappa - \epsilon$ turbulence model has been applied to compute the velocity field in this case.

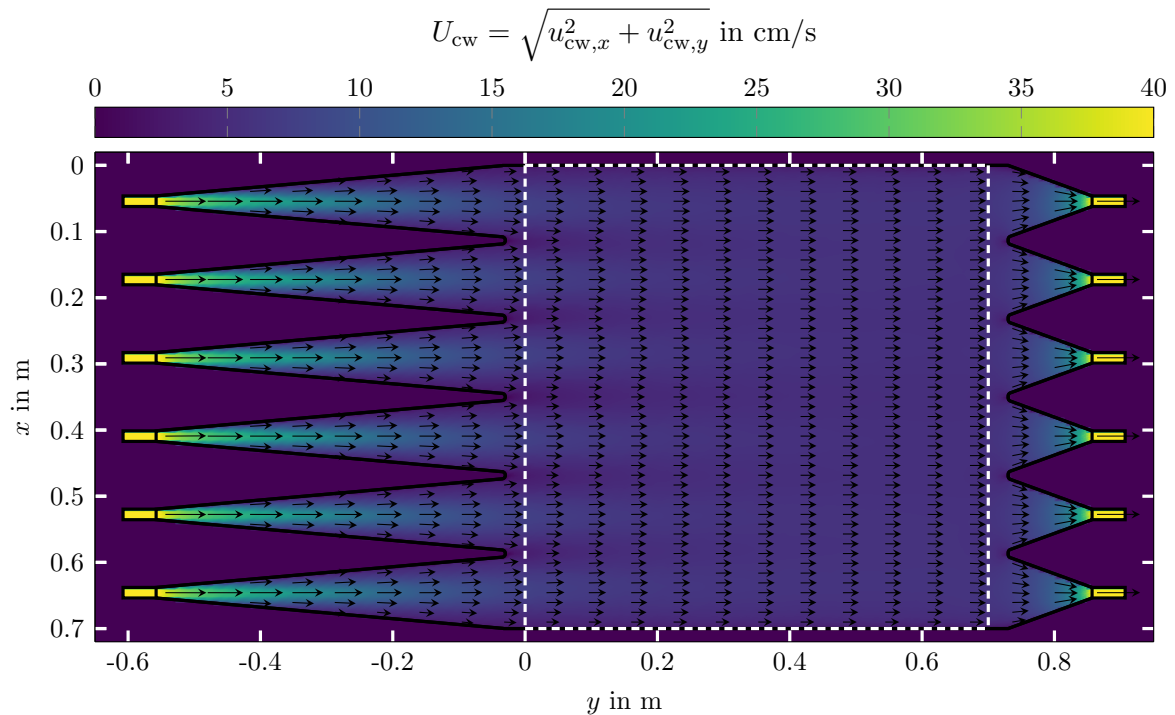$$U_{\mathrm{cw}} = \sqrt{u_{\mathrm{cw},x}^2 + u_{\mathrm{cw},y}^2} \text{ in cm/s}$$



Figure B.1: The absolute velocity of the cooling water flow with superimposed arrows indicating the direction of the fluid motion.

In the first numerical simulations, the angle of the diffusers $\Theta_{\mathrm{diff}}$ indicated in figure 3.8 has been varied in between $\Theta_{\mathrm{diff}} \in [10°, 20°]$, while the angle of the nozzles has been adapted, respectively, such that $\Theta_{\mathrm{diff}} = \Theta_{\mathrm{nozz}}$. This range of the angles has been chosen, as those hold out the prospect of a directed cooling water flow without flow separation, but would still be suited to keep the entire length of the experimental setup within reasonable limits. However, the results of the simulations have shown, that the angle of the nozzles only has a minor effect compared to the angle of the diffusers. Hence, with respect to

a considerable reduction of the dimensions of the experimental setup, the angle of the nozzles has been increased to $\Theta_{\text{nozz}} = 40°$ and has not been changed anymore, since this angle does still not yield any undesirable effects, as for example a flow separation towards the nozzles. Accordingly, in the further numerical investigations only the diffuser angle has been varied in the range from $\Theta_{\text{diff}} = 10°$ up to $\Theta_{\text{diff}} = 20°$.

As estimated based on the results of the studies [138, 139], a diffuser angle of $\Theta_{\text{diff}} = 10°$ is in this case adequate to impede flow separation in the cooling water flow according to the numerical simulations. The result for the absolute horizontal velocity of the cooling water flow $U_{\text{cw}} = (u_{\text{cw},x}^2 + u_{\text{cw},y}^2)^{1/2}$ is depicted in figure B.1, in which the direction of the fluid motion is indicated by the superimposed arrows, that have been rescaled for a better illustration. It shall also be noted that the spatial resolution of the vectors in $x$- and $y$-direction has been decreased considering the distinguishability of the vectors. In figure B.1 the suitability of the frame above the cooling plate of the Rayleigh-Bénard cell is confirmed, because the cooling water is streaming from the inlet to the outlet without any discontinuities. Especially, in the white marked frame, which indicates the position of the Rayleigh-Bénard cell, only small differences of the absolute horizontal velocity can be seen. In order to better visualize those differences, the profile of the main velocity component $u_{\text{cw},y}(x)$ directed towards the outlet is plotted for different positions along the plate in the figure B.2a. From this figure it becomes obvious, that the differences of the velocity are slightly larger in close vicinity to the diffusers and are equalized in flow direction. In particular, the profile at $y = 0.1\,\text{m}$ shows, that the local maxima of the velocity are in each case located on the center line of a diffuser, while the local minima are obtained at the border of the frame and at the transition between two diffusers, respectively. However, all in all those small differences of the velocity do not considerably effect the temperature distribution on the cooling plate, as the velocity is in general large enough to prevent distinctive temperature variations of the cooling water, particularly due to the large heat capacity of water.

The results for the diffuser angles ranging in between $12° \leq \Theta_{\text{diff}} \leq 20°$ can be seen in the figures B.2b - B.2f. While the differences of the velocity are still moderate for $\Theta_{\text{diff}} = 12°$, those grow further with increasing diffuser angle. Flow reversals become apparent starting from $\Theta_{\text{diff}} = 14°$, indicated by negative values of $u_{\text{cw},y}(x)$. Comparing the results for the different diffuser angles it becomes also obvious that the local maxima and minima are non-systematically shifted, showing that the cooling water does not flow symmetrically through the diffusers, but is randomly deflected to its outline. Due to the symmetry of the diffusers, it is also reasonable that the flow is not preferentially deflected to only one side, which has already been outlined in the work [138]. Thus, as expected, the results confirm that the diffuser angle strongly affects the flow and must be designed properly, resulting in $\Theta_{\text{diff}} = 10°$ in this case. It is emphasized again, that the small variations of the velocity according to figure B.2a can here be accepted, since their effect on the temperature distribution is negligible compared to that of flow reversals or other remarkable discontinuities in the flow field.

Finally, in order to assure that this design of the diffusers is suited for the present application, two other values for the velocity at the inlet of the diffusers were adjusted to represent the effect of the flow rate in the cooling circuit, even though the flow rate is kept constant at $\dot{V}_{\text{cw}} = 30\,\text{l/min} \pm 0.1\,\text{l/min}$ for the flow measurements. However, during the design this flow rate was not known yet. The results for the two additional velocities corresponding to the flow rates of $\dot{V}_{\text{cw}} = 20\,\text{l/min}$ and $\dot{V}_{\text{cw}} = 40\,\text{l/min}$ are depicted in figure B.3 besides the results for $\dot{V}_{\text{cw}} = 30\,\text{l/min}$. For these flow rates the profile of the main

velocity component $u_{\mathrm{cw},y}(x)$ can be seen, again for different positions along the cooling plate, but only close to the diffusers at $y = 0.1\,\mathrm{m}$ and close to the nozzles at $y = 0.6\,\mathrm{m}$ in this case. As the profiles show, the magnitude of the velocity varies according to the increasing or decreasing of the flow rate in each case, however, a considerable change of the profiles in qualitative terms cannot be found. Hence, it is proven that variations of the flow rate to some extent do not affect the velocity profiles in an undesirable way and, therefore, this design of the diffusers is applicable from the practical point of view.
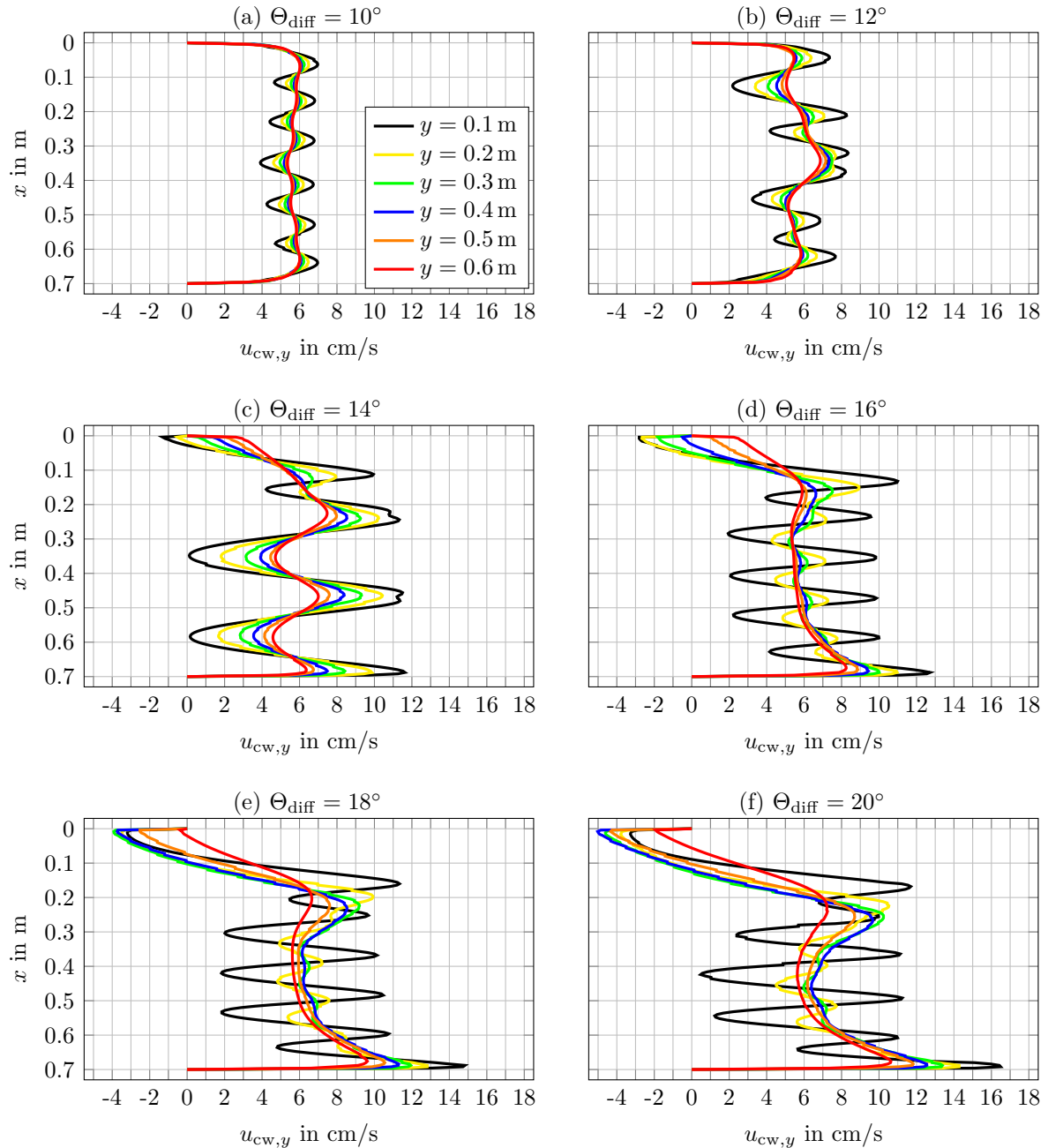


Figure B.2: The velocity profile in the main flow direction of the cooling water for different positions along the cooling plate and varying diffuser angles $\Theta_{\mathrm{diff}}$. The positions given in the legend of figure B.2a are valid for all the different diffuser angles.
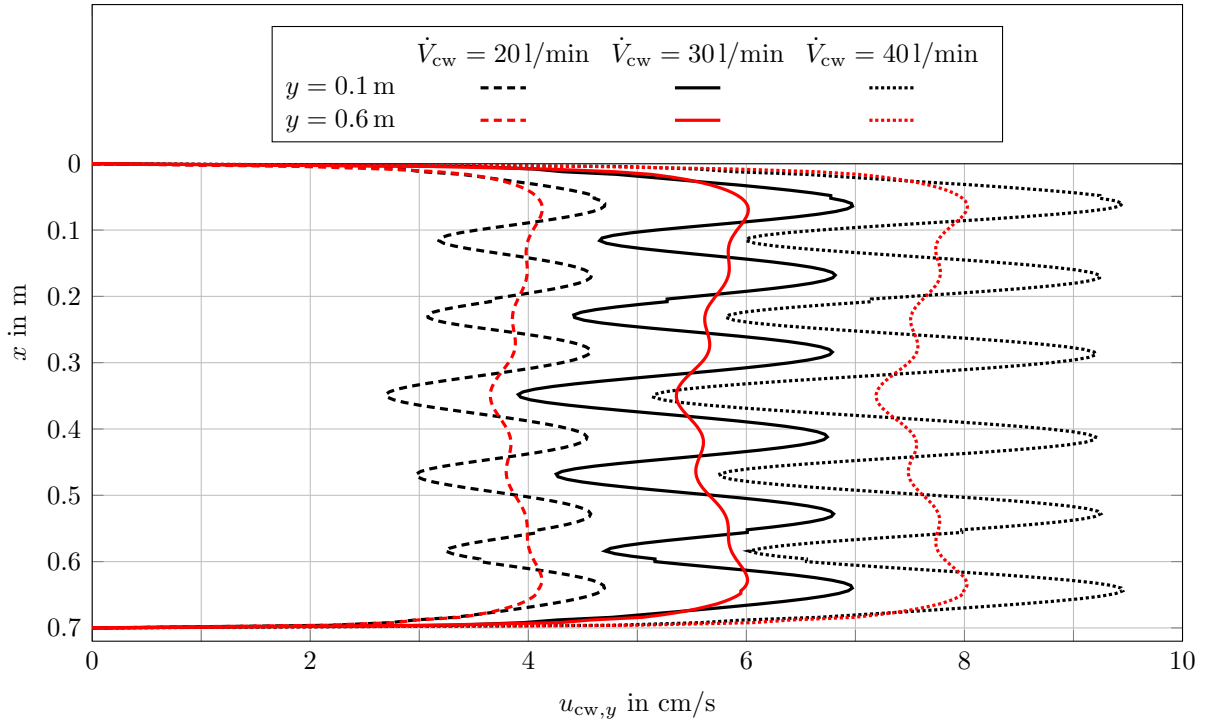
Figure B.3: The velocity profile in the main flow direction of the cooling water close to the diffusers and the nozzles for a varying flow rate $\dot{V}_{\mathrm{cw}}$.

## B.2 The mechanical stress of the cooling plate

One of the most important features of the experimental setup is the optical accessibility of the entire Rayleigh-Bénard cell. However, the use of the large glass plates enclosing the cooling water circuit requires special carefulness with respect to the risk of glass breakage. Hence, the plates made of thermally toughened glass were designed considering the maximum mechanical stress and deformation. For a first estimation, this was done analytically based on the equation (B.1) for the maximum stress $\sigma_{\mathrm{gp,max}}$, which occurs at the center of the edges, and equation (B.2) for the maximum deformation $\gamma_{\mathrm{gp,max}}$ in the center of the glass plates [175].

$$\sigma_{\mathrm{gp,max}} = \frac{c_\sigma \, p \, l^2}{t_{\mathrm{gp}}^2} \tag{B.1}$$

$$\gamma_{\mathrm{gp,max}} = \frac{c_\gamma \, p \, l^4}{E \, t_{\mathrm{gp}}^3} \tag{B.2}$$

Those equations are valid for the case of a uniformly distributed load on a plate with fixed edges. As the pressure drop of the cooling water flow along the plates is small due to the lower velocity in this region and the large flow area, it is reasonable to assume a uniform load in this case, denoted as the pressure $p$ in the equations. The dimensions of the square plates are considered in the equations by the edge length $l = 0.7\,\mathrm{m}$ and the plates' thickness $t_{\mathrm{gp}}$, that has to be determined. Furthermore, the elastic modulus $E$ of the plates is necessary to estimate the deformation. For glass a typical value of $E = 70\,\mathrm{GPa}$ can be found [176], which is assumed here. Furthermore, the geometry-dependent coefficients $c_\sigma$ and $c_\gamma$ in the equations (B.1) and (B.2) are obtained from the literature [175], amounting to $c_\sigma = 0.3078$ and $c_\gamma = 0.0138$ for the square glass plates in the present application.

However, in order to design the thickness of the plates according to equation (B.2), the pressure of the cooling water between the plates as indicated in figure B.4 must be estimated at first. Using *Bernoulli's principle*, the latter can be derived from the pressure conditions at another point in the system. For this, the highest point of the cooling circuit right in front of the tank of the thermostatic bath, also shown in figure B.4, is chosen. Thus, *Bernoulli's principle* yields

$$p_1 + 1/2\,\rho\,v_1^2 + \rho\,g\,h_1 = p_2 + 1/2\,\rho\,v_2^2 + \rho\,g\,h_2 + \Delta p_{\text{loss}}, \tag{B.3}$$

where $p_1$ and $p_2$ is the static pressure, respectively, while the pressure loss resulting from viscous friction and further flow resistances downstream of the glass plates is represented by $\Delta p_{\text{loss}}$. Here, the variation of the hydrostatic pressure between the two glass plates is neglected due to the small change of the height, such that the same pressure is obtained for the design of both plates. Since the highest point of the system is very close to the open end of the hose, which leads the flow back into the tank of the thermostatic bath, the static pressure $p_2$ nearly equals the ambient pressure $p_\infty$. Furthermore, as the velocity $v_1$ between the plates is much smaller compared to the velocity in the hoses $v_2$, the dynamic pressure $1/2\,\rho\,v_1^2$ can be neglected. Accordingly, the relative static pressure $p_{1,\text{rel}}$ yielding the deformation of the plates can be estimated with equation (B.4).

$$p_{1,\text{rel}} = p_1 - p_\infty = 1/2\,\rho\,v_2^2 + \rho\,g\,(h_2 - h_1) + \Delta p_{\text{loss}} \tag{B.4}$$

In order to determine the pressure components, the mass density $\rho$ of the cooling water is taken as $\rho = 1000\,\text{kg/m}^3$ for simplification. Moreover, the velocity in the six outlet hoses, which have the same diameter $d_{\text{out}} = 16\,\text{mm}$ as the six inlet hoses, amounts to $v_{\text{out}} = 0.41\,\text{m/s}$, assuming that the total flow rate of $\dot{V}_{\text{cw}} = 30\,\text{l/min}$ is equally split up into the outlet hoses. Therefore, the dynamic pressure is $1/2\,\rho\,v_2^2 \approx 84\,\text{Pa}$. In this case, the difference of the height levels $h_2 - h_1 = 0.8\,\text{m}$ causes a much larger pressure of $\rho\,g\,(h_2 - h_1) = 7848\,\text{Pa}$. The third component on the right hand side of equation (B.4), which is the pressure loss $\Delta p_{\text{loss}}$, is analytically difficult to determine. However, it has thoroughly been taken into account in the design of the setup to keep the pressure loss as small as possible by the gradual tapering of the flow area in the nozzles at the outlet of the frame above the cooling plate and by the use of short outlet hoses with a large diameter. Hence, the pressure loss is not significantly large and is considered by rounding up the sum of the other two components, resulting in the relative static pressure of $p_{1,\text{rel}} = 10000\,\text{Pa} = 0.1\,\text{bar}$. As it will be shown at the end of this section, this assumption is also justified.

The thickness of the glass plates $t_{\text{gp}}$ was designed by means of rearranging the equation (B.2), such that the maximum deformation is an input argument. Here, a maximum permissible deformation of $\gamma_{\text{gp,max}} = 1\,\text{mm}$ was defined, which is a suitable choice considering the large horizontal dimensions of the plates. It should be emphasized at this point, that this maximum deformation was only used for the design. Such a deformation does not occur at the lower glass plate, i.e. the cooling plate of the Rayleigh-Bénard cell, during the experiments, since the water level in the reservoirs connected to the cell via a hose nearly compensates the pressure in the cooling circuit, yielding a maximum deformation of the cooling plate of $\gamma_{\text{gp,maax}} \ll 1\,\text{mm}$. With the assumption $\gamma_{\text{gp,max}} = 1\,\text{mm}$ a plate thickness of $t_{\text{gp}} \geq 7.8\,\text{mm}$ is required, resulting in $t_{\text{gp}} = 8\,\text{mm}$. Applying this thickness, the maximum mechanical stress then amounts to $\sigma_{\text{gp,max}} \approx 23.6\,\text{N/mm}^2$. This mechanical stress is considerably smaller than the tensile bending strength of thermally toughened
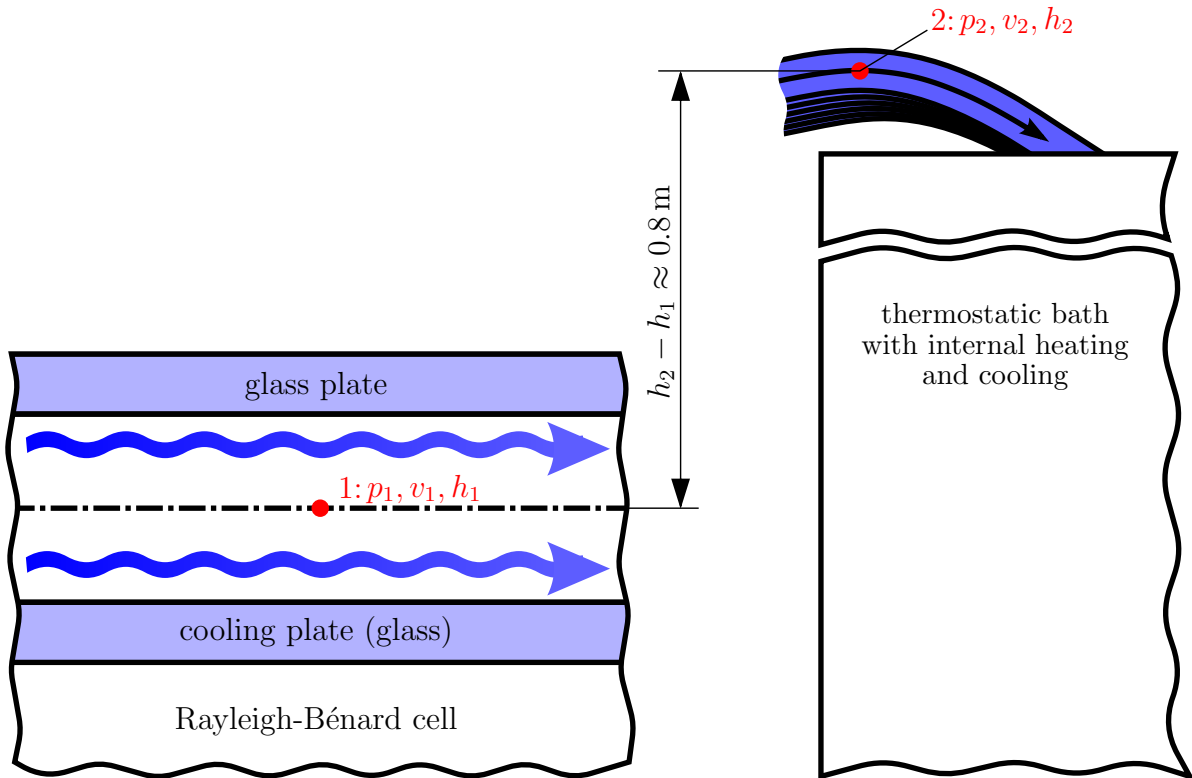
Figure B.4: A sketch showing the two points of the cooling circuit, which are chosen for the analytical estimation of the pressure between the glass plates via *Bernoulli's principle*.

glass, which is around $120\,\mathrm{N/mm^2}$ [177], thereby already proving the mechanical stability of the plates, as the compression strength of glass is usually substantially higher.

In order to further confirm this analytical estimation, numerical simulations were performed for determining the deformation and the mechanical stress of the glass plates with the thickness of $t_{\mathrm{gp}} = 8\,\mathrm{mm}$. The boundary conditions of the simulations have been defined equally, i.e. a uniform pressure load of $p_{1,\mathrm{rel}} = 0.1\,\mathrm{bar}$ strains the plate, which is fixed at the edges. The results obtained from the simulations for the deformation in figure B.5 and for the mechanical stress in figure B.6 show a good agreement with the analytically estimated results.

Furthermore, as aforementioned the appropriateness of assuming $p_{1,\mathrm{rel}} = 0.1\,\mathrm{bar}$ as the relative pressure between the plates has been checked. Without considering the pressure loss downstream of the glass plates $\Delta p_{\mathrm{loss}}$, a relative pressure of about $p_{1,\mathrm{rel,ideal}} = 0.08\,\mathrm{bar}$, mainly caused by the hydrostatic pressure, has been obtained above. Hence, the additional pressure loss is assumed to be about $\Delta p_{\mathrm{loss}} = 0.02\,\mathrm{bar}$, resulting in a slightly larger deformation of the plates. This has also been investigated by means of comparing the deformation for $p_{1,\mathrm{rel}} = 0.1\,\mathrm{bar}$ with that for $p_{1,\mathrm{rel}} = 0.08\,\mathrm{bar}$ obtained from a further numerical simulation. Taking the integral of this difference of the deformation over the entire plate yields a volume displacement of about $30\,\mathrm{ml}$, that can be compared with the volume of the water displaced in the experiment. For this, a ruler has been fixed at one of the two hoses connected to the cell, in order to check the rising water level after switching on the cooling water system. The water level usually reaches the mid area of the connected reservoirs, however, as it can be seen in figure B.7, a relatively low water level has been adjusted in this case, aiming for the visualization of the increasing water level inside the hose. While figure B.7a shows the level for the state of rest, i.e. when only the hydrostatic
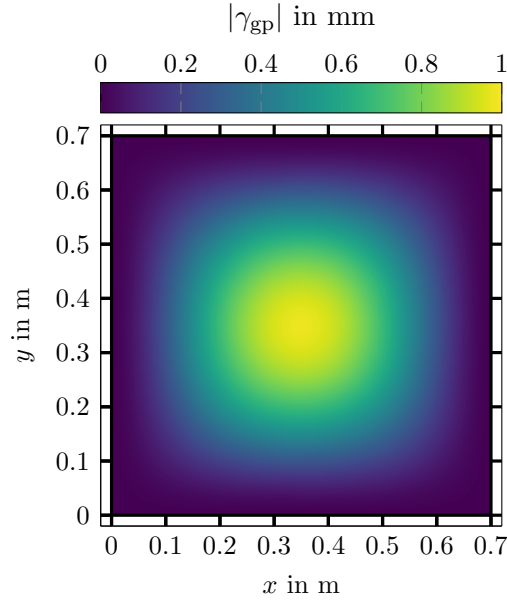
$|\gamma_{\mathrm{gp}}|$ in mm

Figure B.5: Estimation of the maximum deformation of the glass plates enclosing the cooling circuit for a uniform pressure load of $p_{1,\mathrm{rel}} = 0.1\,\mathrm{bar}$, roughly corresponding to the flow rate $\dot{V}_{\mathrm{cw}} = 30\,\mathrm{l/min}$ adjusted in the cooling circuit. However, during the flow measurements the water reservoirs connected to the cell are filled up, resulting in a counteracting hydrostatic pressure, such that the deformation of the lower glass plate, which is the cooling plate of the Rayleigh-Bénard cell, is much smaller.
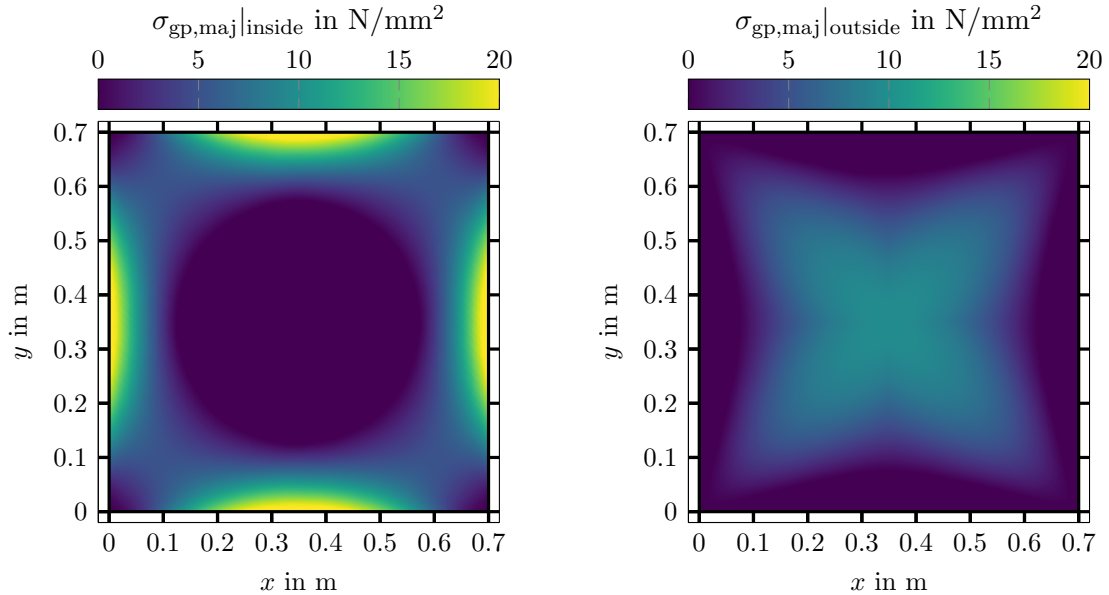


(a) Major principal stress at the surface inside the cooling circuit

(b) Major principal stress at the surface outside the cooling circuit

Figure B.6: Major principal stress of the two glass plates at the surface inside and outside the cooling circuit. The positive sign of the major principal stress indicates that it corresponds to the tensile stress. The minor principle stress with a negative sign representing the compressive stress is not depicted here, since it can be derived from the major principle stress in this case according to $\sigma_{\mathrm{gp,min}}|_{\mathrm{inside}} = -\sigma_{\mathrm{gp,maj}}|_{\mathrm{outside}}$ and $\sigma_{\mathrm{gp,min}}|_{\mathrm{outside}} = -\sigma_{\mathrm{gp,maj}}|_{\mathrm{inside}}$. As it can be seen, the maximum stress $\sigma_{\mathrm{gp,max}}$ occurs in the center of the fixed edges.

pressure yields a small deformation of the cooling plate, figure B.7b represents the water level for the flow rate $\dot{V}_{\text{cw}} = 30\,\text{l/min}$ applied in the experiments. The water level rises by about $7\,\text{cm}$, which corresponds to a water displacement of about $11\,\text{ml}$, considering that two hoses are connected to the cell. As this water displacement is even smaller than the volume displacement of about $30\,\text{ml}$ obtained from the comparison of the deformation in the numerical simulations for $p_{1,\text{rel}} = 0.1\,\text{bar}$ and $p_{1,\text{rel}} = 0.08\,\text{bar}$, assuming a relative pressure of $p_{1,\text{rel}} = 0.1\,\text{bar}$ for the design is justified.
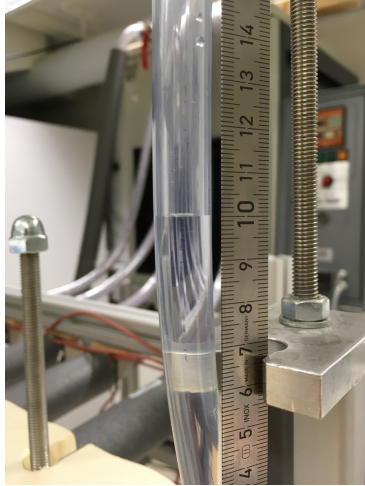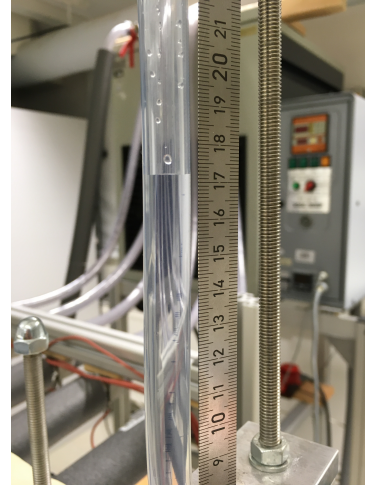


(a) Stagnant cooling water                    (b) $\dot{V}_{\text{cw}} = 30\,\text{l/min}$

Figure B.7: Visualization of the pressure increase resulting from the cooling water flow by means of the rising water-level in the hose connected to the Rayleigh-Bénard cell.

# Analytical estimation of the limit of $\Delta T$

Due to the fact that the cooling plate of the Rayleigh-Bénard cell is made of glass, the possible temperature differences between the bottom and top of the cell are strongly limited by its low thermal conductivity Therefore, using an oversize thickness of the plate for reasons of safety is not appropriate, which is why the thickness was designed properly as shown in the appendix B. This thickness of $t_{\mathrm{gp}} = 8\,\mathrm{mm}$ allows to adjust certain temperature differences with respect to the achievable range of Rayleigh numbers and also ensures the mechanical stability. Based on experimental investigations with this setup, it is demonstrated in section 3.1.3, which temperature differences can be obtained in this case. However, this had to be estimated already during the design for making sure that a suitable experimental facility is set up. For this, a simplified analytical model incorporating those components of the setup, that determine the occurring temperatures, was used. The model is sketched in figure C.1, showing that the sidewalls are not considered, which is reasonable due to their minor influence when cells with large aspect ratios are applied. Besides the heating and cooling plate as well as the Rayleigh-Bénard cell, only the insulation at the bottom side of the heating plate is taken into account. Hence, as indicated in figure C.1, in this model the occurrence of three different heat fluxes is assumed. While $\dot{q}_{\mathrm{cell}}$ represents the heat flux from the heating to the cooling plate, the heat fluxes $\dot{q}_{\mathrm{amb,1}}$ and $\dot{q}_{\mathrm{amb,2}}$ denote the heat loss to the surroundings or the heat absorption from the surroundings, depending on the ambient temperature $T_\infty$. In this case, $T_\infty = 20\,^\circ\mathrm{C}$ is assumed. Furthermore, in order to get a better idea of the variation of the horizontally averaged temperature $\langle T \rangle_{x,y}$ along the vertical axis, it is qualitatively depicted in figure C.1, clearly showing the large temperature drop across the cooling plate.

In the first step of the modeling, the thermal resistances of the solid bodies labeled as ①, ②, ④, ⑥ and ⑧ in figure C.1 are determined according to $r_i = h_i/\lambda_{\mathrm{th},i}$, with $h_i$ and $\lambda_{\mathrm{th},i}$ being the height and the thermal conductivity of each body with the label $i$. The main body of the heating plate ③ is here not considered as a thermal resistance, since the heating water is flowing through it in meandering copper tubes with a very high thermal conductivity, embedded in special profiles made of aluminum, such that the temperature drop to the enclosing plates ② and ④ is negligible. Therefore, the temperature of the heating water $T_{\mathrm{hw}}$ decreases across the covering of the heating plate ④, the water in the Rayleigh-Bénard cell ⑤ and the cooling plate ⑥ to the temperature of the cooling water $T_{\mathrm{cw}}$, as indicated in figure C.1. The temperature drop from the upper surface of the cooling plate ⑥ to the cooling water temperature is neglected in the model, as the thermal resistance for convection is expected to be very small due to the strong cooling water flow. The height of each solid body and fluid layer for the calculation of the thermal
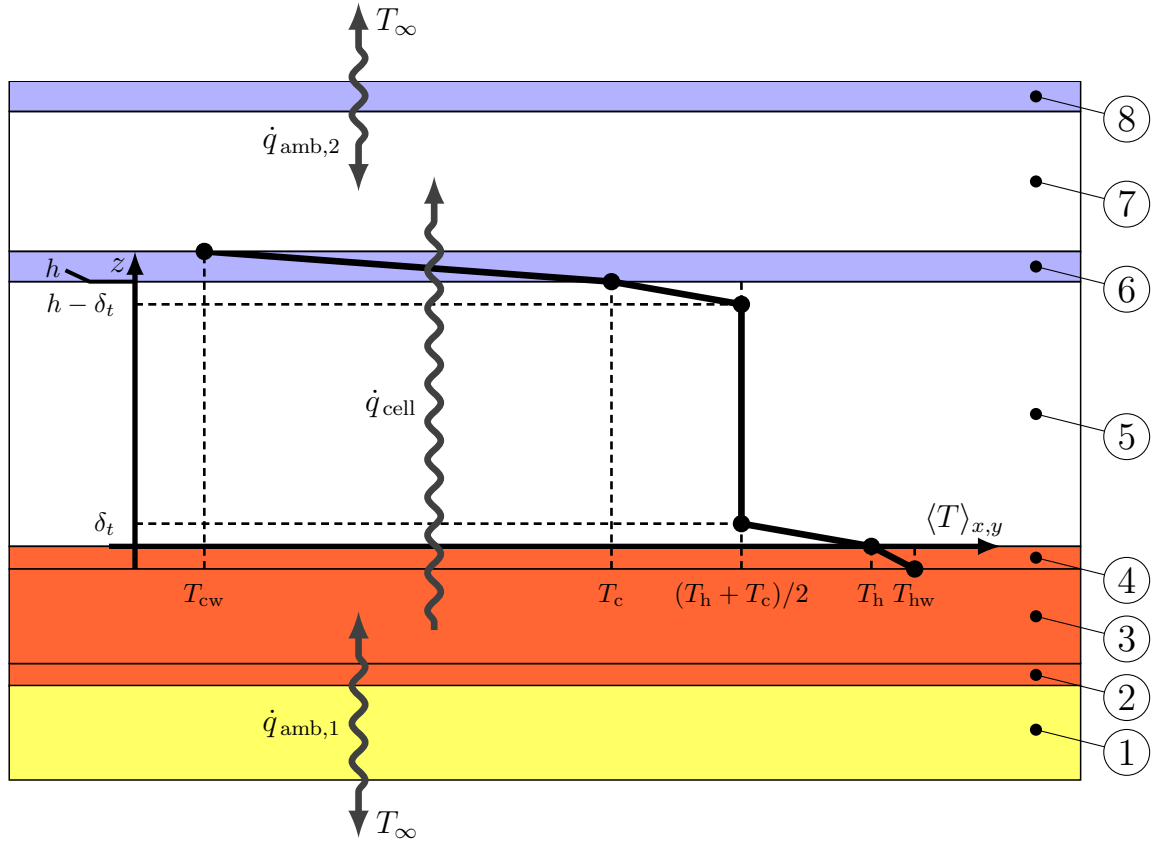
Figure C.1: A qualitative sketch of the temperature variation from the heating to the cooling water circuit, with the numbers at the right side indicating the main components of the experimental setup, which determine the temperature boundary conditions. In ascending order, the numbers represent ① - the insulation made of extruded polystyrene foam (XPS), ② - the base of the heating plate, ③ - the main body of the heating plate, ④ - the covering of the heating plate, ⑤ - the water in the Rayleigh-Bénard cell, ⑥ - the cooling plate made of glass, ⑦ - the cooling water and ⑧ - the covering glass plate of the cooling circuit.

resistances is listed in table C.1, while the thermal conductivities are given in table C.2. It should be noted, that the thermal conductivities of the solid bodies are assumed to be constant, since those are not considerably affected by temperature changes under standard conditions.

| $h_1$ | $h_2$ | $h_3$ | $h_4$ | $h_5\vert_{\Gamma=25}$ | $h_5\vert_{\Gamma=10}$ | $h_6$ | $h_7$ | $h_8$ |
|---|---|---|---|---|---|---|---|---|
| 25 mm | 6 mm | 25 mm | 6 mm | 28 mm | 70 mm | 8 mm | 37 mm | 8 mm |

Table C.1: The height of the different components of the experimental setup considered in the analytical model sketched in figure C.1.

Due to the Rayleigh-Bénard flow, the thermal resistance of the water in the cell is strongly decreased compared to the state of rest, in which heat is only transported via conduction across the whole fluid layer. As explained by means of figure 1.2 in the introduction, conduction only dominates in the small thermal boundary layers at the bottom and top plate, while the heat is significantly better transported in the bulk, when thermal convection sets in. Thus, as commonly the thermal resistance is reduced to that of

| XPS | aluminum | glass | water | | | |
|---|---|---|---|---|---|---|
| $i = ①$ | $i = ②, ③, ④$ | $i = ⑥, ⑧$ | $i = ⑤, ⑦$ | | | |
| $\lambda_{\mathrm{th},i}$ | $\lambda_{\mathrm{th},i}$ | $\lambda_{\mathrm{th},i}$ | $\lambda_{\mathrm{th},i}$ | $\alpha_i \cdot 10^4$ | $\nu_i \cdot 10^6$ | $\kappa_i \cdot 10^7$ |
| $0.03\,\frac{\mathrm{W}}{\mathrm{m\,K}}$ | $204\,\frac{\mathrm{W}}{\mathrm{m\,K}}$ | $0.78\,\frac{\mathrm{W}}{\mathrm{m\,K}}$ | $0.60\,\frac{\mathrm{W}}{\mathrm{m\,K}}$ | $2.07\,\frac{1}{\mathrm{K}}$ | $1.00\,\frac{\mathrm{m}^2}{\mathrm{s}}$ | $1.43\,\frac{\mathrm{m}^2}{\mathrm{s}}$ |

Table C.2: The thermal conductivities of extruded polystyrene foam (XPS) [178], aluminum and glass [179] as well as different fluid properties of water for $T = 20\,°\mathrm{C}$ [180] considered in the analytical model. The numbers in the second row indicate the components according to the labels in figure C.1, respectively.

the thermal boundary layers in the analytical model. The reduction of the entire thermal resistance of the water due to the flow is represented by the Nusselt number Nu, i.e. $r_5 = h_5/(\mathrm{Nu}\,\lambda_{\mathrm{th},5})$. However, neither the Nusselt number nor the temperature-dependent thermal conductivity of the water $\lambda_{\mathrm{th},5}$ is known, because fixed values of the temperature at the heating and cooling plate are not given a priori. Since the Nusselt number depends on the Rayleigh number, it can be obtained from the results of previous numerical simulations as outlined in section 3.1, yielding the relations Nu(Ra) for the aspect ratio $\Gamma = 25$ [57] and $\Gamma = 10$ [137] according to the equations (C.1a) and (C.1b).

$$\mathrm{Nu}|_{\Gamma=25} = 0.133\,\mathrm{Ra}^{0.298} \tag{C.1a}$$

$$\mathrm{Nu}|_{\Gamma=10} = 0.152\,\mathrm{Ra}^{0.290} \tag{C.1b}$$

Since the experimental results should be comparable to that of numerical simulations, a range of desirable Rayleigh numbers has been defined for both aspect ratios. When defining those ranges, the suitability of the required temperature differences $\Delta T^* = \mathrm{Ra}^* \nu^* \kappa^* / (\alpha^* g\, h^3)$ has already been taken into account, presuming that large temperature differences of $\Delta T > 10\,\mathrm{K}$ might be very hard to achieve. But, the quantities labeled with an asterisk in the latter equation and in the following can only be considered as initial values, as the absolute temperatures of the water in the cell are not known yet and the average temperature of $\langle T \rangle = T_\infty = 20\,°\mathrm{C}$ was assumed for the estimation of the fluid properties. Based on this, the initial ranges of the Rayleigh number of $\mathrm{Ra}^* \in [1 \cdot 10^5, 3 \cdot 10^6]$ for $\Gamma = 25$ and $\mathrm{Ra}^* \in [1 \cdot 10^6, 5 \cdot 10^7]$ for $\Gamma = 10$ were determined. Therefore, initial Nusselt numbers $\mathrm{Nu}^*$ can be calculated with the equations (C.1a) and (C.1b), in order to get the initial thermal resistance $r_5{}^* = h_5/(\mathrm{Nu}^* \lambda_{\mathrm{th},5}^*)$ and accordingly the heat flux density from the bottom to the top of the cell $\dot{q}_{\mathrm{cell}}^* = \Delta T^*/r_5^*$. Knowing the initial heat flux density and the initial thermal resistance of the water, the absolute temperatures can be determined according to the equations (C.2a) - (C.2d).

$$T_{\mathrm{h}}^* = \langle T \rangle^* + \Delta T^*/2 = T_\infty + \Delta T^*/2 \tag{C.2a}$$

$$T_{\mathrm{c}}^* = \langle T \rangle^* - \Delta T^*/2 = T_\infty - \Delta T^*/2 \tag{C.2b}$$

$$T_{\mathrm{hw}}^* = T_{\mathrm{h}}^* + \dot{q}_{\mathrm{cell}}^*\, r_4 \tag{C.2c}$$

$$T_{\mathrm{cw}}^* = T_{\mathrm{c}}^* - \dot{q}_{\mathrm{cell}}^*\, r_6 \tag{C.2d}$$

Due to the large thermal resistance of the cooling plate $r_6$, the temperature of the cooling water $T_{\mathrm{cw}}^*$ must be considerably smaller than the cooling plate temperature $T_{\mathrm{c}}^*$

itself, especially in the case of a large temperature difference $\Delta T^*$ and consequently a large heat flux density $\dot{q}_{\text{cell}}^*$. However, very small temperatures of the cooling water close to the freezing point are not suitable with regard to the formation of a condensate film on the upper glass plate of the cooling circuit, which strongly disturbs the optical access to the Rayleigh-Bénard cell. In order to impede this, a cooling water temperature of $T_{\text{cw}}^{**} = 15\,°\text{C}$ is now assumed, so that the temperature of the cooling and heating plate are changed according to the equations (C.3a) and (C.3b), in which the labeling with the two asterisks indicates the relation to the assumption for the cooling water temperature $T_{\text{cw}}^{**}$.

$$T_{\text{c}}^{**} = T_{\text{cw}}^{**} + \dot{q}_{\text{cell}}^* \, r_6 \tag{C.3a}$$

$$T_{\text{h}}^{**} = T_{\text{c}}^{**} + \Delta T^* \tag{C.3b}$$

On the basis of this assumption, the temperatures $T_{\text{h}}^{**}$ and $T_{\text{c}}^{**}$ are now better suited from the practical point of view. Therefore, those are considered as the final temperatures resulting from the estimation, i. e. $T_{\text{h}} := T_{\text{h}}^{**}$ and $T_{\text{c}} := T_{\text{c}}^{**}$. However, the assumption for the temperature of the cooling water $T_{\text{cw}}^{**}$ also yields a shifting mean temperature in the cell, such that the final temperature of the heating water $T_{\text{hw}}$ and cooling water $T_{\text{cw}}$ must again be corrected according to the equation (C.4a) and (C.4b), using the final heat flux density $\dot{q}_{\text{cell}}$. As it can be seen on the right hand side of those equations, this requires to determine again the Nusselt number Nu according to the equations (C.1a) and (C.1b), based on the final temperature difference $\Delta T = T_{\text{h}} - T_{\text{c}}$ and the resulting Rayleigh number Ra. For the determination of the final temperature of the heating water $T_{\text{hw}}$ and cooling water $T_{\text{cw}}$, all the fluid properties were calculated for the final mean temperature in the cell via linear interpolation of the tabular values given in reference [180].

$$T_{\text{hw}} = T_{\text{h}} + \dot{q}_{\text{cell}} \, r_4 = T_{\text{h}} + \Delta T \, r_4/r_5 = T_{\text{h}} + \Delta T \, r_4 \, \text{Nu} \, \lambda_{\text{th},5}/h \tag{C.4a}$$

$$T_{\text{cw}} = T_{\text{c}} - \dot{q}_{\text{cell}} \, r_6 = T_{\text{c}} - \Delta T \, r_6/r_5 = T_{\text{c}} - \Delta T \, r_6 \, \text{Nu} \, \lambda_{\text{th},5}/h \tag{C.4b}$$

Thus, this analytical model allows to estimate the four temperatures $T_{\text{h}}$, $T_{\text{c}}$, $T_{\text{hw}}$, $T_{\text{cw}}$ in dependency of the temperature difference $\Delta T$ imposed to achieve a certain Rayleigh number Ra. For a better imagination, the results for those temperatures are shown in figure C.2 for the aspect ratios $\Gamma = 25$ and $\Gamma = 10$. It can be seen that the temperature of the heating plate and of the heating water are nearly overlapping in each case due to the excellent thermal conductivity of the heating plate made of aluminum, while there is a large difference between the temperature of the cooling plate and the cooling water, caused by the low thermal conductivity of the glass plate. In particular for a large $\Delta T$, the deviation of the temperature of the cooling plate to that of the cooling water $T_{\text{c}} - T_{\text{cw}}$ is much higher than the temperature difference between the plates $\Delta T$ itself. Hence, the temperature of the cooling water drastically decreases for the largest temperature differences $\Delta T$, nearly reaching the freezing point of water in the case of $\Gamma = 25$. However, as aforementioned the temperature of the cooling water should not be that small, in order to overcome issues with respect to condensation on the top side of the covering glass plate. The final value of this temperature can be smaller than $T_{\text{cw}}^{**} = 15\,°\text{C}$, as initially assumed, but it should not be considerably smaller than $T_{\text{cw}} = 10\,°\text{C}$, as further addressed at the end of the appendix C. The largest temperature differences of $\Delta T \approx 10\,\text{K}$ could thus only be achieved, when all the temperatures are shifted towards higher values, which is disadvantageous, because the increasing temperature in the cell yields larger heat losses to the surroundings under common laboratory conditions. It can therefore be concluded,

that a maximum temperature difference of about $\Delta T \approx 8\,\text{K}$ can be obtained for both aspect ratios.
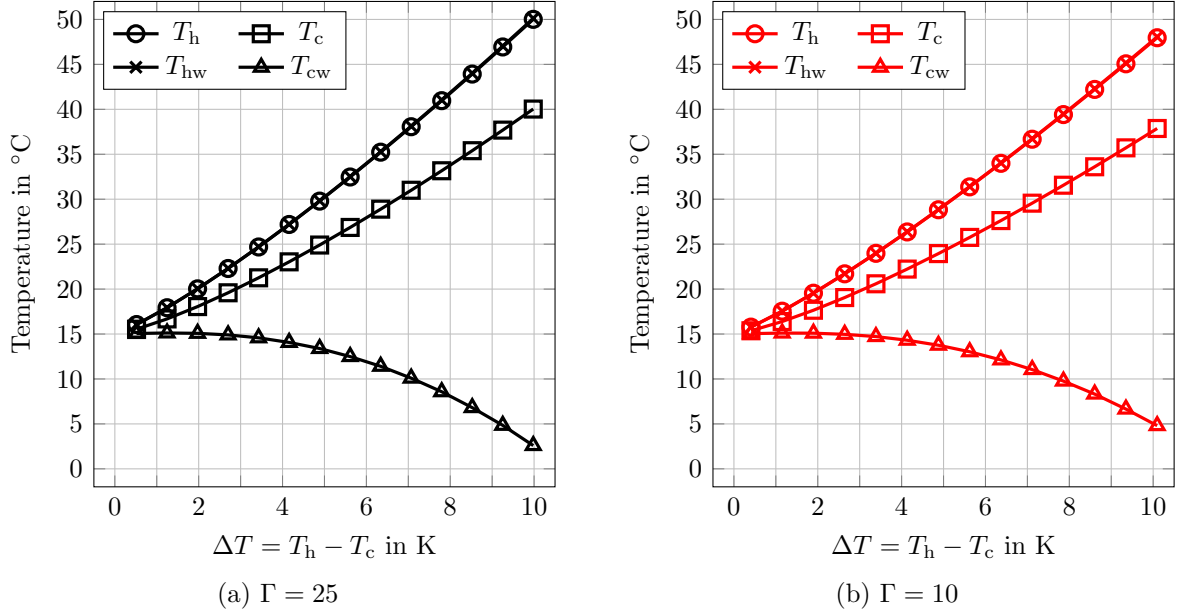


Figure C.2: Results of the analytical estimation for the temperature of the heating plate $T_{\text{h}}$, the cooling plate $T_{\text{c}}$, the heating water $T_{\text{hw}}$ and the cooling water $T_{\text{cw}}$ for the two Rayleigh-Bénard cells with the aspect ratio $\Gamma = 25$ (a) and $\Gamma = 10$ (b) for varying temperature differences between the plates $\Delta T = T_{\text{h}} - T_{\text{c}}$.

The achievable Rayleigh numbers, which differ from the initial ranges Ra* mentioned above due to the varying mean temperature in the cell, are depicted in figure C.3. From this figure it becomes obvious that the final ranges for the Rayleigh number are extended towards larger values. Considering that temperature differences up to $\Delta T \approx 8\,\text{K}$ can be reached and the temperature difference should not be considerably smaller than $\Delta T = 0.5\,\text{K}$ with respect to an accurate controlling of the thermal boundary conditions, the Rayleigh number can approximately be varied within Ra $\in [1 \cdot 10^5, 6 \cdot 10^6]$ for $\Gamma = 25$ and Ra $\in [1 \cdot 10^6, 1 \cdot 10^8]$ for $\Gamma = 10$. Therefore, it is confirmed on the basis of this analytical model that the two cells are suited to experimentally investigate RBC, as the experimental results can be compared to the results of numerical simulations for similar Rayleigh numbers.

Finally, the maximum occurring heat losses from the heating water to the surroundings $\dot{q}_{\text{amb},1}$ and the maximum heat absorption of the cooling water from the surroundings $\dot{q}_{\text{amb},2}$ are shortly discussed. Due to the very small thermal conductivity of the insulation made of XPS ①, the heat flux density at the bottom side can be estimated according to equation (C.5), without considering further thermal resistances, e.g. for heat conduction across the base of the heating plate ② and for thermal radiation at the lower side of the insulation. Even for the maximum temperature of the heating water $T_{\text{hw}} \approx 50.3\,^{\circ}\text{C}$ obtained above, the heat flux density only amounts to $\dot{q}_{\text{amb},1} \approx 36.4\,\text{W/m}^2$, which is negligible compared to the corresponding heat flux density in the Rayleigh-Bénard cell of about $\dot{q}_{\text{cell}} \approx 3608.5\,\text{W/m}^2$.

$$\dot{q}_{\text{amb},1} \approx (T_{\text{hw}} - T_{\infty})/r_1 \tag{C.5}$$

For the estimation of the heat absorption at the top side of the experimental setup, not only the thermal resistance for heat conduction must be taken into account, but also
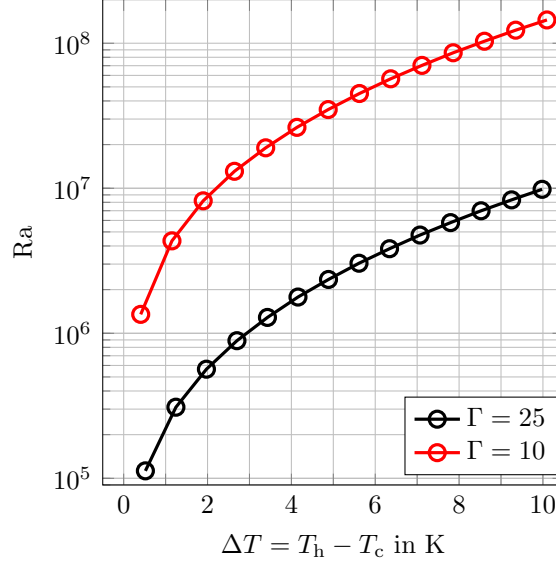
Figure C.3: Results of the analytical estimation for the achievable ranges of the Rayleigh numbers for the aspect ratios $\Gamma = 25$ and $\Gamma = 10$.

the thermal resistance for the heat transfer at the top surface of the glass plate, which is much larger than the thermal resistance at its lower side, where the cooling water flow strongly enhances the convective heat transfer. At the upper side the ambient air in the lab environment is almost stagnant, yielding a very large thermal resistance for convection and, therefore, a significant reduction of the heat transfer across the glass plate. Hence, it can be assumed that at the surface heat is only transported via thermal radiation, which is also small in these temperature ranges. The maximum heat flux density $\dot{q}_{\mathrm{amb,2}}$ for the heat absorption is determined based on the prerequisite that no moisture content of the ambient air condenses on the upper surface of the glass plate. Assuming common laboratory conditions with a temperature of $T_\infty = 20\,°\mathrm{C}$ and a relative humidity of $\varphi_{\mathrm{r}} = 50\,\%$ in the environment, the dew-point temperature $T_{\mathrm{dp}}$ and accordingly also the minimum permissible temperature at the upper side of the covering glass plate $T_{\mathrm{8,top}}$ amount to $T_{\mathrm{8,top}} = T_{\mathrm{dp}} \approx 9.3\,°\mathrm{C}$ [181]. In this case, a maximum heat flux density of $\dot{q}_{\mathrm{amb,2}} \approx 52\,\mathrm{W/m^2}$ is obtained using equation (C.6), with the *Stefan-Boltzmann* constant $\sigma_{\mathrm{SB}} = 5.67 \cdot 10^{-8}\,\mathrm{W/(m^2\,K^4)}$ and an emissivity for thermal radiation of $\epsilon = 0.9$ as typical for glass [182]. Aiming to avoid condensation on the surface of the glass plate, the minimum temperature for the cooling water can then be determined according to equation (C.7), in which the comparatively small thermal resistance for the convective heat transfer at the lower side of the glass plate is neglected, resulting in $T_{\mathrm{cw,min}} \approx 8.8\,°\mathrm{C}$.

$$\dot{q}_{\mathrm{amb,2}} = \epsilon\,\sigma_{\mathrm{SB}}\left(T_\infty^4 - T_{\mathrm{8,top}}^4\right) \tag{C.6}$$

$$T_{\mathrm{cw,min}} = T_{\mathrm{8,top}} - \dot{q}_{\mathrm{amb,2}}\,h_8/\lambda_{\mathrm{th,8}} \tag{C.7}$$

# Infrared imaging of the cooling plate

The main goal during the design of the cooling circuit of the experimental setup was to keep any temperature inhomogeneities of the transparent cooling plate as small as possible, such that the Rayleigh-Bénard flow and especially the arrangement of the turbulent superstructures in the flow is not considerably affected. Contrary to the heating plate with its covering made of aluminum, which can compensate for the slight temperature differences of the heating water very efficiently due the large thermal conductivity, the cooling plate made of glass requires further investigations. The temperature measurements with the immersible PT100 sensor in each of the inlets and outlets of the frame above the cooling plate already confirm, that due to the large flow rate of the cooling water of $\dot{V}_{\mathrm{cw}} = 30\,\mathrm{l/min}$ its temperature increase mostly amounts to only a few hundredth Kelvin and does not exceed $\Delta T_{\mathrm{cw,in \to out}} = 0.2\,\mathrm{K}$ in the flow measurements performed for this work. Based on the results of the numerical simulations presented in section B.1 it can also be expected, that no considerable local temperature inhomogeneities on the cooling plate are caused by the cooling water flow, since the water is almost uniformly streaming above its surface. In order to ensure this, images of the setup were recorded with an infrared camera (VarioCAM hr head, InfraTec GmbH) from the top, thereby enabling to assess the two-dimensional temperature distribution. However, since the lower surface of the cooling plate is not accessible for infrared imaging, the measurements were performed on the covering glass plate as it can be seen on the left side of figure D.1. Since both glass plates enclosing the cooling water flow have the same thickness of $t_{\mathrm{gp}} = 8\,\mathrm{mm}$, those measurements on the upper plate allow to estimate the effect of the cooling water flow on the temperature distribution at the lower side of the cooling plate. For improving the reliability of the infrared measurements, a spare of the covering glass plate was inserted with an adhesive black foil on the top side to maximize the thermal radiation, which is also obvious from figure D.1. Furthermore, during the infrared recordings the setup was accurately protected from the surroundings with large insulating plates, such that heat sources in the lab environment do not disturb the measurements.

For a better imagination an exemplary temperature field obtained from the infrared measurements is at first qualitatively shown on the right side of figure D.1. While the bordering warmer part represents the insulation, the cold part in the center is the square glass plate, which is slightly distorted due to optical aberrations. In the calibration of the physical dimensions, the distortion is corrected with a simple calibration, using small markers cut out from an aluminum sheet, that can be clearly identified in the infrared recordings because of the differing emission coefficient. A marker was placed in each of the four corners as well as in the center of the edges, resulting in eight known marker
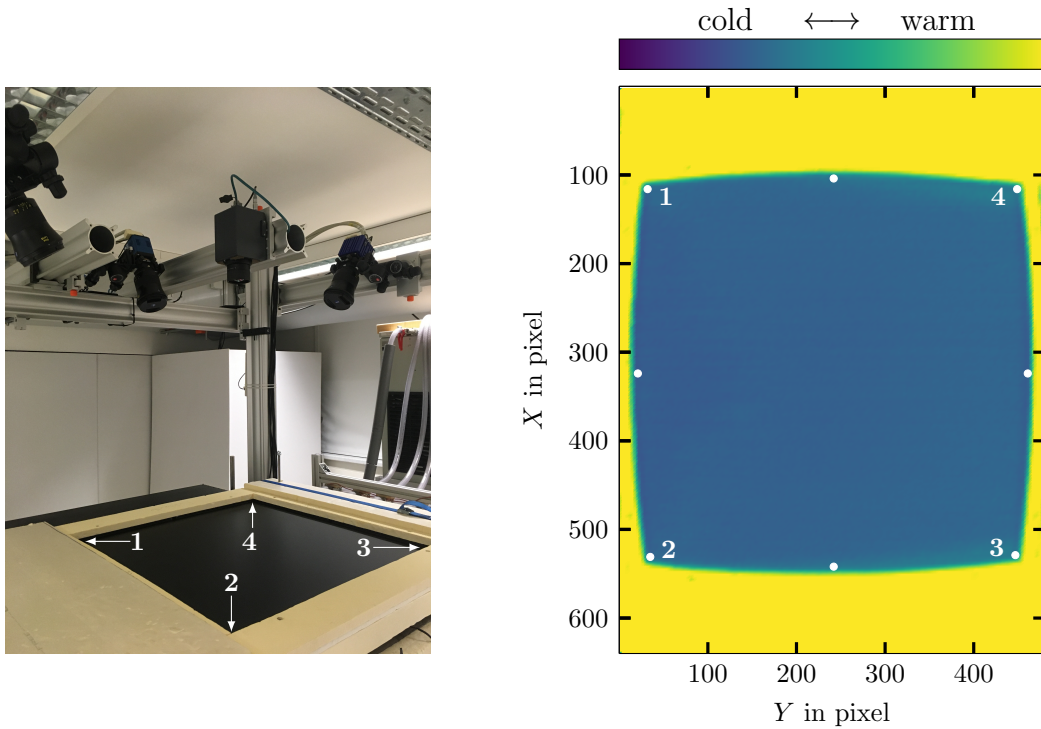
Figure D.1: The experimental setup for the infrared measurements (left) and a qualitative visualization of an exemplary temperature field obtained from the infrared camera (right), with the white dots showing the position of the markers used for the calibration of the physical dimensions. In addition, the numbers in both the photograph and the visualization of the temperature field indicate the corresponding corners of the glass plate.

positions indicated in figure D.1, which is sufficient for the dimensional calibration of those measurements. Based on this, the relation of each of the camera's pixel to the position in physical dimensions was derived with a cubical interpolation approach.

Since the flow rate of the cooling water considerably affects its temperature increase, the temperature distribution on the upper glass plate was measured for the different flow rates $\dot{V}_{cw} = 5\,\mathrm{l/min}$, $\dot{V}_{cw} = 10\,\mathrm{l/min}$, $\dot{V}_{cw} = 20\,\mathrm{l/min}$ and $\dot{V}_{cw} = 30\,\mathrm{l/min}$. For ensuring the comparability, the temperature at the thermostatic bath of the cooling water was adapted in each case to achieve similar temperature differences in the Rayleigh-Bénard cell, ranging between $\Delta T = 2.7\,\mathrm{K} \pm 0.1\,\mathrm{K}$ for all the adjusted flow rates. The results of the measurements are depicted in figure D.2, however, not the absolute temperatures are shown, but the temperature variation on the surface $\Delta T_{\mathrm{gp,top}}$, which is determined by subtracting the minimum occurring temperature from the absolute temperatures. The minimum was in each case obtained from the rectangle with the white dashed border lines delineated in figure D.2, which are $4\,\mathrm{cm}$ away from the outer rim of the cooling water area. Hence, the temperatures at the margin are excluded, since those are affected by the fixation, especially by the clamping elements at the top side of the plate, that can be seen in figure A.7. Looking at the temperature variation in the figures D.2a - D.2d it gets obvious, that the flow rate of the cooling water has a strong effect. For the lower flow rates $\dot{V}_{cw} = 5\,\mathrm{l/min}$ and $\dot{V}_{cw} = 10\,\mathrm{l/min}$ temperature inhomogeneities can clearly be observed. In particular, in close vicinity to the edges large deviations of $\Delta T_{\mathrm{gp,top}} > 0.5\,\mathrm{K}$ appear. Furthermore, the temperature variations along the $x$-axis in vertical direction for $0.1\,\mathrm{m} < y < 0.25\,\mathrm{m}$ are very conspicuous, with the distance between the most distinctive minima reminding of

the diffusers' arrangement, as depicted in figure B.1. Those outstanding inhomogeneities are probably caused by the fact, that the cooling water does not symmetrically stream through the diffusers, but preferentially flows along one of the two boundaries despite the small diffuser angle, which is more likely to occur for small flow velocities and accordingly low Reynolds numbers, as demonstrated in the work [138]. However, as the results of the numerical simulations in the appendix B.1 have shown, the cooling water streams almost uniformly above the cooling plate for higher flow rates. Here, this is also assured by the results for the higher flow rates $\dot{V}_{\mathrm{cw}} = 20\,\mathrm{l/min}$ and $\dot{V}_{\mathrm{cw}} = 30\,\mathrm{l/min}$, which yield a significant improvement regarding the temperature homogeneity.
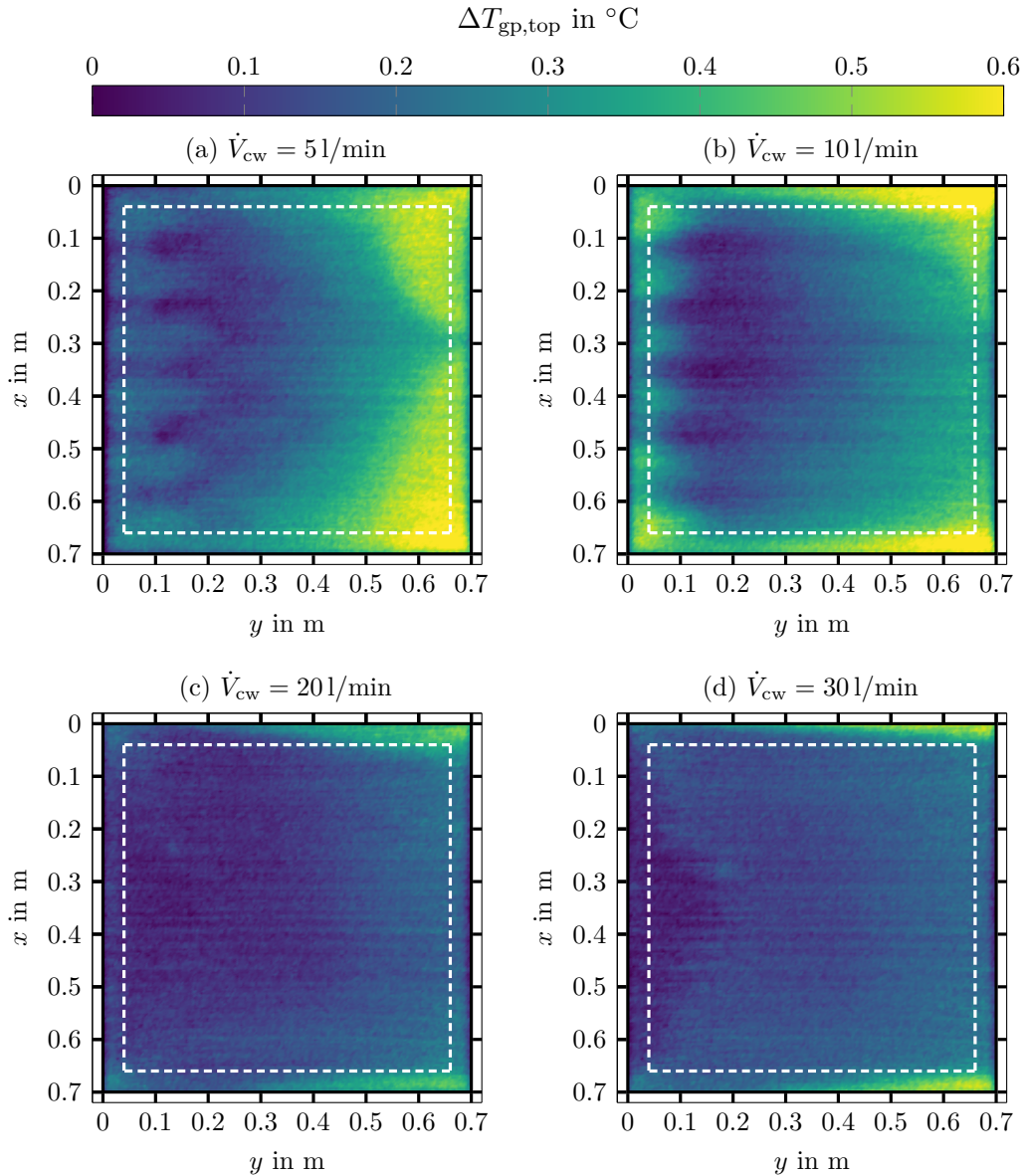


Figure D.2: The temperature variation on the glass plate above the cooling water $\Delta T_{\mathrm{gp,top}}$ for different flow rates. It is noted that the rectangle with the dashed border lines indicates the section of the infrared measurement, which is not considerably affected by the fixation of the glass plate at its edges, respectively.

In order to allow for a better comparison of the results for the different flow rates, the mean value is taken along the axis, respectively, thereby determining the profiles of the

average temperature variation in flow direction of the cooling water and in transverse direction. For the averaging the border area outside the white frames shown in figure D.2, which is considerably affected by the fixation at the edges, is not taken into account. Moreover, from each profile its minimum inside the averaging limits is subtracted, respectively, such that the average temperature variation is directly obvious from the profiles, denoted by the labeling with the asterisks of $\langle \Delta T_{\mathrm{gp,top}} \rangle_x^*$ and $\langle \Delta T_{\mathrm{gp,top}} \rangle_y^*$ in the following. Those profiles can be seen in figure D.3 and clearly confirm the trend of the decreasing temperature variation with increasing flow rate. Considering the assigned limits of the measurement area indicated by the dashed lines, which correspond to the white frames in figure D.2, the maximum temperature increase in flow direction amounts to about $\langle \Delta T_{\mathrm{gp,top}} \rangle_x^* \approx 0.14\,\mathrm{K}$ for $\dot{V}_{\mathrm{cw}} = 20\,\mathrm{l/min}$ and $\dot{V}_{\mathrm{cw}} = 30\,\mathrm{l/min}$, while the temperature rises by $\langle \Delta T_{\mathrm{gp,top}} \rangle_y^* \approx 0.1\,\mathrm{K}$ in transversal direction. Even though the maximum temperature variations for those two flow rates are quite similar, the flow rate $\dot{V}_{\mathrm{cw}} = 30\,\mathrm{l/min}$ was chosen for the experiments in this work, because the overall trend suggests to adjust higher flow rates.



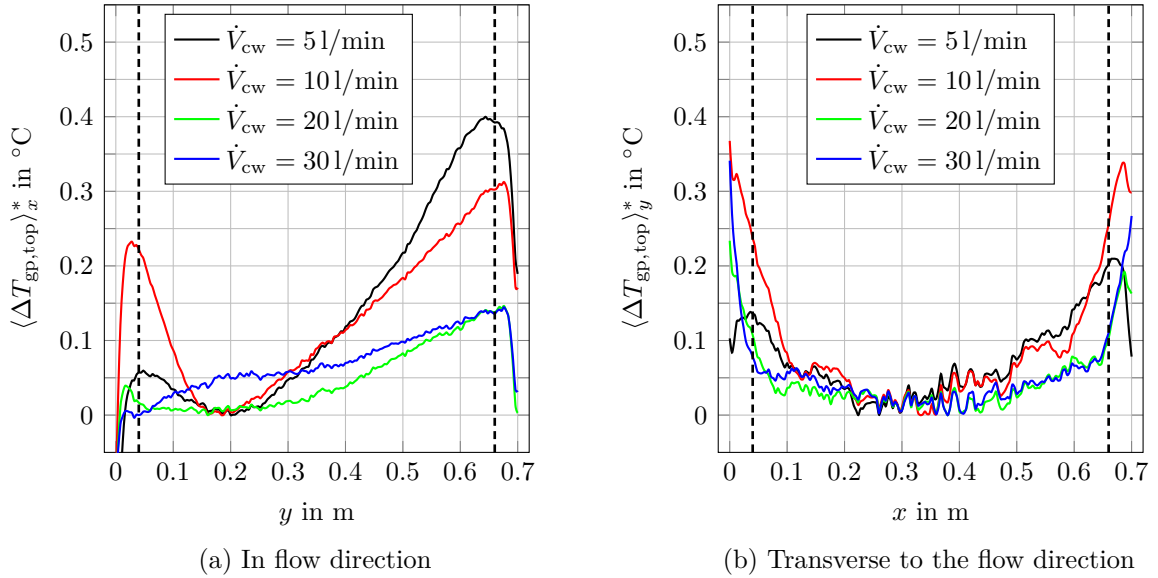(a) In flow direction                    (b) Transverse to the flow direction

Figure D.3: The profiles of the average temperature variation on the glass plate above the cooling water for different flow rates. It is noted that the dashed lines indicate the section of the infrared measurement, which is not considerably affected by the fixation of the glass plate at its edges and used for the averaging, respectively.

As aforementioned, the temperature difference in the Rayleigh-Bénard cell was adjusted to $\Delta T = 2.7\,\mathrm{K} \pm 0.1\,\mathrm{K}$ for the varying flow rates. However, since also higher temperature differences up to about $\Delta T = 4.5\,\mathrm{K}$ are applied for the study of RBC in the present work, the infrared measurements were performed for two higher temperature differences at $\dot{V}_{\mathrm{cw}} = 30\,\mathrm{l/min}$, too. Besides the temperature variation for the previously adjusted smaller $\Delta T$, the results for the higher temperature differences of $\Delta T = 3.8\,\mathrm{K}$ and $\Delta T = 4.8\,\mathrm{K}$ are depicted in figure D.4. As it can be expected, the temperature increase on the surface of the top glass plate is slightly larger in flow direction of the cooling water flow and in the transversal direction, when the temperature difference in the cell is higher. Taking into account the limits of the measurement area indicated by the dashed lines, the maximum temperature deviation is obtained for $\Delta T = 4.8\,\mathrm{K}$ in flow direction of the cooling water and amounts to $\langle \Delta T_{\mathrm{gp,top}} \rangle_x^* \approx 0.19\,\mathrm{K}$. According to the measurements with the immersible

169

PT100 elements in the inlet and outlet for the cooling water, its temperature increases by
about $\Delta T_{\text{cw,in}\to\text{out}} = 0.16\,\text{K}$ in this case, which is in good agreement when considering the
measurement uncertainties. Therefore, it can finally be concluded, that the cooling water
flow only yields slight temperature inhomogeneities on the cooling plate, which are very
small compared to the temperature difference between the heating and cooling plate of
the Rayleigh-Bénard cell.



(a) In flow direction
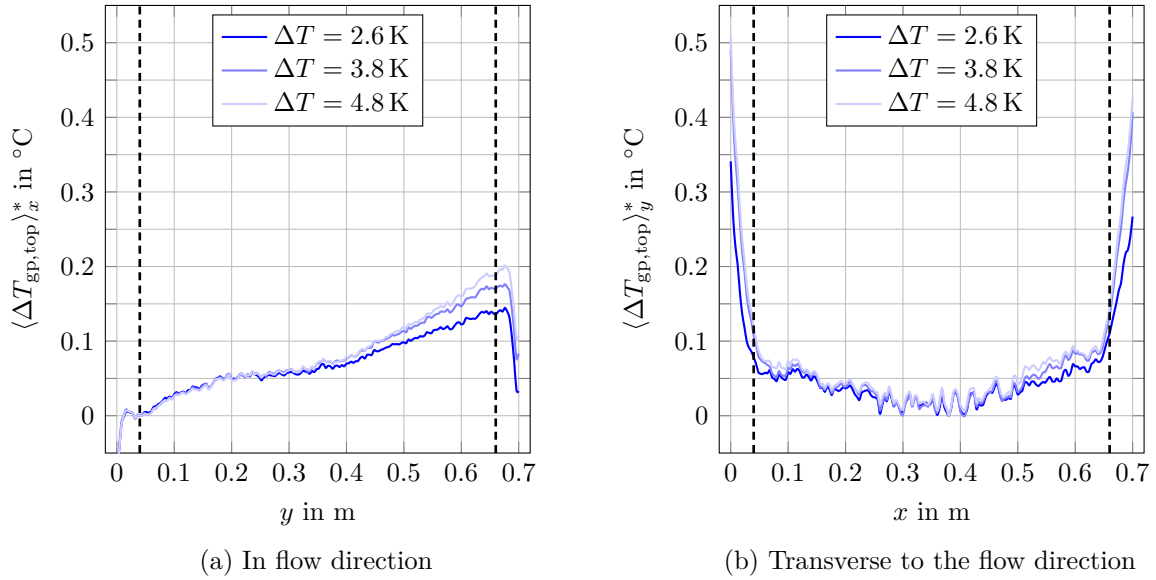
(b) Transverse to the flow direction

Figure D.4: The profiles of the average temperature variation on the glass plate above the cooling
water for different temperature differences in the Rayleigh-Bénard cell $\Delta T$. It is noted that the
dashed lines indicate the section of the infrared measurement, which is not considerably affected
by the fixation of the glass plate at its edges and used for the averaging, respectively.

# On the application of TLCs
# with different specifications

The dependency of the color of TLCs on the illumination spectrum and observation angle has been discussed in section 2.2 in detail. In order to investigate the effect of the illumination spectrum on the color play of the TLCs, a white light source incorporating six LEDs with different central emission wavelengths and independently adjustable power has been used. Based on the comparison of the results for two different illumination spectra it has been shown, that similar integral intensities in the red, green and blue wavelength range are advantageous to obtain a large dynamic range of the color play of the TLCs, which is beneficial for a low uncertainty of the temperature measurement. Even though the white light source (Spectra X Light Engine, Lumencor Inc.) was very useful for this investigation in the small experimental setup presented in section 2.2, it is not applied for the illumination of the TLCs in the large Rayleigh-Bénard cell demonstrated in section 3.1. The main reason is that the light is emitted through a single fiber and would have to be strongly expanded to shape a white light sheet covering the whole horizontal cross-section of the cell, yielding not only a drastic decrease of the illumination level, but also chromatic aberration that might be difficult to correct. Therefore, a light source with many horizontally aligned white LEDs and a specially designed light sheet optic has been built up, as outlined in section 3.2. However, since the illumination spectrum of the white LEDs is not adjustable, its suitability with regard to inducing a distinctive color play of TLCs has been tested. For this, calibration measurements have been performed, following the same procedure as the measurements described in section 2.2. Thus, the color of the TLCs has been studied in dependency of the temperature for six different observation angles, ranging from $\varphi_{\mathrm{cc}} = 40°$ up to $\varphi_{\mathrm{cc}} = 90°$ in steps of 10°. The color of the TLCs has again been analyzed in a central section of the small cylindrical cell, as indicated in figure 2.5. For each combination of the temperature level and observation angle fifty images have been recorded with a frequency of $f = 5\,\mathrm{Hz}$. Furthermore, the correlation between the color and the temperature has been determined for the TLCs R20C20W and R25C50W, which have been used for the temperature measurements in the scope of this work. The results are depicted in the figure E.1.

The calibration curves in figure E.1 clearly show, that the light source with the white LEDs is suited to obtain a strong color play of the TLCs. For the observation angles $40° \leq \varphi_{\mathrm{cc}} \leq 70°$, the time-averaged hue approximately varies in between $\langle H \rangle_t = 0$ and $\langle H \rangle_t = 2/3$, which corresponds to the color change from red to blue with increasing temperature. For the observation angles $\varphi_{\mathrm{cc}} = 80°$ and $\varphi_{\mathrm{cc}} = 90°$ the hue even varies up to
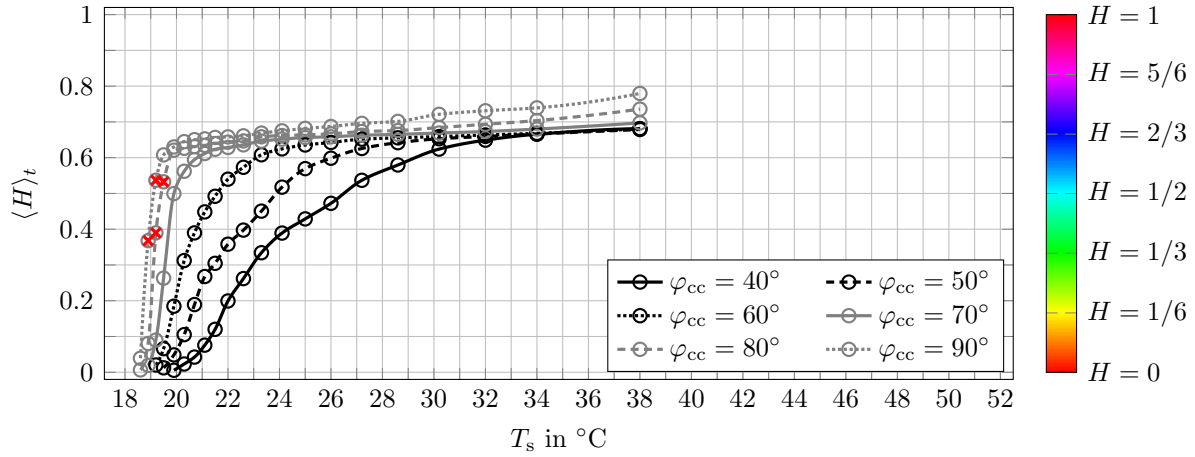
(a) TLCs of type R20C20W
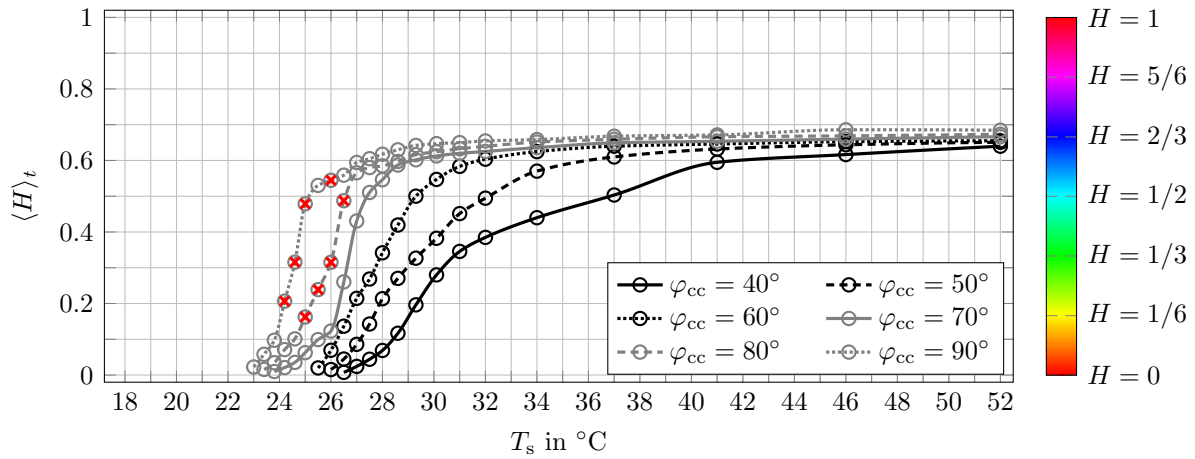


(b) TLCs of type R25C50W

Figure E.1: Color appearance of the TLCs R20C20W (a) and R25C50W(b) in terms of the hue $\langle H \rangle_t$ in dependency of the set temperature $T_s$ for a varying observation angle $\varphi_{cc}$. The colorbar on the right side shows the color corresponding to the hue values.

$\langle H \rangle_t = 3/4$ or slightly more, when the TLCs R20C20W are applied. However, hue values in the range $2/3 \leq H \leq 3/4$, which indicate the transition from the blue to the violet color shade, are not of interest for the measurements, since the temperature measuring range is always adjusted in the way that the occurring hue values do mostly not exceed $H = 2/3$, in order to achieve a low measurement uncertainty. For the TLCs R25C50W, hue values considerably larger than $\langle H \rangle_t = 2/3$ do not appear in this case, because the calibration has not been performed to the upper limit of their nominal temperature range.

In qualitative terms, the same effect of the observation angle on the correlation between the hue and the temperature as for the Spectra X Light Engine, discussed in section 2.2, is obvious from figure E.1. Hence, the color of the TLCs changes from red to blue within a smaller temperature range, when larger observation angles are used. Furthermore, the temperature of the red start is shifted towards lower temperatures with increasing observation angle. When comparing the results for the TLCs R20C20W in figure E.1a with those for the TLCs R25C50W in figure E.1b, two main differences can be seen at the first glance. One the one hand, the temperature of the red start is shifted by about 5 K in average, as can be expected according to the nominal specifications of the

TLCs. One the other hand, the hue varies more gradually with temperature for the TLCs R25C50W, especially for the lower observation angles. This means, that the temperature can be measured over larger ranges, however, the measurement uncertainty in the useful measuring range typically increases when the same observation angle is applied, due to the decreasing gradient of the hue [78]. This is shown in section 4.2, in which the calibration measurements with these types of TLCs in the Rayleigh-Bénard facility are presented.

For the sake of completeness it must be noted, that for the observation angles $\varphi_{\mathrm{cc}} = 80°$ and $\varphi_{\mathrm{cc}} = 90°$ some problems have occurred at temperature levels close above the red start temperature, which are marked in the figures E.1a and E.1b with red cross symbols, respectively. At those temperature levels, the light reflected by the TLCs was considerably less intense despite a sufficiently high seeding concentration, such that the hue values could not be determined properly and did not result in a smooth transition of the calibration curve. Therefore, those calibration points have been corrected with curve fitting techniques for the illustration. As those results have been obtained from measurements in a specific experimental setup, this cannot be considered as a general issue related to the applied white LEDs in combination with large observation angles. Nevertheless, with regard to the measurements in the Rayleigh-Bénard facility in the present work this has demonstrated, that special care has to be taken for the arrangement of the color camera, so that the color shade of the TLCs can be measured reliably at each position within the camera's field of view. Thus, the calibration has been checked accurately for each type of the TLCs, as shown in section 4.2.

# References

[1] Y. Shabany. *Heat Transfer*. Taylor & Francis (2009).

[2] M. Panjeshahi, Abtin Ataei, and Mona Gharaie. A Comprehensive Approach to an Optimum Design and Simulation Model of a Mechanical Draft Wet Cooling Tower. *Iranian Journal of Chemistry and Chemical Engineering*, 29(1):21–32 (2010).

[3] S.A. Thorpe. Recent developments in the study of ocean turbulence. *Annual Review of Earth and Planetary Sciences*, 32(1):91–109 (2004).

[4] B. Stevens. Atmospheric moist convection. *Annual Review of Earth and Planetary Sciences*, 33(1):605–643 (2005).

[5] M. Gurnis. Large-scale mantle convection and the aggregation and dispersal of supercontinents. *Nature*, 332(6166):695–699 (1988).

[6] J. Schumacher and K. Sreenivasan. Colloquium: Unusual dynamics of convection in the sun. *Reviews of Modern Physics*, 92(4):041001 (2020).

[7] M. Kühn, J.Bosbach, and C. Wagner. Experimental parametric study of forced and mixed convection in a passenger aircraft cabin mock-up. *Building and Environment*, 44(5):961–970 (2009).

[8] Y. Zhang, J. Li, M. Liu, J.Liu, and C. Wang. Experimental investigation of large-scale flow structures in an aircraft cabin mock-up. *Building and Environment*, 184:107224 (2020).

[9] U. Burr and U. Müller. Rayleigh–Bénard convection in liquid metal layers under the influence of a vertical magnetic field. *Physics of Fluids*, 13(11):3247–3257 (2001).

[10] A. Cramer, J. Pal, and G. Gerbeth. Model experiments for the Czochralski crystal growth technique. *The European Physical Journal Special Topics*, 220(1):259–273 (2013).

[11] A. Pandey, J. D. Scheel, and J. Schumacher. Turbulent superstructures in Rayleigh–Bénard convection. *Nature Communications*, 9:2118 (2018).

[12] E. Bodenschatz, W. Pesch, and G. Ahlers. Recent developments in Rayleigh–Bénard convection. *Annual Review of Fluid Mechanics*, 32(1):709–778 (2000).

[13] Q. Zhou, H.-D. Xi, S.-Q. Zhou, C. Sun, and K.-Q. Xia. Oscillations of the large-scale circulation in turbulent Rayleigh–Bénard convection: the sloshing mode and its relationship with the torsional mode. *Journal of Fluid Mechanics*, 630:367–390 (2009).

[14] P. K. Mishra, A. K. De, M. K. Verma, and V. Eswaran. Dynamics of reorientations and reversals of large-scale flow in Rayleigh–Bénard convection. *Journal of Fluid Mechanics*, 668:480–499 (2011).

[15] R. du Puits, C. Resagk, and A. Thess. Breakdown of wind in turbulent thermal convection. *Physical review E, Statistical, nonlinear, and soft matter physics*, 75(1):016302 (2007).

[16] E. Poel, R. Stevens, K. Sugiyama, and D. Lohse. Flow states in two-dimensional Rayleigh–Bénard convection as a function of aspect-ratio and Rayleigh number. *Physics of Fluids*, 24(8):085104 (2012).

[17] C. R. Doering and J. D. Gibbon. *Applied Analysis of the Navier-Stokes Equations.* Cambridge Texts in Applied Mathematics. Cambridge University Press (1995).

[18] F. Chillà and J. Schumacher. New perspectives in turbulent Rayleigh–Bénard convection. *The European Physical Journal E*, 35(7):58 (2012).

[19] H. Jeffreys. Some cases of instability in fluid motion. *Proceedings of the Royal Society of London. Series A, Containing Papers of a Mathematical and Physical Character*, 118(779):195–208 (1928).

[20] A. Pellew and R. V. Southwell. On maintained convective motion in a fluid heated from below. *Proceedings of the Royal Society of London. Series A. Mathematical and Physical Sciences*, 176(966):312–343 (1940).

[21] S. Grossmann and D. Lohse. Scaling in thermal convection: a unifying theory. *Journal of Fluid Mechanics*, 407:27–56 (2000).

[22] K. P. Iyer, J. D. Scheel, J. Schumacher, and K. R. Sreenivasan. Classical 1/3 scaling of convection holds up to Ra $= 10^{15}$. *Proceedings of the National Academy of Sciences*, 117(14):7594–7598 (2020).

[23] G. Ahlers, S. Grossmann, and D. Lohse. Heat transfer and large scale dynamics in turbulent Rayleigh–Bénard convection. *Review of Modern Physics*, 81(2):503–537 (2009).

[24] S. Moller, C. Resagk, and C. Cierpka. Long-time experimental investigation of turbulent superstructures in Rayleigh–Bénard convection by noninvasive simultaneous measurements of temperature and velocity fields. *Experiments in Fluids*, 62(4):64 (2021).

[25] J. E. Wesfreid. Henri Bénard: Thermal convection and vortex shedding. *Comptes Rendus Mécanique*, 345(7):446–466 (2017).

[26] H. Bénard and D. Avsec. Travaux récents sur les tourbillons cellulaires et les tourbillons en bandes. Applications à l'astrophysique et à la météorologie. *Journal de Physique et le Radium*, 9(11):486–500 (1938).

[27] S. J. Vanhook, M. F. Schatz, J. B. Swift, W. D. Mccormick, and H. L. Swinney. Long-wavelength surface-tension-driven Bénard convection: experiment and theory. *Journal of Fluid Mechanics*, 345:45–78 (1997).

[28] M. J. Block. Surface Tension as the Cause of Bénard Cells and Surface Deformation in a Liquid Film. *Nature*, 178(4534):650–651 (1956).

[29] J. R. A. Pearson. On convection cells induced by surface tension. *Journal of Fluid Mechanics*, 4(5):489–500 (1958).

[30] D. A. Nield. Surface tension and buoyancy effects in cellular convection. *Journal of Fluid Mechanics*, 19(3):341–352 (1964).

[31] E. L. Koschmieder. On convection under an air surface. *Journal of Fluid Mechanics*, 30(1):9–15 (1967).

[32] E. L. Koschmieder and M. I. Biggerstaff. Onset of surface-tension-driven Bénard convection. *Journal of Fluid Mechanics*, 167:49–64 (1986).

[33] Lord Rayleigh. LIX. On convection currents in a horizontal layer of fluid, when the higher temperature is on the under side. *The London, Edinburgh, and Dublin Philosophical Magazine and Journal of Science*, 32(192):529–546 (1916).

[34] E.L. Koschmieder and S.G. Pallas. Heat transfer through a shallow, horizontal convecting fluid layer. *International Journal of Heat and Mass Transfer*, 17(9):991–1002 (1974).

[35] J. D. Scheel, M. S. Emran, and J. Schumacher. Resolving the fine-scale structure in turbulent Rayleigh–Bénard convection. *New Journal of Physics*, 15(11):113063 (2013).

[36] J. Scheel and J. Schumacher. Local boundary layer scales in turbulent Rayleigh–Bénard convection. *Journal of Fluid Mechanics*, 758:344–373 (2014).

[37] R. du Puits, C. Resagk, A. Tilgner, F. H. Busse, and A. Thess. Structure of thermal boundary layers in turbulent Rayleigh–Bénard convection. *Journal of Fluid Mechanics*, 572:231–254 (2007).

[38] R. H. Kraichnan. Turbulent Thermal Convection at Arbitrary Prandtl Number. *The Physics of Fluids*, 5(11):1374–1389 (1962).

[39] X. Chavanne, F. Chillà, B. Castaing, B. Hébral, B. Chabaud, and J. Chaussy. Observation of the ultimate regime in Rayleigh–Bénard convection. *Physical Review Letters*, 79(19):3648–3651 (1997).

[40] S. Grossmann and D. Lohse. Multiple scaling in the ultimate regime of thermal convection. *Physics of Fluids*, 23(4):045108 (2011).

[41] L. F. Richardson. Weather prediction by numerical process. *Quarterly Journal of the Royal Meteorological Society*, 48(203):282–284 (1922).

[42] R. Stevens, H. Clercx, and D. Lohse. Heat transport and flow structure in rotating Rayleigh–Bénard convection. *European Journal of Mechanics - B/Fluids*, 40:41–49 (2013).

[43] Y. Tasaka, K. Igaki, T. Yanagisawa, T. Vogt, T. Zuerner, and S. Eckert. Regular flow reversals in Rayleigh–Bénard convection in a horizontal magnetic field. *Physical Review E*, 93(4):043109 (2016).

[44] G. Freund, W. Pesch, and W. Zimmermann. Rayleigh–Bénard convection in the presence of spatial temperature modulations. *Journal of Fluid Mechanics*, 673:318–348 (2011).

[45] M. Jovanovic, D. Zivkovic, and J. Petrović. Rayleigh–Bénard convection instability in the presence of temperature variation at the lower wall. *Thermal Science*, 16(Suppl. 2):281–294 (2012).

[46] X. Zhu, R. J. A. M. Stevens, O. Shishkina, R. Verzicco, and D. Lohse. $Nu \sim Ra^{1/2}$ scaling enabled by multiscale wall roughness in Rayleigh–Bénard turbulence. *Journal of Fluid Mechanics*, 869:R4 (2019).

[47] J. Schumacher and O. Pauluis. Buoyancy statistics in moist turbulent Rayleigh–Bénard convection. *Journal of Fluid Mechanics*, 648:509 – 519 (2010).

[48] M. J. Tummers and M. Steunebrink. Effect of surface roughness on heat transfer in Rayleigh–Bénard convection. *International Journal of Heat and Mass Transfer*, 139:1056–1064 (2019).

[49] T. Hartlep, A. Tilgner, and F. H. Busse. Large scale structures in Rayleigh–Bénard convection at high Rayleigh numbers. *Physical Review Letters*, 91(6):064501 (2003).

[50] T. Hartlep, A. Tilgner, and F. H. Busse. Transition to turbulent convection in a fluid layer heated from below at moderate aspect ratio. *Journal of Fluid Mechanics*, 544:309–322 (2005).

[51] J. von Hardenberg, A. Parodi, G. Passoni, A. Provenzale, and E.A. Spiegel. Large-scale patterns in Rayleigh–Bénard convection. *Physics Letters A*, 372(13):2223–2229 (2008).

[52] J. Bailon-Cuba, M. S. Emran, and J. Schumacher. Aspect ratio dependence of heat transfer and large-scale flow in turbulent convection. *Journal of Fluid Mechanics*, 655:152–173 (2010).

[53] R. J. A. M. Stevens, A. Blass, X. Zhu, R. Verzicco, and D. Lohse. Turbulent thermal superstructures in Rayleigh–Bénard convection. *Physical Review Fluids*, 3(4):041501 (2018).

[54] M. S. Emran and J. Schumacher. Large-scale mean patterns in turbulent convection. *Journal of Fluid Mechanics*, 776:96–108 (2015).

[55] P. J. Sakievich, Y. T. Peet, and R. J. Adrian. Large-scale thermal motions of turbulent Rayleigh–Bénard convection in a wide aspect-ratio cylindrical domain. *International Journal of Heat and Fluid Flow*, 61(Part A):183–196 (2016).

[56] C. Schneide, A. Pandey, K. Padberg-Gehle, and J. Schumacher. Probing turbulent superstructures in Rayleigh–Bénard convection by lagrangian trajectory clusters. *Physical Review Fluids*, 3(11):113501 (2018).

[57] E. Fonda, A. Pandey, J. Schumacher, and K. R. Sreenivasan. Deep learning in turbulent convection networks. *Proceedings of the National Academy of Sciences*, 116(18):8667–8672 (2019).

[58] D. Krug, D. Lohse, and R. J. A. M. Stevens. Coherence of temperature and velocity superstructures in turbulent Rayleigh–Bénard flow. *Journal of Fluid Mechanics*, 887:A2 (2020).

[59] G. Green, D. G. Vlaykov, J. P. Mellado, and M. Wilczek. Resolved energy budget of superstructures in Rayleigh–Bénard convection. *Journal of Fluid Mechanics*, 887:A21 (2020).

[60] C. Cierpka, C. Kästner, C. Resagk, and J. Schumacher. On the challenges for reliable measurements of convection in large aspect ratio Rayleigh–Bénard cells in air and sulfur-hexafluoride. *Experimental Thermal and Fluid Science*, 109:109841 (2019).

[61] M. Raffel, C. E. Willert, F. Scarano, C. J. Kähler, S. T. Wereley, and J. Kompenhans. *Particle Image Velocimetry*. Springer International Publishing (2018).

[62] C. Kästner, C. Resagk, J. Westphalen, M. Junghähnel, C. Cierpka, and J. Schumacher. Assessment of horizontal velocity fields in square thermal convection cells with large aspect ratio. *Experiments in Fluids*, 59(11):171 (2018).

[63] B. S. Mitchell. *An Introduction to Materials Engineering and Science*. John Wiley & Sons (2003).

[64] S. Kumar and S.-W. Kang. Liquid crystals. In F. Bassani, G. L. Liedl, and P. Wyder, editors, *Encyclopedia of Condensed Matter Physics*, pages 111–120. Elsevier, Oxford (2005).

[65] D. Andrienko. Introduction to liquid crystals. *Journal of Molecular Liquids*, 267:520–541 (2018).

[66] G. Vertogen and W. H. de Jeu. *Thermotropic Liquid Crystals, Fundamentals*. Springer Berlin Heidelberg (2011).

[67] K. V. Axenov and S. Laschat. Thermotropic ionic liquid crystals. *Materials*, 4(1):206–259 (2011).

[68] G. Friedel. Les états mésomorphes de la matière. *Annales de Physique*, 9(18):273–474 (1922).

[69] X.-J. Wang and Q.-F. Zhou. *Liquid Crystalline Polymers*. World Scientific (2004).

[70] P. Oswald and P. Pieranski. *Nematic and Cholesteric Liquid Crystals*. CRC Press (2005).

[71] D. Dabiri. Digital particle image thermometry/velocimetry: a review. *Experiments in Fluids*, 46(2):191–241 (2008).

[72] I. Dierking. Chiral liquid crystals: Structures, phases, effects. *Symmetry*, 6(2):444–472 (2014).

[73] S. S. Lee and S.-H. Kim. Controlled encapsulation of cholesteric liquid crystals using emulsion templates. *Macromolecular Research*, 26(12):1054–1065 (2018).

[74] J. V. Gandhi, X.‑D. Mi, and D.‑K. Yang. Effect of surface alignment layers on the configurational transitions in cholesteric liquid crystals. *Physical Review E*, 57(6):6761–6766 (1998).

[75] A. Taugerbeck and C. J. Booth. Design and synthesis of chiral nematic liquid crystals. In J. W. Goodby, P. J. Collings, T. Kato, C. Tschierske, H. Gleeson, and P. Raynes, editors, *Handbook of Liquid Crystals*, volume 3, chapter 14, pages 1–63. American Cancer Society (2014).

[76] J. Stasiek, M. Jewartowski, and T. A. Kowalewski. The use of liquid crystal thermography in selected technical and medical applications – recent development. *Journal of Crystallization Process and Technology*, 4(1):46–59 (2014).

[77] A. Günther and Ph. Rudolf von Rohr. Influence of the optical configuration on temperature measurements with fluid-dispersed TLCs. *Experiments in Fluids*, 32(5):533–541 (2002).

[78] S. Moller, J. König, C. Resagk, and C. Cierpka. Influence of the illumination spectrum and observation angle on temperature measurements using thermochromic liquid crystals. *Measurement Science and Technology*, 30(8):084006 (2019).

[79] W. Chik, M. Barry, S. Thavapalachandran, C. Midekin, J. Pouliopoulos, T.‑W. Lim, G. Sivagangabalan, S. Thomas, D. Ross, A. Mcewan, P. Kovoor, and A. Thiagalingam. High Spatial Resolution Thermal Mapping of Radiofrequency Ablation Lesions Using a Novel Thermochromic Liquid Crystal Myocardial Phantom. *Journal of cardiovascular electrophysiology*, 24(11):1278–1286 (2013).

[80] S. Funatani and N. Fujisawa. Simultaneous measurement of temperature and three velocity components in planar cross section by liquid-crystal thermometry combined with stereoscopic particle image velocimetry. *Measurement Science and Technology*, 13(8):1197–1205 (2002).

[81] T. A. Kowalewski. Particle image velocimetry and thermometry for two-phase flow problems. *Annals of the New York Academy of Sciences*, 972(1):213–222 (2002).

[82] M. Ciofalo, M. Signorino, and M. Simiano. Tomographic particle-image velocimetry and thermography in Rayleigh–Bénard convection using suspended thermochromic liquid crystals and digital image processing. *Experiments in Fluids*, 34(2):156–172 (2003).

[83] D. Schmeling, J. Bosbach, and C. Wagner. Measurements of the dynamics of thermal plumes in turbulent mixed convection based on combined PIT and PIV. *Experiments in Fluids*, 56(6):134 (2015).

[84] I. Ataei-Dadavi, M. Chakkingal, S. Kenjeres, C. R. Kleijn, and M. J. Tummers. Experiments on mixed convection in a vented differentially side-heated cavity filled with a coarse porous medium. *International Journal of Heat and Mass Transfer*, 149:119238 (2020).

[85] H. G. Park and M. Gharib. Experimental study of heat convection from stationary and oscillating circular cylinder in cross flow. *Journal of Heat Transfer*, 123(1):51–62 (2000).

[86] X. Ma, G.E. Karniadakis, H. Park, and M. Gharib. DPIV/T-driven convective heat transfer simulation. *International Journal of Heat and Mass Transfer*, 45(17):3517–3527 (2002).

[87] R. Segura, C. Cierpka, M. Rossi, S. Joseph, H. Bunjes, and C. J. Kähler. Non-encapsulated thermo-liquid crystals for digital particle tracking thermography/velocimetry in microfluidics. *Microfluidics and Nanofluidics*, 14(3-4):445–456 (2013).

[88] R. Segura, M. Rossi, C. Cierpka, and C. J. Kähler. Simultaneous three-dimensional temperature and velocity field measurements using astigmatic imaging of non-encapsulated thermo-liquid crystal (TLC) particles. *Lab on a Chip*, 15(3):660–663 (2015).

[89] C. Huck, H. Zidek, T. Ebner, K. Wagner, and A. Wixforth. Liquid crystal thermography on coated saw devices. *2012 IEEE International Ultrasonics Symposium*, pages 2493–2496 (2012).

[90] H. Babinsky and J. A. Edwards. Automatic liquid crystal thermography for transient heat transfer measurements in hypersonic flow. *Experiments in Fluids*, 21(4):227–236 (1996).

[91] V. U. Kakade, G. D. Lock, M. Wilson, J. M. Owen, and J. E. Mayhew. Accurate heat transfer measurements using thermochromic liquid crystal. part 2: Application to a rotating disc. *International Journal of Heat and Fluid Flow*, 30(5):950–959 (2009).

[92] J. L. Fergason. Cholesteric structure-1 optical properties. *Molecular Crystals*, 1(2):293–307 (1966).

[93] J. L. Fergason. Liquid crystals in nondestructive testing. *Applied Optics*, 7(9):1729–1737 (1968).

[94] D. J. Farina, J. M. Hacker, R. J. Moffat, and J. K. Eaton. Illuminant invariant calibration of thermochromic liquid crystals. *Experimental Thermal and Fluid Science*, 9(1):1–12 (1994).

[95] M. Behle, K. Schulz, W. Leiner, and M. Fiebig. Color-based image processing to measure local temperature distributions by wide-band liquid crystal thermography. *Applied Scientific Research*, 56(2-3):113–143 (1996).

[96] H. Matsuda, K. Ikeda, Y. Nakata, F. Otomo, T. Suga, and Y. Fukuyama. A new thermochromic liquid crystal temperature identification technique using color space interpolations and its application to film cooling effectiveness measurements. *Journal of Flow Visualization and Image Processing*, 7(2):103–121 (2000).

[97] Y. Rao and S. Zang. Calibrations and the measurement uncertainty of wide-band liquid crystal thermography. *Measurement Science and Technology*, 21(1):015105 (2009).

[98] C. Camci, K. Kim, and S. A. Hippensteele. A new hue capturing technique for the quantitative interpretation of liquid crystal images used in convective heat transfer studies. *Journal of Turbomachinery*, 114(4):765–775 (1992).

[99]   V. U. Kakade, G. D. Lock, M. Wilson, J. M. Owen, and J. E. Mayhew. Accurate heat transfer measurements using thermochromic liquid crystal. part 1: Calibration and characteristics of crystals. *International Journal of Heat and Fluid Flow*, 30(5):939–949 (2009).

[100]  D. Dabiri and M. Gharib. Digital particle image thermometry: The method and implementation. *Experiments in Fluids*, 11(2):77–86 (1991).

[101]  D. Dabiri and M. Gharib. The effects of forced boundary conditions on flow within a cubic cavity using digital particle image thermometry and velocimetry (DPITV). *Experimental Thermal and Fluid Science*, 13(4):349–363 (1996).

[102]  N. Fujisawa and S. Funatani. Simultaneous measurement of temperature and velocity in a turbulent thermal convection by the extended range scanning liquid crystal visualization technique. *Experiments in Fluids*, 29(1):158–165 (2000).

[103]  S. Funatani, Nobuyuki Fujisawa, and T. Matsuura. Multipoint calibration technique of liquid crystal thermometry and its application to three-dimensional temperature measurement of thermal convection. *Journal of Flow Visualization and Image Processing*, 7(4):353–366 (2000).

[104]  N. Fujisawa, S. Funatani, and N. Katoh. Scanning liquid-crystal thermometry and stereo velocimetry for simultaneous three-dimensional measurement of temperature and velocity field in a turbulent Rayleigh–Bénard convection. *Experiments in Fluids*, 38(3):291–303 (2004).

[105]  D. Schiepel, D. Schmeling, and Claus Wagner. Simultaneous velocity and temperature measurements in turbulent Rayleigh–Bénard convection based on combined Tomo-PIV and PIT. In *18th International Symposium on the Application of Laser and Imaging Techniques to Fluid Mechanics*, Lisbon, Portugal (2016).

[106]  S. Anders, D. Noto, Y. Tasaka, and S. Eckert. Simultaneous optical measurement of temperature and velocity fields in solidifying liquids. *Experiments in Fluids*, 61(4):113 (2020).

[107]  M. Loesdau, S. Chabrier, and A. Gabillon. Hue and saturation in the RGB color space. In *Lecture Notes in Computer Science*, pages 203–212. Springer International Publishing (2014).

[108]  A. Vadivel S. G. Shaila. *Textual and Visual Information Retrieval using Query Refinement and Pattern Analysis*. Springer Singapore (2018).

[109]  R. G. Kuehni and A. Schwarz. *Color Ordered: A Survey of Color Systems from Antiquity to the Present*. Oxford University Press (2007).

[110]  D. Androutsos, K. N. Plataniotis, and A. N. Venetsanopoulos. A novel Vector-Based Approach to Color Image Retrieval Using a Vector Angular-Based Distance Measure. *Computer Vision and Image Understanding*, 75(1-2):46–58 (1999).

[111]  J. W. Baughn, M. R. Anderson, J. E. Mayhew, and J. D. Wolf. Hysteresis of thermochromic liquid crystal temperature measurement based on hue. *Journal of Heat Transfer*, 121(4):1067–1072 (1999).

[112] M. R. Anderson and J. W. Baughn. Hysteresis in liquid crystal thermography. *Journal of Heat Transfer*, 126(3):339–346 (2004).

[113] D. R. Sabatino, T. J. Praisner, and C. R. Smith. A high-accuracy calibration technique for thermochromic liquid crystal temperature measurements. *Experiments in Fluids*, 28(6):497–505 (2000).

[114] P. Stephan, E. Wagner, and R. Nasarek. Liquid crystal technique for measuring temperature. In Dongqing Li, editor, *Encyclopedia of Microfluidics and Nanofluidics*, pages 1012–1022. Springer US (2008).

[115] R. Wiberg and N. Lior. Errors in thermochromic liquid crystal thermometry. *Review of Scientific Instruments*, 75(9):2985–2994 (2004).

[116] J. L. Hay and D. K. Hollingsworth. Calibration of micro-encapsulated liquid crystals using hue angle and a dimensionless temperature. *Experimental Thermal and Fluid Science*, 18(3):251–257 (1998).

[117] P. T. Ireland and T. V. Jones. The response time of a surface thermometer employing encapsulated thermochromic liquid crystals. *Journal of Physics E: Scientific Instruments*, 20(10):1195–1199 (1987).

[118] D. Mukerji and J. Eaton. Discrete green's function measurements in a single passage turbine model. *Journal of Heat Transfer*, 127(4):366–377 (2005).

[119] P. M. Kodzwa, C. J. Elkins, D. Mukerji, and J. K. Eaton. Thermochromic liquid crystal temperature measurements through a borescope imaging system. *Experiments in Fluids*, 43(4):475–486 (2007).

[120] K. Toriyama, S. Tada, K. Ichimiya, S. Funatani, and Y. Tomita. A new method of temperature measurement using thermochromic liquid crystals (extension of measurable range based on spectral intensity in the narrow-band wavelength). *International Journal of Heat and Mass Transfer*, 92:483–489 (2016).

[121] J. Vejrazka and Ph. Marty. An alternative technique for the interpretation of temperature measurements using thermochromic liquid crystals. *Heat Transfer Engineering*, 28(2):154–162 (2007).

[122] S. Moller, C. Resagk, and C. Cierpka. On the application of neural networks for temperature field measurements using thermochromic liquid crystals. *Experiments in Fluids*, 61(4):111 (2020).

[123] J. L. Hay and D. K. Hollingsworth. A comparison of trichromic systems for use in the calibration of polymer-dispersed thermochromic liquid crystals. *Experimental Thermal and Fluid Science*, 12(1):1–12 (1996).

[124] C. C. Aggarwal. *Neural Networks and Deep Learning.* Springer International Publishing (2018).

[125] A. K. Jain, M. Jianchang, and K. M. Mohiuddin. Artificial neural networks: a tutorial. *Computer*, 29(3):31–44 (1996).

[126] I. Kimura, Y. Kuroe, and M. Ozawa. Application of neural networks to quantitative flow visualization. *Journal of Flow Visualization and Image Processing*, 1(4):261–269 (1993).

[127] H. G. Park, D. Dabiri, and M. Gharib. Digital particle image velocimetry/thermometry and application to the wake of a heated circular cylinder. *Experiments in Fluids*, 30(3):327–338 (2001).

[128] G. Grewal, M. Bharara, J. Cobb, V. Dubey, and D. Claremont. A novel approach to thermochromic liquid crystal calibration using neural networks. *Measurement Science and Technology*, 17(7):1918–1924 (2006).

[129] M. H. Beale, M. T. Hagan, and H. B. Demuth. *Deep Learning Toolbox - User's Guide. Matlab R2021a.* The MathWorks, Inc. URL: https://www.mathworks.com/help/pdf_doc/deeplearning/nnet_ug.pdf (accessed 26 May 2021).

[130] S. Haykin. *Neural Networks and Learning Machines.* Pearson Education (2009).

[131] K. Levenberg. A method for the solution of certain non-linear problems in least squares. *Quarterly of Applied Mathematics*, 2(2):164–168 (1944).

[132] D. W. Marquardt. An algorithm for least-squares estimation of nonlinear parameters. *Journal of the Society for Industrial and Applied Mathematics*, 11(2):431–441 (1963).

[133] H. Yu and B. M. Wilamowski. Levenberg-Marquardt Training. In B. M. Wilamowski and J. D. Irwin, editors, *The Industrial Electronics Handbook*, volume 5, chapter 12, pages 1–16. CRC Press (2011).

[134] F. Burden and D. Winkler. Bayesian regularization of Neural Networks. In D. J. Livingstone, editor, *Artificial Neural Networks*, chapter 3, pages 23–42. Humana Press (2008).

[135] R. Caruana, S. Lawrence, and L. Giles. Overfitting in Neural Nets: Backpropagation, Conjugate Gradient, and Early Stopping. In *Proceedings of the 13th International Conference on Neural Information Processing Systems*, NIPS'00, page 381–387, Cambridge, MA, USA (2000).

[136] D. M. Hawkins. The Problem of Overfitting. *Journal of Chemical Information and Computer Sciences*, 44(1):1–12 (2004).

[137] T. Hartlep. *Strukturbildung und Turbulenz. Eine numerische Studie zur turbulenten Rayleigh–Bénard Konvektion.* PhD thesis, Georg-August-Universität Göttingen (2004).

[138] C. A. Moore, Jr. and S. J. Kline. Some effects of vanes and turbulence in two-dimensional wide-angle subsonic diffusers. Technical Report TN 4080, National Advisory Committee for Aeronautics (NACA), Washington (1958).

[139] D. L. Cochran and S. J. Kline. Use of short flat vanes for producing efficient wide-angle two-dimensional subsonic diffusers. Technical Report TN 4309, National Advisory Committee for Aeronautics (NACA), Washington (1958).

[140] N. Granzow. Supercontinuum white light lasers: a review on technology and applications. In Bernhard Zagar, Pawel Mazurek, Maik Rosenberger, and Paul-Gerald Dittrich, editors, *Photonics and Education in Measurement Science 2019* (2019).

[141] J. König, S. Moller, N. Granzow, and C. Cierpka. On the application of a supercontinuum white light laser for simultaneous measurements of temperature and velocity fields using thermochromic liquid crystals. *Experimental Thermal and Fluid Science*, 109:109914 (2019).

[142] D. Schmeling, J. Bosbach, and C. Wagner. Simultaneous measurement of temperature and velocity fields in convective air flows. *Measurement Science and Technology*, 25(3):035302 (2014).

[143] A. Henderson. *Guide to Laser Safety*. Springer US (1997).

[144] Keigo Iizuka. *Engineering Optics*. Springer-Verlag (2019).

[145] A. K. Prasad. Stereoscopic particle image velocimetry. *Experiments in Fluids*, 29(2):103–116 (2000).

[146] Gerd Keiser. *Optical Fiber Communications*. McGraw-Hill Book Co. (2010).

[147] N. J. Lawson and J. Wu. Three-dimensional particle image velocimetry: error analysis of stereoscopic techniques. *Measurement Science and Technology*, 8(8):894–900 (1997).

[148] C. E. Willert. Assessment of camera models for use in planar velocimetry calibration. *Experiments in Fluids*, 41(1):135–143 (2006).

[149] Y. I. Abdel-aziz and H. Karara. Direct Linear Transformation from Comparator Coordinates into Object Space Coordinates in Close-Range Photogrammetry. *Photogrammetric Engineering and Remote Sensing*, 81(2):103–107 (1971).

[150] R. Tsai. A versatile camera calibration technique for high-accuracy 3d machine vision metrology using off-the-shelf TV cameras and lenses. *IEEE Journal on Robotics and Automation*, 3(4):323–344 (1987).

[151] S. M. Soloff, R. J. Adrian, and Z.-C. Liu. Distortion compensation for generalized stereoscopic particle image velocimetry. *Measurement Science and Technology*, 8(12):1441–1454 (1997).

[152] B. Wieneke. Stereo-PIV using self-calibration on particle images. *Experiments in Fluids*, 39(2):267–280 (2005).

[153] J. Westerweel. *Digital Particle Image Velocimetry - Theory and Application*. PhD thesis, Delft University of Technology (1993).

[154] R. J. Adrian and J. Westerweel. *Particle Image Velocimetry*. Cambridge University Press (2010).

[155] C. E. Willert and M. Gharib. Digital particle image velocimetry. *Experiments in Fluids*, 10(4):181–193 (1991).

[156]  H. Lamb. *Hydrodynamics*. Cambridge Mathematical Library. Cambridge University Press (1993).

[157]  K. Stapor. *Introduction to Probabilistic and Statistical Methods with Examples in R*. Springer International Publishing (2020).

[158]  N. A. Fomin. *Speckle Photography for Fluid Mechanics Measurements*. Springer Berlin Heidelberg (1998).

[159]  D. Dabiri and C. Pecora. *Particle Tracking Velocimetry*. Institute of Physics Publishing (2019).

[160]  G. E. Elsinga, F. Scarano, B. Wieneke, and B. W. van Oudheusden. Tomographic particle image velocimetry. *Experiments in Fluids*, 41(6):933–947 (2006).

[161]  M. Novara, K. J. Batenburg, and F. Scarano. Motion tracking-enhanced MART for tomographic PIV. *Measurement Science and Technology*, 21(3):035401 (2010).

[162]  C. Cierpka, M. Rossi, R. Segura, and C. J. Kähler. On the calibration of astigmatism particle tracking velocimetry for microflows. *Measurement Science and Technology*, 22(1):015401 (2010).

[163]  R. Barnkob, C. J. Kähler, and M. Rossi. General defocusing particle tracking. *Lab on a Chip*, 15(17):3556–3560 (2015).

[164]  C. Cierpka, R. Hain, and N. A. Buchmann. Flow visualization by mobile phone cameras. *Experiments in Fluids*, 57(6):108 (2016).

[165]  A. A. Aguirre-Pablo, M. K. Alarfaj, E. Q. Li, J. F. Hernández-Sánchez, and S. T. Thoroddsen. Tomographic Particle Image Velocimetry using Smartphones and Colored Shadows. *Scientific Reports*, 7(1):3714 (2017).

[166]  T. Käufer, J. König, and C. Cierpka. Stereoscopic PIV measurements using low-cost action cameras. *Experiments in Fluids*, 62(3):57 (2021).

[167]  J. Westerweel and F. Scarano. Universal outlier detection for PIV data. *Experiments in Fluids*, 39(6):1096–1100 (2005).

[168]  R. D. Keane and R. J. Adrian. Optimization of particle image velocimeters: II. Multiple pulsed systems. *Measurement Science and Technology*, 2(10):963–974 (1991).

[169]  S. Scharnowski and C. J. Kähler. Particle image velocimetry - Classical operating rules from today's perspective. *Optics and Lasers in Engineering*, 135:106185 (2020).

[170]  K. R. Rao, D. N. Kim, and J.-J. Hwang. *Fast Fourier Transform - Algorithms and Applications*. Springer Publishing (2010).

[171]  M. Weeks. *Digital Signal Processing Using MATLAB & Wavelets*. Jones and Bartlett Publishers (2010).

[172]  D. T. J. Hurle, E. Jakeman, and E. R. Pike. On the solution of the Bénard problem with boundaries of finite conductivity. *Proceedings of the Royal Society of London. Series A. Mathematical and Physical Sciences*, 296(1447):469–475 (1967).

[173] R. Verzicco. Effects of nonperfect thermal sources in turbulent thermal convection. *Physics of Fluids*, 16(6):1965–1979 (2004).

[174] P. Vieweg, J. Scheel, and J. Schumacher. Supergranule aggregation for constant heat flux-driven turbulent convection. *Physical Review Research*, 3:013231 (2021).

[175] R. G. Budynas and A. M. Sadegh. *Roark's Formulas for Stress and Strain.* McGraw-Hill Book Co (2020).

[176] E. L. Bourhis. *Glass.* Wiley-VCH (2014).

[177] B. Weller, K. Härth, S. Tasche, and S. Unnewehr. *Glass in Building.* Birkhäuser Verlag (2009).

[178] A. Lyons. *Materials for Architects and Builders.* Taylor & Francis (2010).

[179] G. N. Tiwari and R. K. Mishra. *Advanced Renewable Energy Sources.* The Royal Society of Chemistry (2012).

[180] *VDI Heat Atlas.* Springer Berlin Heidelberg (2010).

[181] M. Raupach and T. Büttner. *Concrete Repair to EN 1504.* CRC Press, 2014.

[182] W. S. Janna. *Engineering Heat Transfer. Second Edition.* CRC Press (1999).